

**CHARACTERISTICS AND MECHANISMS OF COASTAL  
UPWELLING IN THE GULF OF THAILAND**



**Miss Pacharamon Sripoonpan**

**จุฬาลงกรณ์มหาวิทยาลัย  
CHULALONGKORN UNIVERSITY**

**A Thesis Submitted in Partial Fulfillment of the Requirements  
for the Degree of Master of Science in Marine Science  
Department of Marine Science  
FACULTY OF SCIENCE  
Chulalongkorn University  
Academic Year 2019  
Copyright of Chulalongkorn University**

ลักษณะและกลไกการเกิดปรากฏการณ์น้ำผุดในอ่าวไทย



วิทยานิพนธ์นี้เป็นส่วนหนึ่งของการศึกษาตามหลักสูตรปริญญาวิทยาศาสตรมหาบัณฑิต

สาขาวิชาวิทยาศาสตร์ทางทะเล ภาควิชาวิทยาศาสตร์ทางทะเล

คณะวิทยาศาสตร์ จุฬาลงกรณ์มหาวิทยาลัย

ปีการศึกษา 2562

ลิขสิทธิ์ของจุฬาลงกรณ์มหาวิทยาลัย



Thesis Title                    CHARACTERISTICS AND MECHANISMS  
  OF COASTAL UPWELLING IN THE GULF  
  OF THAILAND  
By                                    Miss Pacharamon Sripoonpan  
Field of Study                    Marine Science  
Thesis Advisor                  Assistant Professor SURIYAN SARAMUL,  
  Ph.D.

---

Accepted by the FACULTY OF SCIENCE, Chulalongkorn  
University in Partial Fulfillment of the Requirement for the Master of  
Science

..... Dean of the FACULTY OF  
  SCIENCE  
(Professor POLKIT SANGVANICH, Ph.D.)

THESIS COMMITTEE

..... Chairman  
(Assistant Professor SANIT  
PIYAPATTANAKORN, Ph.D.)

..... Thesis Advisor  
(Assistant Professor SURIYAN SARAMUL,  
Ph.D.)

..... Examiner  
(Assistant Professor PATAMA SINGHRUCK,  
Ph.D.)

..... External Examiner  
(Jitraporn Phaksopa, Ph.D.)

พรหมน ศรีพูนพันธ์ : ลักษณะและกลไกการเกิดปรากฏการณ์น้ำผุดในอ่าวไทย. (  
**CHARACTERISTICS AND MECHANISMS OF COASTAL  
 UPWELLING IN THE GULF OF THAILAND**) อ.ที่ปรึกษาหลัก : ผศ.  
 ดร.สุริยชัย สาระมูล

ศึกษาลักษณะและกลไกการเกิดปรากฏการณ์น้ำผุดในอ่าวไทยโดยใช้ 2 วิธีการ คือ 1) คำนวณการเกิดปรากฏการณ์น้ำผุดด้วยการคำนวณ Ekman transport ( $UI_{ET}$ ) และดัชนีบ่งชี้การเกิดปรากฏการณ์น้ำผุดจากผลความแตกต่างของอุณหภูมิบริเวณชายฝั่งและบริเวณกลางอ่าวไทย ( $UI_{SS}$ ) และ 2) แบบจำลองอุทกพลศาสตร์แบบ 3 มิติ Delft3D-FLOW ภายใต้อิทธิพลของน้ำขึ้นน้ำลง ลมที่เปลี่ยนแปลงเชิงพื้นที่ อุณหภูมิพื้นทะเล ความเค็ม ปริมาณน้ำท่าและความร้อน ผลการศึกษาพบว่า  $UI_{ET}$  แสดงโอกาสการเกิดปรากฏการณ์น้ำผุดส่วนใหญ่ตามแนวชายฝั่งตะวันตกของอ่าวไทยในช่วงมรสุมตะวันออกเฉียงเหนือในเดือนมกราคมจนถึงเดือนมีนาคม และตามแนวชายฝั่งตะวันออกในช่วงมรสุมตะวันตกเฉียงใต้ในเดือนสิงหาคมจนถึงเดือนตุลาคม ผลจาก  $UI_{SS}$  แสดงโอกาสเกิดปรากฏการณ์น้ำผุดตามแนวชายฝั่งตะวันตกของอ่าวไทยตอนกลางและชายฝั่งตะวันตกของแหลมญวนในช่วงมรสุมตะวันออกเฉียงเหนือและมรสุมตะวันตกเฉียงใต้ ส่วนผลการศึกษาจากแบบจำลองพบว่ามีน้ำชายฝั่งที่มีอุณหภูมิต่ำกว่าอุณหภูมิของน้ำบริเวณกลางอ่าวไทยเกิดขึ้นอย่างชัดเจนบริเวณชายฝั่งตะวันตกของอ่าวไทยตอนบนและอ่าวไทยตอนกลาง และชายฝั่งตะวันตกของแหลมญวนในช่วงมรสุมตะวันออกเฉียงเหนือและมรสุมตะวันตกเฉียงใต้ และเกิดขึ้นเล็กน้อยในช่วงเดือนมีนาคมและตุลาคม โอกาสการเกิดปรากฏการณ์น้ำผุดที่พิจารณาจาก  $UI_{ET}$  มีความแตกต่างจากผลการศึกษาจาก  $UI_{SS}$  และแบบจำลอง เนื่องจาก  $UI_{ET}$  แสดงปรากฏการณ์น้ำผุดจากอิทธิพลของ Ekman transport และทิศทางลมโดยตรง ในขณะที่  $UI_{SS}$  พิจารณาผลจากความแตกต่างของอุณหภูมิมิวน้ำพื้นทะเล เช่นเดียวกับแบบจำลองที่พิจารณาจากความแตกต่างของอุณหภูมิมิวน้ำพื้นทะเล ซึ่งเกิดภายใต้อิทธิพลของน้ำขึ้นน้ำลง ลม อุณหภูมิ ความเค็ม ปริมาณน้ำท่าและความร้อน ซึ่งลักษณะปรากฏการณ์น้ำผุดที่พบอาจมีความสำคัญต่อการจัดการและอนุรักษ์ทรัพยากรทางทะเลรวมทั้งเดิมเดิมความรู้เกี่ยวกับลักษณะการกระจายตัวสารอาหารในอ่าวไทยให้สมบูรณ์



สาขาวิชา วิทยาศาสตร์ทางทะเล

ลายมือชื่อนิติ

ปีการศึกษา 2562

ลายมือชื่อ อ.ที่ปรึกษาหลัก

# # 6172011523 : MAJOR MARINE SCIENCE

KEYWORD upwelling, Gulf of Thailand, upwelling index

D:

Pacharamon Sripoonpan : CHARACTERISTICS AND MECHANISMS OF COASTAL UPWELLING IN THE GULF OF THAILAND. Advisor: Asst. Prof. SURIYAN SARAMUL, Ph.D.

The characteristics and mechanisms of coastal upwelling in the Gulf of Thailand was investigated through 2 approaches; 1) Ekman transport upwelling index ( $UI_{ET}$ ) and sea surface temperature upwelling index ( $UI_{SST}$ ), and 2) Hydrodynamics model DELFT3D-FLOW under the influences of tide, spatially varying wind, water temperature, salinity and river discharge. The  $UI_{ET}$  indicated favorable upwelling conditions along the west coast of the GoT mostly during northeast monsoon in January and 1<sup>st</sup> inter-monsoon in March, while the favorable upwelling condition indicated by  $UI_{SST}$  was found along the east coast during southwest monsoon in August and 2<sup>nd</sup> inter-monsoon in October. The model expressed the favorable upwelling conditions along the west coast of the upper gulf and the west coast of Ca Mau Cape during northeast monsoon and southwest monsoon. Besides, the model results shown the upwelling with the obvious cooler coastal water along the west coast of the upper gulf and the central gulf and along the west coast of Ca Mau Cape during northeast monsoon and southwest monsoon, and with slightly cooler coastal water during 1<sup>st</sup> inter-monsoon in March and 2<sup>nd</sup> inter-monsoon in October. The coastal upwelling associated with  $UI_{ET}$  was different from  $UI_{SST}$  and the model simulation. The  $UI_{ET}$  indicated the wind-driven coastal upwelling directly connecting with directions of Ekman transport and wind. In contrast, the  $UI_{SST}$  was estimated using the satellite-observed sea surface temperature. Also, the upwelling found in the model simulation was generated using different forces, e.g., tide, wind, temperature, salinity, river discharge and heat. The tracked coastal upwelling in this study might be vital for fisheries resources managements and conservation, and to complete the knowledge of nutrient distributions in the Gulf of Thailand.

CHULALONGKORN UNIVERSITY

Field of Study: Marine Science

Student's Signature

Academic Year: 2019

Advisor's Signature

Year:

.....

## ACKNOWLEDGEMENTS

I gratefully gratitude to the funding received towards my Master study from H.M. the King Bhumibhol Adulyadej's 72nd Birthday Anniversary Scholarship.

I sincerely thank my thesis advisor, Assistant Professor Dr. Suriyan Saramul, for the guidance, patience and encouragement in carrying out this work.

I also would like to thank thesis committee; Assistant Professor Dr. Patama Singhruck, and Dr. Jitraporn Phaksopa, for their encouragements, comments and questions.

I also thank my family and my friends for all supporting me.

Pacharamon Sripoonpan

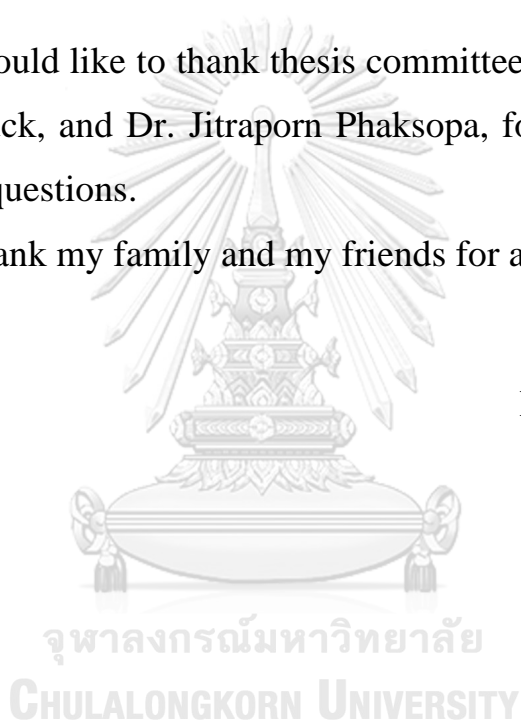


## TABLE OF CONTENTS

	<b>Page</b>
ABSTRACT (THAI) .....	iii
ABSTRACT (ENGLISH).....	iv
ACKNOWLEDGEMENTS .....	v
TABLE OF CONTENTS.....	vi
CHAPTER 1 .....	6
Introduction.....	6
1.1. Rational .....	6
1.2. Hypothesis .....	7
1.3. Objective .....	8
1.4. Study framework .....	8
1.5. Expected beneficial outcome.....	8
CHAPTER 2 .....	9
Theory and literature reviews .....	9
2.1. Upwelling .....	9
2.2. The Gulf of Thailand (GoT).....	11
2.3. Satellite observation of upwelling.....	11
2.4. Delft3D modeling suite .....	11
2.5. Coastal High Frequency (HF) radar system .....	15
3.1. Upwelling index estimations .....	16
3.2. Numerical model .....	18
CHAPTER 4 .....	23
Results and discussions.....	23
4.1. Upwelling index estimations .....	23
4.2. Numerical model results.....	33
4.3. Surface current comparison.....	42

4.4. Seasonal sea surface temperature and current in the GoT.....	49
4.5. Seasonal distribution of water temperature in the GoT.....	53
4.6. Seasonal sea surface salinity in the GoT .....	57
4.7. Seasonal distribution of water salinity in the GoT.....	58
4.8. Seasonal distribution of vertical velocity in the GoT.....	63
4.9. Simulation-oriented the coastal upwelling in the GoT.....	67
4.10. Seasurface temperature along southeastern Vietnam coast during southwest monsoon .....	68
CHAPTER 5 .....	74
Conclusion and Suggestions .....	74
5.1. Conclusion.....	74
5.2. Suggestions.....	75
APPENDIX A. Upwelling Index Estimations .....	76
APPENDIX B. Numerical Model.....	82
REFERENCES .....	162
VITA.....	167

## List of Figures

Fig. 2.1. Zonal wind stress (left), Ekman transport (center), and ocean current gyres (right) of northern hemisphere. ....	10
Fig. 2.2. Coastal upwelling of northern hemisphere. ....	10
Fig. 2.3. Coastal HF radar system. ....	15
Fig. 3.1. Three-dimensional numerical model study area. Red solid lines depict open boundaries, while red dots represent observed water level stations. Area of upwelling index study is shown by the black box. ....	16
Fig. 4.1. Surface wind vector (m/s) of a) Northeast monsoon, b) 1 <sup>st</sup> Inter-monsoon, c) Southwest monsoon, and d) 2 <sup>nd</sup> Inter- monsoon. ....	26
Fig. 4.2. Ekman transport (m <sup>3</sup> /s/m) of a) Northeast monsoon, b) 1 <sup>st</sup> Inter-monsoon, c) Southwest monsoon, and d) 2 <sup>nd</sup> Inter- monsoon. ....	27
Fig. 4.3. Upwelling condition associated with Ekman transport upwelling index ( $UI_{ET}$ ) of a) Northeast monsoon, b) 1 <sup>st</sup> Inter-monsoon, c) Southwest monsoon, and d) 2 <sup>nd</sup> Inter- monsoon. ....	28
Fig. 4.4. Averaged sea surface temperature in degree Celsius during 2003-2018 of a) Northeast monsoon, b) 1 <sup>st</sup> Inter-monsoon, c) Southwest monsoon, and d) 2 <sup>nd</sup> Inter- monsoon. ....	31
Fig. 4.5. Sea surface temperature upwelling index ( $UI_{SST}$ ) (left) and temperature cross section profile (right) of line number 1 (upper) and line number 2 (bottom) extracted from shoreline to offshore of a) Northeast monsoon, b) 1 <sup>st</sup> Inter-monsoon, c) Southwest monsoon, and d) 2 <sup>nd</sup> Inter- monsoon. Blue and red dots represent favorable and unfavorable upwelling condition, respectively. ....	33
Fig. 4.6. Water level, phase and amplitude comparison between first simulation and observed data during January 1-31, 2004 at Kuantan Station. ....	35
Fig. 4.7. Water level, phase and amplitude comparison between first simulation and observed data during January 1-31, 2004 at Ko Lak Station. ....	35
Fig. 4.8. Water level, phase and amplitude comparison between calibration and observed data during January 1-31, 2004 in case Tide2D at Kuantan Station. ....	36
Fig. 4.9. Water level, phase and amplitude comparison between calibration and observed data during January 1-31, 2004 in case Tide2D at Ko Lak Station. ....	36
Fig. 4.10. Water level, phase and amplitude comparison between validation and observed data during January 1-31, 2013 at Kuantan Station. ....	39

Fig. 4.11. Water level, phase and amplitude comparison between validation and observed data during January 1-31, 2013 at Ko Lak Station.....	39
Fig. 4.12. Amphidromic system (amplitude and phase) of M2, S2, K1 and O1 tides found in the GoT.....	42
Fig. 4.13. Coastal HF radar system areas: Upper, East1, East2, and Lower coast (Black patches).....	43
Fig. 4.14. %RMSE and %MAE of surface current velocity off the Upper coast during February 1-28, 2019 in case Wind2D.....	45
Fig. 4.15. %RMSE and %MAE of surface current velocity off the East1 coast during February 1-28, 2019 in case Wind2D.....	46
Fig. 4.16. %RMSE and %MAE of surface current velocity off the East2 coast during February 1-28, 2019 in Wind2D.....	47
Fig. 4.17. %RMSE, %MAE of surface current velocity off the Lower coast during February 1-28, 2019 in case Wind2D.....	48
Fig. 4.18. Averaged 6-hourly wind stress vectors cover the model domain during January 1-December 31, 2012. Red box represents during northeast monsoon. Blue represents during southwest monsoon. ....	49
Fig. 4.19. Seasonal sea surface temperature and current of a) Northeast monsoon, b) 1 <sup>st</sup> Inter-monsoon, c) Southwest monsoon, and d) 2 <sup>nd</sup> Inter- monsoon. ....	50
Fig. 4.20. Seasonal sea surface temperature cross section profile (right) of line number 1 (upper) and line number 2 (bottom) extracted from shoreline to offshore of a) Northeast monsoon, b) 1 <sup>st</sup> Inter-monsoon, c) Southwest monsoon, and d) 2 <sup>nd</sup> Inter-monsoon.....	52
Fig. 4.21. The distribution of monthly averaged water temperature at depth 10, 26, 40 and 50 m in the GoT of Northeast monsoon. ....	54
Fig. 4.22. The distribution of monthly avreaged water temperature at depth 2, 20, 40 and 50 m in the GoT of 1 <sup>st</sup> Inter-monsoon.....	55
Fig. 4.23. The distribution of monthly averaged water temperature at depth 2, 26, 30 and 50 m in the GoT of Southwest monsoon.....	56
Fig. 4.24. The distribution of monthly averaged water temperature at depth 2, 24, 28 and 50 m in the GoT of 2 <sup>nd</sup> Inter-monsoon.....	57
Fig. 4.25. The distribution of monthly averaged sea surface salinity in the GoT of a) Northeast monsoon, b) 1 <sup>st</sup> Inter-monsoon, c) Southwest monsoon, and d) 2 <sup>nd</sup> Inter-monsoon.....	58



Fig. 4.26. The distribution of monthly averaged water salinity at depth 10, 26, 40 and 50 m in the GoT of Northeast monsoon.....	59
Fig. 4.27. The distribution of monthly averaged water salinity at depth 2, 14, 40 and 50 m in the GoT of 1 <sup>st</sup> Inter-monsoon. ....	61
Fig. 4.28. The distribution of monthly averaged water salinity at depth 2, 14, 30 and 50 m in the GoT of Southwest monsoon. ....	62
Fig. 4.29. The distribution of monthly averaged water salinity at depth 2, 14, 30 and 50 m in the GoT of 2 <sup>nd</sup> Inter-monsoon.....	63
Fig. 4.30. The distribution of monthly averaged vertical velocity at depth 2, 26, 40 and 50 m in the GoT of Northeast monsoon.....	64
Fig. 4.31. The distribution of monthly averaged vertical velocity at depth of 2, 20, 40 and 50 m in the GoT of 1 <sup>st</sup> Inter-monsoon.....	65
Fig. 4.32. The distribution of monthly averaged vertical velocity at depth 2, 26, 30 and 50 m in the GoT of Southwest monsoon.....	66
Fig. 4.33. The distribution of monthly averaged vertical velocity at depth 2, 24, 28 and 50 m in the GoT of 2 <sup>nd</sup> Inter-monsoon.....	67
Fig. 4.34. Upwelling area along southeastern coast of Vietnam. ....	69
Fig. 4.35. Averaged monthly sea surface temperature in degree Celsius in June (upper left), July (upper right), August (lower left) and September (lower right) along southeastern coast of Vietnam shown as the red box in Fig. 4.34. ....	70
Fig. 4.36. Sea surface temperature in degree Celsius along southeastern coast of Vietnam in June (upper left) at depth 36 m, July (upper right) at depth 28 m, August (lower left) at depth 24 m and September (lower right) at depth 26 m. ....	71
Fig. 4.37. Vertical velocity distribution (m/s) along southeastern coast of Vietnam in June (upper left) at depth 36 m, July (upper right) at depth 28 m, August (lower left) at depth 24 m and September (lower right) at depth 26 m.....	72
Fig. 4.38. Water salinity distribution (ppt) along southeastern coast of Vietnam in June (upper left) at depth 36 m, July (upper right) at depth 28 m, August (lower left) at depth 24 m and September (lower right) at depth 26 m.....	73
Fig. B40. The distributions of monthly averaged vertical velocity of Northeast monsoon in GoT at depths of 2-70 m. ....	143
Fig. B41. The distributions of monthly averaged vertical velocity of 1 <sup>st</sup> Inter-monsoon in GoT at depths of 2-70 m. ....	149

- Fig. B42. The distributions of monthly averaged vertical velocity of Southwest monsoon in GoT at depths of 2-70 m. .... 155
- Fig. B43. The distributions of monthly averaged vertical velocity of 2<sup>nd</sup> Inter-monsoon in GoT at depths of 2-70 m. .... 161



## List of Tables

Table 4.1. RMSE, MAE, $R^2$ and skill scores of first simulation and Tide2D at 11 stations. ....	37
Table 4.2. Vectorial difference (d) and root summed square vector difference (RSS) of calibrated model (Tide2D) at 11 stations. ....	37
Table 4.3. Amplitude and phase of water levels between calibration (Tide2D) and observation at Kuantan station. ....	38
Table 4.4. Amplitude and phase of water levels between calibration and observation (Tide2D) at Ko Lak station. ....	38
Table 4.5. RMSE, MAE, $R^2$ and skill scores of validated model. ....	40
Table 4.6. Vectorial difference (d) and root summed square vector difference (RSS) of validated model. ....	40
Table 4.9. %RMSE, %MAE and average of surface current velocity off the Upper coast during February 1-28, 2019 in case Wind2D. ....	45
Table 4.10. %RMSE, %MAE and average of surface current velocity off the East1 coast during February 1-28, 2019 in Wind2D. ....	46
Table 4.11. %RMSE, %MAE and average of surface current velocity off the East2 coast during February 1-28, 2019 in case Wind2D. ....	47
Table 4.12. %RMSE, %MAE and average of surface current velocity off the Lower coast during February 1-28, 2019 in case Wind2D. ....	48

# CHAPTER 1

## Introduction

### 1.1. Rational

Coastal upwelling is an important physical process of the dense, cooler and nutrient-rich water moving upward to displace the warmer and nutrient-depleted surface water (Lehmann and Myrberg, 2008). Therefore, the upwelling usually links to the high biological productivity, powerful economic and major fisheries region (Hein et al., 2013; Ndah et al., 2017).

Wind-driven coastal upwelling is generated by along shore winds which induce Ekman transport (ET) in the direction perpendicular to shoreline (Teresa K and James F, 2001). Hence, the Ekman transport upwelling index ( $UI_{ET}$ ), calculated using wind stress components at coastal sea surface, can be used to indicate the magnitude of amount of water upwelling that replaces the surface water driven offshore (Bakun, 1973, 1975). In addition, the sea surface temperature (SST) upwelling index ( $UI_{SST}$ ) is also used as an indicator of coastal upwelling, which is calculated as the difference of coastal and oceanic sea surface temperature at the same latitude (Cropper et al., 2014; Kok et al., 2017).

Coastal upwelling off the west coast of Hainan Island in China Sea was detected by Lü et al. (2008) using satellite remote sensing sea surface temperature, field observations and numerical modeling. The presence of upwelling was verified by monthly SST satellite images showing the coldest water and by field observations showing uplifting contours of decreasing temperature and increasing salinity. Besides, the low SST center and the upwelling velocity were numerically modeled as an evidence of upwelling off west coast of Hainan Island.

Additionally, the contributors of coastal upwelling occurring along the east coast of Peninsular Malaysia (ECPM) throughout southwest monsoon were examined by Kok et al. (2017) using Ekman transport calculation, wind-induced upwelling index ( $UI_{ET}$ ) calculation and SST upwelling index ( $UI_{SST}$ ). Along southern and middle coast, Ekman transport was mostly eastward and perpendicular to coastline in offshore direction, while along north coastline Ekman transport was southeastward parallel to the coast. Maximum upwelling happened when Ekman transport was perpendicular to the coast. The intensity of Ekman transport and the positive values of

upwelling index which indicated favorable upwelling increased from May and peaked in August before declining in September.

Coastal upwelling in the Gulf of Thailand (GoT) was found along east coast during northeast monsoon and along southwest coast during southwest monsoon (Cushing, 1971; Robinson, 1974; Sojisuporn et al., 2010). This finding is associated with the circulation pattern found in Yanagi and Takao (1998a) during southwest monsoon that counterclockwise circulation flows toward the shore along the western coast. Additionally, Singhruck (2001) applied ocean color data to study circulation features in the GoT. The study showed high chlorophyll\_a concentration as a proxy of phytoplankton that might be the evidence of upwelling was found all year round around Samui Island.

Even the upwelling in the GoT has been mentioned in researches above, the knowledge is still incomplete. Understanding coastal upwelling will provide insight geophysical mapping and mechanism of fisheries resources (e.g., habitats, fish eggs and larvae grounds). They would be required for the development of future actions to draw a policy for efficiency fisheries managements including fisheries law, habitat rehabilitation and fisheries enhancement and to deal with fishery problems like exploitation in the GoT (Ahmed et al., 2007; Ingthamjitr and Sricharoendham, 2016; Kongseng et al., 2020b).

Thus, this study aims to analyze the characteristics and mechanisms of coastal upwelling found in the GoT (see black box in Fig. 3.1) under the influences of tide, meteorological forcing, sea surface temperature and salinity using three-dimensional numerical model. Furthermore, to define the area of upwelling in the study area the classical wind-driven coastal upwelling will be studied (black box in Fig. 1.1) through the calculation of upwelling index related to Ekman transport ( $UI_{ET}$ ) and sea surface temperature gradient ( $UI_{SST}$ ).

## 1.2. Hypothesis

The locations of coastal upwelling found in the Gulf of Thailand are seasonally alternated. They occur on the east coast during northeast monsoon and vice versa during southwest monsoon.

### 1.3. Objective

To reveal characteristics and mechanisms of coastal upwelling in the GoT

### 1.4. Study framework

In this study coastal upwelling in the GoT is investigated through two methods: (1) upwelling index estimations and (2) hydrodynamic model (Delft3D-FLOW).

The upwelling index estimation was applied to figure out the possibility of coastal upwelling locations in the study area of 98.5 °E to 105.5 °E and 5.5 °N to 14.0 °N (see Fig. 1.1) through two approaches: (1) Ekman transport upwelling index ( $UI_{ET}$ ) estimation using wind stress components at coastal sea surface to indicate the magnitude of amount of water upwelling to replace the surface water driven offshore, and (2) sea surface temperature index ( $UI_{SST}$ ) estimation using the difference of coastal and oceanic sea surface temperature at the same latitude.

The two-dimensional model covering the study area of 98.0 °E to 112.0 °E and 2.0 °N to 15.0 °N (see Fig. 3.1), was prepared, calibrated and validated. Then, the model was simulated in three dimensions for one-year period under the influences of tides, winds, temperature, salinity and river discharge.

### 1.5. Expected beneficial outcome

To better understand the characteristics and mechanisms of upwelling in the GoT which could be useful for living resource management

## CHAPTER 2

### Theory and literature reviews

#### 2.1. Upwelling

In open ocean, upwelling is associated with spatial variations of zonal wind stresses, patterns of Ekman transport, and ocean current gyres (see Fig. 2.1). When wind is blowing along and beating on ocean surface, the constancy and slowly varying current, Ekman transport, is generated. Due to effects of wind stress and Earth's rotation, the current is flowing in different direction from the wind direction. Typically the speed of Ekman flow is 0.05-0.1 m/s with the depth of 1-100 m extent from the surface (Teresa and James, 2019). The spatial variations of zonal wind stresses with the Coriolis effect cause Ekman transport in the right and the left of the wind direction in northern hemisphere and southern hemisphere, respectively. Ekman convergence contributes to a clockwise current gyre of high sea surface with downwelling in subtropics, while Ekman divergence contributes to a counterclockwise current gyre of low sea surface with upwelling in subpolar.

In coastal ocean of northern hemisphere, the wind blowing parallel to the right of coastline and the Coriolis force leads to Ekman transport and Ekman pumping (see Fig. 2.2). The deeper water is pumped to the surface water which is known as coastal upwelling. The upwelled water is colder and higher of nutrient concentration providing staple energy sources for marine organism, then the upwelling regions offer high fisheries production and major fishing grounds (Kuo et al., 2000b).

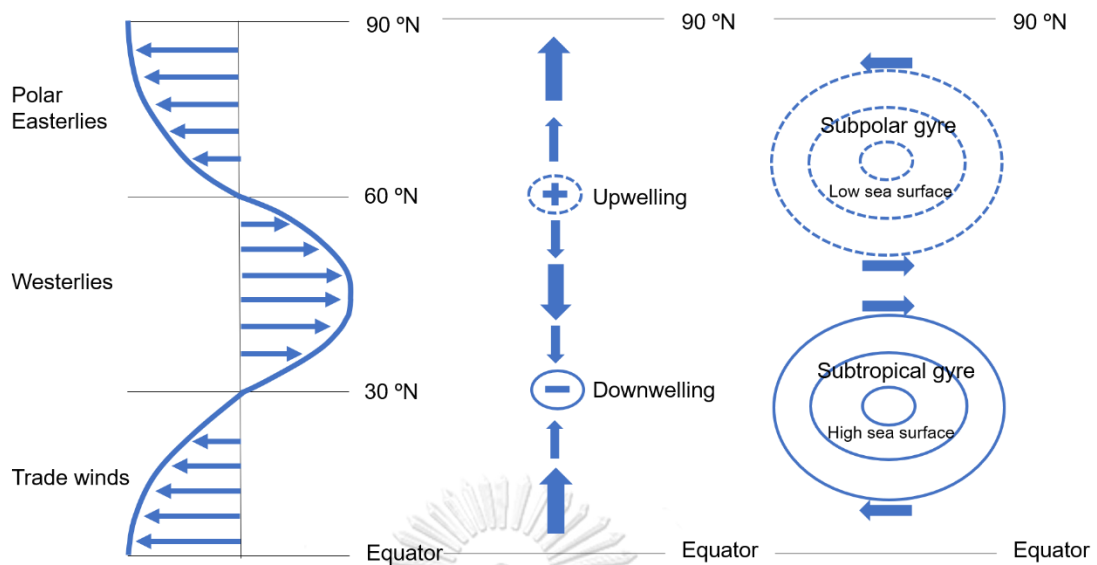


*Fig. 2.1. Zonal wind stress (left), Ekman transport (center), and ocean current gyres (right) of northern hemisphere.*

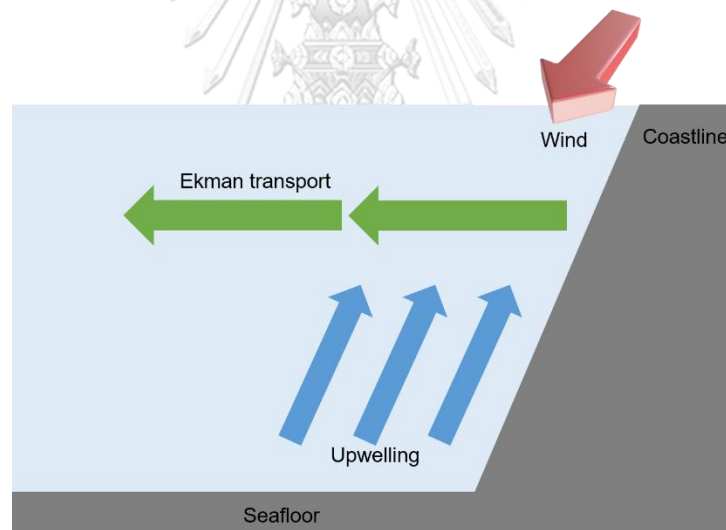


*Fig. 2.2. Coastal upwelling of northern hemisphere.*

The main drivers of coastal upwelling typically are wind-induced Ekman transport and Ekman pumping (Li et al., 2018), however there are other mechanisms used to explain coastal upwelling. The upwelling (shelf-break upwelling) along inshore edge of western boundary currents is related to the dynamic uplift, due to being strong and persistent current with a steeply rising thermocline. In regions of the strong tidal flows, the upwelling is generated by tidal pumping known as tidally induced



upwelling. The topography also leads to upwelling such as in submarine canyons, which generated deep water upwelling moving from the upper continental slope onto the continental shelf (Kämpf and Chapman, 2016).

## 2.2. The Gulf of Thailand (GoT)

The Gulf of Thailand is a shallow semi-enclosed bay in rectangular-like shape bordered by Malaysia, Thailand, Cambodia and Vietnam in the southwestern of South China Sea (SCS) with the length about 720 km, the width about 460 km, the average depth about 40 m and the maximum depth about 80 m in the central gulf (Sojisuorn et al., 2010; Yanagi and Takao, 1998a). The monsoonal wind of northeast and southwest controls circulation patterns over the GoT (Chaiongkarn and Sojisuorn, 2012). The counterclockwise and clockwise circulation develops in the GoT during northeast monsoon of winter time and southwest monsoon of summer time, respectively (Yanagi and Takao, 1998b).

## 2.3. Satellite observation of upwelling

The signal of upwelling is detected using the climatological sea surface temperature satellite images. As the upwelling moves the colder water toward the surface water, the appearance of water colder than the surrounding area in the surface water is an indicator of upwelling (Jing et al., 2011). The temporal satellite remote sensing images is used to figure out the variation and strength of seasonal upwelling in different areas (Su and Pohlmann, 2009). Further, according to Strass (1992)'s study, the upwelling region is related to where the patch of highest chlorophyll\_a concentration located in, a good proxy of primary production, which is detected using satellite-based images (Patti et al., 2010).

## 2.4. Delft3D modeling suite

Delft3D is a numerical model developed by Deltares, Netherlands, which explains wave, currents, sediment transport and bed level changes (Jiao, 2014). The Delft3D-FLOW module is used as a core module in this study, which calculates the momentum and continuity equation in horizontal direction. Delft3D-FLOW in horizontal direction supports Cartesian co-ordinate ( $\xi, \eta$ ) and Spherical co-ordinate ( $\lambda, \phi$ ). The vertical velocities in three dimensions is computed from the continuity equation. The hydrostatic pressure equation is conducted, as the vertical acceleration

is ignored in the vertical momentum equation (Breemen, 2008; Deltares, 2013). Equations used in this modeling suite are shown as following.

*Spherical co-ordinates system*

$$\xi = \lambda \quad (2.1)$$

$$\eta = \phi \quad (2.2)$$

$$\sqrt{G_{\xi\xi}} = R \cos \phi \quad (2.3)$$

$$\sqrt{G_{\eta\eta}} = R \quad (2.4)$$

$\lambda$  is the longitude (deg)

$\phi$  is the latitude (deg)

$R$  is the Earth radius given 6378.137 km (WGS84)

*The  $\sigma$  co-ordinate system*

$$\sigma = \frac{z - \zeta}{d + \zeta} = \frac{z - \zeta}{H} \quad (2.5)$$

$z$  is the vertical co-ordinate in physical space

$\zeta$  is the free space elevation above the reference plane at  $z = 0$

$d$  = the depth below the reference plane (m)

$H$  = the total water depth (given by  $d + \zeta$ ) (m)

*Continuity equation*

$$\frac{\delta \zeta}{\delta t} + \frac{1}{\sqrt{G_{\xi\xi}} \sqrt{G_{\eta\eta}}} \frac{\delta [(d + \zeta) U \sqrt{G_{\eta\eta}}]}{\delta \xi} + \frac{1}{\sqrt{G_{\xi\xi}} \sqrt{G_{\eta\eta}}} \frac{\delta [(d + \zeta) V \sqrt{G_{\xi\xi}}]}{\delta \eta} = (d + \zeta) Q \quad (2.6)$$

$$U = \frac{1}{d + \zeta} \int_d^\zeta u dz = \int_{-1}^0 u d\sigma \quad (2.7)$$

$$V = \frac{1}{d + \zeta} \int_d^\zeta v dz = \int_{-1}^0 v d\sigma \quad (2.8)$$

$$Q = \int_{-1}^0 (q_{in} - q_{out}) d\sigma + P - E \quad (2.9)$$

$U$  and  $V$  is the depth averaged velocities (m/s)

$Q$  is the contributions per unit area due to the discharge or withdrawal of water, precipitation and evaporation

$q_{in}$  and  $q_{out}$  is the local source and sink of water per unit of volume [1/s]

$P$  is the non-local source term of precipitation

$E$  is the non-local sink term due to evaporation

*Momentum equations in horizontal direction*

$$\begin{aligned} \frac{\delta u}{\delta t} + \frac{u}{\sqrt{G_{\xi\xi}}} \frac{\delta u}{\delta \xi} + \frac{v}{\sqrt{G_{\eta\eta}}} \frac{\delta u}{\delta \eta} + \frac{w}{(d+\zeta)} \frac{\delta u}{\delta \sigma} - \frac{v^2}{\sqrt{G_{\xi\xi}}\sqrt{G_{\eta\eta}}} \frac{\delta \sqrt{G_{\eta\eta}}}{\delta \xi} + \\ \frac{uv}{\sqrt{G_{\xi\xi}}\sqrt{G_{\eta\eta}}} \frac{\delta \sqrt{G_{\xi\xi}}}{\delta \eta} - f v = - \frac{1}{\rho_0 \sqrt{G_{\xi\xi}}} P_{\xi} + F_{\xi} + \frac{1}{(d+\zeta)^2} \frac{\delta}{\delta \sigma} \left( u v \frac{\delta u}{\delta \sigma} \right) + M_{\xi} \end{aligned} \quad (2.10)$$

$$\begin{aligned} \frac{\delta v}{\delta t} + \frac{u}{\sqrt{G_{\xi\xi}}} \frac{\delta v}{\delta \xi} + \frac{v}{\sqrt{G_{\eta\eta}}} \frac{\delta v}{\delta \eta} + \frac{w}{(d+\zeta)} \frac{\delta v}{\delta \sigma} + \frac{uv}{\sqrt{G_{\xi\xi}}\sqrt{G_{\eta\eta}}} \frac{\delta \sqrt{G_{\eta\eta}}}{\delta \xi} - \\ \frac{u^2}{\sqrt{G_{\xi\xi}}\sqrt{G_{\eta\eta}}} \frac{\delta \sqrt{G_{\xi\xi}}}{\delta \eta} + f u = - \frac{1}{\rho_0 \sqrt{G_{\eta\eta}}} P_{\eta} + F_{\eta} + \frac{1}{(d+\zeta)^2} \frac{\delta}{\delta \sigma} \left( u v \frac{\delta v}{\delta \sigma} \right) + M_{\eta} \end{aligned} \quad (2.11)$$

$u$  and  $v$  is flow velocities (m/s)

$w$  is flow velocity relative to the horizontal plane (m/s)

$d$  is water depth (m)

$\zeta$  is free surface elevation (m)

$\sigma$  is vertical coordinate defined by  $\frac{z-\zeta}{d+\zeta}$  in which  $z$  = vertical coordinate in

physical space

$f$  is Coriolis parameter (1/s)

$\rho_0$  is reference density of water (kg/m<sup>3</sup>)

$P_{\xi}$  and  $P_{\eta}$  is pressure gradient (kg/m<sup>2</sup>s<sup>2</sup>)

$F_{\xi}$  and  $F_{\eta}$  is turbulent momentum flux (Reynold's stresses) (m/s<sup>2</sup>)

$M_{\xi}$  and  $M_{\eta}$  is the contributions due to external sources or sinks of momentum

$\nu_v$  is vertical eddy viscosity (m<sup>2</sup>/s)

*Pressure term*

$$\frac{1}{\rho_0} P_x = g \frac{\delta \zeta}{\delta x} + g \frac{\delta + \zeta}{\rho_0} \int_{\sigma}^0 \left( \frac{\delta \rho}{\delta x} + \frac{\delta \sigma'}{\delta x} \frac{\delta \rho}{\delta \sigma'} \right) \delta \sigma' \quad (2.12)$$

$$\frac{1}{\rho_0} P_y = g \frac{\delta \zeta}{\delta y} + g \frac{\delta + \zeta}{\rho_0} \int_{\sigma}^0 \left( \frac{\delta \rho}{\delta y} + \frac{\delta \sigma'}{\delta y} \frac{\delta \rho}{\delta \sigma'} \right) \delta \sigma' \quad (2.13)$$

$g$  is gravitational constant ( $\text{m/s}^2$ )

$\rho$  is density of water including the effect of salt ( $\text{kg/m}^3$ )

*Water level elevation*

$$H(t) = A_0 + \sum_{i=1}^k A_i F_i \cos(\omega_i t + (V_0 + u)_i - G_i) \quad (2.14)$$

$H(t)$  is water level at time  $t$  (m)

$A_0$  is mean water level over a certain period (m)

$k$  is number of relevant constituents

$i$  is index of a constituents

$A_i$  is local tidal amplitude of a constituent (m)

$F_i$  is nodal amplitude of a constituent

$\omega_i$  is angular velocity ( $\text{deg/s}$ )

$t$  = time (s)

$(V_0 + u)$  is astronomical argument (deg)

$G_i$  is local phase lag (deg)

*Salinity*

$$\frac{\delta c}{\delta t} + \frac{\delta uc}{\delta x} + \frac{\delta vc}{\delta y} + \frac{\delta wc}{\delta z} - \frac{\delta}{\delta x} \left( \varepsilon_{s,x} \frac{\delta c}{\delta x} \right) - \frac{\delta}{\delta y} \left( \varepsilon_{s,y} \frac{\delta c}{\delta y} \right) - \frac{\delta}{\delta z} \left( \varepsilon_{s,z} \frac{\delta c}{\delta z} \right) = 0 \quad (2.15)$$

$c$  is salinity concentration (ppt)

$u, v$  and  $w$  is flow velocity (for each dimension  $x, y$  and  $z$ ) ( $\text{m/s}$ )

$\varepsilon$  is eddy diffusivity (for each dimension  $x, y$  and  $z$ ) ( $\text{m}^2/\text{s}$ )

### 2.5. Coastal High Frequency (HF) radar system

The coastal HF radar system is used to measure sea surface current and ocean wave based on the doppler shift of the reflected ocean wave of the half the radio wavelength as presented in Fig. 2.3 (Wyatt, 2000). The reflected wave is measured by the high frequency (3-30 MHz) radar receiver located on the coast. The radar system can also measure the ocean wave of more than 100 km offshore every 10 min to hour with the resolution of 250 m to 15 km (Wyatt et al., 2011).

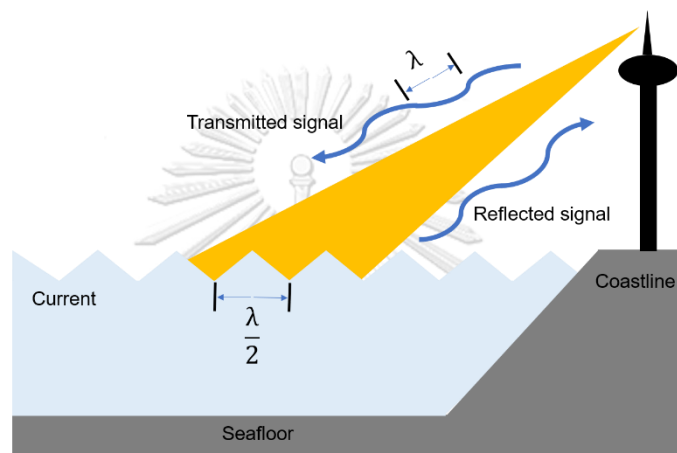


*Fig. 2.3. Coastal HF radar system.*

## CHAPTER 3

### Methodology

The coastal upwelling event in the GoT is investigated through 2 approaches, upwelling index and numerical model. Details of these 2 approaches are described below.

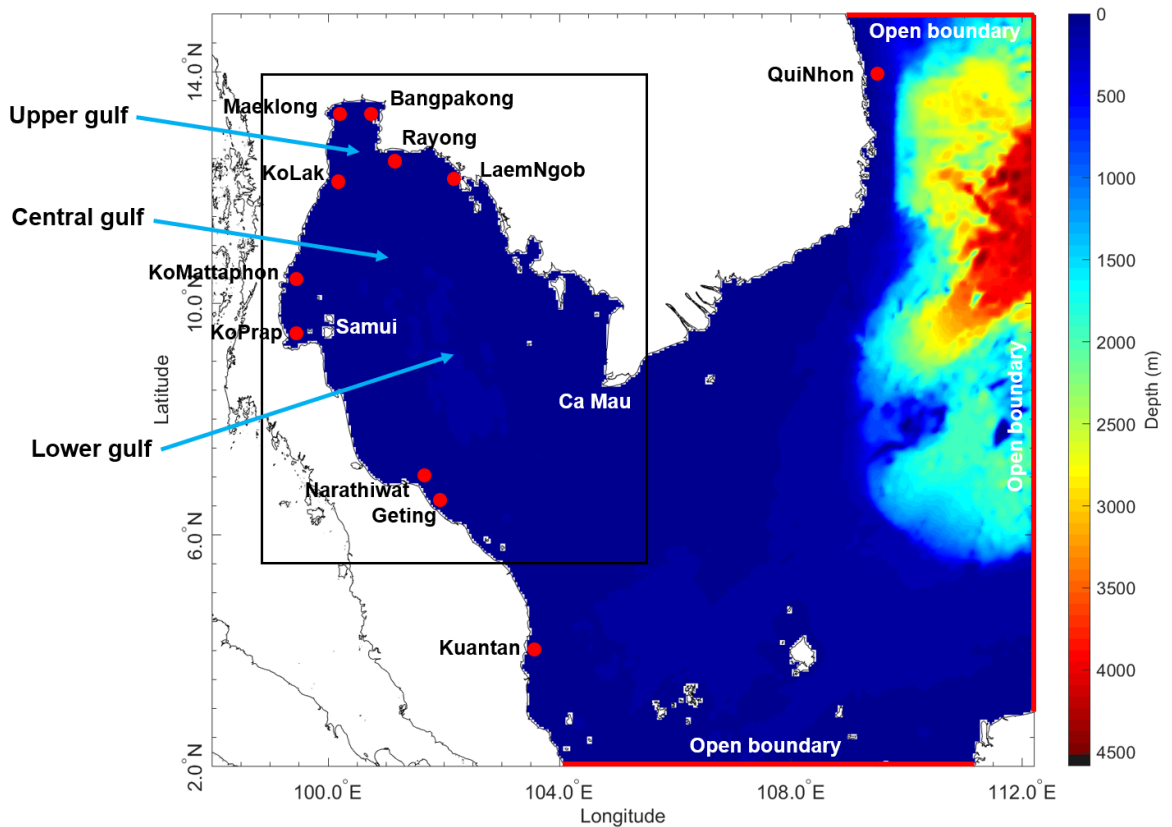


*Fig. 3.1. Three-dimensional numerical model study area. Red solid lines depict open boundaries, while red dots represent observed water level stations. Area of upwelling index study is shown by the black box.*

### 3.1. Upwelling index estimations

#### 3.1.1. Ekman transport upwelling index ( $UI_{ET}$ ) estimation

The alongshore wind components are considered for estimating the wind stress (Eqs. (3.1) – (3.4)) and Ekman transport upwelling index (Eq. (3.5)). A positive value of  $UI_{ET}$  corresponds to a favorable upwelling condition, while a negative value of  $UI_{ET}$  corresponds to an unfavorable

upwelling condition (Alvarez et al., 2011; Santos et al., 2012). Where  $\tau$  is the wind stress,  $\rho_w = 1025 \text{ kg m}^{-3}$  is the density of seawater, and  $f = 2\Omega \sin\theta$  is the Coriolis parameter,  $\Omega = 7.292 \times 10^{-5} \text{ rad s}^{-1}$  is the Earth's angular velocity, and  $\theta$  is the latitude. The variables with  $x$  and  $y$  subscripts refer to the zonal and meridional, respectively.  $\rho_a = 1.22 \text{ kg m}^{-3}$  is the density of air,  $C_d = 1.3 \times 10^{-3}$  is the constant dimensionless drag coefficient.  $Q$  is Ekman transport ( $\text{m}^3\text{s}^{-1}\text{m}^{-1}$ ).  $W$  is the wind speed at 10 m and  $\varphi$  is the angle between coast line and equator (Kok et al., 2017).

$$Q_x = \frac{\tau_y}{\rho_w f} \quad (3.1)$$

$$Q_y = -\frac{\tau_x}{\rho_w f} \quad (3.2)$$

$$\tau_x = \rho_a C_d W_x (W_x^2 + W_y^2)^{1/2} \quad (3.3)$$

$$\tau_y = \rho_a C_d W_y (W_x^2 + W_y^2)^{1/2} \quad (3.4)$$

$$UI_{ET} = -\left(\sin\left(\varphi - \frac{\pi}{2}\right) Q_y + \cos\left(\varphi - \frac{\pi}{2}\right) Q_x\right) \quad (3.5)$$

In this study, monthly means of daily means wind velocity components with resolution  $0.25^\circ \times 0.25^\circ$  at 10 m above sea surface during 2003-2018 were downloaded from the European Centre Medium-range Weather Forecast (ECMWF) Interim Reanalysis (ERA-Interim). The zonal and meridional wind velocities were used to calculate the Ekman transport upwelling index using Eq. (3.1) – (3.5). The upwelling characteristics/locations in the GoT were then identified.

### 3.1.2. Sea surface temperature upwelling index ( $UI_{SST}$ ) estimation

The gradient SST between coastal SST nearest to the coast ( $SST_{Coastal}$ ) and the oceanic SST ( $SST_{Oceanic}$ ) with the distance of 2 degree at the same latitude were calculated using Eq. (3.6) and visualized to reveal upwelling characterization. A negative value of  $UI_{SST}$  indicates a favorable upwelling condition while a positive  $UI_{SST}$  indicates an unfavorable upwelling condition (Benazzouz et al., 2014; Gomez-Gesteira et al., 2008).

$$UI_{SST} = SST_{Coastal} - SST_{Oceanic} \quad (3.6)$$

Daily multi-scale ultra-high resolution (MUR) sea surface temperature (SST) analysis data is the sea surface temperature mapped mostly from instruments like MODIS, AVHRR, AMSR-E, WindSat, buoys and ships. MUR-SST data set during 2003-2018 were obtained from <https://oceancolor.gsfc.nasa.gov/>. The monthly averaged of these data were then used to estimate sea surface temperature upwelling index using Eq. (3.6).

## 3.2. Numerical model

### 3.2.1. Data collection

Some of required data were used for model input and some were used for model calibration and validation. The required data are described as following.

#### 3.2.1.1. Model setup

- Extracted shoreline covering the GoT and SCS (see Fig. 3.1) from GEODAS software provided by NOAA was used to defined model domain.
- Bathymetry data from nautical charts surveyed by Hydrographic Department, Royal Thai Navy, and General Bathymetric Chart of the Oceans (GEBCO) were used for depth interpolation in model grid.

#### 3.2.1.2. Driving forces

- Harmonic constituents from Global Tide Model of OSU TOPEX/Poseidon Global Inverse Solution TPXO Version 8.0 (Egbert and Erofeeva, 2002) were applied as driving forces of model at open boundaries (red lines in Fig. 3.1).
- Spatial and temporal surface wind data with the 6-hour temporal resolution, total cloud cover, dew point and air temperature obtained from ERA-Interim (Dee et al., 2011) of ECMWF (European for Medium-Range Weather Forecast) from <http://www.ecmwf.int> was used as a driving force of model at the surface.
- Monthly climatology sea surface temperature and salinity data on 0.5° grid from the World Atlas 2018 (WOA 2018) downloaded from <http://www.nodc.noaa.gov> was used to define



the spatial-temporal distribution of temperature and salinity in the model domain.

- River discharge data of Mae Klong River and Ta Chin River downloaded from <http://hydro-7.go.th>, Chaopraya River downloaded from <http://hydro-5.go.th>, and Bangpakong River downloaded from <http://hydro-6.go.th>, and Mekong River from The Mekong River Commission, was monthly averaged and applied at river mouths in the model domain to investigate the impact of fresh water on the circulation.

#### 3.2.1.3. Model calibration and validation

- Observed water level surrounding the GoT from Hydrographic Department, Royal Thai Navy, Marine Department, and University of Hawaii Sea Level Center were utilized for tidal analysis, model calibration and validation (two-dimensional simulation).
- Sea surface current covering the upper, east and south GoT downloaded from <http://coastalradar.gistda.co.th> was compared with modeled surface current (three-dimensional simulation).

#### 3.2.2. Model preparation

- The rectangular grid model domain with the resolution of  $0.0416^\circ \times 0.0416^\circ$  degree covering the area of  $98.0^\circ \text{E}$  to  $112.0^\circ \text{E}$  and  $2.0^\circ \text{N}$  to  $15.0^\circ \text{N}$  was prepared using Delft3D-RGFGRID module (see Fig.3.1).
- Bathymetry data obtained from 3.2.1.1 was interpolated into model grid prepared from 3.2.2.1 using Delft3D-QUICKIN module.
- Generated water level using sixteen harmonic constituents (A0, M2, S2, N2, K2, K1, O1, P1, Q1, MF, MM, M4, MS4, MN4, SA and SSA) obtained from 3.2.1.2 was applied at three open boundaries (see red lines in Fig. 3.1).

#### 3.2.3 Model simulation

Open boundary conditions (tidal signal) and other forces were applied in the GoT model using prepared model grid and bathymetry as mentioned in section 3.2.2. Model calibration and model validation were performed

to check whether prepared GoT model is valid (to simulate for other applications). Details of model calibration and validation are shown below.

#### 3.2.3.1 Model calibration (Case Tide2D)

The GoT model was simulated for one month to obtain the modeled water level at each station (red dot) depicts in Fig 1.1. Both amplitude and phase of 8 tidal components (M2, S2, N2, K2, K1, O1, P1, Q1) obtained from harmonic analysis of one-month modeled water level using TIDE module were compared with the observed one together with one-month water level comparison between model and observed. Model performance was examined using various indices as mentioned in 3.2.4. Adjustment of amplitudes and phases of harmonic constituents at the open boundaries or other parameters were conducted until the modeled and observed water levels were satisfactory agreement.

#### 3.2.3.2 Model validation

Calibrated model (Tide2D) obtained from 3.2.3.1 was validated by simulating water level of different time period. Various indices mentioned in 3.2.4 were applied to see the model performance.

#### 3.2.3.3 Surface current comparison (Case Wind2D)

In this model study, the spatially varying wind from 3.2.1.6. was added into the Tide2D modeling case. The model was simulated to cover the period of February 1-28, 2019, where observed surface current obtained from HF radar system were available. The modeled surface currents covering upper, east and south gulf were compared with HF radar surface currents (see Fig. 4.13 for locations of available area coverage). Statistical indices, %RMSE and %MAE, were applied to see the model performance.

#### 3.2.3.4 Full three-dimensional (3D) simulation

For full three-dimensional model simulation, the temperature and salinity from 3.2.1.7, and river discharge from 3.2.1.8 were applied into Tide2D model to see the characteristics and mechanisms of coastal upwelling in the GoT covering area of black box in Fig. 3.1. Hence, Tide2D model was modified to have a full three-dimensional. The 10 layers of sigma coordinate, which has thickness of 2%, 3%, 4%, 6%, 8%, 10%, 12%, 15%, 20% and 20% of water depth measure from surface to bottom, was

assigned. For stability of the 3D model, the maximum depth the model domain was set to 250 m. In addition, ocean heat flux calculated from total cloud cover, dew point and air temperature from 3.2.1.2 was also applied in the model known as TWH3D case to investigate the circulation pattern, temperature and salinity distribution in the Gulf of Thailand.

### 3.2.4 Model performance

Root mean square error (RMSE), mean absolute error (MAE), vectorial difference (d) (Foreman et al., 1993; Tsimplis et al., 1995), root summed square vector difference (RSS) and skill score (Liu and Huang, 2019) (see Eq. 3.1-3.5) that are statistical indices were examined to show the model performance.

*Root mean square error (RMSE)*

$$RMSE = \sqrt{\frac{1}{N} \sum_{i=1}^N ((Y_c)_i - (Y_o)_i)^2} \quad (3.1)$$

*Mean absolute error (MAE)*

$$MAE = \frac{1}{N} \sum_{i=1}^N |(Y_c)_i - (Y_o)_i| \quad (3.2)$$

*Skill score*

$$Skill\ score = 1 - \frac{\sum_{i=1}^N |(Y_c)_i - (Y_o)_i|^2}{\sum_{i=1}^N [|(Y_c)_i - \bar{Y}_o| + |(Y_o)_i - \bar{Y}_o|]^2} \quad (3.3)$$

*Vectorial difference (d)*

$$d = \sqrt{(A_o \cos H_o - A_c \cos H_c)^2 + (A_o \sin H_o - A_c \sin H_c)^2} \quad (3.4)$$

*Root summed square vector difference (RSS)*

$$RSS = \sqrt{\sum_{i=1}^N |x_i|^2} \quad (3.5)$$

$N$  is the total number of data points

$Y_c$  is the predicted water level (m)

$Y_o$  is the observed water level (m)

$\bar{Y}_o$  is the mean value of the observed water level (m)

$A_o$  is the amplitude of observation data (m)

$A_c$  is the amplitude of modeled data (m)

$H_o$  is the phase of observation data (degree)

$H_c$  is the amplitude of modeled data (degree)

$x_i$  is the vectorial difference of each harmonic constituent (cm)



## CHAPTER 4

### Results and discussions

This study aims to figure out the characteristics of coastal upwelling in the GoT through two approaches: 1) upwelling index estimations and 2) numerical model.

#### 4.1. Upwelling index estimations

##### 4.1.1. Seasonal wind patterns

The seasonal wind patterns of 16-year monthly averaged wind vectors were represented in Fig. 4.1. During northeast monsoon represented with January in Fig. 4.1a, the upper gulf and the entrance of the gulf was dominated by northeasterly winds, while the easterly wind controlled the central gulf. The wind speed of 4-5 m/s was observed at the lower gulf, then gradually slowed down to 1-2 m/s at the upper gulf. During March describing the 1<sup>st</sup> inter-monsoon in Fig. 4.1b the wind run westward in the lower gulf, northwestward in the central gulf and northward in the upper gulf with the magnitude about 4-5 m/s covering the whole gulf. In August during southwest monsoon (see Fig. 4.1c) winds in the central gulf prevailed east-northeastward, while northeastward winds controlled the upper gulf and the lower gulf with the magnitude of 4-5 m/s for the whole domain. During 2<sup>nd</sup> inter-monsoon attributed by October in Fig. 4.1d, weak winds with 1-2 m/s in the upper gulf and the central gulf run southward to southeastward, respectively. Therefore, the seasonal monsoon winds effect on the wind patterns in the gulf during both seasons. The northeastward and southwestward winds covered the upper gulf and the lower gulf depending on monsoonal winds, whereas winds in the central gulf blown easterly and westerly during northeast monsoon and southwest monsoon, respectively. Surface wind vector of February, April, May, June, July, September, November and December were shown in Appendix A1.

##### 4.1.2. Ekman transport upwelling index ( $UI_{ET}$ )

The seasonal wind velocity components in section 4.1.1 was used to estimate the magnitude and direction of Ekman transport displayed in Fig. 4.2. Theoretically, the Ekman moved in the right and the left of the wind vector in the northern hemisphere and the southern hemisphere,

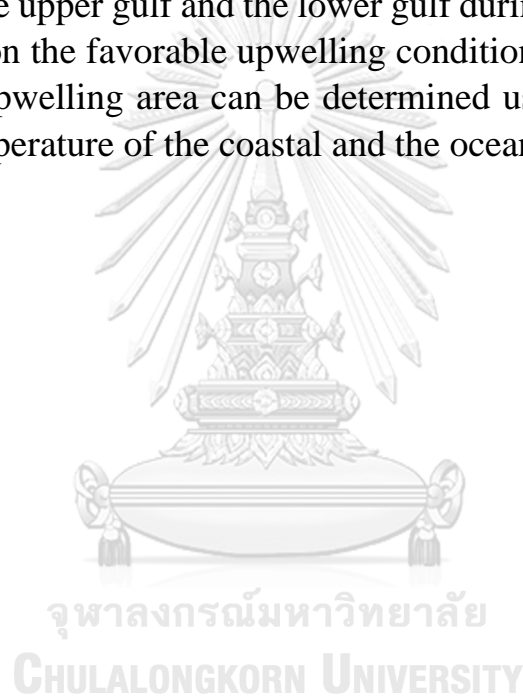
respectively. The more amount of water mass had been transported when the wind speed was stronger. During northeast monsoon in January (see Fig. 4.2a), the transport in the central gulf moved strongly northward, while the transport moved northwestward in both the upper gulf and the lower gulf. As the result of wind speed in Fig. 4.1, the transport in the upper gulf was weaker than in the lower. In March during 1<sup>st</sup> inter-monsoon (see Fig. 4.2b) the transport was still strong in the lower gulf and weak in the upper gulf. The transport run northward from the lower gulf, then turned northeastward in the central gulf and eastward in the upper gulf, which may lead the water to pile up on the eastern GoT. In August during southwest monsoon (see Fig. 4.2c) the water in the gulf was transported out of the gulf since the winds moved strongly east-northeastward for the whole gulf.

During 2<sup>nd</sup> inter-monsoon in October, the transport magnitude in Fig. 4.2d was multiplied with 10 as the obtained transport was very small. In contrast to the transport direction of 1<sup>st</sup> inter monsoon, the transport clearly moved to toward the western GoT, that caused the water was piling up in the western gulf. Therefore, the Ekman transport pushed water in and out the gulf during the northeast monsoon and southwest monsoon, respectively. The results shown agreement with a result in Fig. 8a-d in (Saramul and Ezer, 2014), which shown the higher sea level during northeast monsoon, November-February, and lower sea level during southwest monsoon, May-September. Besides, a result in (Saramul, 2017) shown that the surface current near Samui Island moved northwestward during northeast monsoon, and eastward during southwest monsoon. The water was pushed toward the eastern GoT during 1<sup>st</sup> inter-monsoon, and the western GoT during 2<sup>nd</sup> inter-monsoon. Ekman transport ( $\text{m}^3\text{s}^{-1}\text{m}^{-1}$ ) of February, April, May, June, July, September, November and December were shown in Appendix A2.

To investigate the upwelling/downwelling areas, the transport direction to the shoreline angle with the respect to the Equator in Fig. 4.2 was considered to determined Ekman upwelling index in Fig. 4.3. The transport with seaward direction and shoreward direction will be considered as upwelling favorable and unfavorable, respectively. In Fig. 4.2 Ekman transport during northeast monsoon and southwest monsoon, and during 1<sup>st</sup> inter-monsoon and 2<sup>nd</sup> inter-monsoon, moved in the opposite direction. The upwelling and downwelling areas also occurred in the opposite locations depening on the considered monsoon.

During northeast monsoon and 1<sup>st</sup> inter-monsoon in Fig. 4.3a and 4.3b, the favorable upwelling conditions generally occurred along the west coast, except the west coast of the upper gulf down to the central gulf. In contrast, the favorable upwelling conditions existed along the east coast of the upper gulf during northeast monsoon and the west side of Ca Mau Cape during the 1<sup>st</sup> inter-monsoon. During southwest and 2<sup>nd</sup> inter-monsoon in Fig. 4.3c and 4.3d, the favorable upwelling conditions were generally found along the east coast of GoT, except the east coast of the upper gulf during southwest monsoon and the west side of Ca Mau Cape during the 2<sup>nd</sup> inter-monsoon. The favorable upwelling conditions also were found along the west coast of the upper gulf and the lower gulf during southwest monsoon.

In this section the favorable upwelling conditions were caused only by wind, yet the upwelling area can be determined using gradients between sea surface temperature of the coastal and the oceanic described in section 4.1.3.



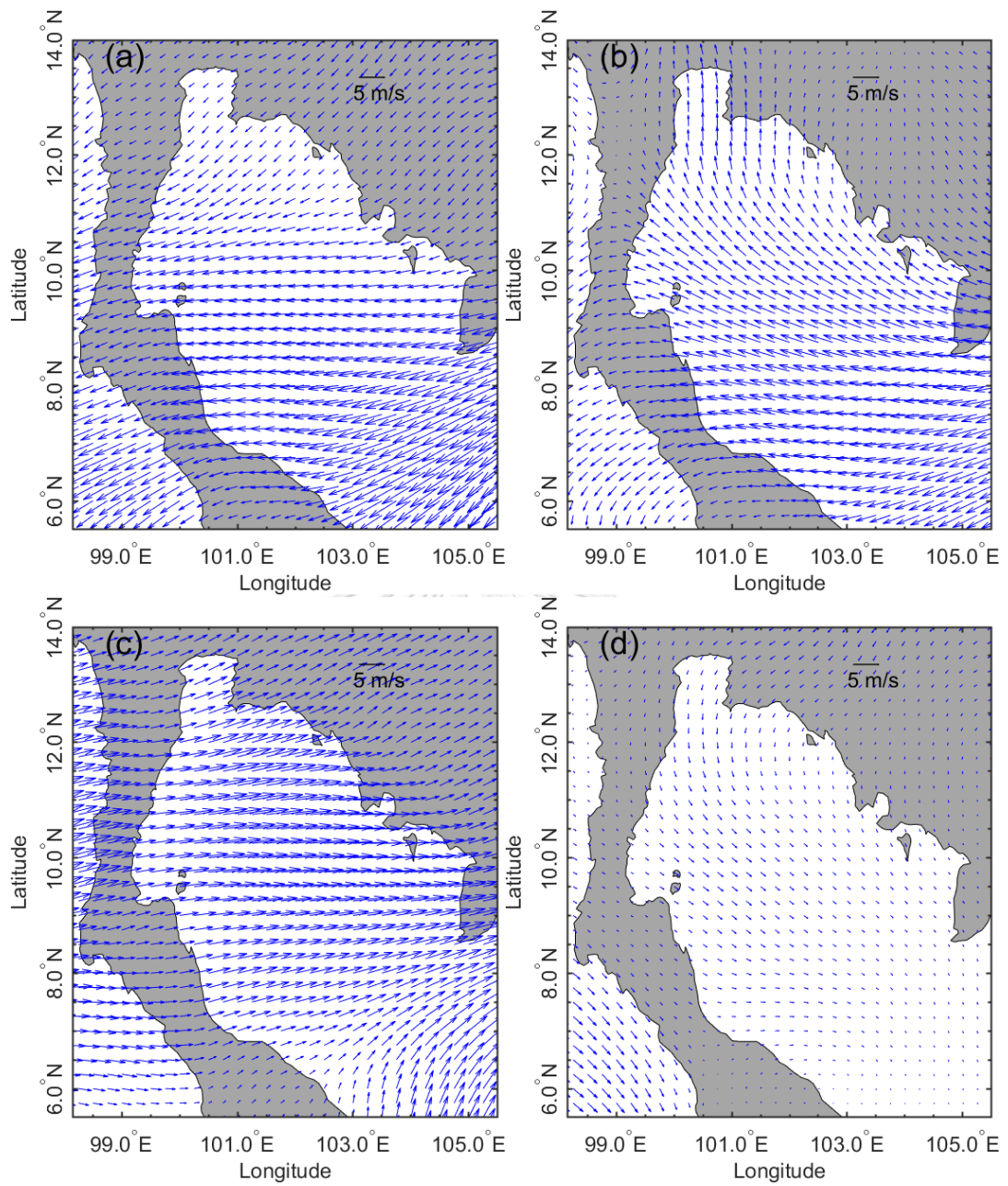


*Fig. 4.1. Surface wind vector (m/s) of a) Northeast monsoon, b) 1<sup>st</sup> Inter-monsoon, c) Southwest monsoon, and d) 2<sup>nd</sup> Inter-monsoon.*



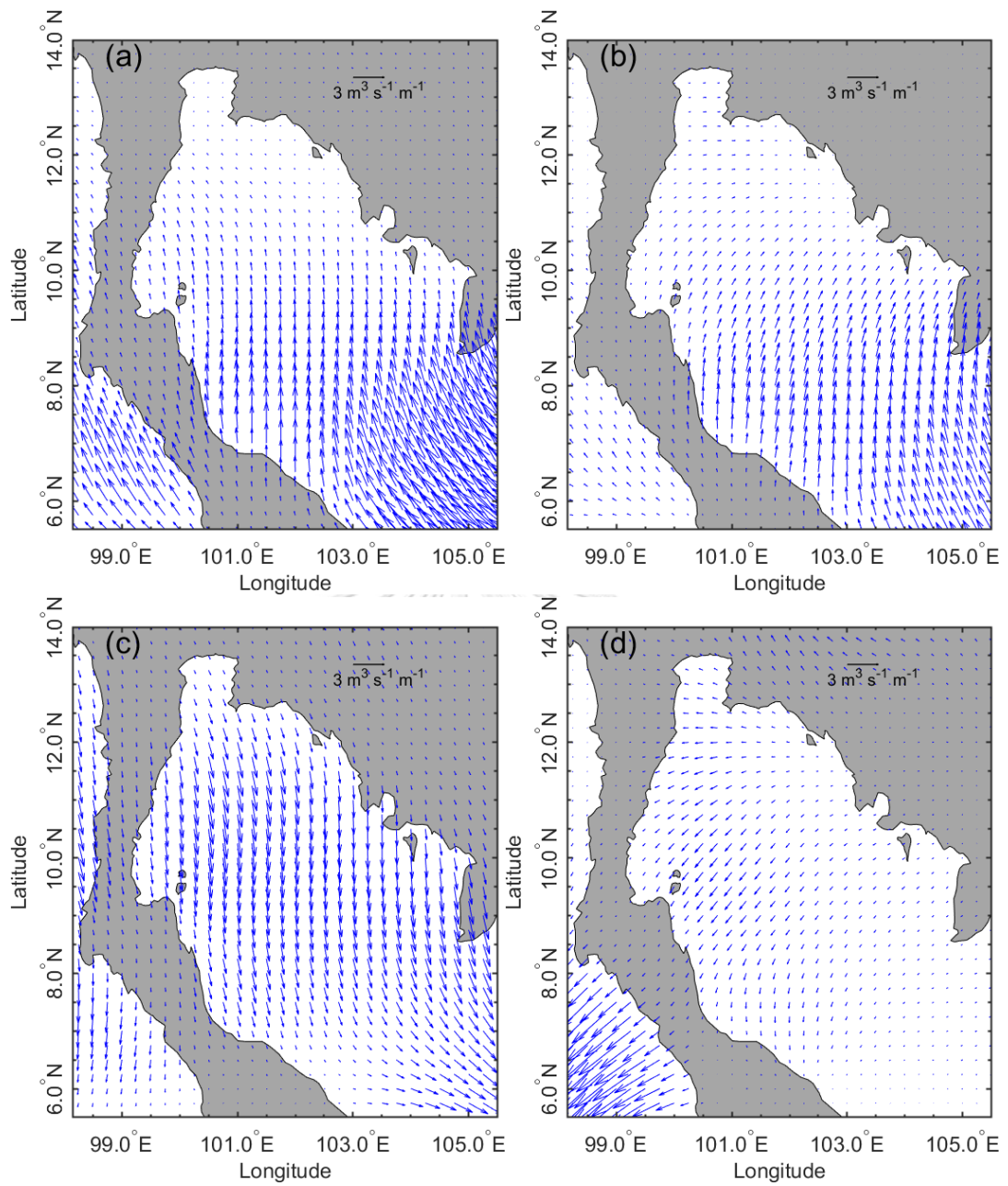


*Fig. 4.2. Ekman transport ( $\text{m}^3/\text{s}/\text{m}$ ) of a) Northeast monsoon, b) 1<sup>st</sup> Inter-monsoon, c) Southwest monsoon, and d) 2<sup>nd</sup> Inter-monsoon.*

*Remark: the magnitude of blue arrows in d) are 10 times of the real value.*

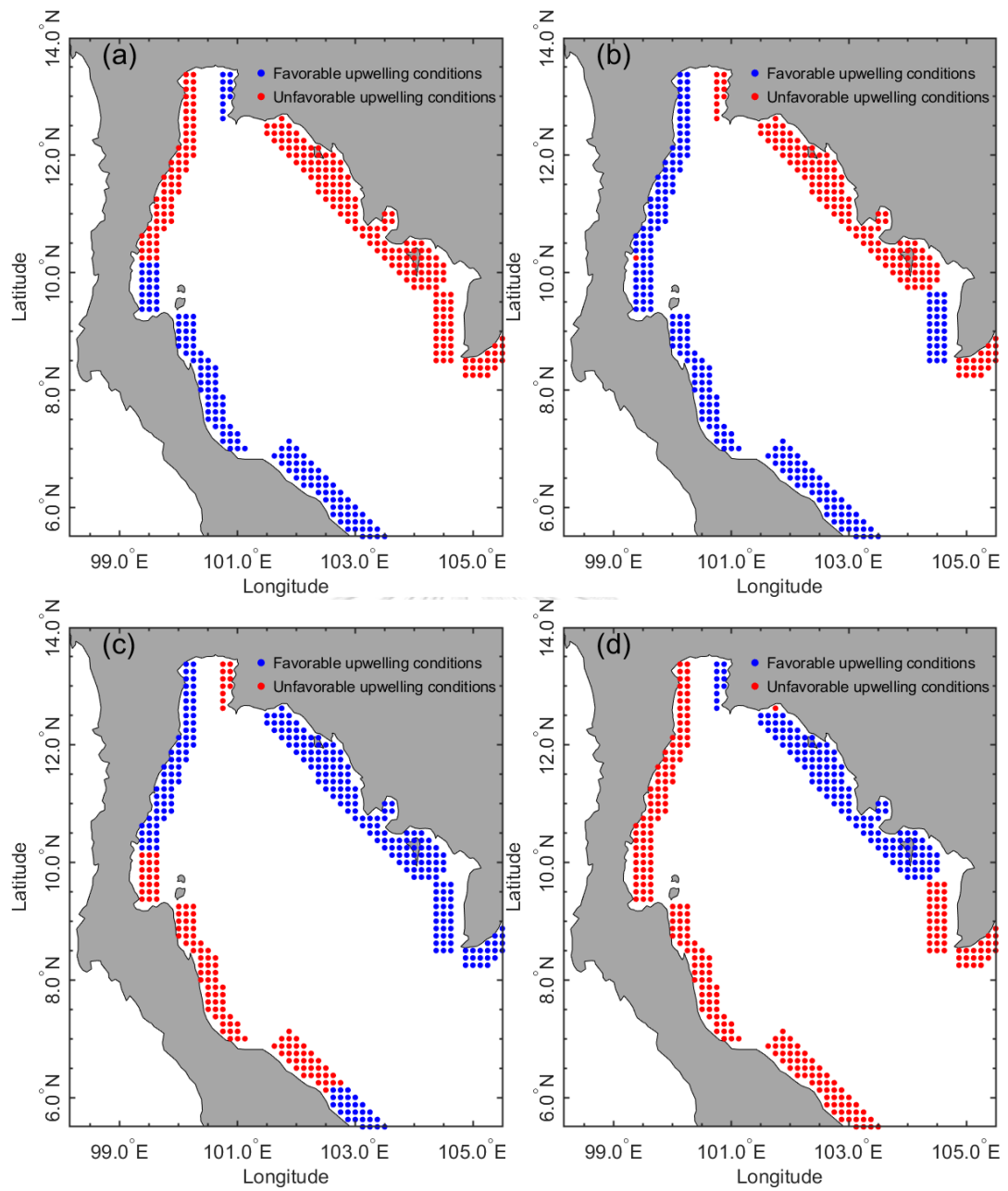


*Fig. 4.3. Upwelling condition associated with Ekman transport upwelling index ( $UI_{ET}$ ) of a) Northeast monsoon, b) 1<sup>st</sup> Inter-monsoon, c) Southwest monsoon, and d) 2<sup>nd</sup> Inter-monsoon.*

#### 4.1.3. Sea surface temperature upwelling index ( $UI_{SST}$ )

The 16-year monthly averaged seasonal sea surface temperature is shown in Fig. 4.4. During northeast monsoon in January (see Fig. 4.4a), the whole gulf was covered with the cooler water of 25.0-29.0 degree Celsius. Along the west coast of the upper gulf and the lower gulf near Ca Mau Cape, the clear cooler front of 25.0-27.0 degree Celsius was found since the strong transport pushed the SCS water mass into the GoT. During 1<sup>st</sup> inter-monsoon in Fig. 4.4b, the warm water generally developed for the whole gulf with the temperature about 29.5 degree Celsius and with the warmer degree mostly in the shallow area. The cooler water with the temperature rising to 27.0-29.0 degree Celsius continued existing near Ca Mau Cape. In the upper gulf, especially near the northern part of the upper gulf, the cooler front from northeast monsoon was replaced with the warmer of 29.0-32.0 degree Celsius.

In August during southwest monsoon in Fig. 4.4c, in the upper gulf the warm water of 31.0-32.0 degree Celsius dispersed southward toward the central gulf, and was also found in along the west coast of the lower gulf. Near the entrance of the gulf the temperature was getting warmer, while near the east coast remained the same degree as in 1<sup>st</sup> inter-monsoon. In October of 2<sup>nd</sup> inter-monsoon, the warmer water in the upper gulf and the east gulf dispersed seaward, while the warmer water in the west coast of the lower gulf was more concentrate near coastline. Further, the center of the gulf and the west of Ca Mau Cape were with the wide patch of cooler water of 28.5-29.5 degree Celsius.

The SST is clearly seasonally changed in Fig.4.4. Owing to the heat lose in winter, the water during northeast monsoon was cooler than other seasons. Cooler water from SCS intruded into the GoT via the gulf entrance between Kotabaru in Malaysia and Ca Mau Cape in Vietnam. Due to the heat gain in the summer, the warm SST was developed almost for the whole gulf during 1<sup>st</sup> and 2<sup>nd</sup> inter-monsoon. Conversely, the cooler water was still intruding from SCS during 1<sup>st</sup> inter-monsoon and disappeared during southwest monsoon and 2<sup>nd</sup> inter-monsoon. The found characteristics of SST will be utilized to obtain the SST upwelling index later.

Fig. 4.5 shows the seasonal variability of sea surface temperature upwelling index ( $UI_{SST}$ ) and sea surface temperature cross sections along two transect lines number 1 and 2 off the west and east coast, respectively. The distance of a transect line was two degrees from shoreline toward

offshore on the same latitude degree. The offshore with higher temperature attributes the favorable upwelling condition (blue color). In Fig. 4.5a during northeast monsoon, the favorable upwelling conditions with a difference about 0.6 degree Celsius appeared along the west coast and around Samui Island, and with a difference about 0.8 degree Celsius along the south of east coast around Ca Mau Cape. In August during southwest monsoon (see Fig. 4.5c), the favorable upwelling conditions with the difference of 0.4 degree Celsius existed along the west coast, and with the difference of 0.4 degree Celsius near Ca Mau Cape. As the result, the favorable upwelling conditions were clearly developed during northeast monsoon and southwest monsoon. It was existed only in the northern part of the west gulf and the west coast of the Ca Mau Cape, while the unfavorable upwelling conditions were dominated the rest of the GoT.

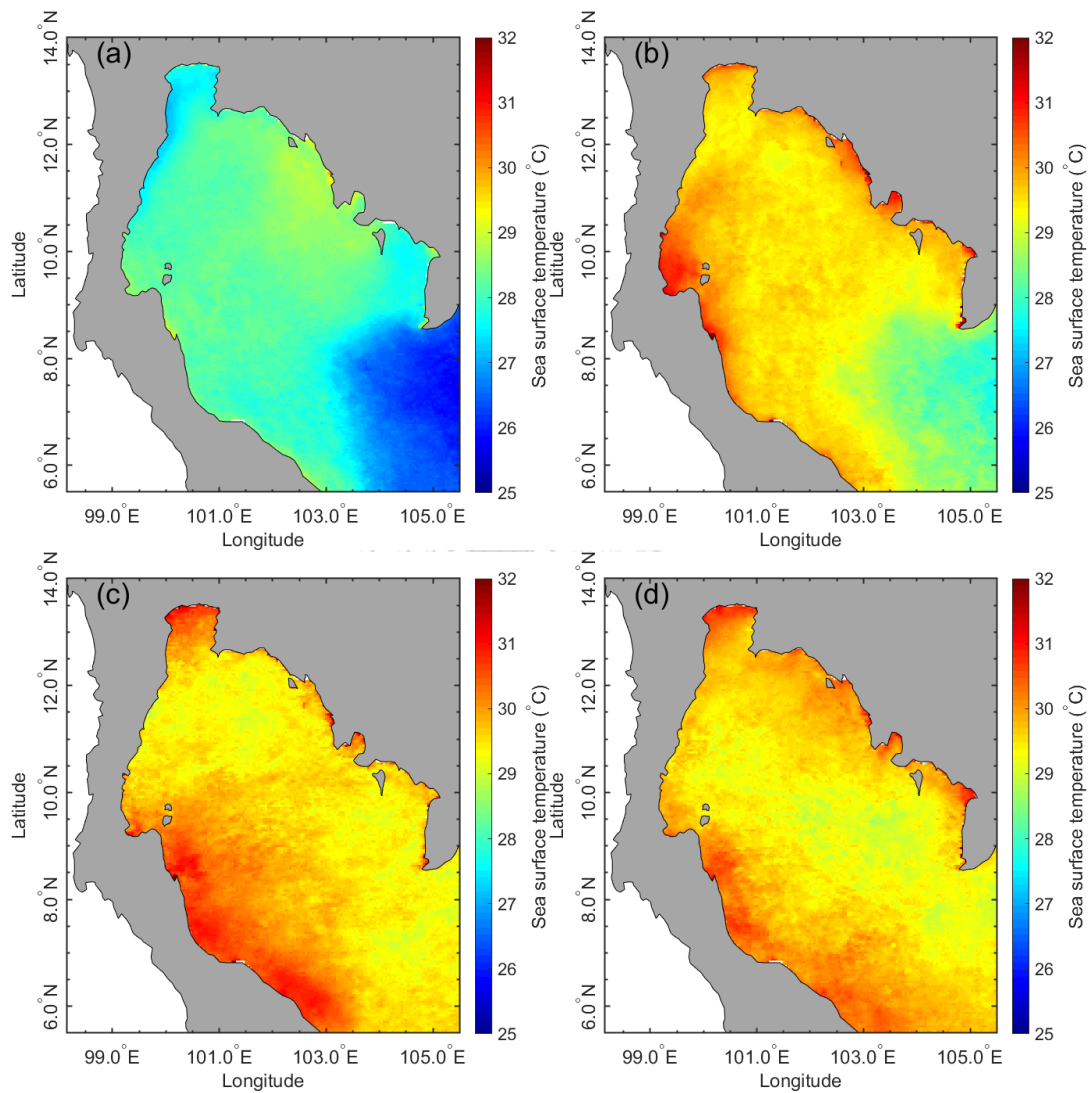
During the 1<sup>st</sup> inter-monsoon and the 2<sup>nd</sup> inter-monsoon, the unfavorable upwelling conditions were existed for the whole gulf as shown in Fig. 4.5b and 4.5c. The unfavorable upwelling conditions was depicted with the higher coastal sea surface temperature than the oceanic sea surface temperature.

#### 4.1.4. Relations of Ekman transport upwelling index ( $UI_{ET}$ ) and sea surface temperature upwelling index ( $UI_{SST}$ ) in GoT

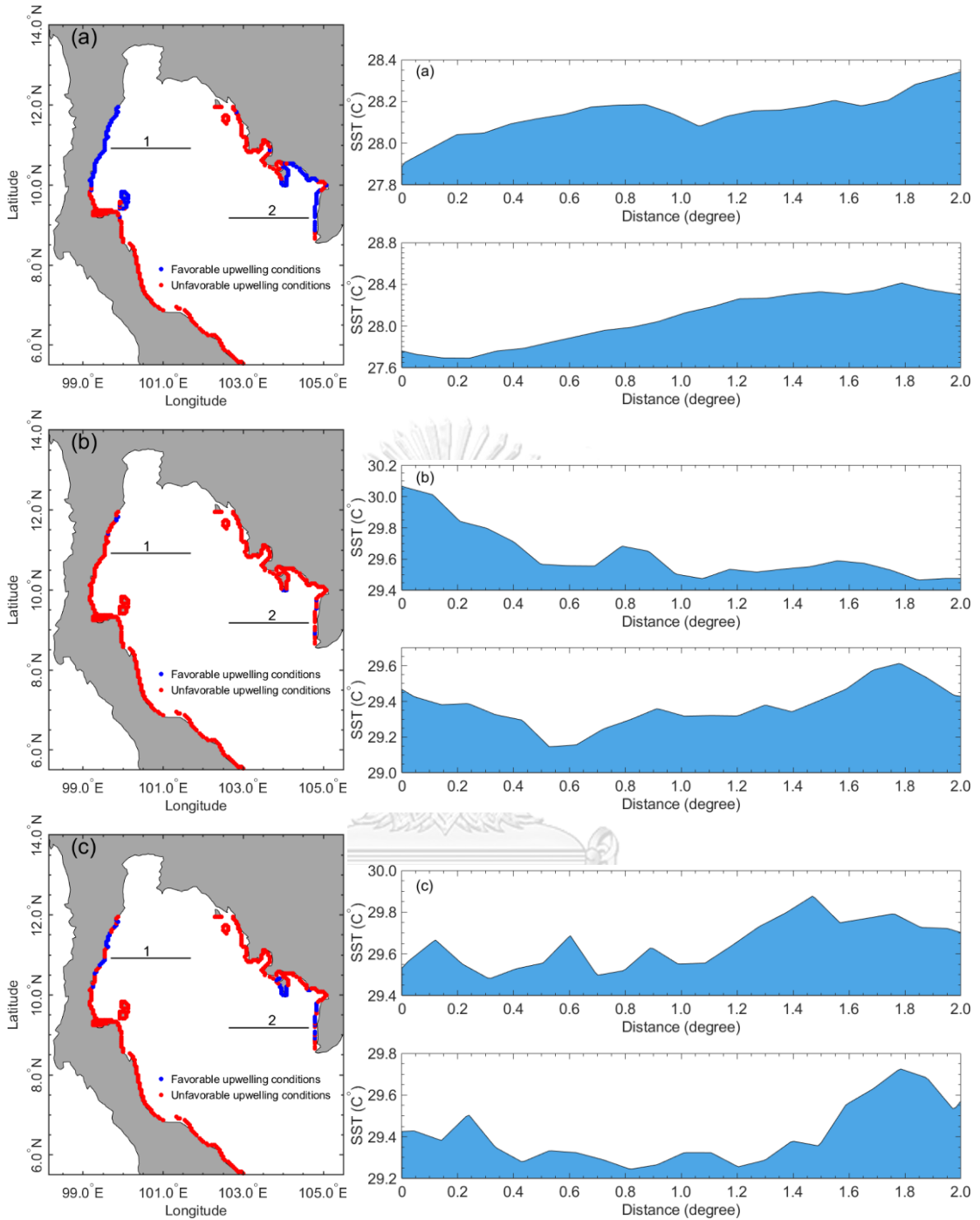
As results mentioned in 4.1.3, the favorable upwelling condition of  $UI_{SST}$  was showed along the northern part of the west coast and the western part of Ca Mau Cape during northeast monsoon and southwest monsoon. The signal was also found around Samui Island during northeast monsoon. Compared with the obtained favorable upwelling condition of  $UI_{ET}$ , during northeast monsoon only around Samui Island shown an agreement. Further, during southwest monsoon the conditions around the northern part of the west coast of the GoT and west coast of Ca Mau Cape agreed with the favorable condition of  $UI_{ET}$ .

However, several locations in the GoT expressed the disagreement between the obtained favorable condition of  $UI_{ET}$  and  $UI_{SST}$ . The discrepancy may come from the following. The  $UI_{ET}$  is directly contributed to alongshore surface wind direction. In northern hemisphere the Ekman transport is directed at the right angle to the wind stress. During northeast monsoon the Ekman transport was flowing mostly northward. It was pushing upward the water along the west coast of the lower gulf, which

was considered as the area of the favorable upwelling index. As the same reason of the Ekman transport direction and the wind stress direction, the result related to  $UI_{ET}$  was not in an agreement with the  $UI_{SST}$  during 1<sup>st</sup> inter-monsoon and 2<sup>nd</sup> inter-monsoon.



*Fig. 4.4. Averaged sea surface temperature in degree Celsius during 2003-2018 of a) Northeast monsoon, b) 1<sup>st</sup> Inter-monsoon, c) Southwest monsoon, and d) 2<sup>nd</sup> Inter- monsoon.*



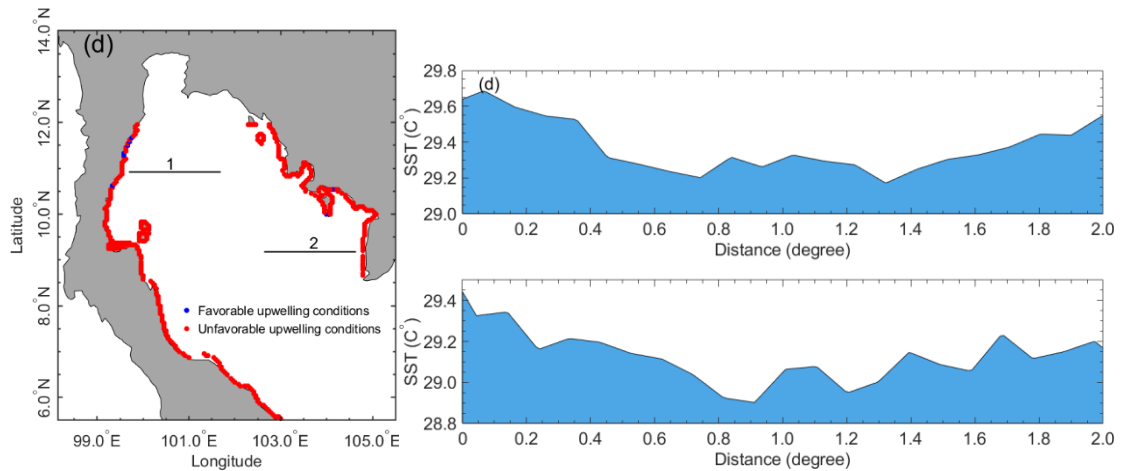


*Fig. 4.5. Sea surface temperature upwelling index ( $UI_{SST}$ ) (left) and temperature cross section profile (right) of line number 1 (upper) and line number 2 (bottom) extracted from shoreline to offshore of a) Northeast monsoon, b) 1<sup>st</sup> Inter-monsoon, c) Southwest monsoon, and d) 2<sup>nd</sup> Inter-monsoon. Blue and red dots represent favorable and unfavorable upwelling condition, respectively.*

#### 4.2. Numerical model results

The model was setup and simulated during January 1-31, 2004 with 11 water level observation stations (see Fig. 1.1); Bangpakong River (BK), Rayong (RY), Ko Lak (KL), Ko Prap (KP), Kuantan (KT), LaemNgob (LG), MaeKlong River (MK), Ko Mattaphon (MP), Narathiwat (NR), Qui Nhon (QN) and Getting (GT). Phase and amplitude values of the first simulated water levels were compared with observed water levels without non-tidal signal, which was filtered through Godin low-pass filter. After the first simulation, amplitude and phase values of eight harmonic constituents at open boundaries were adjusted until modeled and observed water levels were satisfactory in agreement. This process is called the calibration.

The model validation was performed using calibration model (case Tide2D as mentioned above), but it was simulated in different period, which was January 1-31, 2013. The root mean square error (RMSE), mean absolute error (MAE),  $R^2$ , vectorial difference (d), root summed square vector difference (RSS) and skill scores were used to see the differences between simulated water levels and observed water levels. After prepared model was calibrated and validated, spatial and temporal winds were applied as a driving force at the surface to see the effect of tides and winds



on sea surface current circulation in the GoT (case Wind2D). The sea surface currents during February 1-28, 2019 were simulated and compared with coastal HF radar.

Then, the model was setup to 3D model. The depth model was divided into 10 layers with thickness 2%, 3%, 4%, 6%, 8%, 10%, 12%, 15%, 20% and 20% of the water depth (Deltares, 2013). The thickness was measured from the bottom of overlying layer to the bottom of each layer. The temperature, salinity and river discharged data mentioned in 3.2.1, were applied to the model. Then, the model was simulated for two-year period of 2015 and 2016 to see the characteristics coastal upwelling in the GoT.

#### 4.2.1. First model simulation and calibration

Figures 4.6. and 4.7. show water level and tidal constituent comparison between modeled data obtained from the first simulation (before model tuning) and observed data during January 1-31, 2004 at Kuantan and Ko Lak stations as the representative of all 11 stations. Red and blue colors represent the modeled and observed data, respectively. From Figs 4.6 and 4.7, it was clearly seen high discrepancy between modeled and observed for both water level and tidal constituents at both stations. The  $R^2$  for both stations were small (less than 0.3), hence the modeled and observed data were disagreed. The amplitudes and phases at open boundaries of 2D model were therefore adjusted until reaching the best agreement between modeled and observed data (see Figs. 4.8. and 4.9). From Figs. 4.8 and 4.9, it was clearly shown the improvement of modeled water level and tidal constituents at both stations. The RMSE, MAE,  $R^2$ , skill scores, vectorial difference and Root-summed vector difference of the first simulation and after calibration (case Tide2D) were represented in Tables 4.1 and 4.2. The results of other 9 stations were shown in Appendix B1 and B2. From Table 4.1, the ranges of RMSE and MAE was 14.28-38.74 cm and 11.44-31.16 cm, respectively. The value of  $R^2$  is in the range of 0.73-0.83. Skill score is one of indices representing the excellent performance of the model was in the range of 0.92-0.96. The vectorial difference (d) and root summed square vector difference (RSS) was calculated using phases and amplitudes of tides at each station and shown in Table 4.2. The difference between the first simulated and calibrated was maximum at Kuantan station and minimum at Geting station. The comparisons of amplitude and phase between calibration and observation at Kuantan station and Ko Lak station were shown in Tables. 4.3 and 4.4, respectively.



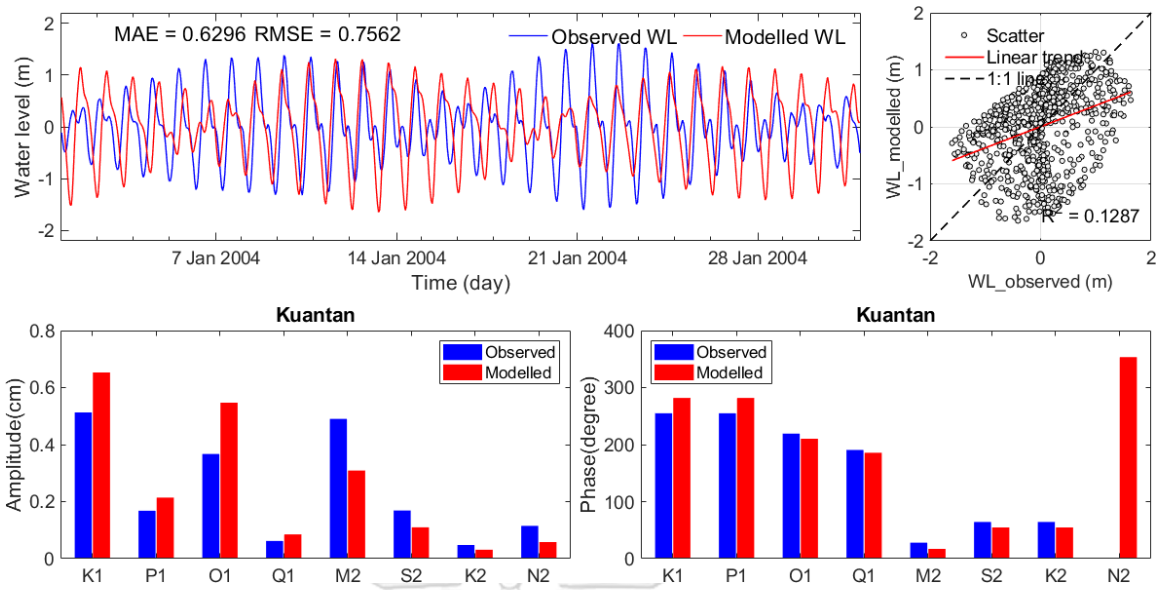


Fig. 4.6. Water level, phase and amplitude comparison between first simulation and observed data during January 1-31, 2004 at Kuantan Station.

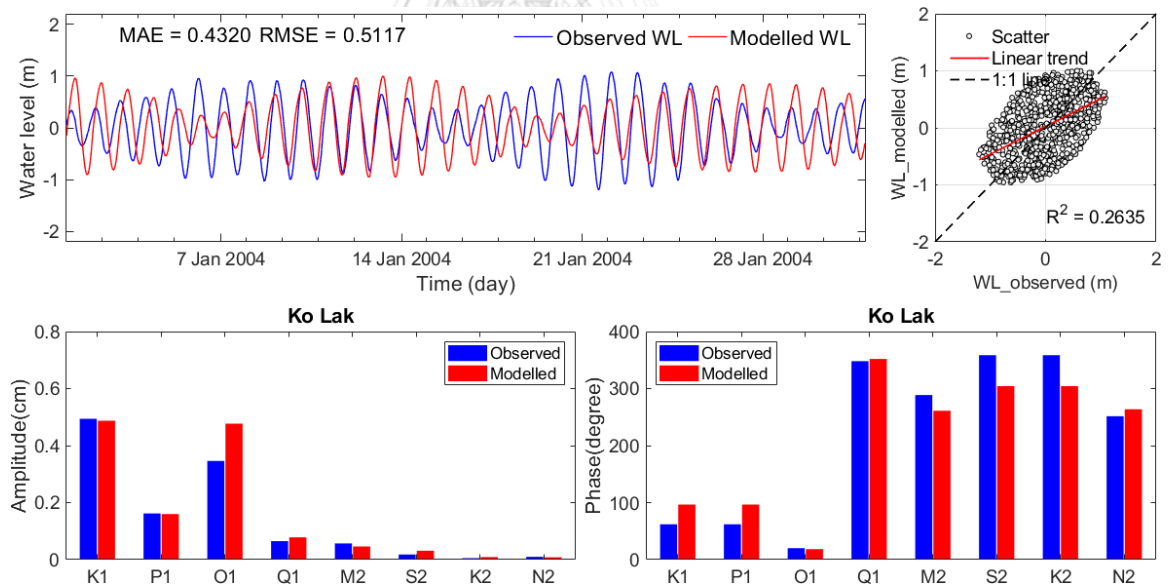


Fig. 4.7. Water level, phase and amplitude comparison between first simulation and observed data during January 1-31, 2004 at Ko Lak Station.

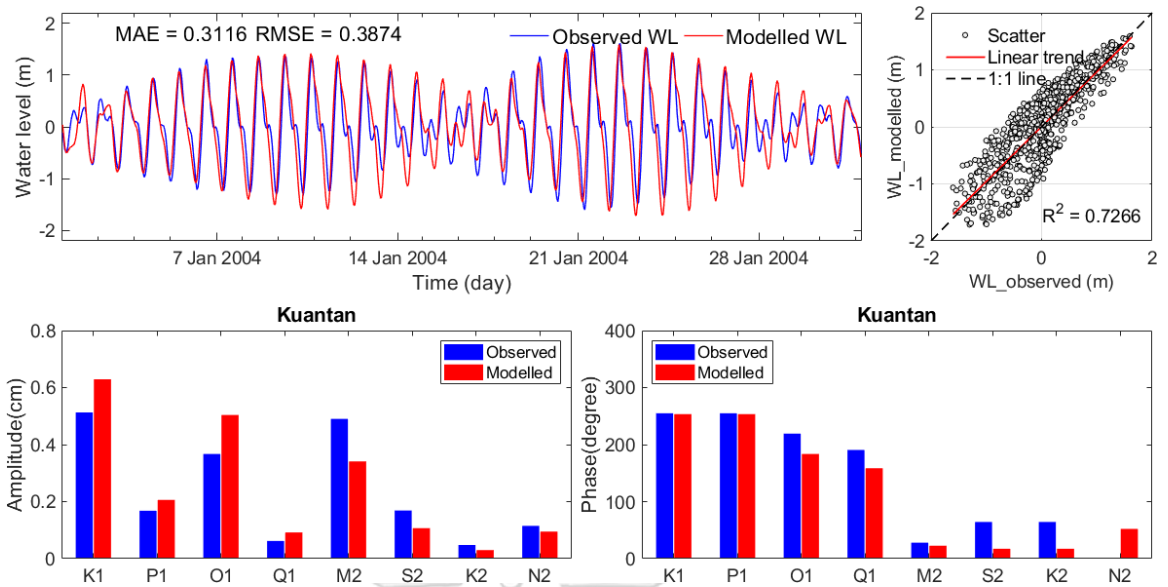


Fig. 4.8. Water level, phase and amplitude comparison between calibration and observed data during January 1-31, 2004 in case Tide2D at Kuantan Station.

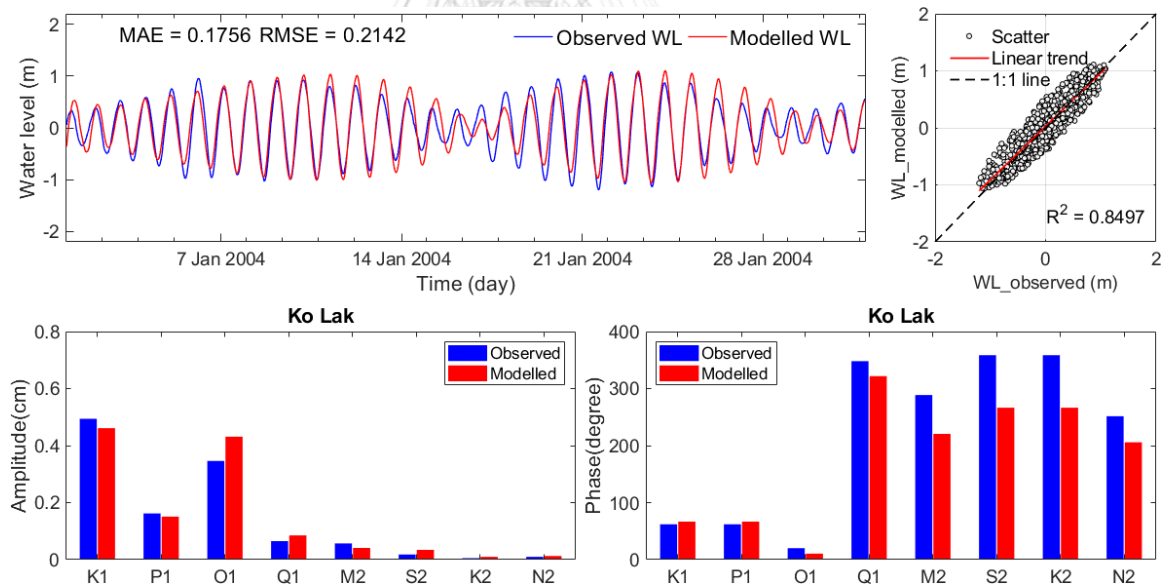


Fig. 4.9. Water level, phase and amplitude comparison between calibration and observed data during January 1-31, 2004 in case Tide2D at Ko Lak Station.

*Table 4.1. RMSE, MAE,  $R^2$  and skill scores of first simulation and Tide2D at 11 stations.*

Station	First simulation			Tide2D			skill scores
	RMSE (cm)	MAE (cm)	$R^2$	RMSE (cm)	MAE (cm)	$R^2$	
BK	73.13	59.97	0.26	36.26	29.23	0.82	0.95
GT	31.28	25.53	0.24	14.28	11.44	0.86	0.95
KL	51.17	43.20	0.26	21.42	17.56	0.85	0.96
KP	50.76	42.03	0.25	25.48	20.58	0.78	0.94
KT	75.62	62.96	0.13	38.74	31.16	0.73	0.92
LG	47.95	40.73	0.25	20.56	17.20	0.84	0.95
MK	75.53	61.91	0.26	36.30	29.13	0.81	0.95
MP	45.34	38.46	0.27	20.29	16.58	0.83	0.95
NR	28.50	22.84	0.21	14.41	11.74	0.82	0.93
QN	43.40	36.43	0.09	15.38	12.95	0.85	0.95
RY	54.49	45.90	0.26	23.47	19.60	0.84	0.96

*Table 4.2. Vectorial difference (d) and root summed square vector difference (RSS) of calibrated model (Tide2D) at 11 stations.*

Station	Vectorial difference (d) in cm								RSS (cm)
	K1	P1	O1	Q1	M2	S2	K2	N2	
BK	19.40	6.37	17.79	3.01	10.64	6.65	1.89	1.67	30.11
GT	54.03	17.72	45.40	7.42	27.09	15.02	4.26	4.79	79.69
KL	33.60	11.02	31.90	4.72	18.21	11.15	3.17	2.39	52.56
KP	47.08	15.44	41.26	6.85	21.18	13.05	3.71	2.83	69.60
KT	60.38	19.80	51.38	7.88	31.78	17.32	4.91	5.52	90.03
LG	8.52	2.80	6.06	0.56	3.78	1.39	0.40	0.46	11.58
MK	28.04	9.20	25.47	4.04	17.80	10.78	3.06	2.25	44.54
MP	40.62	13.32	35.14	5.77	18.99	11.69	3.32	2.55	60.08
NR	50.50	6.56	42.63	7.23	25.98	14.99	4.25	4.12	75.02
QN	2.22	0.73	4.67	0.17	2.35	0.08	0.03	0.14	5.73
RY	15.94	5.23	9.47	1.63	5.00	2.34	0.67	0.71	20.12

*Table 4.3. Amplitude and phase of water levels between calibration (Tide2D) and observation at Kuantan station*

Constituents	Tide2D		Observation	
	Amplitude (cm)	Phase (deg)	Amplitude (cm)	Phase (deg)
M2	0.629	253.450	0.513	254.900
N2	0.206	253.450	0.168	254.900
S2	0.504	183.519	0.367	219.300
K2	0.092	158.458	0.062	190.500
K1	0.341	22.668	0.490	28.000
O1	0.107	17.202	0.169	64.400
Q1	0.030	17.202	0.048	64.400
P1	0.095	52.162	0.115	0.800

*Table 4.4. Amplitude and phase of water levels between calibration and observation (Tide2D) at Ko Lak station*

Constituents	Tide2D		Observation	
	Amplitude (cm)	Phase (deg)	Amplitude (cm)	Phase (deg)
M2	0.461	66.737	0.494	62.000
N2	0.151	66.737	0.162	62.000
S2	0.431	10.371	0.346	20.000
K2	0.085	321.860	0.065	348.100
K1	0.041	220.501	0.057	288.600
O1	0.034	266.406	0.018	358.600
Q1	0.010	266.406	0.005	358.600
P1	0.013	205.799	0.010	251.400

#### 4.2.2. Model Validation

Results of water levels simulated during January 1-31, 2013, at Kuantan station and Ko Lak station were shown in Fig. 4.10 and 4.11. Results of other nine stations were shown in an Appendix B3. RMSE, MAE,  $R^2$  and skill scores of validation were shown in Table. 4.5. The range of RMSE and MAE was 13.54-38.81 cm and 11.14-31.39 cm, respectively.  $R^2$  is between 0.73-0.83. Skill score was represented the excellent performance with a range of 0.68-0.86. The vectorial difference (d) and root summed square vector difference (RSS) was shown in Table 4.6. The difference between the simulated and calibrated was maximum at Kuantan station and minimum at Geting station. The results of validation at Rayong,

Bangpakong, Narathiwat, Ko Mattaphon, MeaKlong, LaemNgob, Ko Prap, Getting and Qui Nhon stations were shown in Appendix B3. The comparisons of amplitude and phase between validation and observation at Kuantan station and Ko Lak station were shown in Tables. 4.7 and 4.8, respectively.

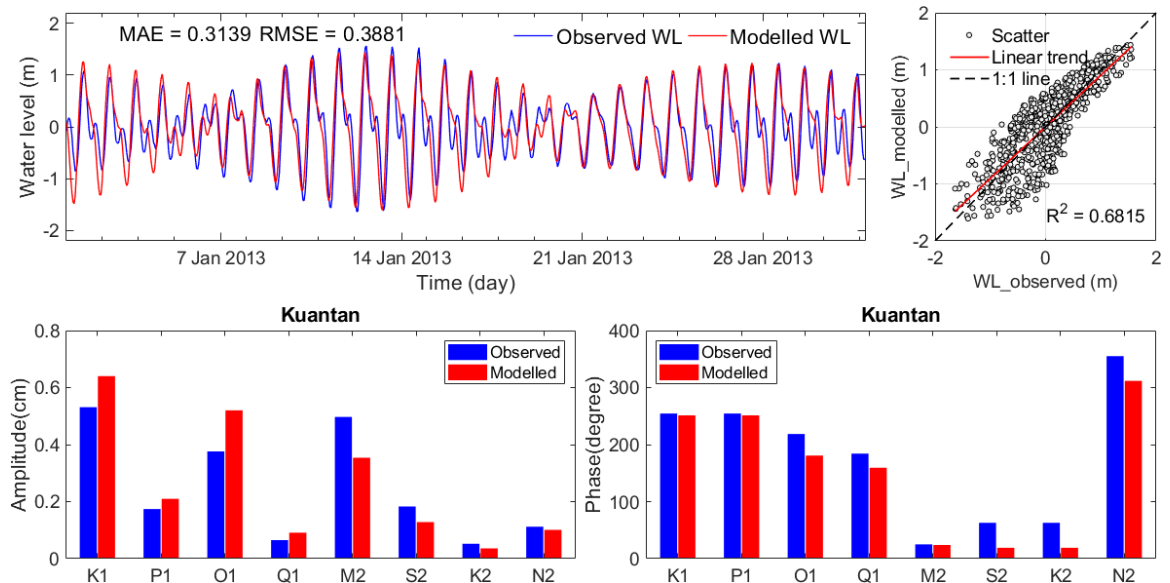


Fig. 4.10. Water level, phase and amplitude comparison between validation and observed data during January 1-31, 2013 at Kuantan Station.

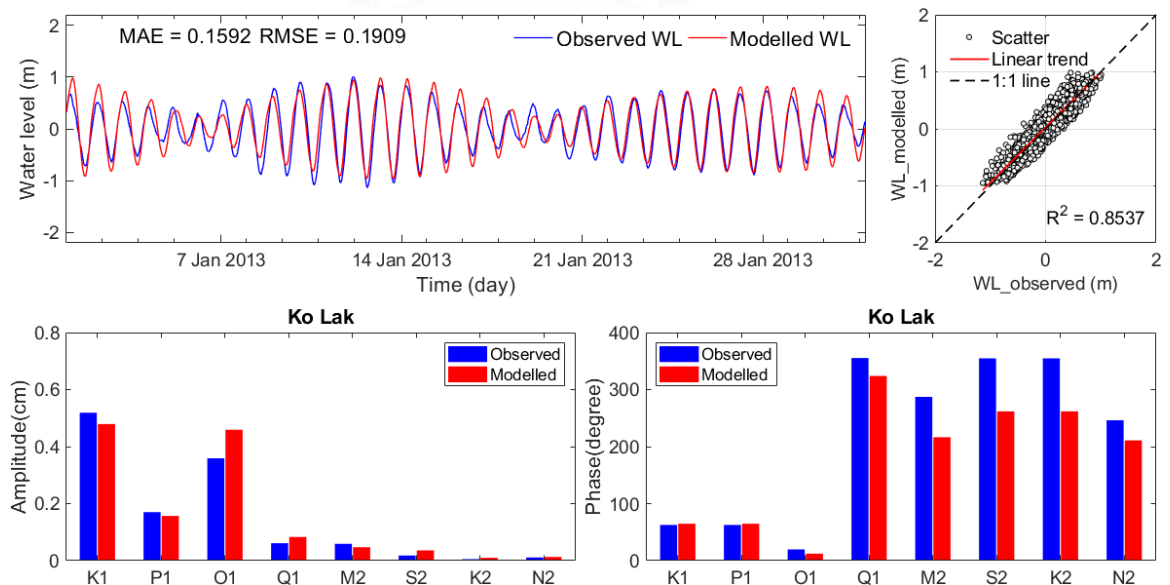


Fig. 4.11. Water level, phase and amplitude comparison between validation and observed data during January 1-31, 2013 at Ko Lak Station.

Table 4.5. RMSE, MAE,  $R^2$  and skill scores of validated model

Station	Validated model			
	RMSE (cm)	MAE (cm)	$R^2$	Skill score
BK	32.65	26.27	0.84	0.95
GT	14.24	11.14	0.85	0.94
KL	19.09	15.92	0.85	0.96
KP	24.30	20.04	0.76	0.93
KT	38.81	31.39	0.68	0.91
LG	18.89	15.88	0.84	0.95
MK	34.91	27.07	0.81	0.94
MP	22.04	18.38	0.75	0.93
NR	14.68	11.54	0.82	0.92
QN	13.54	11.36	0.86	0.95
RY	20.27	17.31	0.86	0.96

Table 4.6. Vectorial difference ( $d$ ) and root summed square vector difference (RSS) of validated model

Station	Vectorial difference ( $d$ ) in cm of validated model								RSS (cm)
	K1	P1	O1	Q1	M2	S2	K2	N2	
BK	12.90	4.23	22.00	3.11	8.62	6.60	1.88	3.04	28.44
GT	46.39	15.21	44.21	6.83	20.80	14.18	4.02	6.33	71.24
KL	29.35	9.63	33.02	4.72	13.94	10.01	2.84	4.69	48.90
KP	39.99	13.11	41.44	6.24	15.73	12.33	3.49	5.33	62.99
KT	56.14	18.41	45.44	7.16	24.34	14.65	4.15	6.92	80.49
LG	6.42	2.10	6.21	1.58	1.42	2.77	0.79	0.95	9.89
MK	22.50	7.38	28.72	4.53	13.29	9.70	2.75	4.50	41.29
MP	33.48	10.98	35.76	5.13	14.55	10.67	3.02	4.90	53.90
NR	43.48	14.26	43.35	6.35	18.46	13.48	3.82	5.70	67.70
QN	2.43	0.80	4.70	0.56	0.56	1.35	0.38	0.42	5.61
RY	8.87	2.91	13.19	2.21	3.64	3.98	1.13	1.45	17.28

#### 4.2.3. Characteristics of principal tidal constituents in the GoT

The co-range and co-tidal charts of M2, S2, K1 and O1 are presented in Fig. 4.12. The amphidromic system of M2 and S2 obtained from Tide2D model rotated in clockwise direction with an amphidromic point off the east coast near Ca Mau Cape. The M2 and S2 waves run from SCS into the GoT along Vietnam's coast with highest amplitude found in front of Mekong River. However, after passing tip of Ca Mau, generally small amplitudes were found for the whole gulf, except at the upper GoT, where tidal signal was amplified due to shallowness of bathymetry. For K1 and O1 tidal waves, they also propagated from the SCS reaching the entrance of the GoT and moved northwestward toward the upper GoT. Both tidal waves seemed to propagate along the axis of the GoT, that laid in northwest and southeast direction. Hence, the trough of diurnal tidal waves was found around the lower GoT, while the crests were found at the upper GoT and the entrance of the GoT. The amphidromic point of K1 positioned on the southwest of the GoT with the rotation in counterclockwise direction. Except for O1 tidal waves, the amphidromic points of other 3 tidal waves were in agreement with what were found by Zu et al. (2008). The amphidromic point of O1 was located along the west coast of the GoT with the rotation in counterclockwise direction. Even there was no point of O1 obviously located, the O1 point was likely to occur around the same location as in the mentioned studies. Furthermore, the amphidromic system of O1 tides also shown counterclockwise rotation.

The discrepancy found in this study compared to other studies might due to the insufficient of tidal stations in ocean (Fang et al., 1999), that leads to the shortage in accurate harmonic data. In this model study, the open boundaries were assigned at the north, the east and the south of the model domain (see Fig. 1.1). Most of the north and the east open boundaries was located in SCS without tidal stations. The applied harmonic constituents were based on the adjusting phase and amplitude values to give water levels with the perfect match to observed water levels. Thus, the adjusted phase and amplitude values might not be accurate values and effected the pattern of amphidromic system of O1 tidal wave.

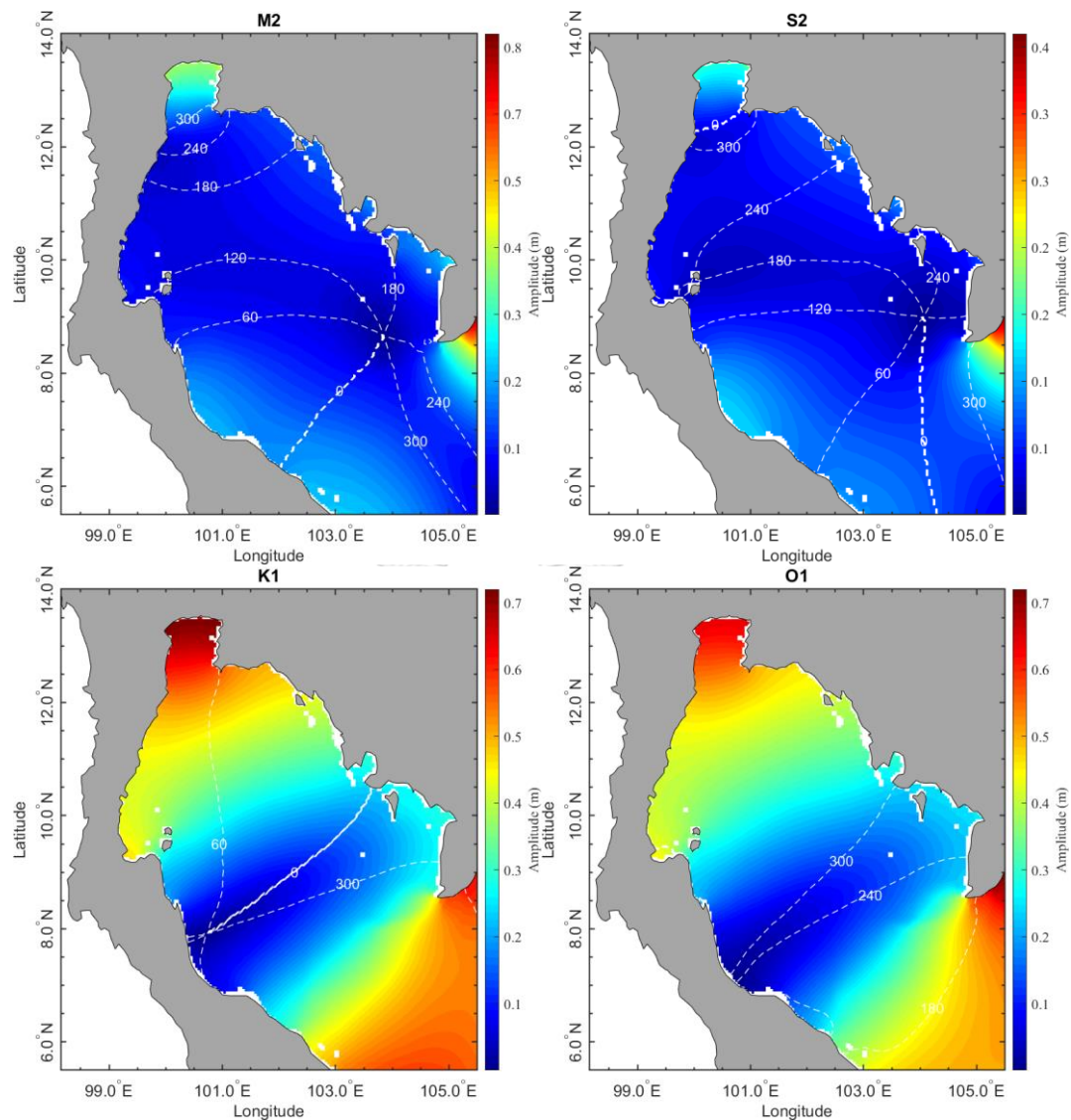


Fig. 4.12. Amphidromic system (amplitude and phase) of M2, S2, K1 and O1 tides found in the GoT.

#### 4.3. Surface current comparison

In the Wind2D case, the model was simulated during February 1-28, 2019 and applied spatio-temporal wind fields at the surface. In order to obtain the modeled and observed HF surface current at the same location, modeled surface current data were interpolated into a grid, which was created based on position and resolution of the observed HF surface current data. Besides, surface current from the coastal HF radar were filtered using Godin Filter to get rid of the non-tidal signals. The simulated surface current off four coasts, Upper, East1, East2 and Lower, were compared



with observed HF surface current. The locations of 85% of observed data off upper, east1, and east2 coast, and 75% of observed data off lower coast were compared as shown in Fig.4.13 (black patch color). The statistical indices, %RMSE and %MAE (see Eqs. (4.1) and (4.2)) of u and v velocity components, were estimated to see the performance of the Wind2D model.

$$\%RMSE = \frac{RMSE \text{ of } u \text{ or } v \text{ velocity component at each position}}{\text{range of RMSE of all } u \text{ or } v \text{ velocity components}} \times 100 \quad (4.1)$$

$$\%MAE = \frac{MAE \text{ of } u \text{ or } v \text{ velocity component at each position}}{\text{range of MAE of all } u \text{ or } v \text{ velocity components}} \times 100 \quad (4.2)$$

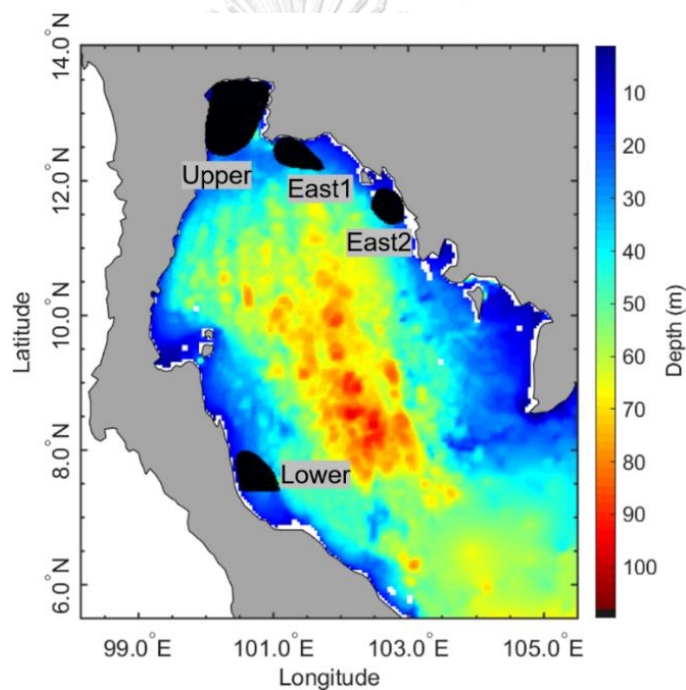


*Fig. 4.13. Coastal HF radar system areas: Upper, East1, East2, and Lower coast (Black patches).*

The %RMSE and %MAE of surface current velocity off mentioned four coasts were shown in Figs. 4.14-4.17 and Tables. 4.9-4.12. Off the Upper coast in Fig. 4.14. the maximum difference of u-velocity was near Bangpakong River Mouth and Maeklong River Mouth. The maximum difference of v-velocity was widely in the southeast of area. The average %RMSE of u-velocity and v-velocity was 5.32 and 14.16, respectively shown in Table. 4.9. Spatially averaged surface current velocity In Fig. 4.15 the maximum difference of u-velocity off East1 coast was in the

northwest of area with the average of 13.37 cm/s, while of v-velocity was in southwest area with the average of 13.58 cm/s as mentioned in Table. 4.10. The %RMSE and %MAE off the East2 coast was shown in Fig. 4.16 and Table. 4.11. The maximum difference of u-velocity widely spread in the south of area with the average of 17.05. The maximum difference of v-velocity was in the center and the west of area with the average of 16.90 cm/s. Off the lower coast the difference of u and v-velocity was shown in Fig. 4.17 and Table. 4.12. The maximum difference of u-velocity was in the west of area with the average of 15.88 cm/s, while the maximum difference of v-velocity was in the north of area with the average of 17.08 cm/s.

The simulated and HF Radar surface current velocity off four mentioned coasts were spatially averaged and compared with each other. The results of comparison were shown in Appendix B4. The amplitude and phase of simulated u and v-velocity off the Upper coast was in an agreement with the HF Radar, while off East1, East2 and Lower coasts the amplitude and phase patterns of u and v-velocity were not in an agreement with the HF Radar. To fix the discrepancy of velocity found in this study, the more detailed topography and open boundary forcing might be necessary (Davies et al., 2001). Also, the more accurate wind velocities would be valuable (Paduan and Shulman, 2004).

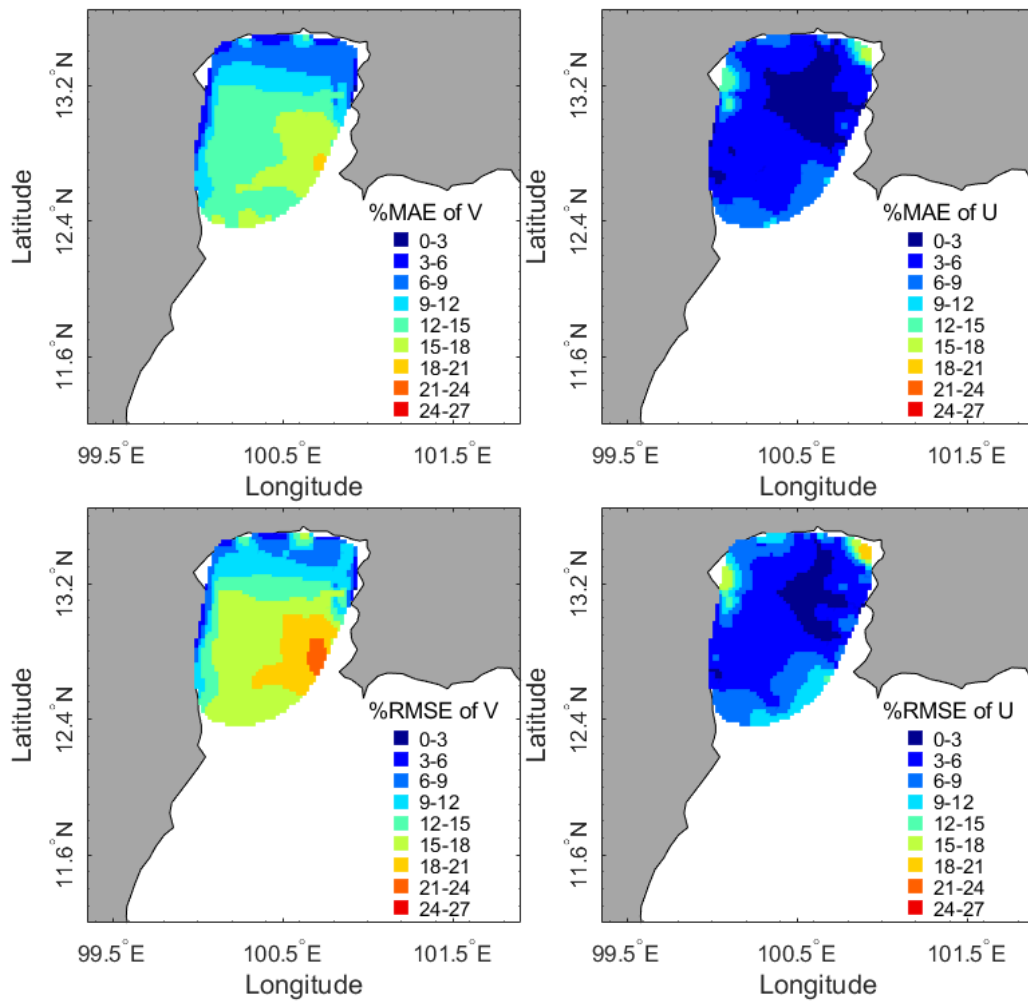


Fig. 4.14. %RMSE and %MAE of surface current velocity off the Upper coast during February 1-28, 2019 in case Wind2D.

Table 4.9. %RMSE, %MAE and average of surface current velocity off the Upper coast during February 1-28, 2019 in case Wind2D

Surface current velocity	%RMSE			%MAE		
	maximum	minimum	average	maximum	minimum	average
u velocity	20.24	1.56	5.33	15.62	1.25	4.26
v velocity	23.46	2.20	14.16	19.08	1.85	12.05

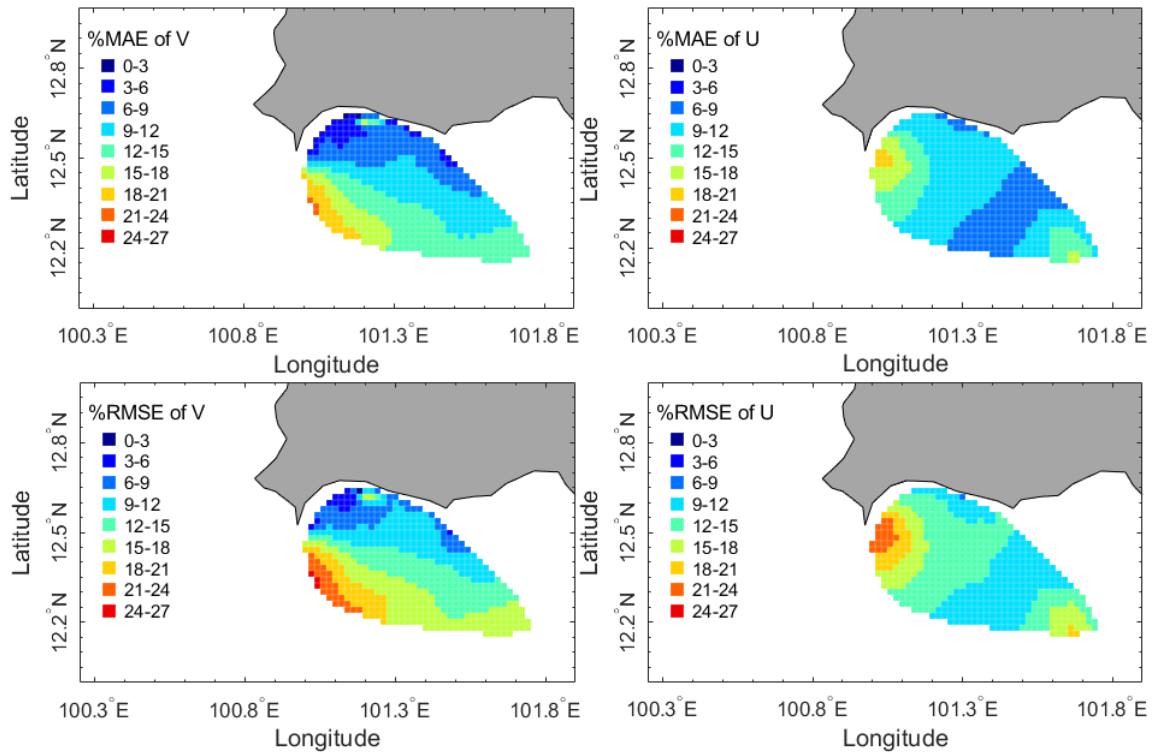


Fig. 4.15. %RMSE and %MAE of surface current velocity off the East1 coast during February 1-28, 2019 in case Wind2D.

Table 4.10. %RMSE, %MAE and average of surface current velocity off the East1 coast during February 1-28, 2019 in Wind2D.

Surface current velocity	%RMSE			%MAE		
	maximum	minimum	average	maximum	minimum	average
u velocity	23.45	8.26	13.37	19.03	6.75	10.68
v velocity	24.77	1.79	13.58	21.56	1.41	11.46

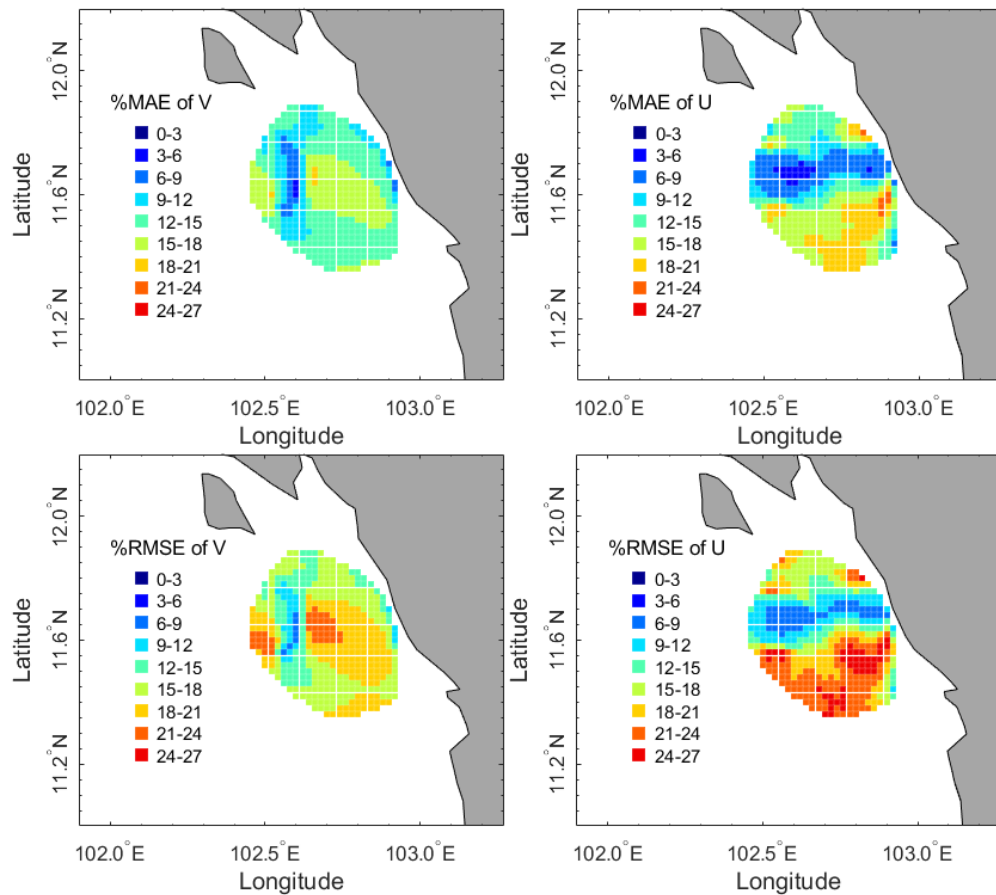


Fig. 4.16. %RMSE and %MAE of surface current velocity off the East2 coast during February 1-28, 2019 in Wind2D.

Table 4.11. %RMSE, %MAE and average of surface current velocity off the East2 coast during February 1-28, 2019 in case Wind2D

Surface current velocity	%RMSE			%MAE		
	maximum	minimum	average	maximum	minimum	average
u velocity	25.35	6.47	17.05	21.89	4.92	13.73
v velocity	22.72	7.39	16.90	18.30	5.93	13.53

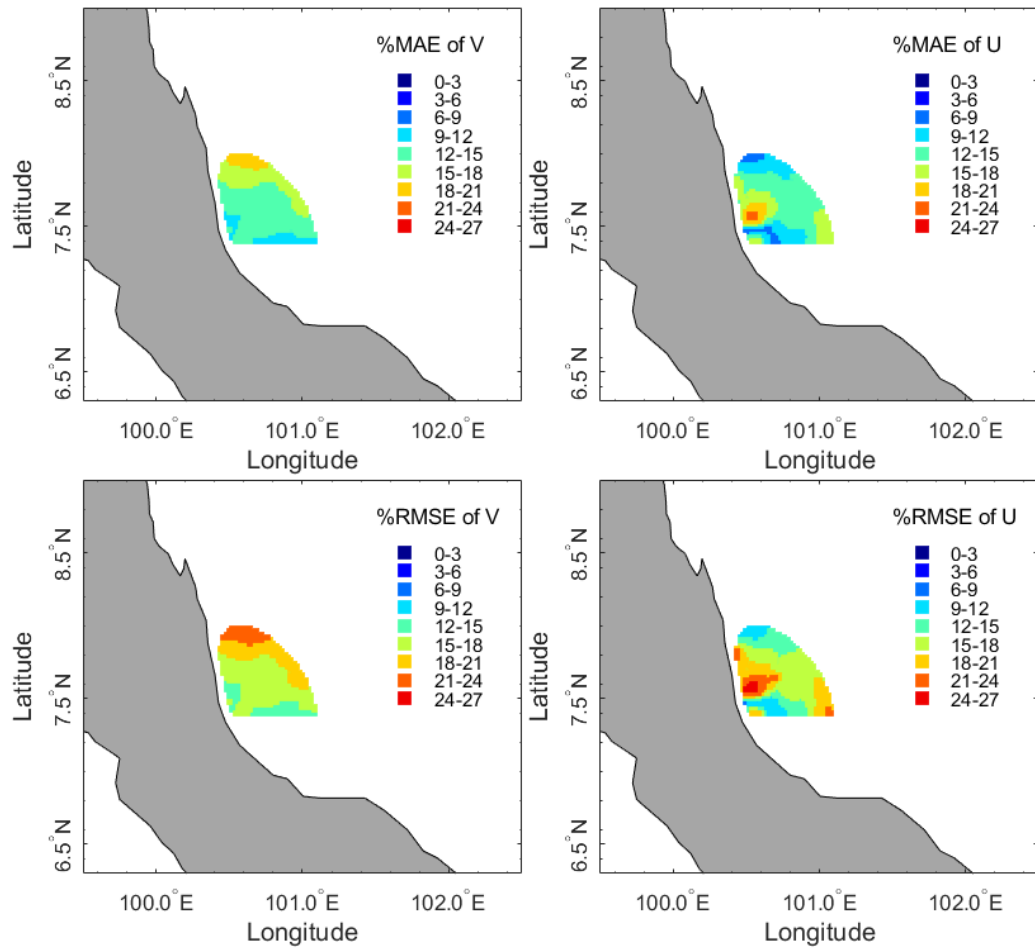


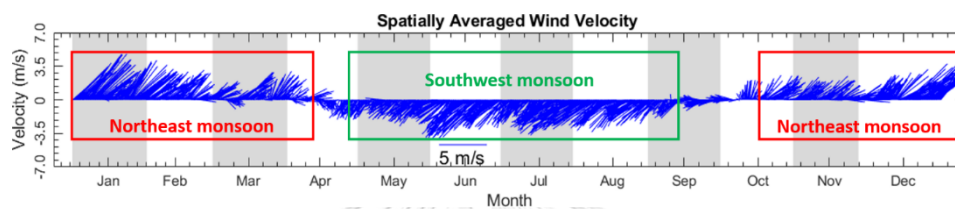
Fig. 4.17. %RMSE, %MAE of surface current velocity off the Lower coast during February 1-28, 2019 in case Wind2D.

Table 4.12. %RMSE, %MAE and average of surface current velocity off the Lower coast during February 1-28, 2019 in case Wind2D.

Surface current velocity	%RMSE			%MAE		
	maximum	minimum	average	maximum	minimum	average
u velocity	25.40	8.17	15.88	21.85	6.51	13.11
v velocity	22.72	12.60	17.08	19.22	10.22	14.04

#### 4.4. Seasonal sea surface temperature and current in the GoT

In the TWH3D case, surface current of 1 January to 31 December of 2012 was hourly simulated to investigate seasonal surface circulations during northeast and southeast monsoons represented by January and August, respectively. In addition, river discharge, surface heat flux, and wind were also applied. The area averaged wind vectors of 2012 used in the model were presented in Fig. 4.18, where the northeasterly winds dominated during November to February, while the southwesterly winds dominated during May to September.



*Fig. 4.18. Averaged 6-hourly wind stress vectors cover the model domain during January 1-December 31, 2012. Red box represents during northeast monsoon. Blue represents during southwest monsoon.*

The monthly averaged sea surface temperature and surface current obtained from the TWH3D is shown in Fig. 4.19. During the northeast monsoon (January) as is shown in Fig. 4.19a, the whole gulf was covered with the cooler water of 26.5-29.5 degree Celsius. The clear cooler waterfront of 26.5-27.5 degree Celsius was found along the west coast of the upper gulf and the central gulf, which was associated with southward flow. It was also found the lower gulf near Ca Mau Cape. At the GoT's entrance, the cooler water of 26.5-27.0 degree Celsius from the SCS flew southwestward toward the Malaysian Peninsular and flew northwestward into the GoT. The counterclockwise current of 28.5 degree Celsius were generated along the west coast of the lower gulf. The water along the west coast of the upper gulf moved southward then moved along the west coast and the east coast before moving southward and westward at the central gulf. The water along the west coast of the lower gulf moved eastward and met the southwestward water from the east coast before moving northward and westward. The coastal water was found cooler than the oceanic water along the west coast of the upper gulf, the central gulf to the lower gulf and the east coast near Ca Mau Cape. The difference of temperature was about



1.0 degree Celsius which was represented as example lines no. 1, 2 and 3 in Fig. 4.24a.

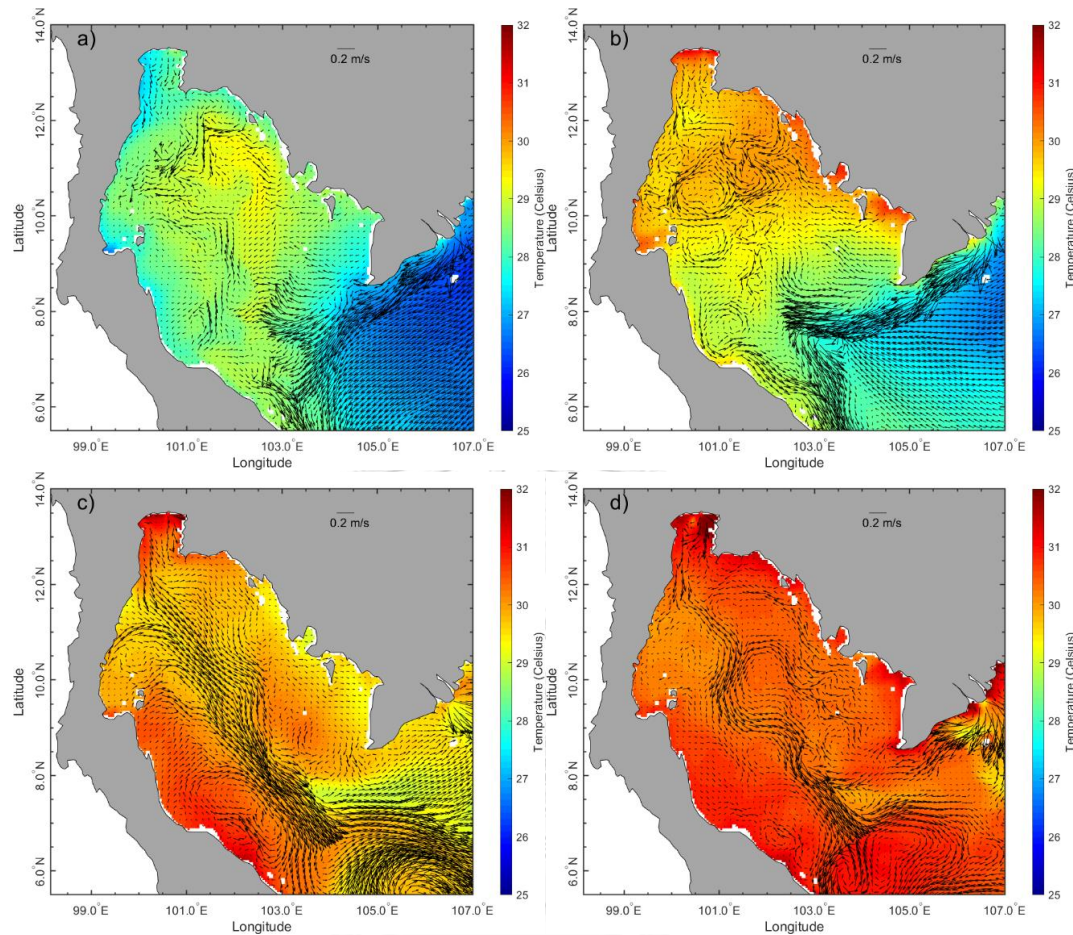


Fig. 4.19. Seasonal sea surface temperature and current of a) Northeast monsoon, b) 1<sup>st</sup> Inter-monsoon, c) Southwest monsoon, and d) 2<sup>nd</sup> Inter-monsoon.

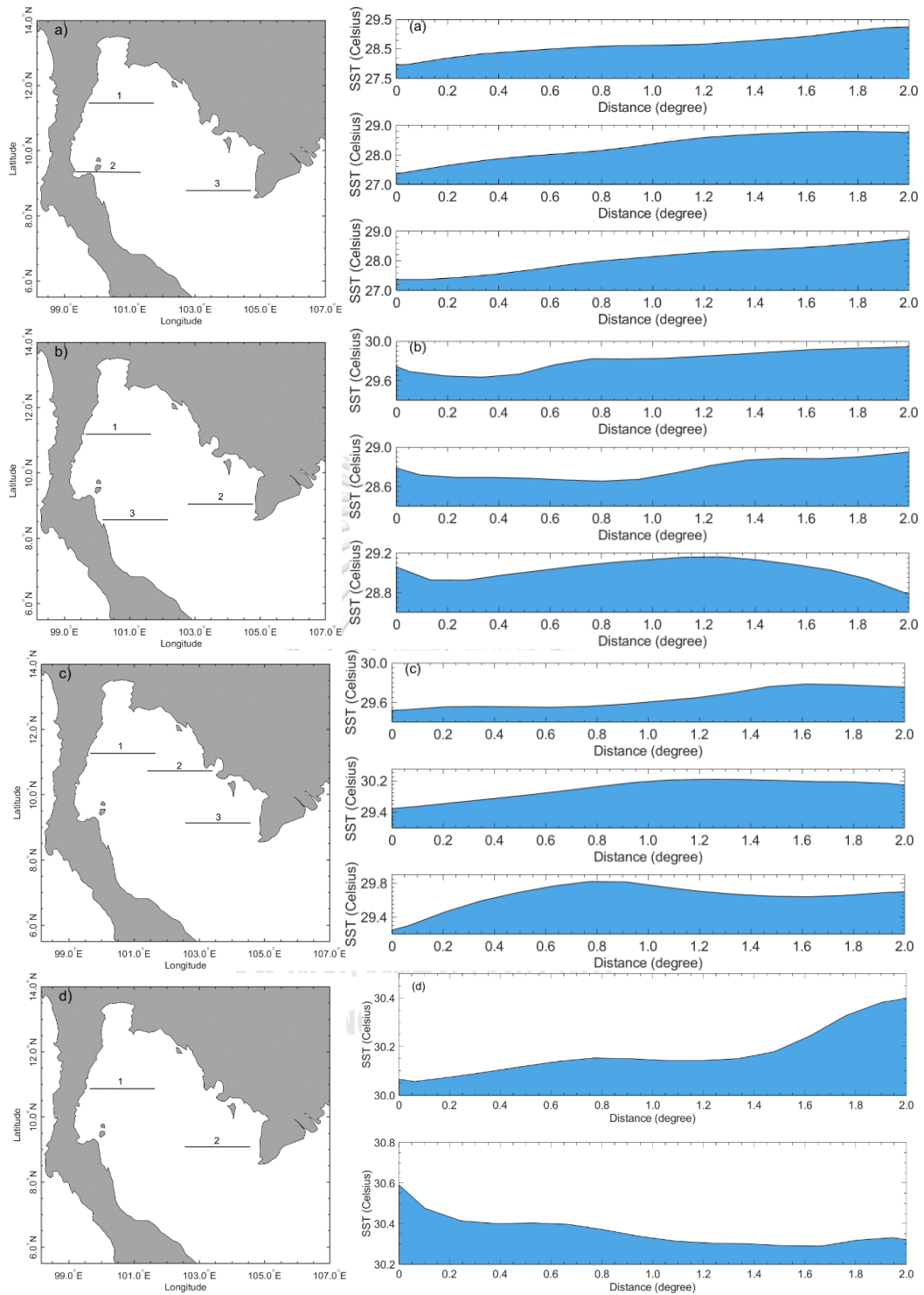
In Fig. 4.19b, during the 1<sup>st</sup> inter-monsoon in March the whole gulf was warmer than during the northeast monsoon. The temperature range was 27.5-31.0 degree Celsius. In the upper gulf, the water along the west coast remained flowing southward, while the water along the east coast moved southward and turned eastward at 100.25°E longitude and 12.0°N latitude where the 28.5 degree Celsius surface water occurred. Furthermore, at the northern part of the upper gulf, warmest surface water was found in the GoT. In the center of the central gulf a counterclockwise and clockwise circulations were developed. The lower gulf was generally dominated with the cooler water of 28.5-29.5 degree Celsius which was the result of cooler



water flowing westward from the SCS. In this period, strong jet of cold water from the SCS intruded into the GoT more than during the northeast monsoon as shown in Fig. 4.19a. The cooler coastal water was found along at the  $100.25^{\circ}\text{E}$  longitude and  $12.0^{\circ}\text{N}$  latitude with the difference of temperature of 0.20 degree Celsius (see line 1. in Fig. 4.20b) and along the west coast of the lower gulf with the difference of 0.15 degree Celsius (see line 2 in Fig. 4.20b). The strong southward flow along the Malaysian Peninsular as existing in Fig. 4.19a still found in this period.

During southwest monsoon as seen in Fig. 4.19c, the warmer water of 29.0-32.0 degree Celsius was covering the whole gulf with the warmest water situated in the upper gulf and along the west coast of the lower gulf. Generally, water in the gulf was moving southeastward from the central gulf to the lower gulf then dispersed southwestward and eastward to the SCS. The southward water from the upper gulf met the northeastward water flowing along the west coast at  $100.5^{\circ}\text{E}$  longitude and  $11.5^{\circ}\text{N}$  latitude, where cooler water of 29.5 degree Celsius occurred then moved southeastward to the lower gulf. The clockwise circulation was generated along the west coast of the lower gulf near the entrance of the gulf. The cooler coastal water was found along the west coast and the east coast with the difference of temperature of 0.60-0.20 degree Celsius (see line 1-3 in Fig. 4.20c). Near the GoT's entrance, flow seemed to propagate northeastward toward the Vietnam's coast.

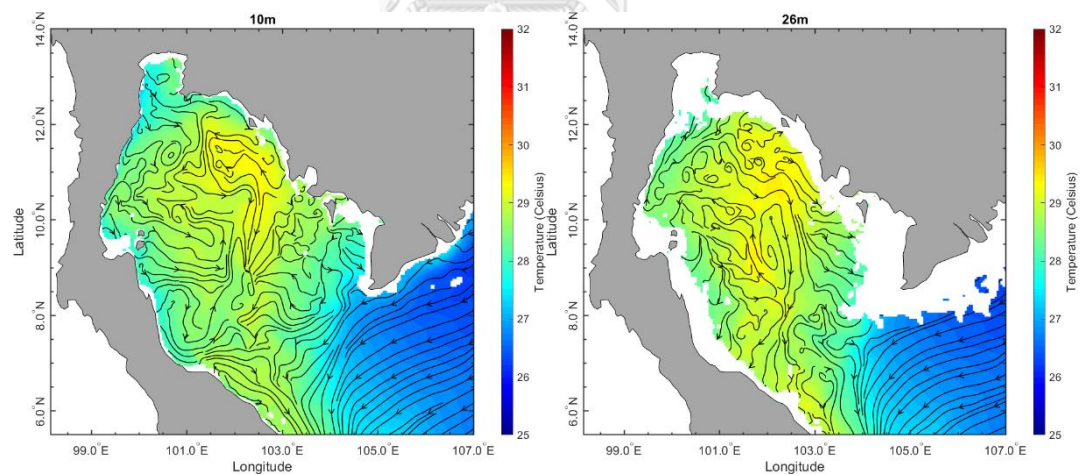
During the 2<sup>nd</sup> inter monsoon as seen in Fig. 4.19d, the warmer water of 29.0-32.0 degree Celsius was remained covering the upper gulf and the west coast of the lower gulf, while the central gulf the surface temperature was about 30.0-31.0 degree Celsius. Strong southeastward jet as previous shown in Fig. 4.19c still existed in the GoT. In addition, large discharge was found at the mouth of Mekong River. It is depicted by the strong jet out of the river mouth (near  $106.5^{\circ}\text{E}$  longitude and  $9.5^{\circ}\text{N}$  latitude). It is also found at Chao Phraya River Mouth in the upper gulf. The counterclockwise circulation was found at the center of the gulf. Like in August the water in the upper gulf mostly flowed southward along the west coast and turned southeastward at where the cooler water of 30.0 degree Celsius occurred with the difference of 0.34 degree Celsius between the coastal and oceanic water (see line 1-2 in Fig. 4.20d).



*Fig. 4.20. Seasonal sea surface temperature cross section profile (right) of line number 1 (upper) and line number 2 (bottom) extracted from shoreline to offshore of a) Northeast monsoon, b) 1<sup>st</sup> Inter-monsoon, c) Southwest monsoon, and d) 2<sup>nd</sup> Inter-monsoon.*

#### 4.5. Seasonal distribution of water temperature in the GoT

In this section, the spatial monthly averaged temperature and flow circulation (streamline) at each layer was investigated. During the northeast monsoon, the movement patterns of water at each layer are shown in Fig. 4.21 and Appendix B5. At the depth 50 m the cooler water of 27.0 degree Celsius from SCS moved northward into the gulf (see also a streamline of flow coming from SCS at the bottom). The water was getting warmer of 29.0-29.5 degree Celsius as the result of mixing with the clockwise warmer water at the center of the gulf. This anti-cyclonic gyre appeared at depth 26 m down to the bottom can lead to the downward movement of underlying water. As a result, warmer water exhibited underneath sublayer. At the depth about 26 m the water along the west coast separated and moved northward to the upper gulf, and southward to the lower gulf. Then, at the depth 10 m the water (26.5-27.0 degree Celsius) in the upper gulf moved southward along the west coast. The water along the east coast at the depth about 14 m (figure is shown in Appendix B5) moved southward to mix the cooler water from SCS. That's why there existed of cooler water near Ca Mau Cape.



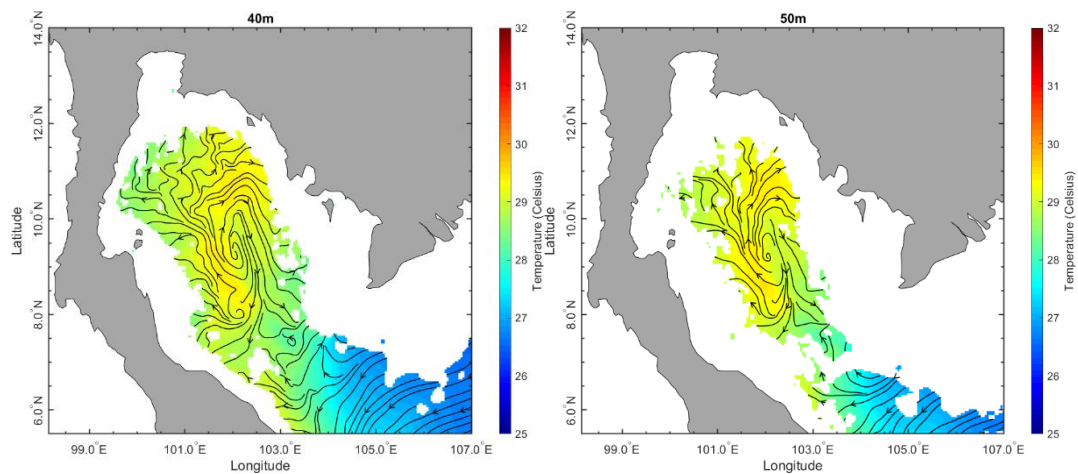


*Fig. 4.21. The distribution of monthly averaged water temperature at depth 10, 26, 40 and 50 m in the GoT of Northeast monsoon.*

During the 1<sup>st</sup> inter-monsoon, the movement patterns of water at each layer are shown in Fig. 4.22 and Appendix B6. In this period, the cold tongue of SCS water was clearly observed at all layers. At the depth about 50.0 m the southwestward cooler water of 26.5-27.0 degree Celsius from SCS was moving northward to the gulf. And, the water dispersed to the west and the east coast. The water turned northeastward and southward along the east coast. At the depth 38 m the water at the center of the lower gulf turned clockwise and moved out to the SCS. The water in the east coast of the central gulf was getting warmer at the depth about 38-40 m. The water in the lower gulf and the west coast of the central gulf remained cooler than along the east coast because of the cooler water from the SCS kept flowing to the west of the lower gulf. The 29.5 degree Celsius water along the west coast of the central gulf existed at bottom toward depth about 20 m then started getting warmer until reaching the surface.

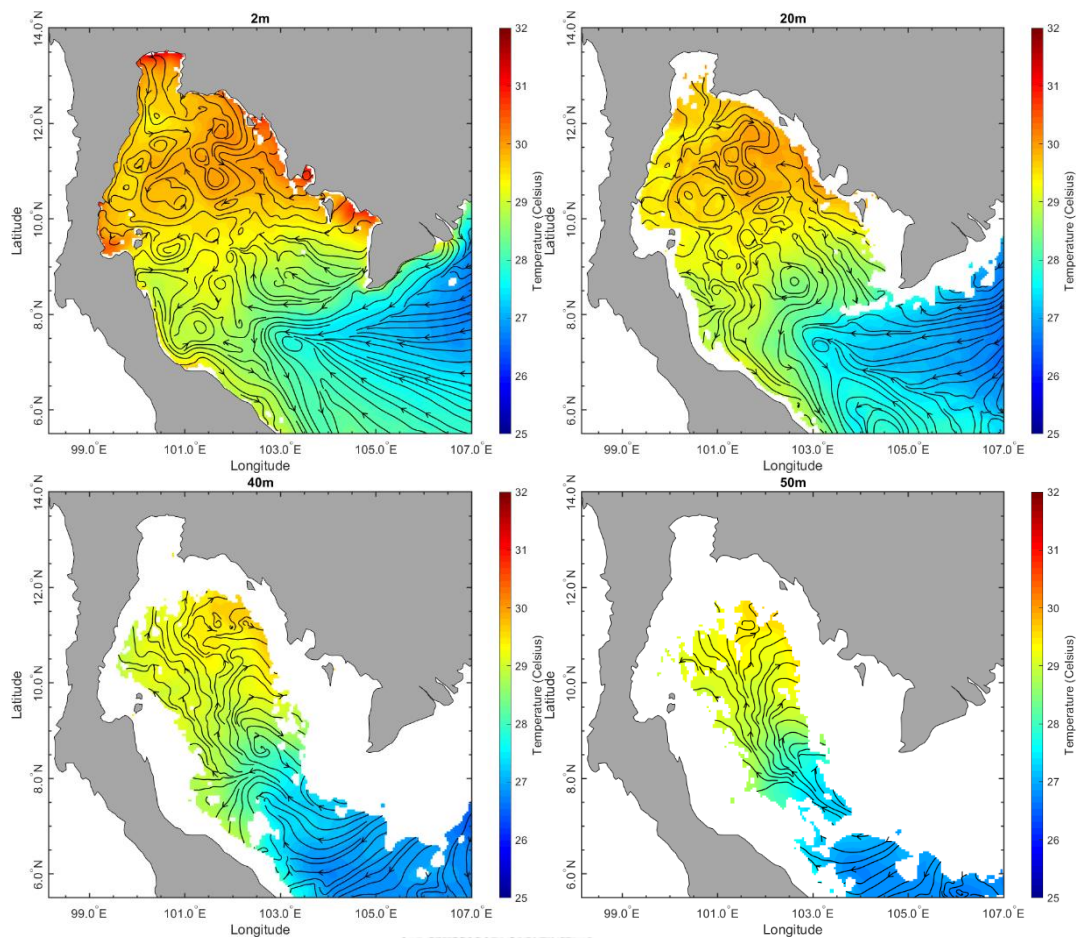


*Fig. 4.22. The distribution of monthly averaged water temperature at depth 2, 20, 40 and 50 m in the GoT of 1<sup>st</sup> Inter-monsoon.*

During the southwest monsoon, the patterns of water at each layer are shown in Fig. 4.23 and Appendix B7. The water of 28.0 degree Celsius flowed northward from the SCS into the lower gulf at the depth about 50 m downward. This signal, especially the bottom water, propagated northward until reaching the central gulf. Along the way north, the SCS water got warmer as it mixed with the local warm water. Until the depth about 30 m the water along the east coast moved in counterclockwise direction, while the water along the west coast started moving in clockwise direction. It caused the cooler water existing along the west and the east coast. Water near surface water (2 m depth), especially along the middle of the gulf axis, seemed to propagate in the southeast direction toward SCS. Hence, it is clear seen that surface and bottom waters propagated in the different direction, moving out the gulf at the top layer and moving in at the lower layer.



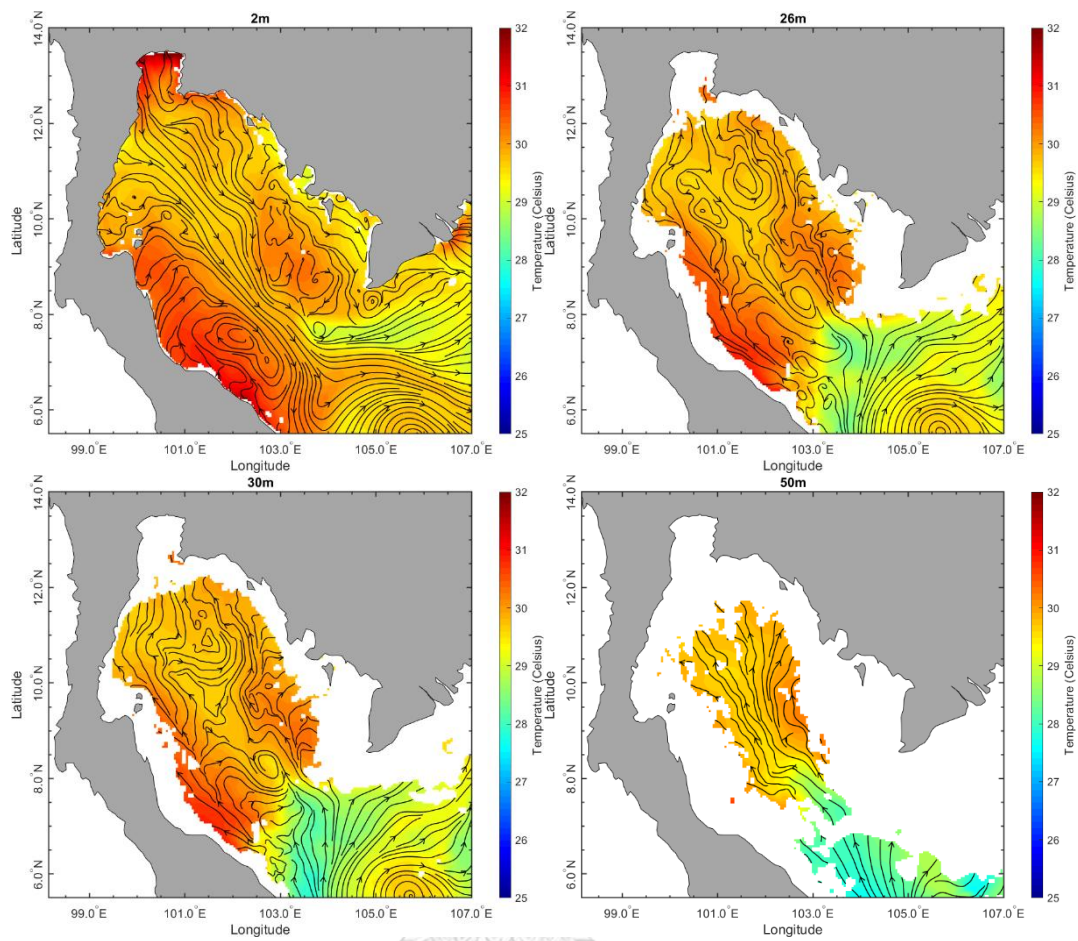


*Fig. 4.23. The distribution of monthly averaged water temperature at depth 2, 26, 30 and 50 m in the GoT of Southwest monsoon.*

During the 2<sup>nd</sup> inter-monsoon, the patterns of water at each layer are shown in Fig. 4.24 and Appendix B8. In this period, the flow patterns in each layer were similar to the southwest monsoon. At the depth about 50 m the cooler water of 28.5-29.0 degree from SCS moved northward to the gulf. The water dispersed to the west and the east coast of the central gulf. About the depth 28 m the cooler water was flowing counterclockwise at the center of the gulf, and clockwise along the west coast of the central gulf. It led the water there to keep cooler than other areas til the depth about 24 m where the water was getting warmer til the surface.

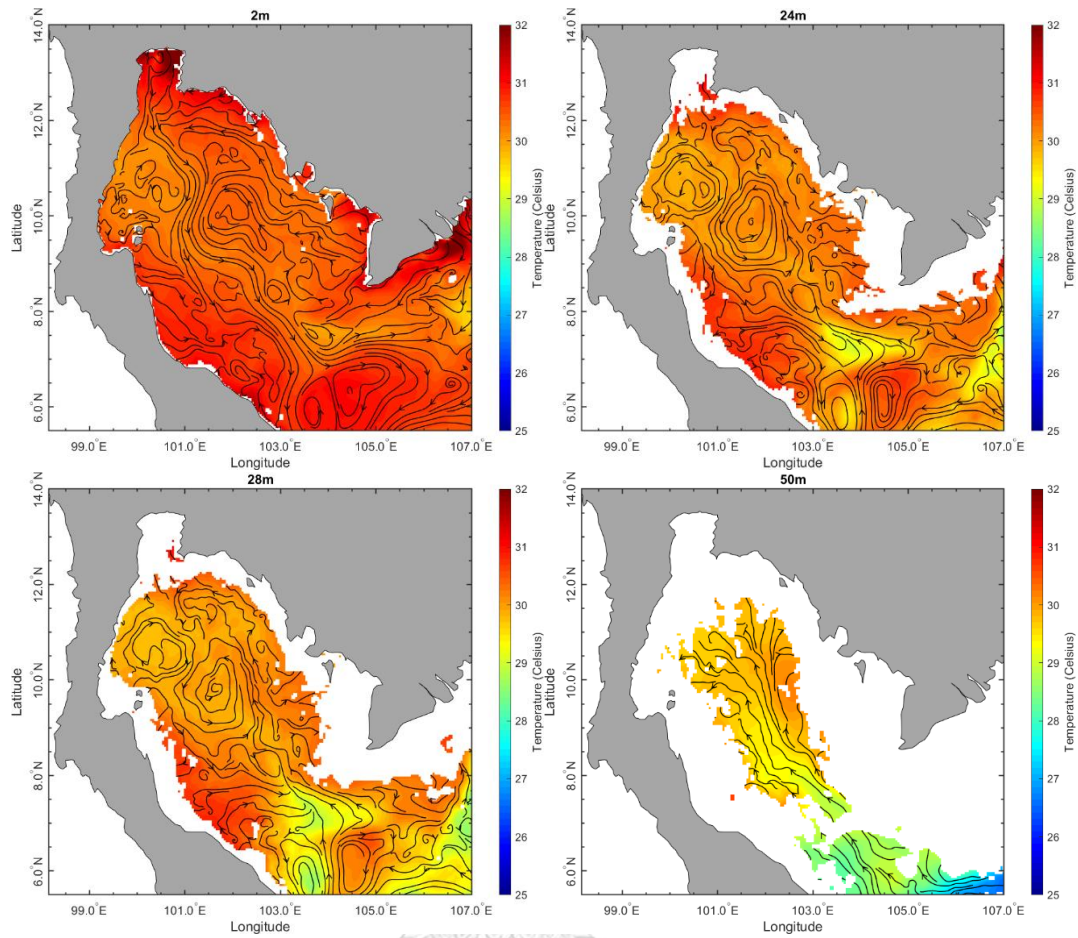


Fig. 4.24. The distribution of monthly averaged water temperature at depth 2, 24, 28 and 50 m in the GoT of 2<sup>nd</sup> Inter-monsoon.

#### 4.6. Seasonal sea surface salinity in the GoT

Generally, the saltier water from SCS was flowing through the central channel into the GoT. It caused the water in the central of the gulf saltier than the coastal water. The bottom water was saltier than the surface water. In January (Fig. 4.25a) and March (Fig. 4.25b), the less salty water was found along the west and the east coast of the upper gulf and near Ca Mau Cape which was a result of discharge from main 4 rivers in the upper gulf and Mekong River, respectively. In August (Fig. 4.25c) and October, saltier water covered the whole GoT, except the upper gulf and Ca Mau Cape, where water remained fresher. The water in the east side of the gulf was saltier than the west side of the gulf because of the saltier water flowing into the GoT from SCS has been pushed to the right due to Coriolis force. The saltier water from SCS kept flowing into the GoT all year round,

especially with the huge amount of water during northeast monsoon (see Fig. 4.25a) and 1<sup>st</sup> inter-monsoon (see Fig. 4.25b).

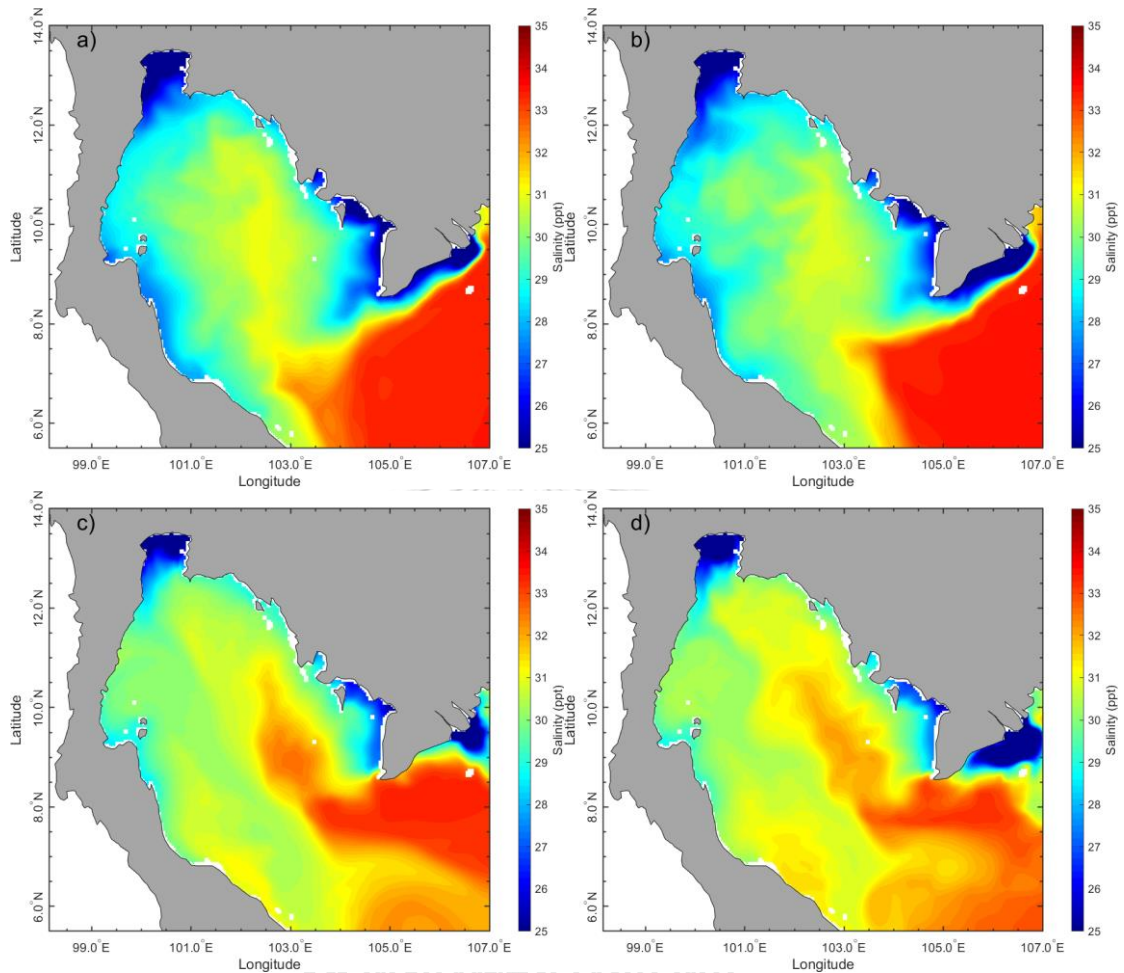


Fig. 4.25. The distribution of monthly averaged sea surface salinity in the GoT of a) Northeast monsoon, b) 1<sup>st</sup> Inter-monsoon, c) Southwest monsoon, and d) 2<sup>nd</sup> Inter-monsoon.

#### 4.7. Seasonal distribution of water salinity in the GoT

The distribution of water salinity during January during northeast monsoon in the GoT is shown in Fig. 4.26 and Appendix B9. The water about 34 ppt was flowing northward from SCS into the gulf. The water was getting less salty about 30.0-30.5 ppt due to the mixing with the clockwise water of at the center of the gulf which appeared at the depth about 26 m. At the depth 26 m the water along the west coast was separating northward and southward. And it was getting less salty of 29.0 ppt. At the depth 14 m (see figure in Appendix B9) the water at the center of the gulf was 30.0-



31.0 ppt, while the coastal water along the west coast and the east coast was about 27.0-28.5 ppt and about 25.5-26.0 ppt in the upper gulf. The water at the west of Ca Mau Cape was 27.0-28.0 ppt and was getting water of 29.0 ppt from Mekong River. At the depth 10 m the water along the west of Ca Mau Cape was getting less salty of 26.5-27.0 ppt as the water from SCS remained flowing into there.

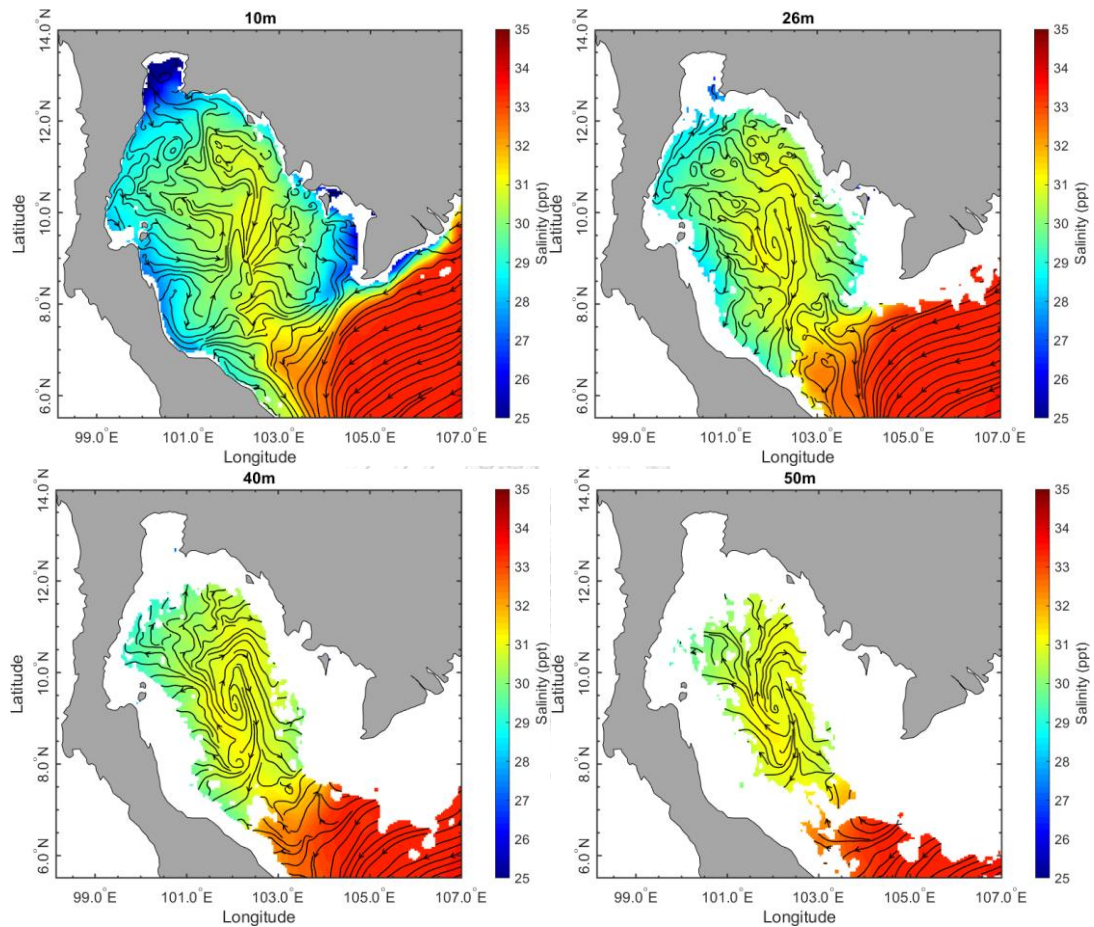


*Fig. 4.26. The distribution of monthly averaged water salinity at depth 10, 26, 40 and 50 m in the GoT of Northeast monsoon.*

The distribution of water salinity in March during 1<sup>st</sup> inter-monsoon is shown in Fig. 4.27 and Appendix B10. The water of 33.0-34.0 ppt from SCS at the depth 50 m was flowing northward into the gulf through the gulf's entrance. Then, the water was 30.5-31.0 ppt due to the mixing with the water at the center of the gulf. At the depth 40 m the water from SCS remained flowing into the gulf. The mixed water of 30.0-31.0 ppt at the center gulf was flowing westward and eastward. And, the eastward water

was flowing in clockwise direction along the east coast to mix with the water from SCS near Ca Mau Cape. At the depth 20 m the water along the east coast kept flowing in southward and was getting less salty of 28.5-29.0 ppt. The water along the west coast also was getting less salty of 27.5-29.0 ppt, especially in the upper gulf with 27.0 ppt. At the depth 12 m (see figures in Appendix B10) the water of 26.0 ppt from Mekong River was flowing to mix with the water near Ca Mau Cape, and let the water there was less salty of 27.5-28.5 ppt. The coastal water kept getting less salty until surface layers, especially in the upper gulf, along the west coast of the lower gulf and around Ca Mau Cape.

During the southwest monsoon in August the distribution of water salinity is shown in Fig. 4.28 and Appendix B11. At the depth 50 m the water of 33.5 ppt from SCS was flowing northward into the gulf. The water was lessened to 32.0-32.5 ppt and remained northward flowing at the center of the gulf. At the depth 30 m the clockwise water along the east coast was 32.0 ppt, while the water along the counterclockwise water occurred along the west coast with 30.5-31.0 ppt. The water at the depth 14 m (see figures in Appendix B11) the coastal water along the west and the east was less salty, especially with 27.5 ppt in the upper gulf, while the water at the east of the lower gulf remained high salinity of 32.5-33.0 ppt. The water around Ca Mau Cape was less salty of 28.5-29.0 ppt as the result of the water from Mekong River, and kept getting less salty until the surface layers.

The distribution of water salinity in October during 2<sup>nd</sup> inter-monsoon is shown in Fig. 4.29 and Appendix B12. The saltier water from SCS remained flowing northward into the gulf at the depth 50 m and was 31.0-32.0 ppt as the result of mixing with the water at the center of the gulf. At the depth 28 m the clockwise water along the west coast of the central gulf was 30.5 ppt, while the water at the east side of the lower gulf and the counterclockwise water at the center of the gulf was saltier of 31.5-32.5 ppt due to the water from SCS flowing northward to mix with the water in the gulf. At the depth 14 m (see figures in Appendix B12) the water generally was getting less salty with 27.5-28.5 ppt in the upper gulf, 29.5-30.0 ppt along the west and the east coast. The water of the east side of the gulf toward the entrance of the gulf was saltier of 31.0-32.0 ppt, especially 33.0 ppt at the gulf entrance. The water from Mekong River remained flowing into the water at the west of Ca Mau Cape and let the water to 29.5-30.5 ppt.

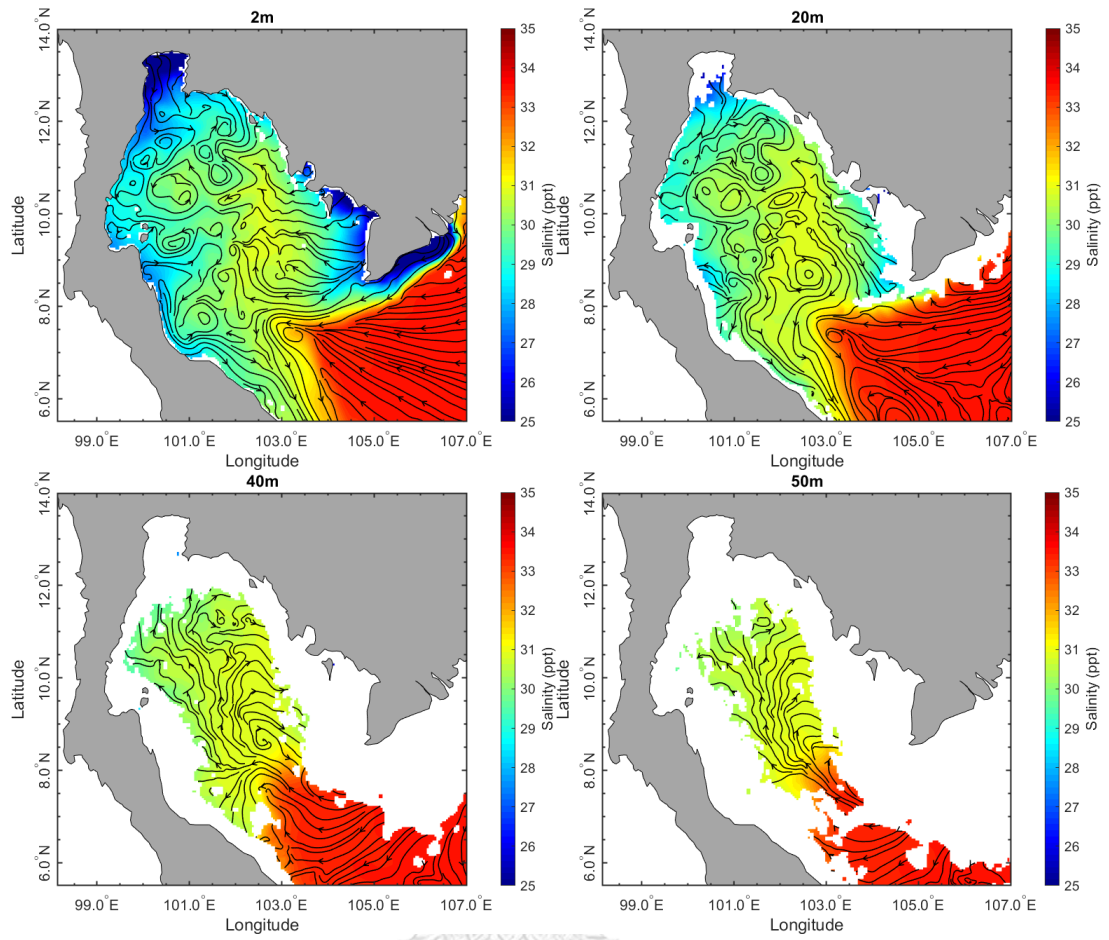


Fig. 4.27. The distribution of monthly averaged water salinity at depth 2, 14, 40 and 50 m in the GoT of 1<sup>st</sup> Inter-monsoon.

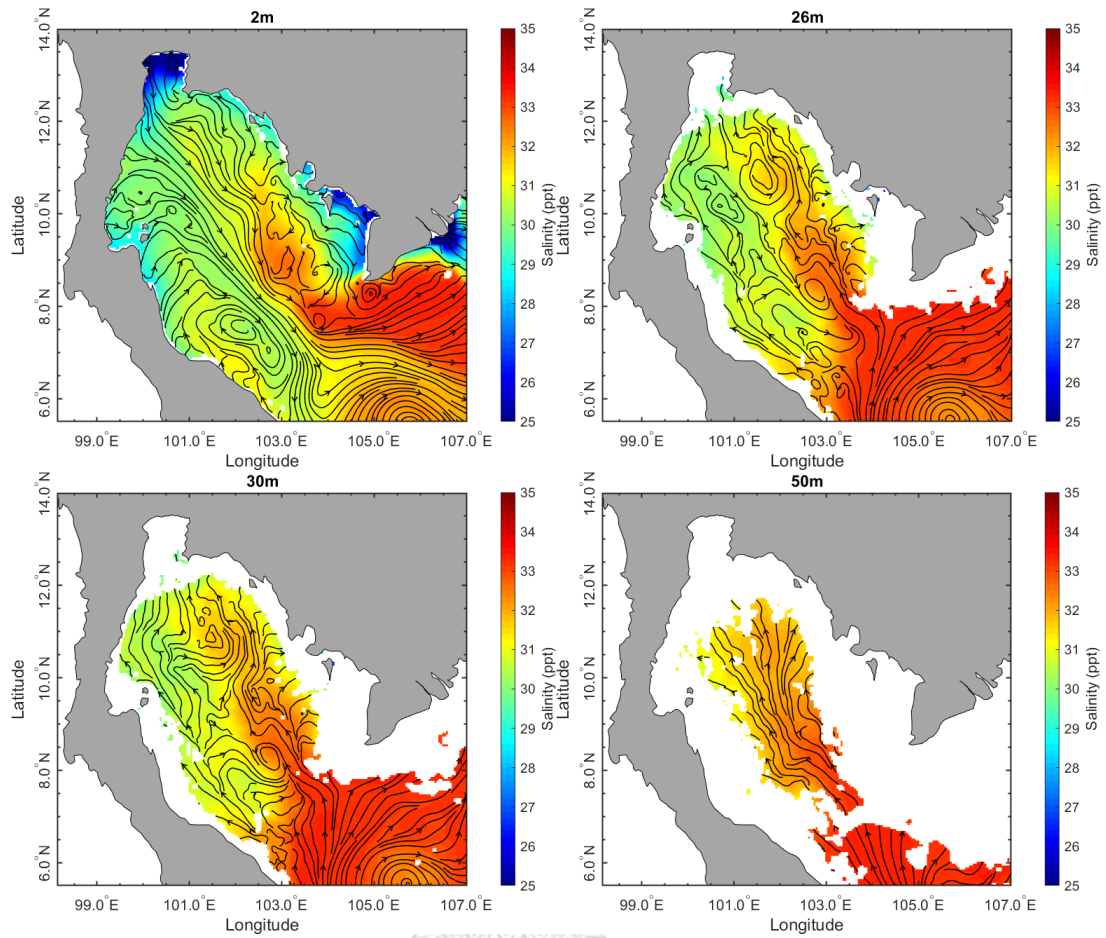


Fig. 4.28. The distribution of monthly averaged water salinity at depth 2, 14, 30 and 50 m in the GoT of Southwest monsoon.

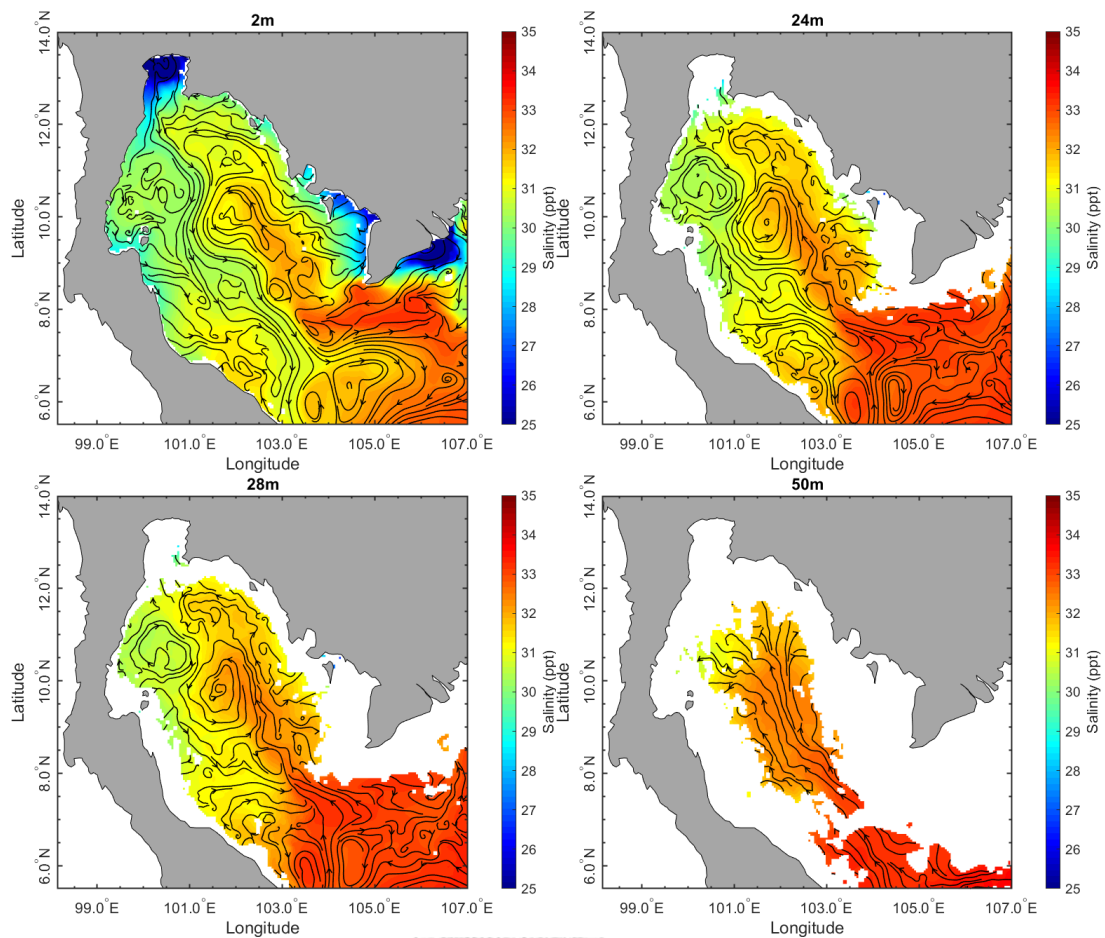


Fig. 4.29. The distribution of monthly averaged water salinity at depth 2, 14, 30 and 50 m in the GoT of 2<sup>nd</sup> Inter-monsoon.

#### 4.8. Seasonal distribution of vertical velocity in the GoT

To investigate the coastal upwelling the vertical velocity also was considered as shown in Fig. 4.30-4.33. The blue color represents a positive vertical velocity on the way up, while the red color represents a negative vertical velocity on the way down. The velocity magnitude directly variants to the color density. Generally, the distribution of vertical velocity did not show the variation in different layers. During northeast monsoon in January shown in Fig. 4.30 and Appendix B13 the vertical velocity in positive and negative direction was occurring widely the whole gulf. As mentioned in Fig. 4.21 the cooler water occurred along the west coast of the gulf in January, there was also the vertical velocity in positive direction at the same location. In March during 1<sup>st</sup> inter-monsoon in Fig. 4.31 and Appendix B14 the water with vertical velocity in positive direction also dispersed the whole gulf, especially the right and left side of the gulf



central, where the warmer water from the gulf flowing southward to mix with the cooler water from SCS. During southwest monsoon in August the cooler water occurred along the west coast of the central gulf and at the entrance's gulf where the patch of vertical velocity in positive direction also happened in Fig. 4.32 and Appendix B15. In October during 2<sup>nd</sup> inter-monsoon the distribution also dispersed the whole gulf like during other monsoons. As mentioned in Fig. 4.33 and Appendix B16 the cooler water occurred at the gulf's entrance at the depth 28 m, but the positive vertical velocity did not obviously happen at the same location.

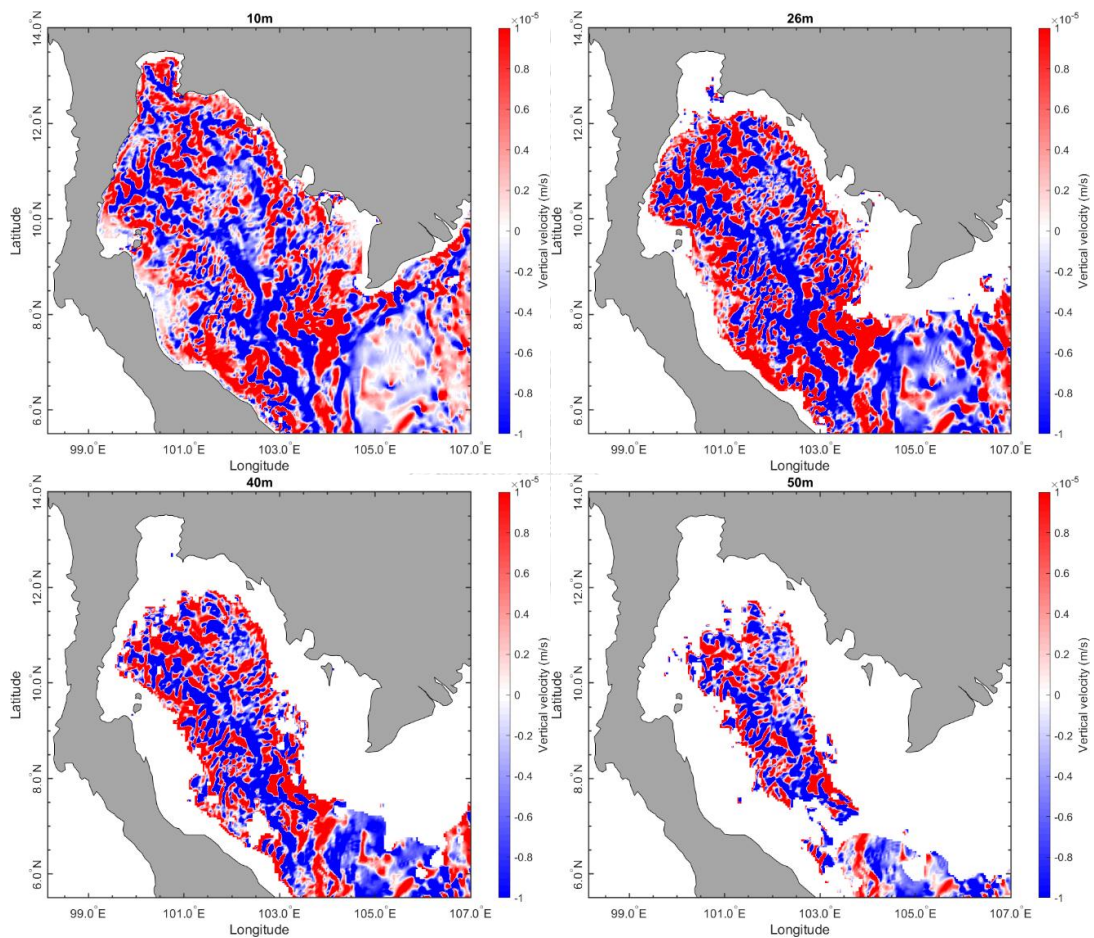


*Fig. 4.30. The distribution of monthly averaged vertical velocity at depth 2, 26, 40 and 50 m in the GoT of Northeast monsoon.*

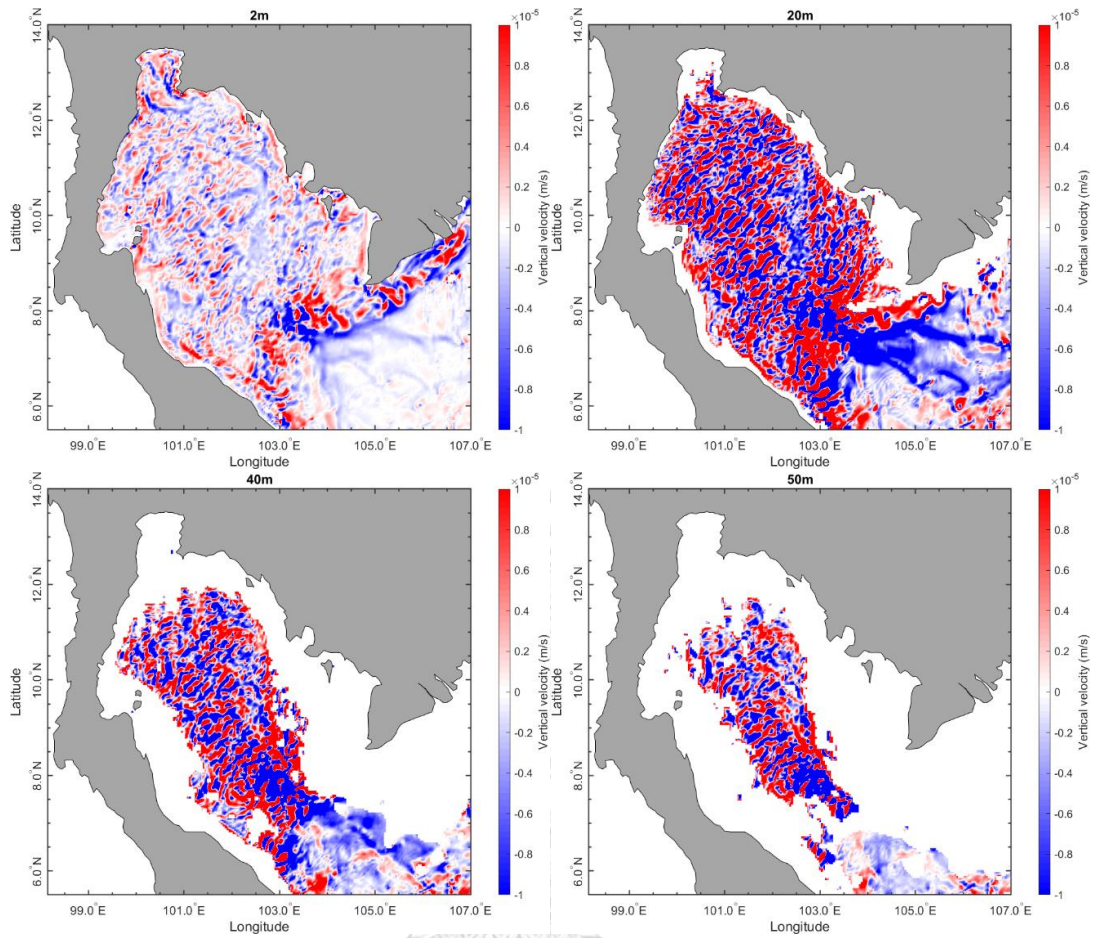
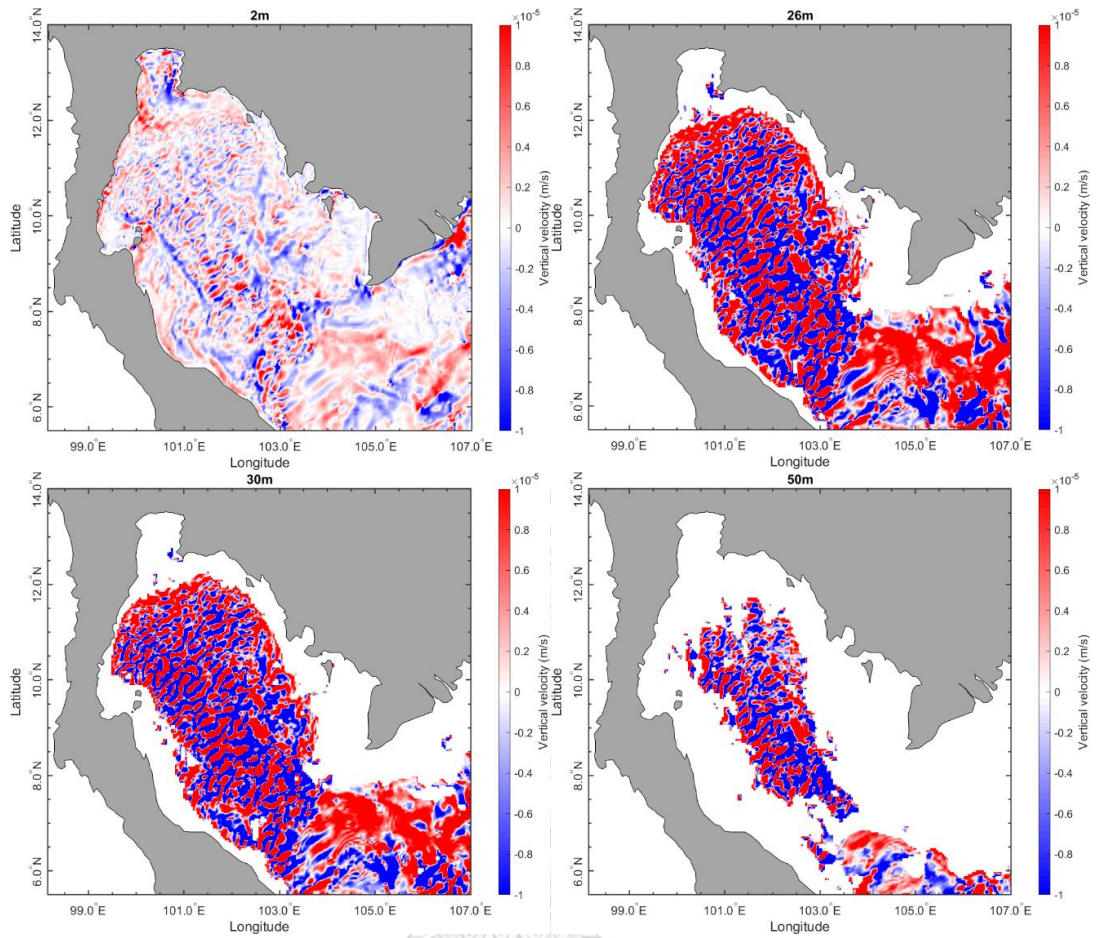


Fig. 4.31. The distribution of monthly averaged vertical velocity at depth of 2, 20, 40 and 50 m in the GoT of 1<sup>st</sup> Inter-monsoon.



*Fig. 4.32. The distribution of monthly averaged vertical velocity at depth 2, 26, 30 and 50 m in the GoT of Southwest monsoon.*



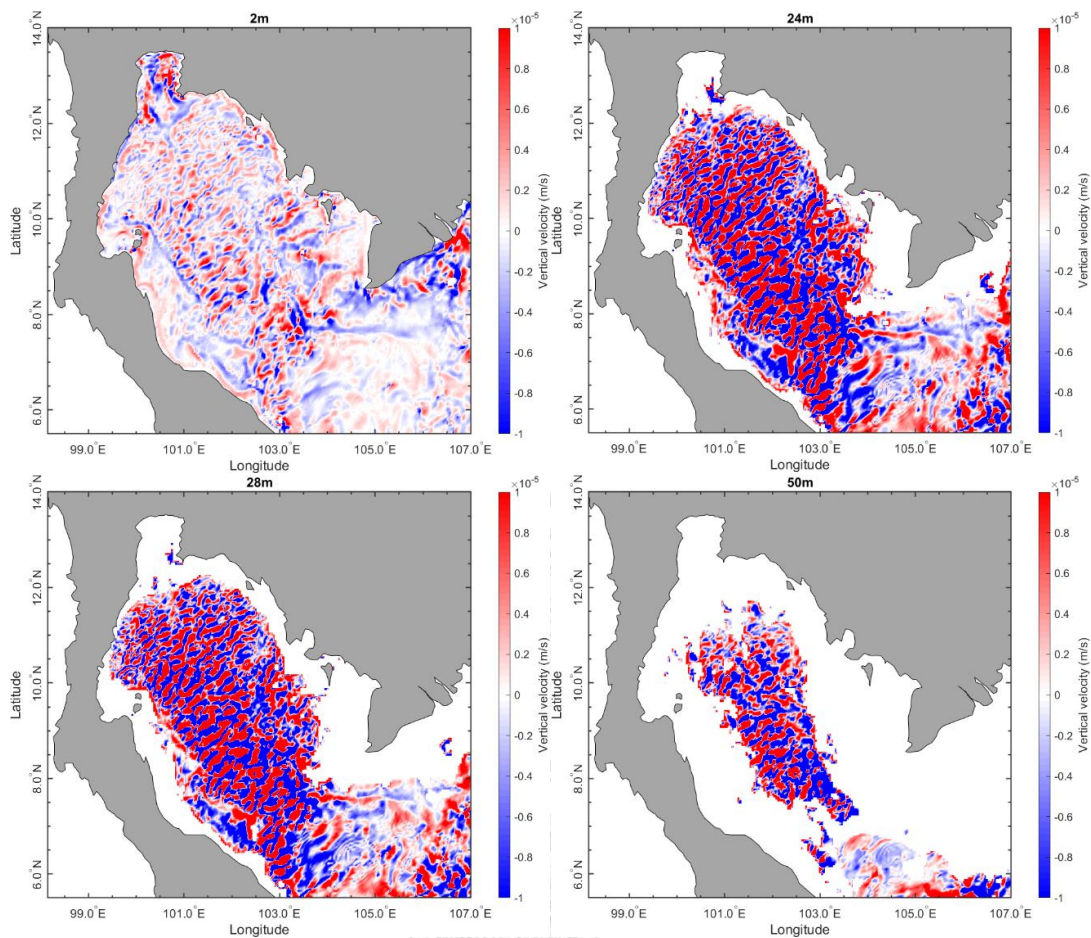


Fig. 4.33. The distribution of monthly averaged vertical velocity at depth 2, 24, 28 and 50 m in the GoT of 2<sup>nd</sup> Inter-monsoon.

#### 4.9. Simulation-oriented the coastal upwelling in the GoT

The coastal upwelling is the movement toward the surface water of the deeper water with cooler temperature and saltier (Kuo et al., 2000a). The distributions of monthly averaged water temperature could indicate the coastal upwelling. While, the salinity distributions did not show the possibility of upwelling in GoT. Neither the saltier water along the coastal nor near the surface water was found. Besides, the distribution of vertical velocity with a positive direction did not completely show the upwelling since the vertical velocity also happened at other locations without the cooler water. As regards to the distributions of water temperature, along the west coast of the GoT the coastal upwelling occurred obviously in January during northeast monsoon and in August during southwest monsoon, slightly in March during 1<sup>st</sup> inter-monsoon and in October during 2<sup>nd</sup> inter-monsoon. Along the east coast, the coastal upwelling was spotted

near Ca Mau Cape in January, March and August. Additionally, the GoT is a potential resources of the short-mackerel. The short-mackerel was spawning all year round with highest peaks during northeast monsoon and southwest monsoon with major spawning grounds of Prachuap Khiri Khan, Pattani, SuratThani, Samut Songkhram and the Mu Ko Chang National Park, Trat Province (Kongseng et al., 2020a). And, around Ca Mau Cape in Cambodia the spawning grounds were along Sihanouk coast with peaks during northeast monsoon and southwest monsoon, and along Kampot coast with the high peak during southwest monsoon (Tint et al., 2020). The locations of the short-mackerel spawning grounds found in the GoT and around Ca Mau Cape shown an agreement with the upwelling areas found in this study.

The distributions of temperature shown the possibility of upwelling in the GoT. In contrast the distributions of salinity did not. It might be effected by reasons as followings. Coastal upwelling regions mostly have the steep and deep coastal like the east coast of Malaysian Penninsular with the steep coast (Malaysia et al., 2014), and southeast coast of Vietnam, where the steep continental slope and the maximum depth 5000 m exists (Dippner et al., 2006). The GoT is the shallow basin with averaged depth 40 m and the maximum depth about 80 m, which might be not deep and steep enough for Ekman current to completely generate and pull upward the deep water to the surface depth. However, detailed model study (local domain for example east coast of Samui Island or other potential upwelling areas) may need to be consider for further study. Further, the heat and solar radiation which was aded into the model needed to be calibrated more in order to get more accurated results. In addition, the modeled surface temperature over some regions was lower/higher than the satellite observations. Since, this model rarely indicate the upwelling phenomena in the GoT, the following section, will demonstrate whether this TWH3D model can generate coastal upwelling in other well documented coastal upwelling area; e.g. Vietnam's coast.

#### 4.10. Seasurface temperature along southeastern Vietnam coast during southwest monsoon

The TWH3D model was subset to the domain covering the southeastern coast of Vietnam (see red box in Fig. 4.34), where the monsoon-induced upwelling had occurred during southwest monsoon (Chen et al., 2012; Xie, 2003). As presented in Fig. 4.35, the cooler water front of upwelling along

the southeastern Vietnam coast started to occur in June, and the signal got stronger in July. Then it reached the coolest of 27.0 degree Celsius in August and started to decay in September. The range of the cooler water was 27.0-28.5 degree Celsius, which was close to the satellite sea surface temperature presented in Xie (2003). The southward longshore currents from the north met the northeastward longshore current from the south off the southeastern Vietnam coast. In June and August, the combined cooler water front moved eastward, while moved northeastward and southeastward in July and September, respectively. The movement pattern of the longshore current in this study showed an agreement with a study result found in Chen et al. (2012). The cooler water was initially generated at the depth about 26-36 m during southwest monsoon (see Fig. 4.36). The upwelling also was clued by the vertical velocity distribution. The counter-clockwise circulation was found around the upwelling areas with the vertical velocity (red color) which was completely higher than surrounding (see Fig. 4.37). While the upwelling was not clued by the salinity distribution as is shown in Fig. 4.38. The water with higher salinity was not generated at the shallower water around where the upwelling area. This may be the evaporation added in the model was not enough.

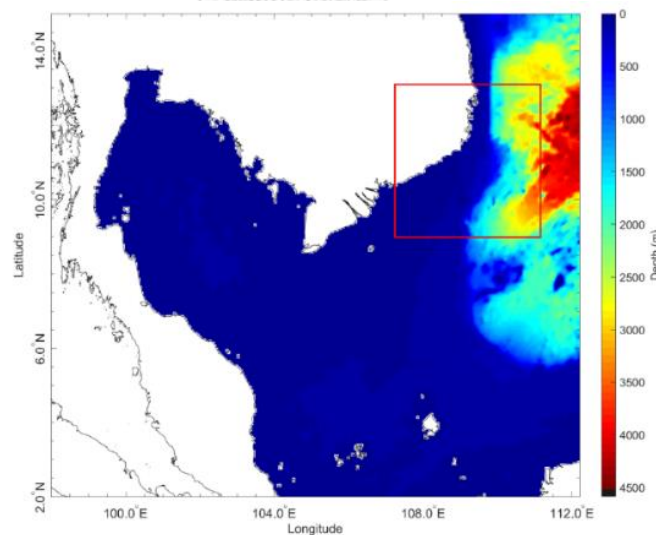


*Fig. 4.34. Upwelling area along southeastern coast of Vietnam.*

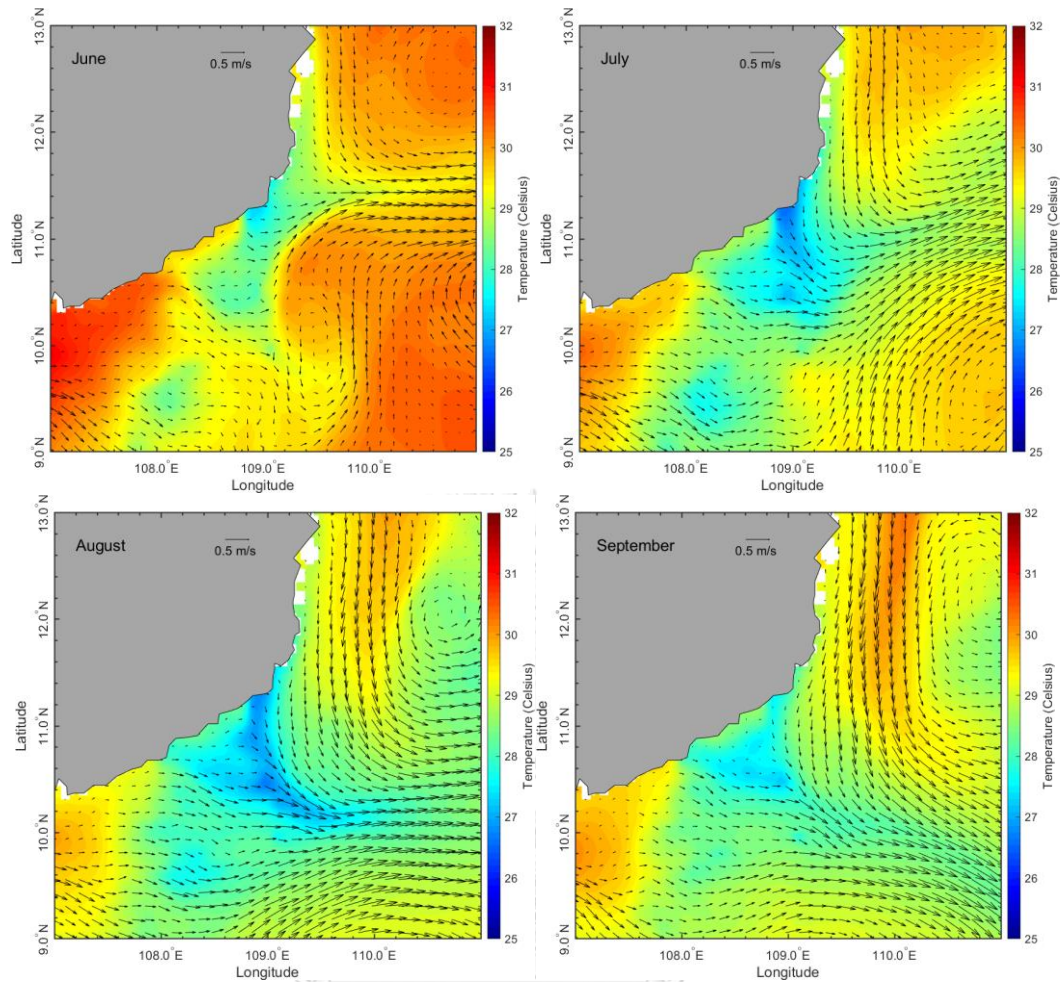


*Fig. 4.35. Averaged monthly sea surface temperature in degree Celsius in June (upper left), July (upper right), August (lower left) and September (lower right) along southeastern coast of Vietnam shown as the red box in Fig. 4.34.*



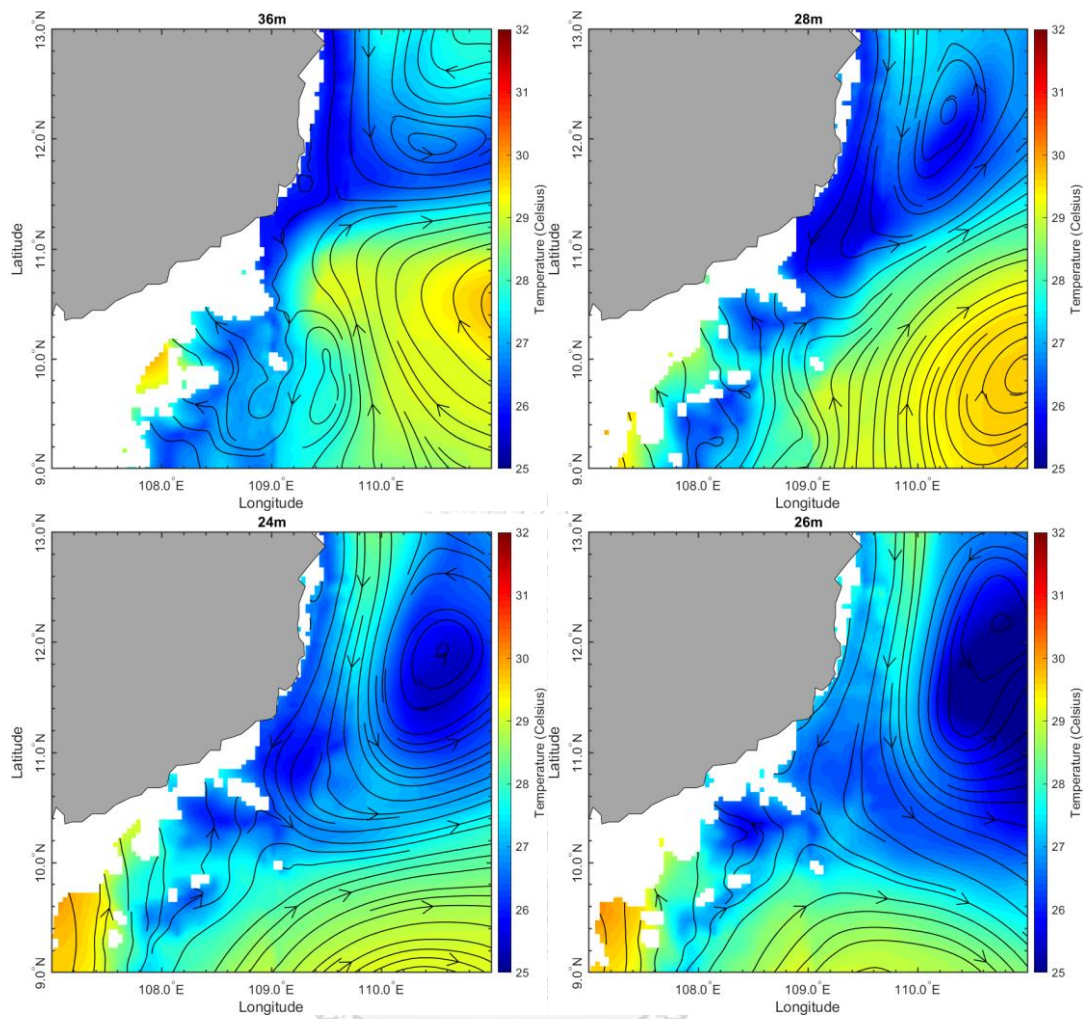


*Fig. 4.36. Sea surface temperature in degree Celsius along southeastern coast of Vietnam in June (upper left) at depth 36 m, July (upper right) at depth 28 m, August (lower left) at depth 24 m and September (lower right) at depth 26 m.*

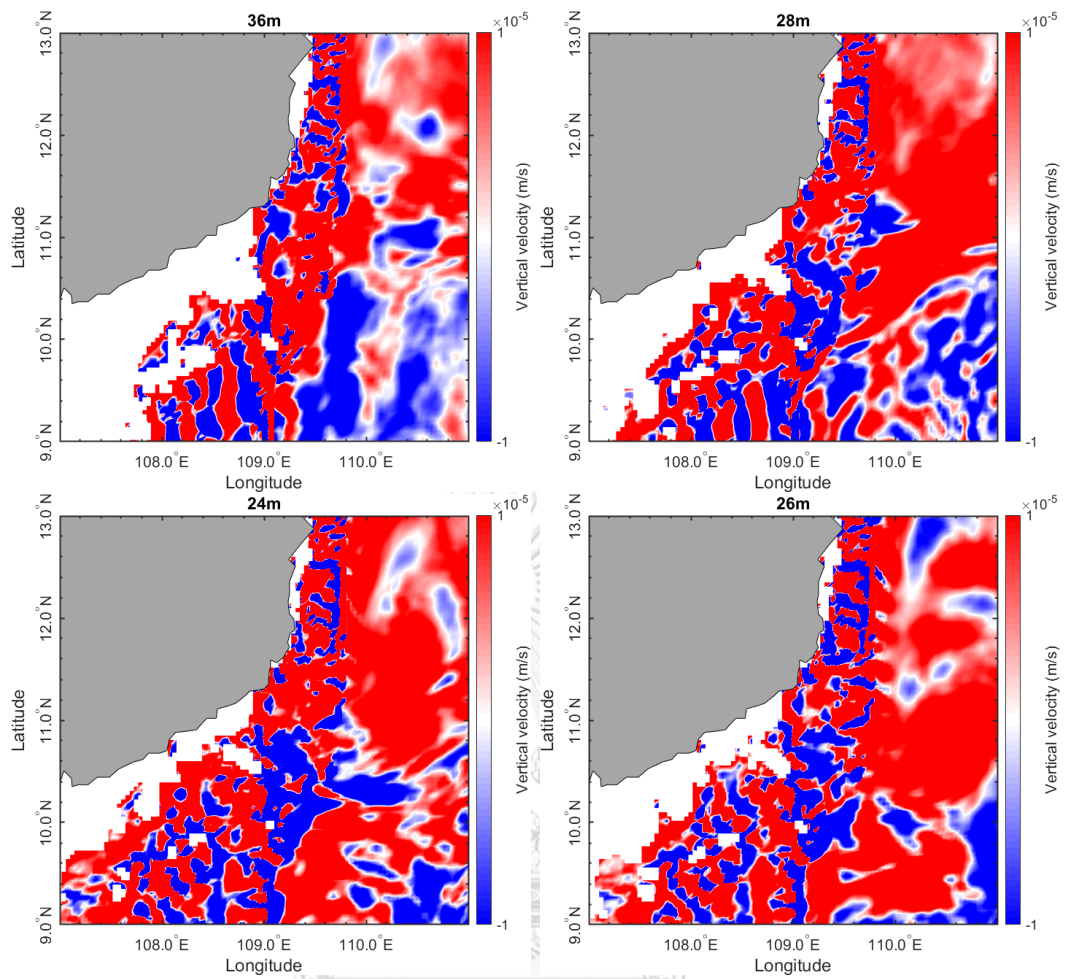


*Fig. 4.37. Vertical velocity distribution (m/s) along southeastern coast of Vietnam in June (upper left) at depth 36 m, July (upper right) at depth 28 m, August (lower left) at depth 24 m and September (lower right) at depth 26 m.*

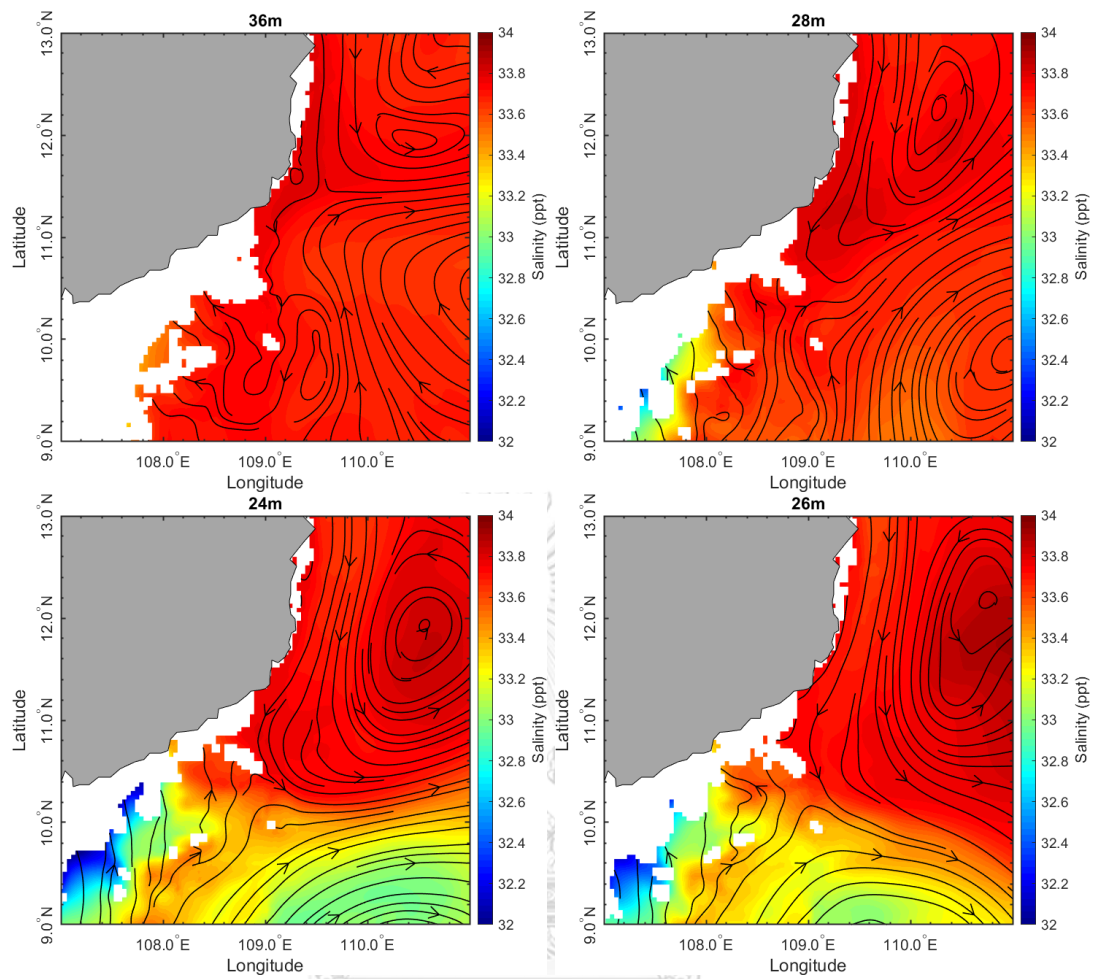


*Fig. 4.38. Water salinity distribution (ppt) along southeastern coast of Vietnam in June (upper left) at depth 36 m, July (upper right) at depth 28 m, August (lower left) at depth 24 m and September (lower right) at depth 26 m.*

## CHAPTER 5

### Conclusion and Suggestions

#### 5.1. Conclusion

The characteristics of coastal upwelling in the Gulf of Thailand was investigated using two methods 1) Ekman transport upwelling index ( $UI_{ET}$ ) and sea surface temperature upwelling index ( $UI_{SST}$ ) and 2) Numerical model under influences of tide, wind, temperature, salinity and river discharge.

The Ekman transport upwelling index expressed the favorable upwelling conditions along the west coast of GoT generally during northeast monsoon and 1<sup>st</sup> inter-monsoon. The favorable upwelling along the east coast of GoT was expressed generally during southwest monsoon and 2<sup>nd</sup> inter-monsoon.

The sea surface temperature upwelling index shown the favorable upwelling conditions along the west coast of the central gulf and the east coast near Ca Mau Cape during northeast monsoon and southwest monsoon.

The model results indicated the possibility of coastal upwelling in GoT with obvious temperature gradient between coastal water and oceanic water during northeast monsoon and southwest monsoon, and with slight gradient during 1<sup>st</sup> inter-monsoon and 2<sup>nd</sup> inter-monsoon. The model results didn't indicate the coastal water with higher salinity which is a characteristic of upwelling. Besides, the coastal upwelling along southeast coast of Vietnam was represented with the cooler coastal water during southwest monsoon in June to September.

The coastal upwelling clued by the  $UI_{ET}$  was different from by the  $UI_{SST}$  and the model simulation. The  $UI_{ET}$  directly indicated the wind-driven coastal upwelling. It was related to Ekman transport direction which was in the right of wind direction in northern hemisphere. And, the locations with offshore Ekman transport was mostly considered as the favorable upwelling conditions. Conversely, the coastal upwelling which  $UI_{SST}$  and the model simulation indicated, was made of the gradient of sea surface temperature between the coastal and the oceanic water. The  $UI_{SST}$  was directly associated with satellite-observed sea surface temperature. The sea surface temperature found in the model simulation was estimated



by factors like tide, wind, temperature, salinity, river discharge and heat. Thus, the marked positions of the coastal upwelling were shown in difference.

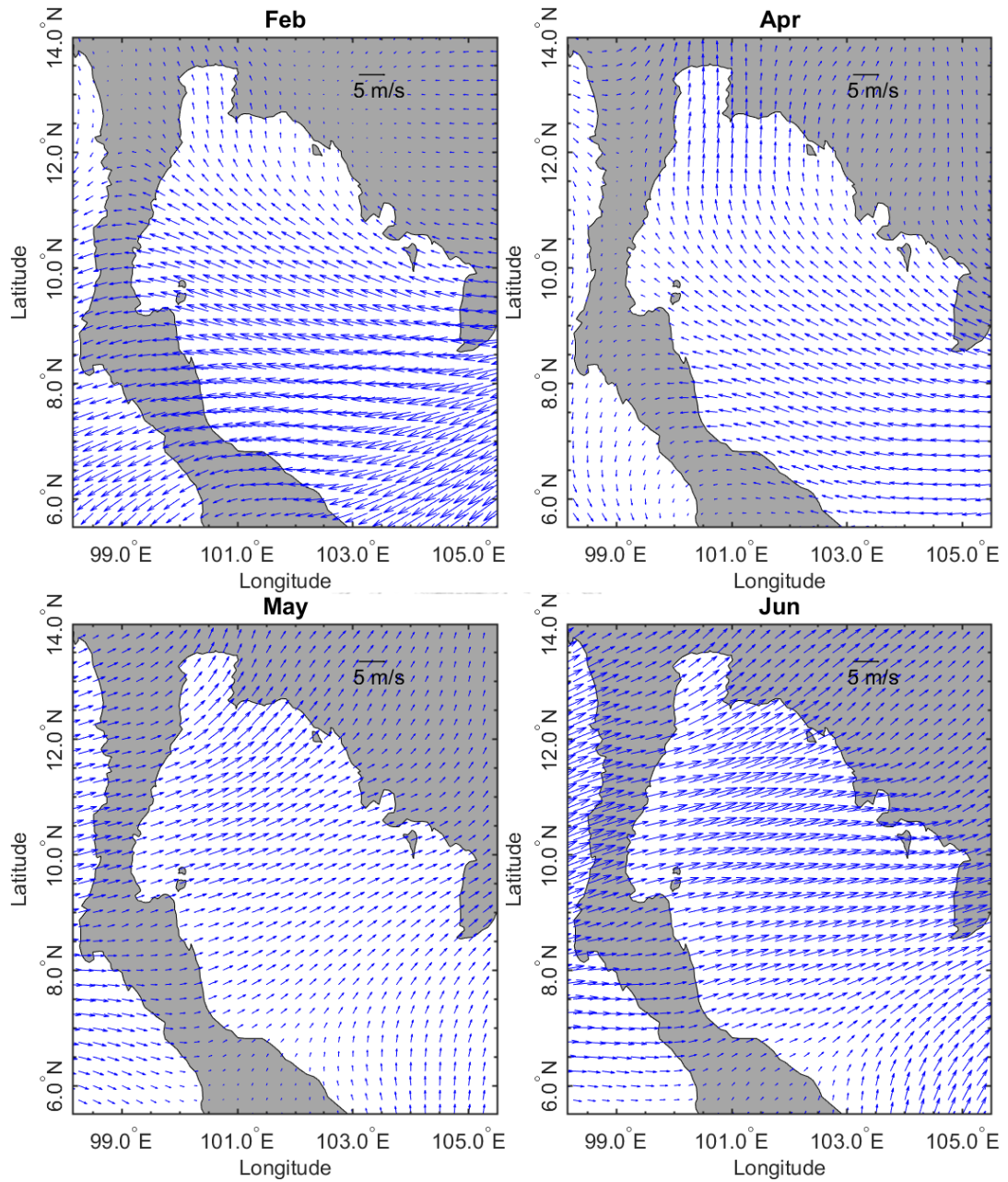
The upwelling plays role in nutrient transport and closely links to significant fisheries grounds. Thus, the clues of upwelling found in this study might address problems and fill the gap of knowledge of nutrient distributions, immediately increasing of plankton bloom and over-exploitation of fisheries resources.

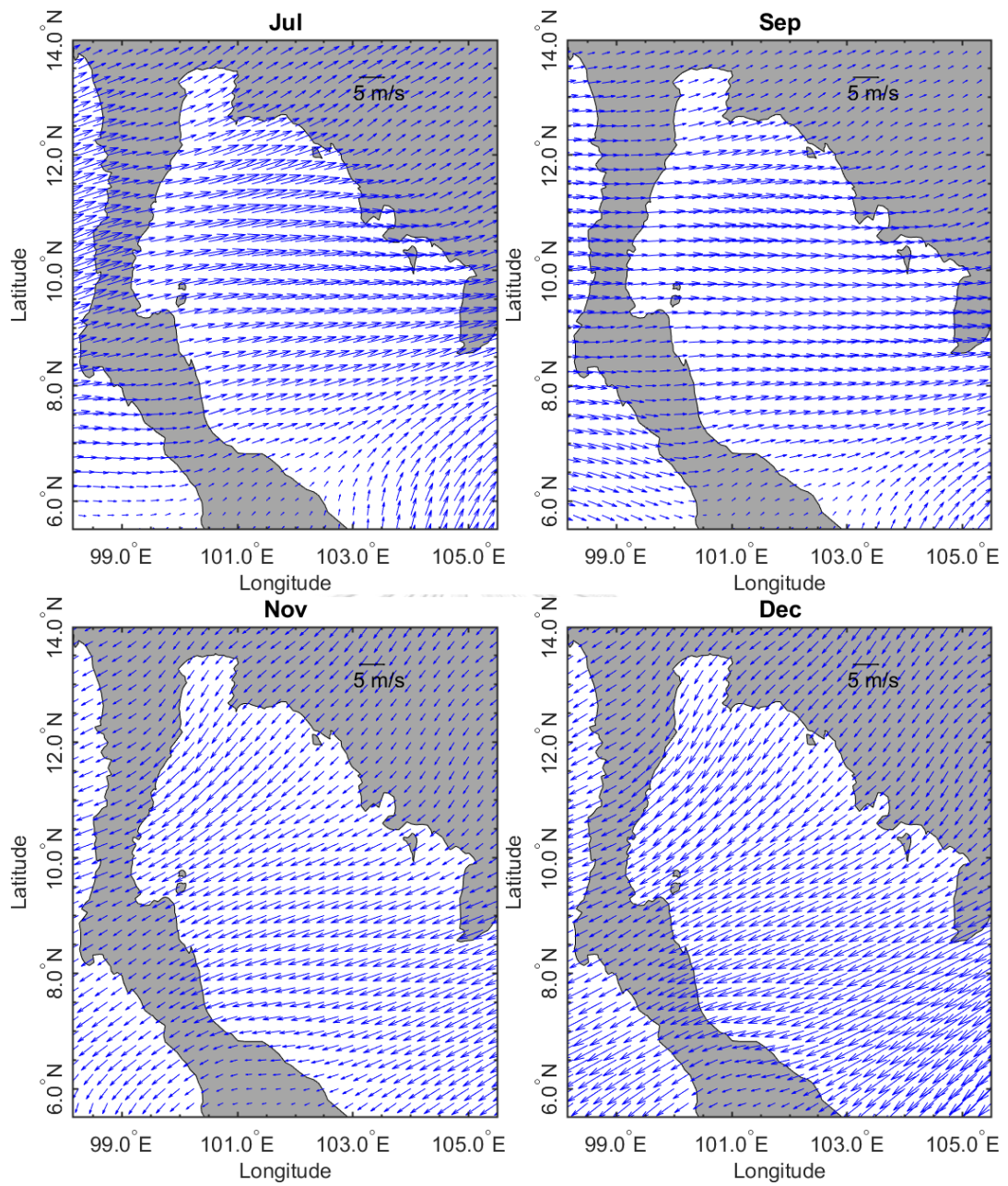
## 5.2. Suggestions

For the further research, the good harmonic components are vital for calibrating the model to get the accurate water levels in the GoT. The huge effort is needed for tuning the heat to generate the accurate water temperature. And, to gain deep knowledge in mechanisms of upwelling in the GoT, further three simulating cases of temperature, salinity and river discharge 1) without wind, 2) without tide, and 3) without wind and tide, should be conducted. In addition, increasing the number of layers (more than 10 layers) defined in the three-dimensional simulation would help for stability issue in the model.

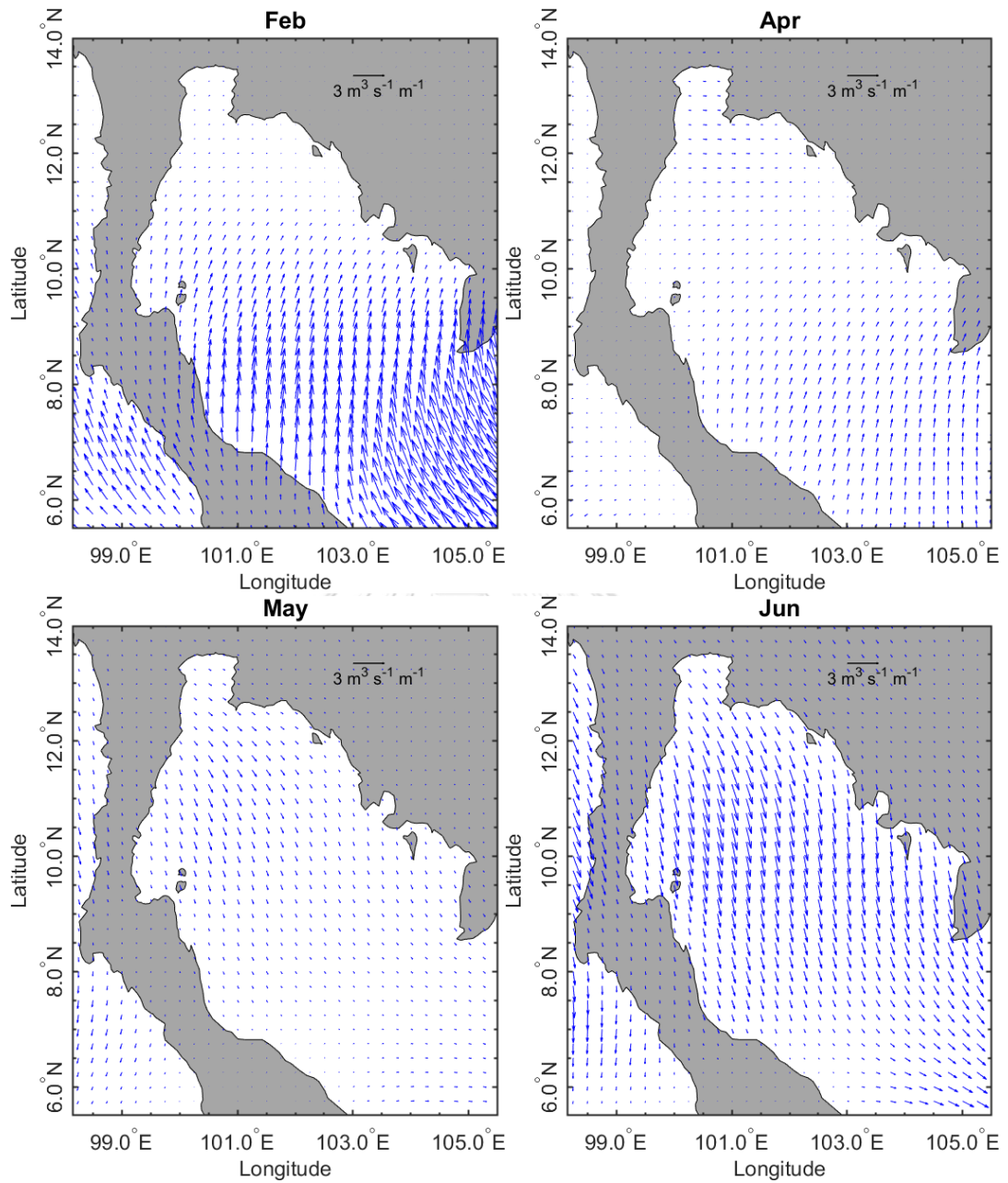
## APPENDIX A. Upwelling Index Estimations

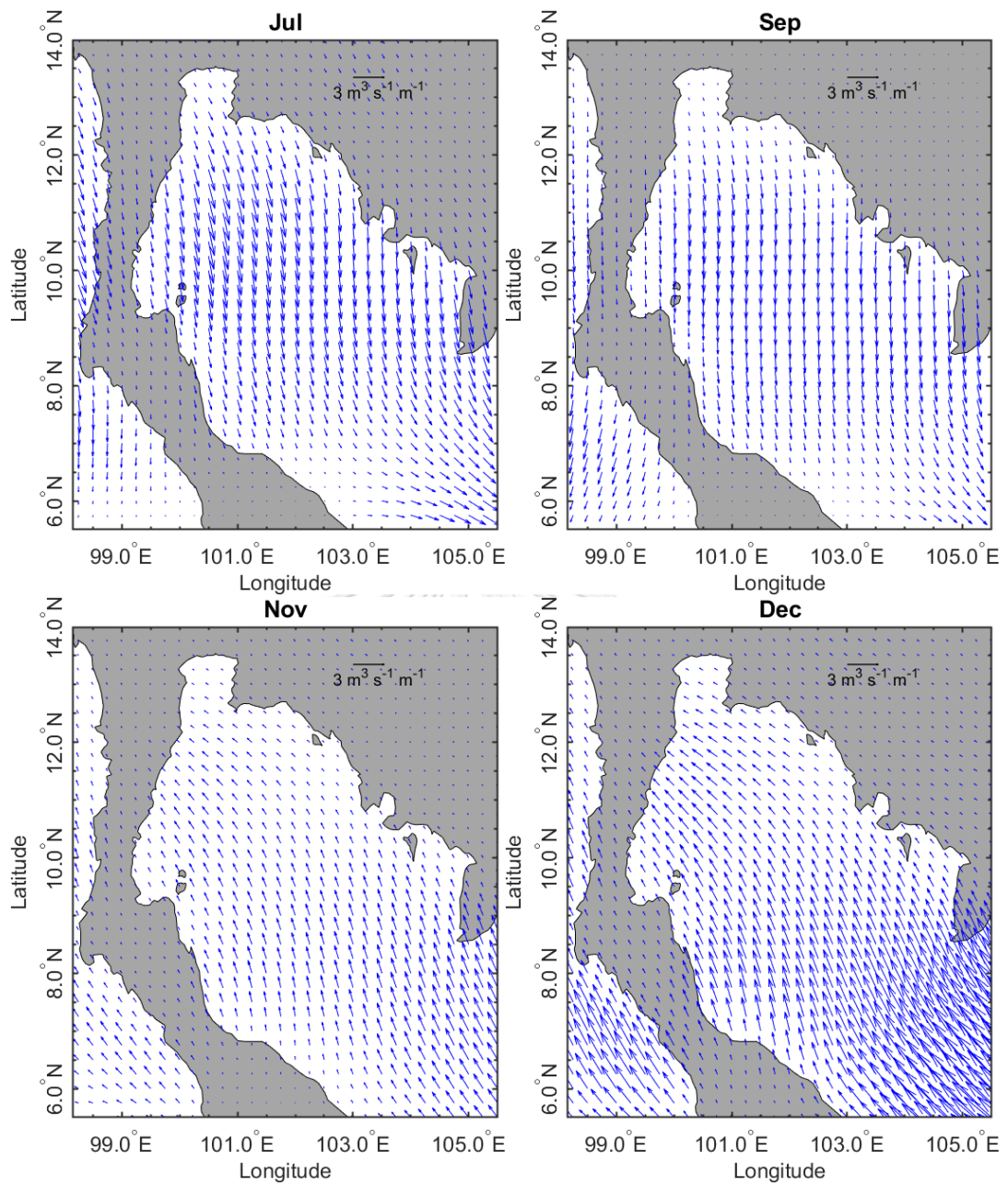
### A1. Monthly averaged surface wind vector (m/s) during 2003-2018





*Fig. A1. Surface wind vector (m/s) of February, April, May, June, July, September, November and December.*

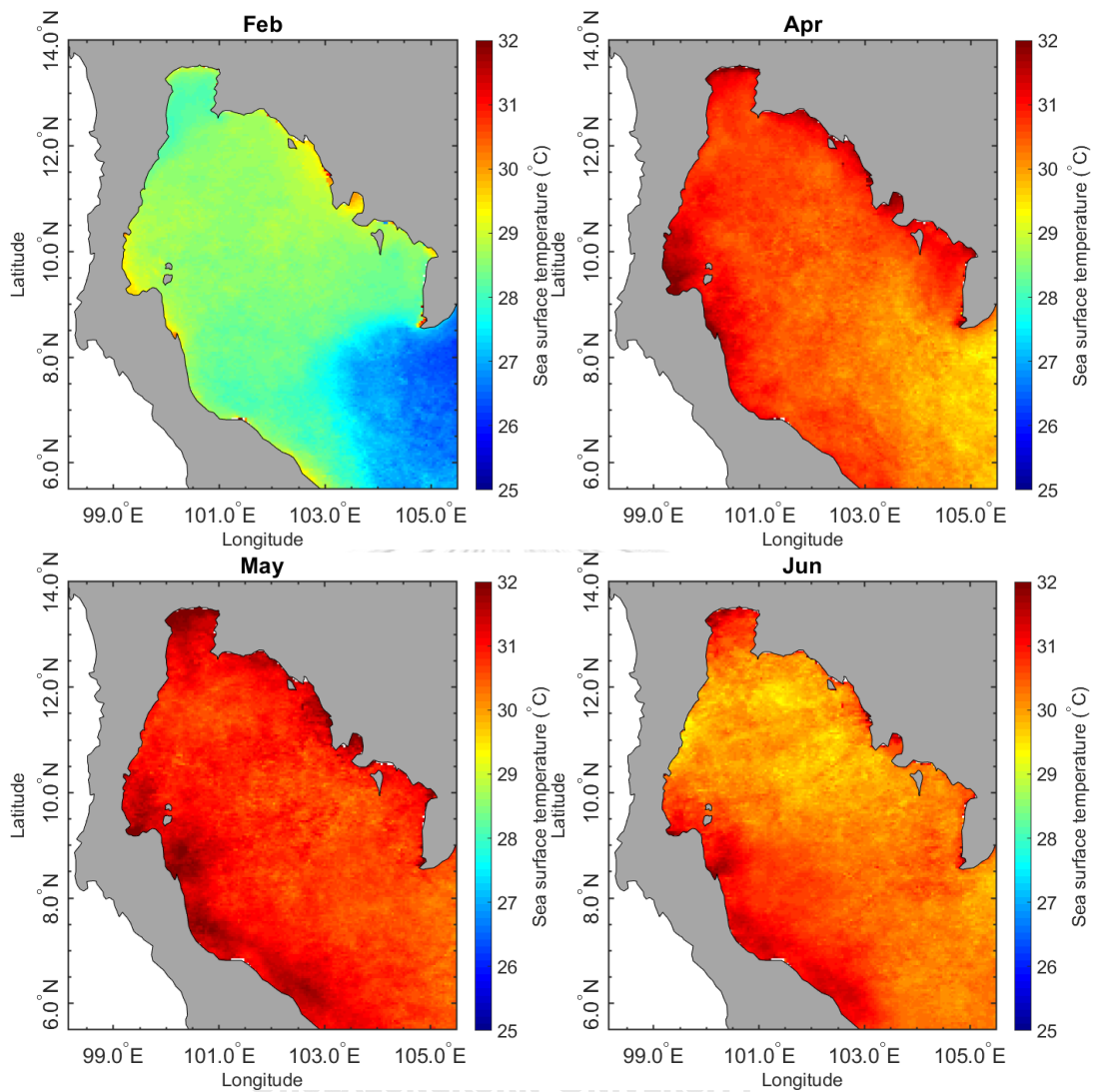
A2. Monthly averaged Ekman transport ( $\text{m}^3\text{s}^{-1}\text{m}^{-1}$ ) during 2003-2018



*Fig. A2. Ekman transport ( $\text{m}^3 \text{s}^{-1} \text{m}^{-1}$ ) of February, April, May, June, July, September, November and December.*



## A3. Monthly averaged sea surface temperature during 2003-2018



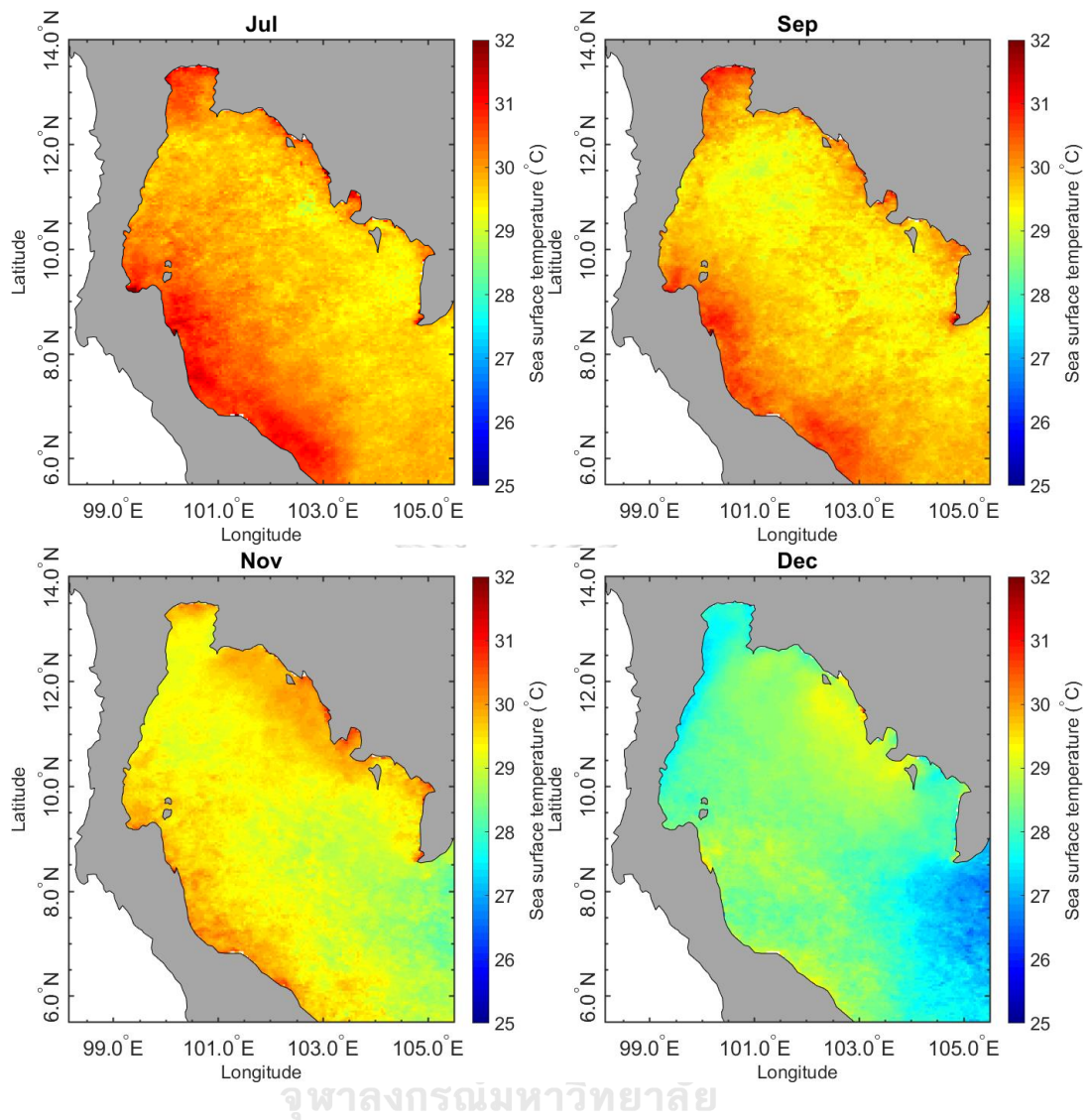


*Fig. A3. Sea surface temperature in degree Celsius during 2003-2018 of February, April, May, June, July, September, November and December.*

## APPENDIX B. Numerical Model

### B1. First simulation

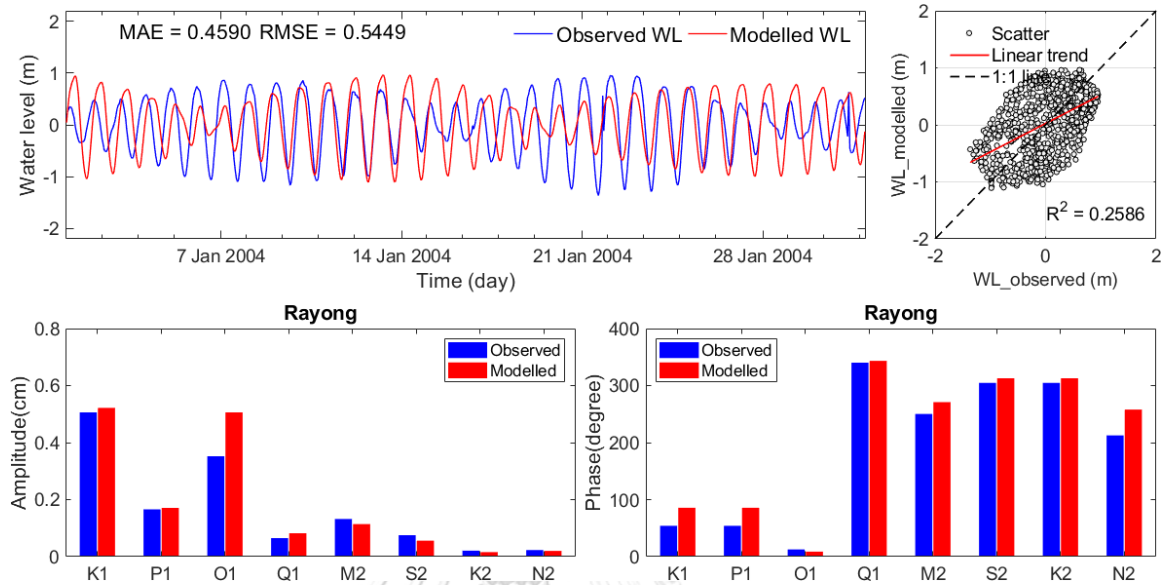


Fig. B1. Water level, phase and amplitude comparison between first simulation and observed data during January 1-31, 2004 at Rayong Station.

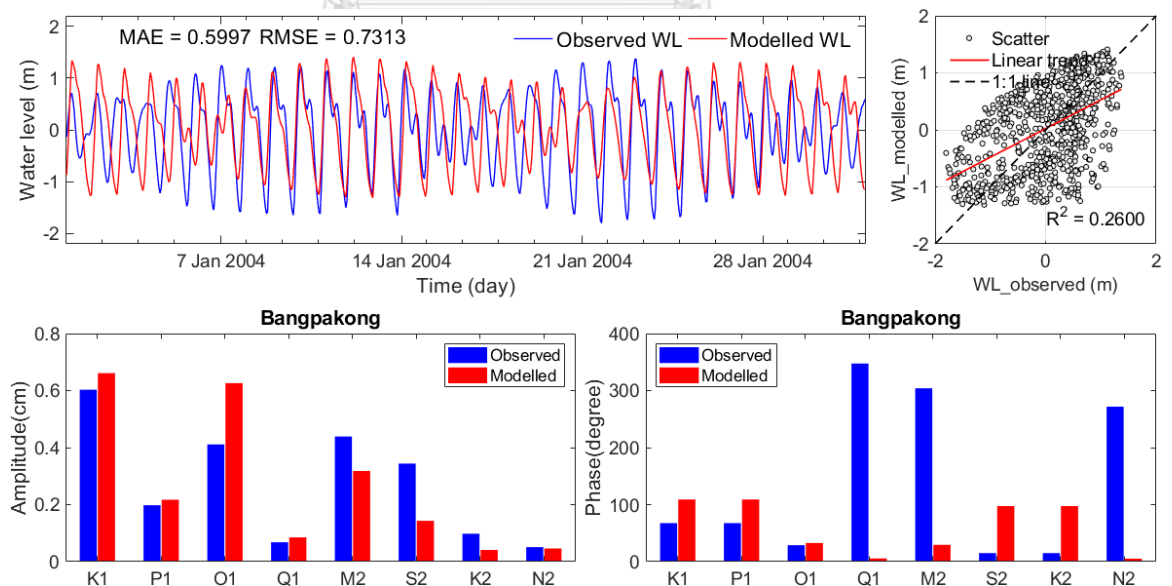


Fig. B2. Water level, phase and amplitude comparison between first simulation and observed data during January 1-31, 2004 at Bangpakong River Station.



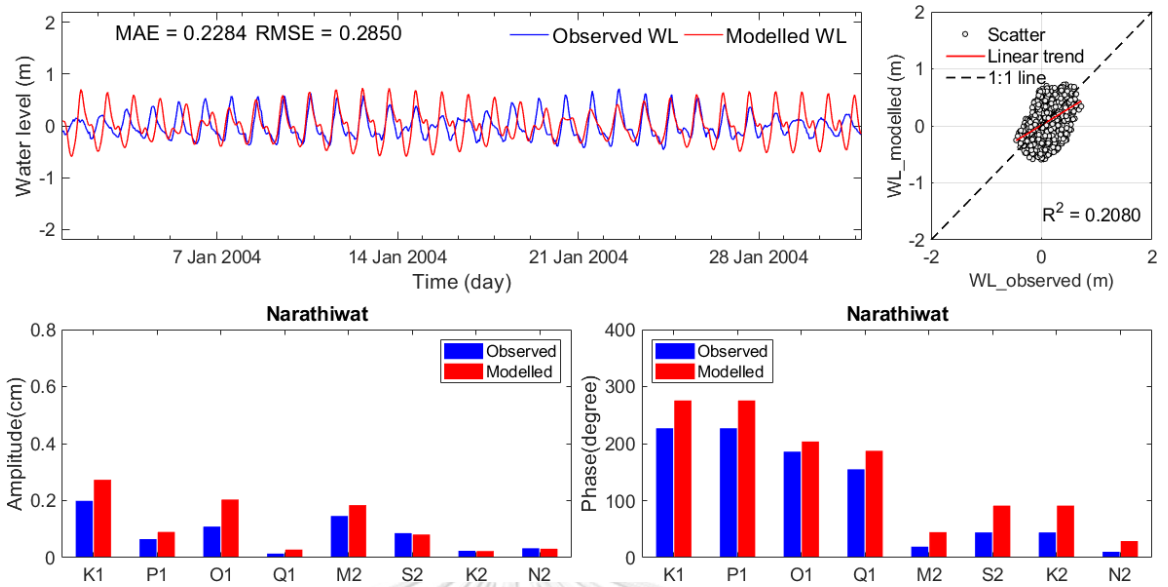


Fig. B3. Water level, phase and amplitude comparison between first simulation and observed data during January 1-31, 2004 at Narathiwat Station.

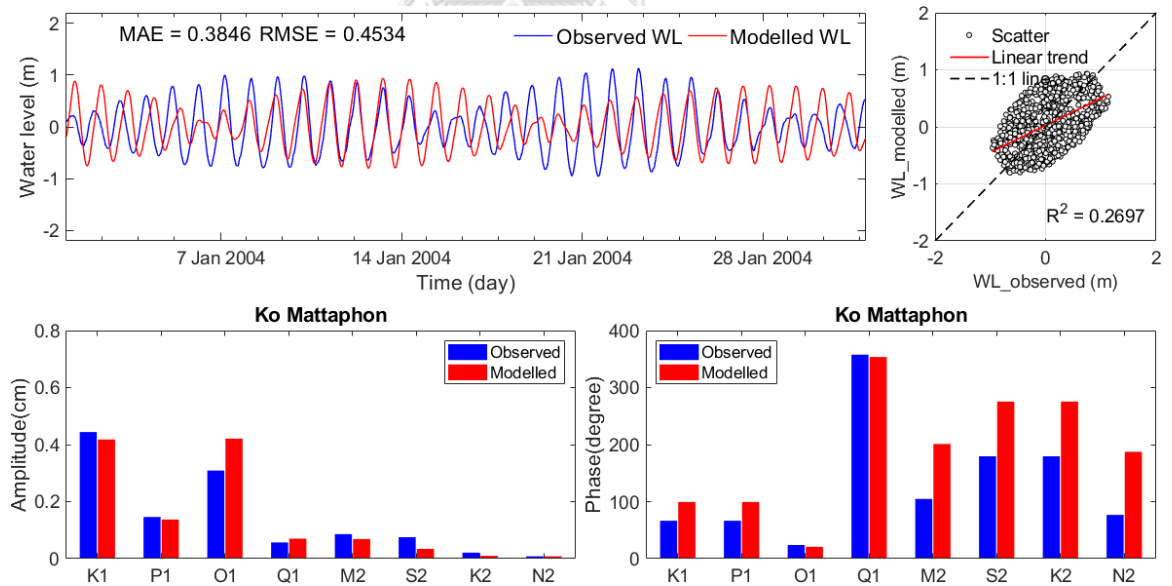


Fig. B4. Water level, phase and amplitude comparison between first simulation and observed data during January 1-31, 2004 at Ko Mattaphon Station.

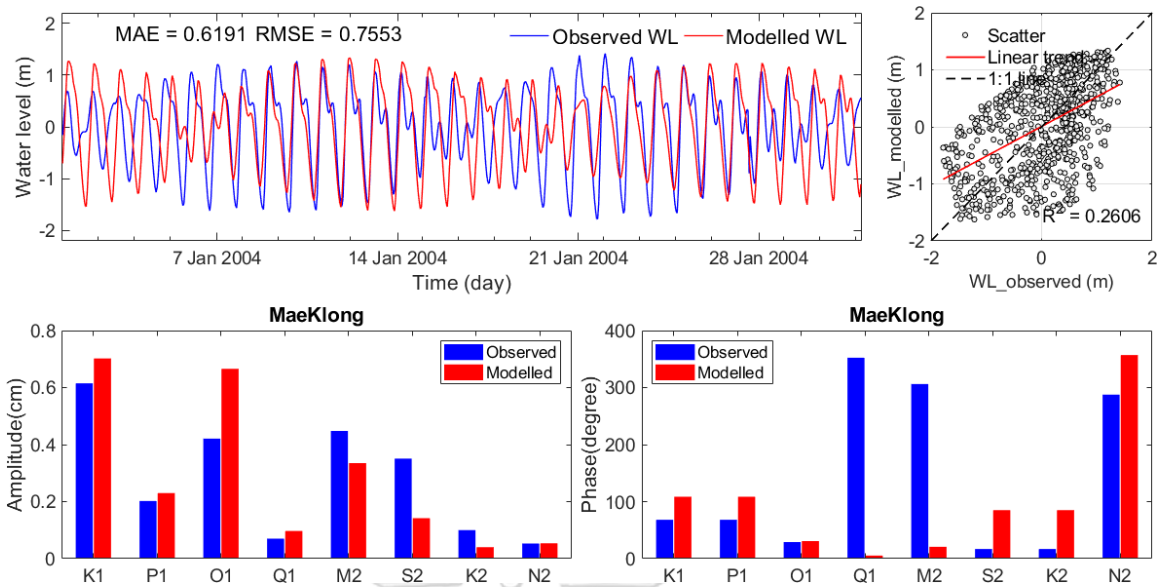


Fig. B5. Water level, phase and amplitude comparison between first simulation and observed data during January 1-31, 2004 at MaeKlong River Station.

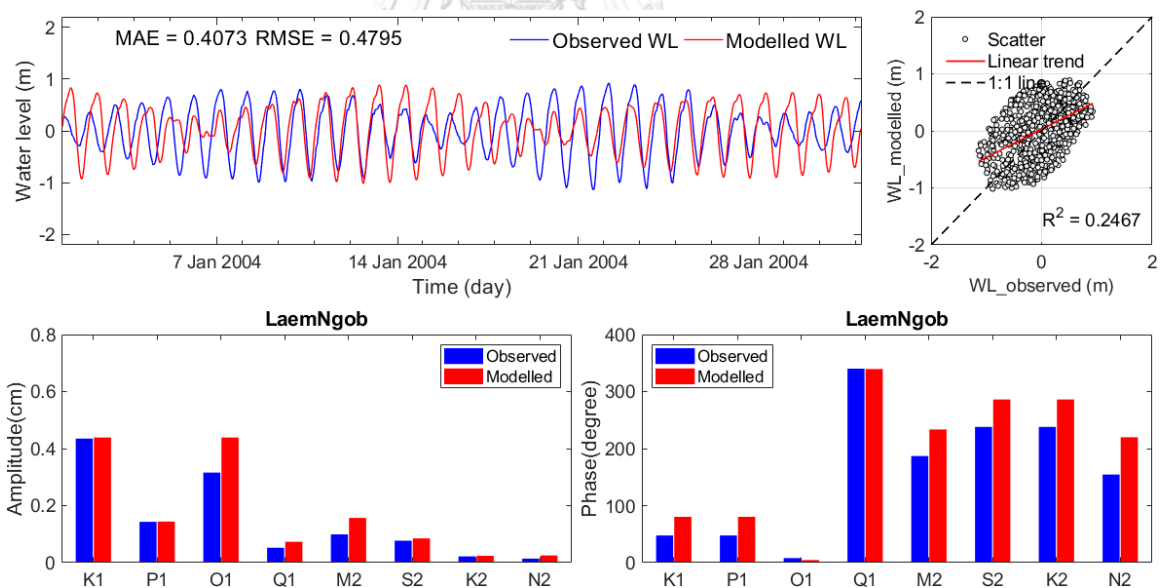


Fig. B6. Water level, phase and amplitude comparison between first simulation and observed data during January 1-31, 2004 at LaemNgob Station.

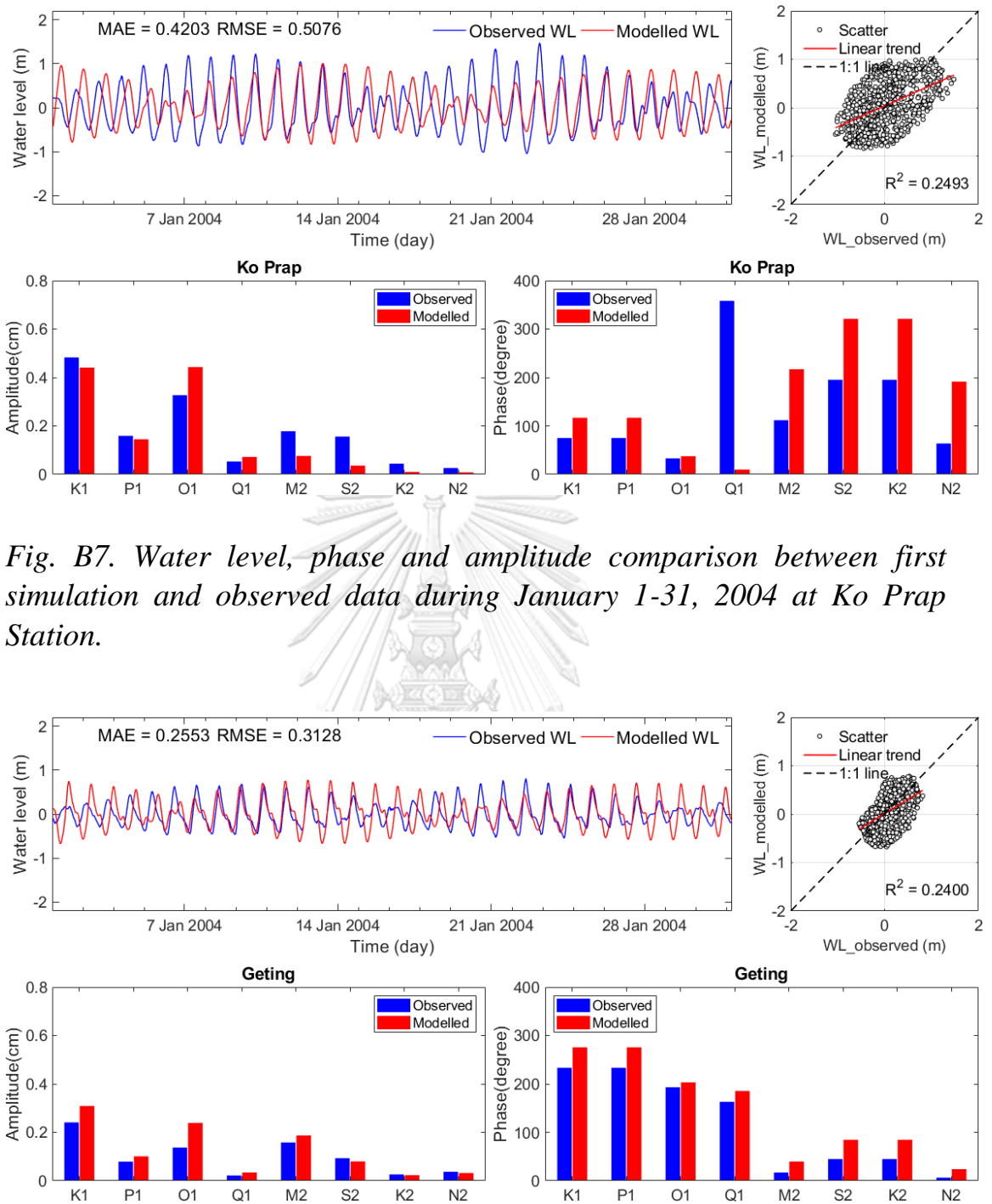


Fig. B7. Water level, phase and amplitude comparison between first simulation and observed data during January 1-31, 2004 at Ko Prap Station.

Fig. B8. Water level, phase and amplitude comparison between first simulation and observed data during January 1-31, 2004 at Geting Station.

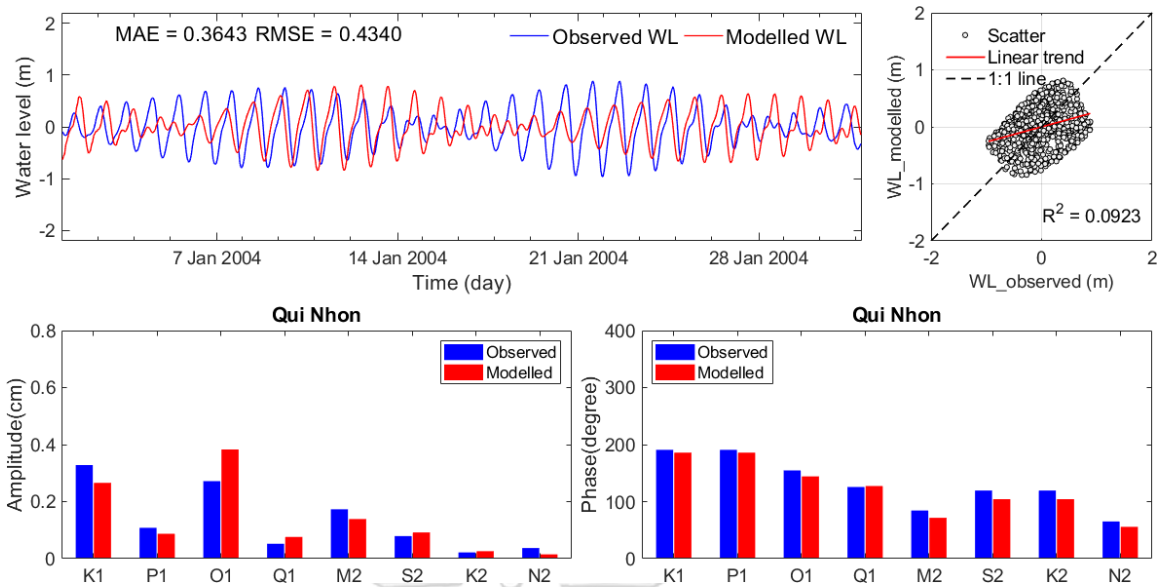


Fig. B9. Water level, phase and amplitude comparison between first simulation and observed data during January 1-31, 2004 at Qui Nhon Station.

## B2. Calibration

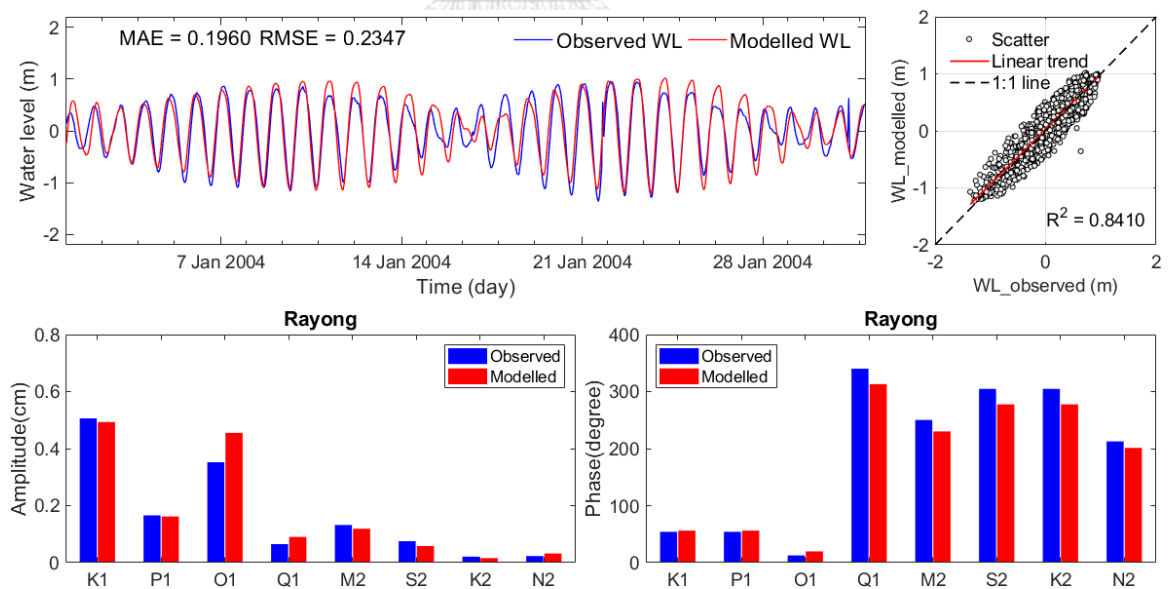


Fig. B10. Water level, phase and amplitude comparison between calibration and observed data during January 1-31, 2004 at Rayong Station.

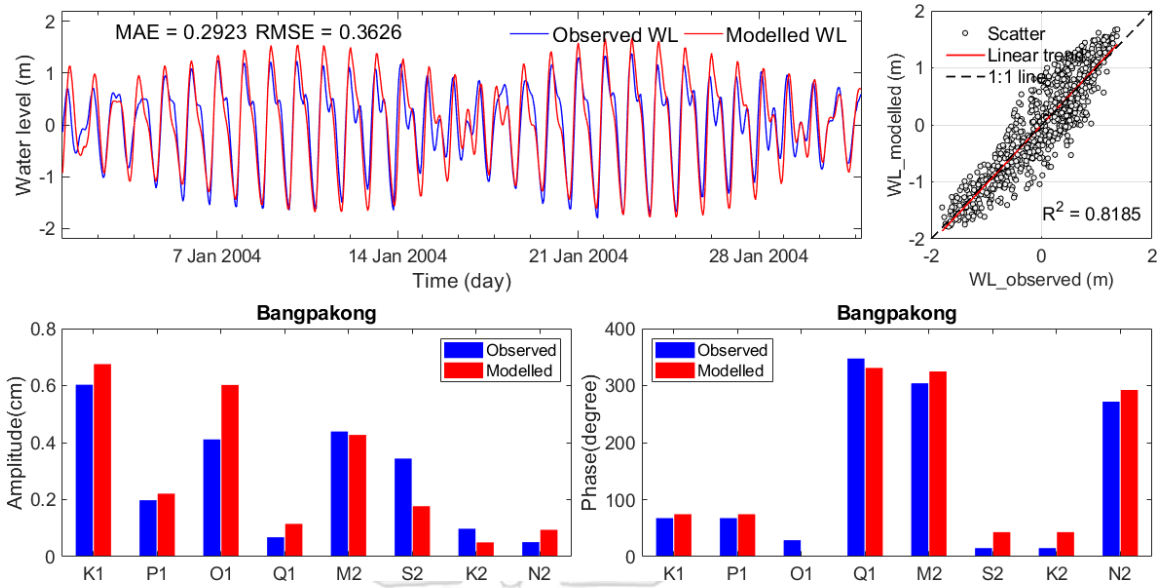


Fig. B11. Water level, phase and amplitude comparison between calibration and observed data during January 1-31, 2004 at Bangkokong Station.

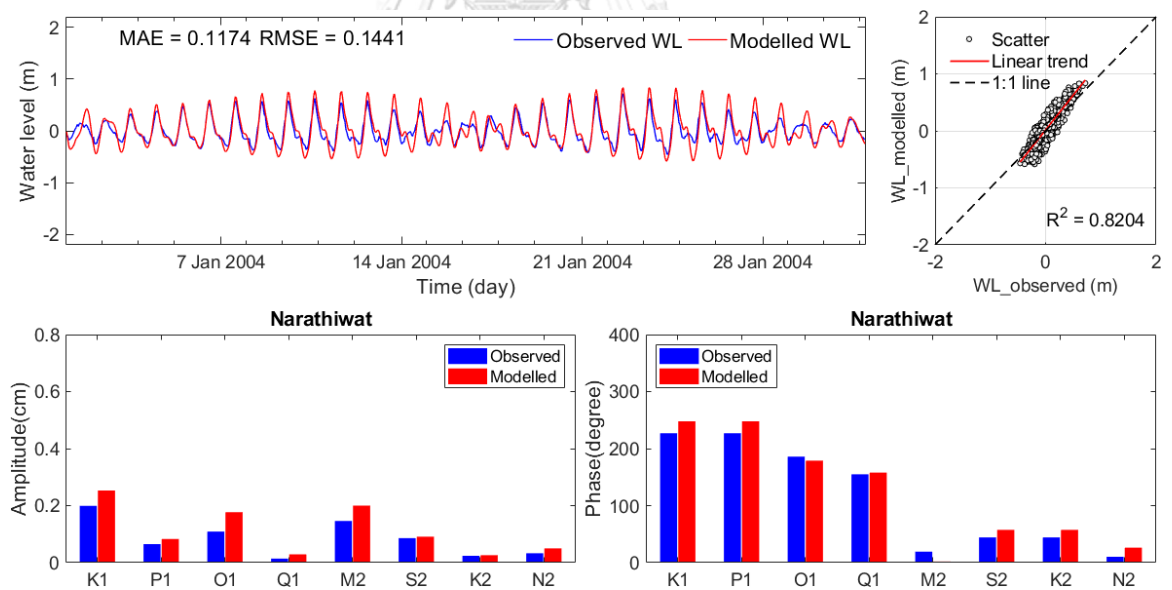


Fig. B12. Water level, phase and amplitude comparison between calibration and observed data during January 1-31, 2004 at Narathiwat Station.

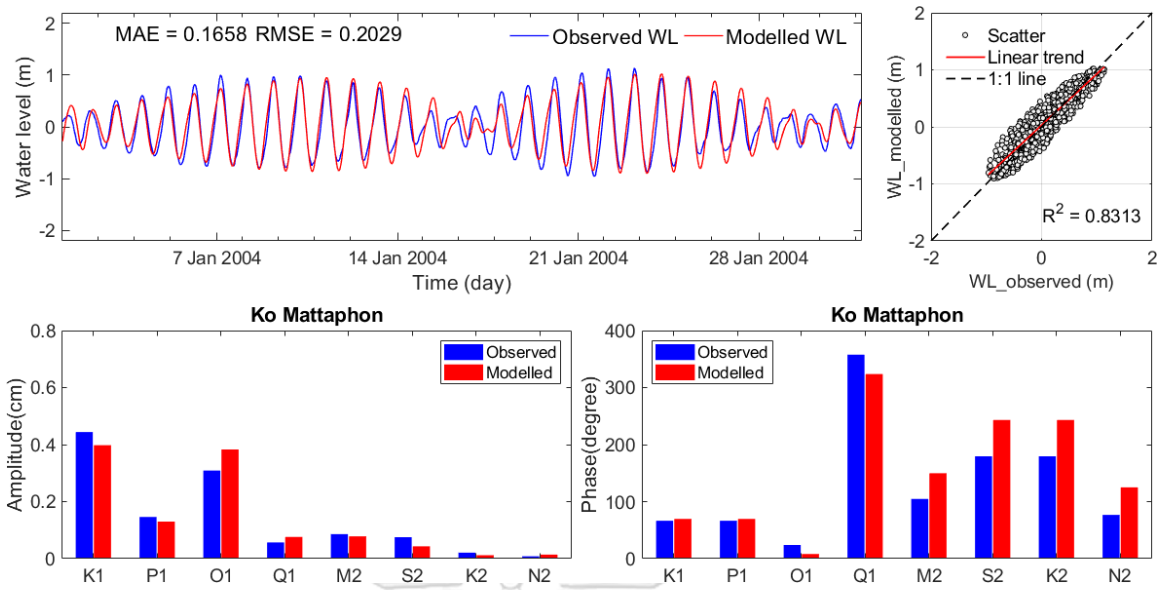


Fig. B13. Water level, phase and amplitude comparison between calibration and observed data during January 1-31, 2004 at Ko Mattaphon Station.

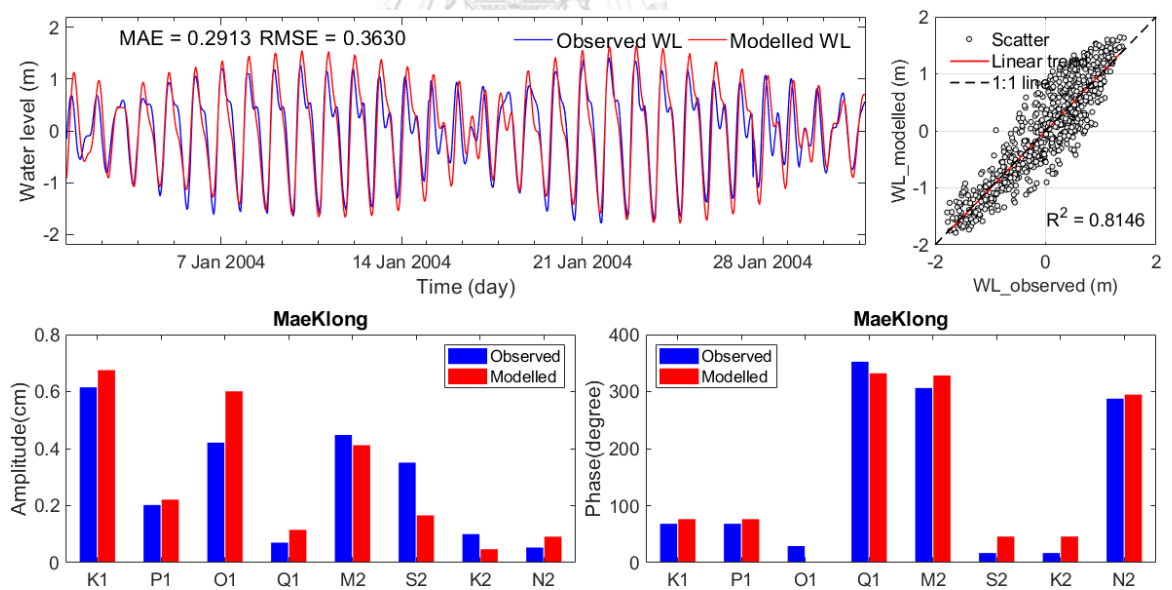


Fig. B14. Water level, phase and amplitude comparison between calibration and observed data during January 1-31, 2004 at MaeKlong Station.

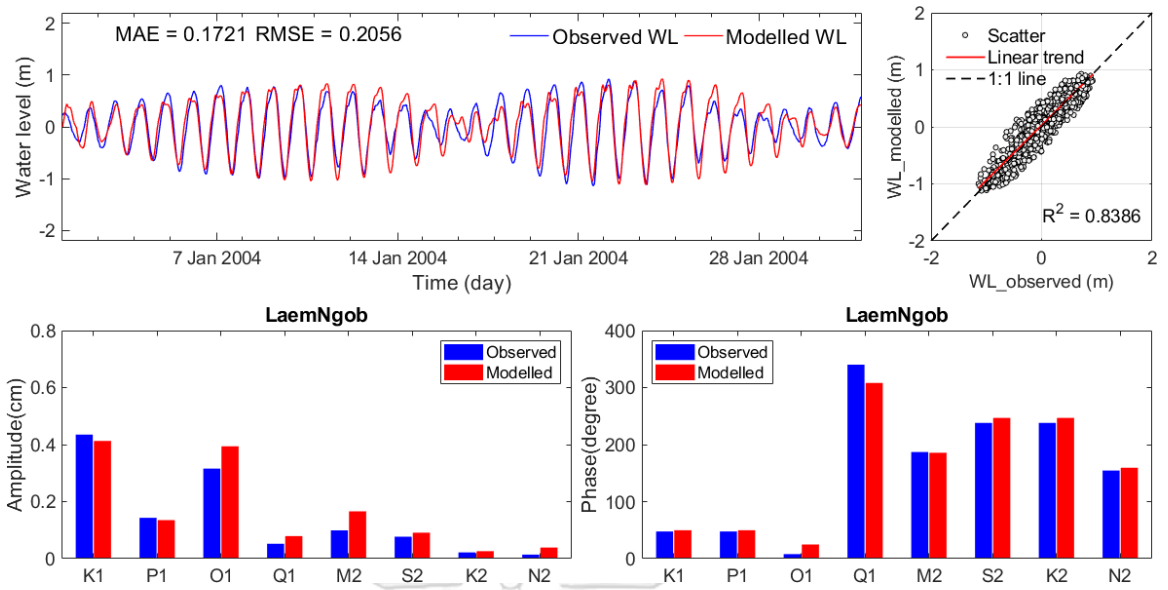


Fig. B15. Water level, phase and amplitude comparison between calibration and observed data during January 1-31, 2004 at LaemNgob Station.

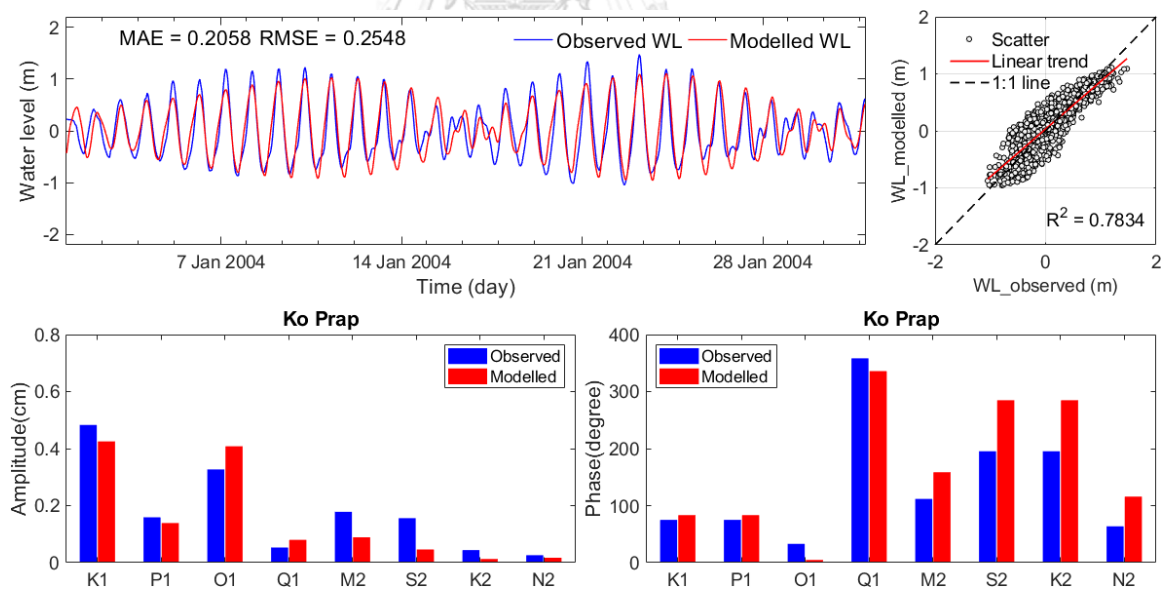


Fig. B16. Water level, phase and amplitude comparison between calibration and observed data during January 1-31, 2004 at Ko Prap Station.



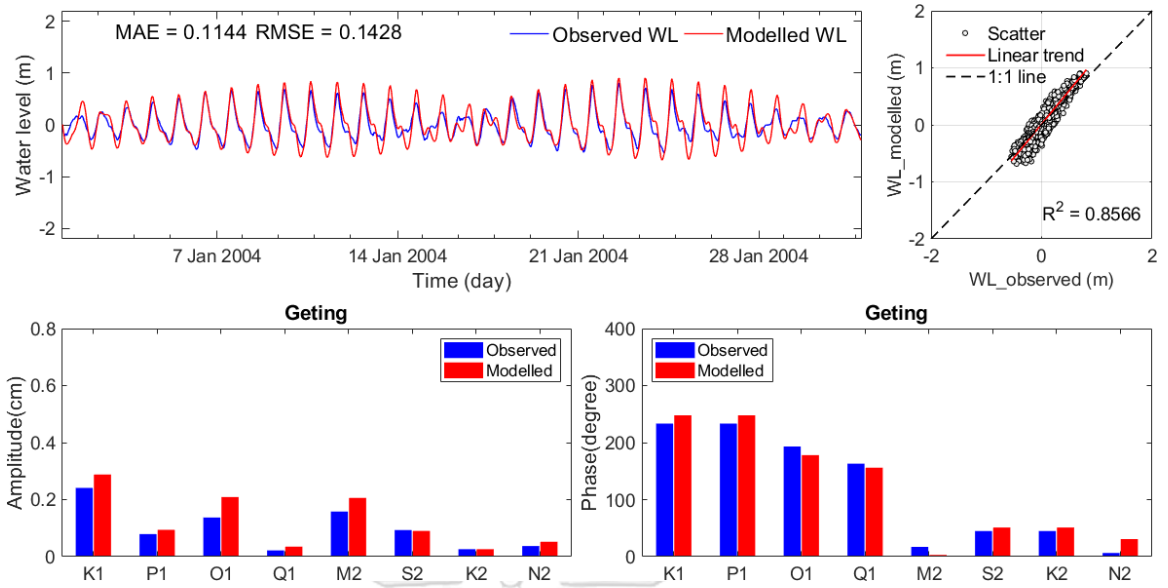


Fig. B17. Water level, phase and amplitude comparison between calibration and observed data during January 1-31, 2004 at Geting Station.

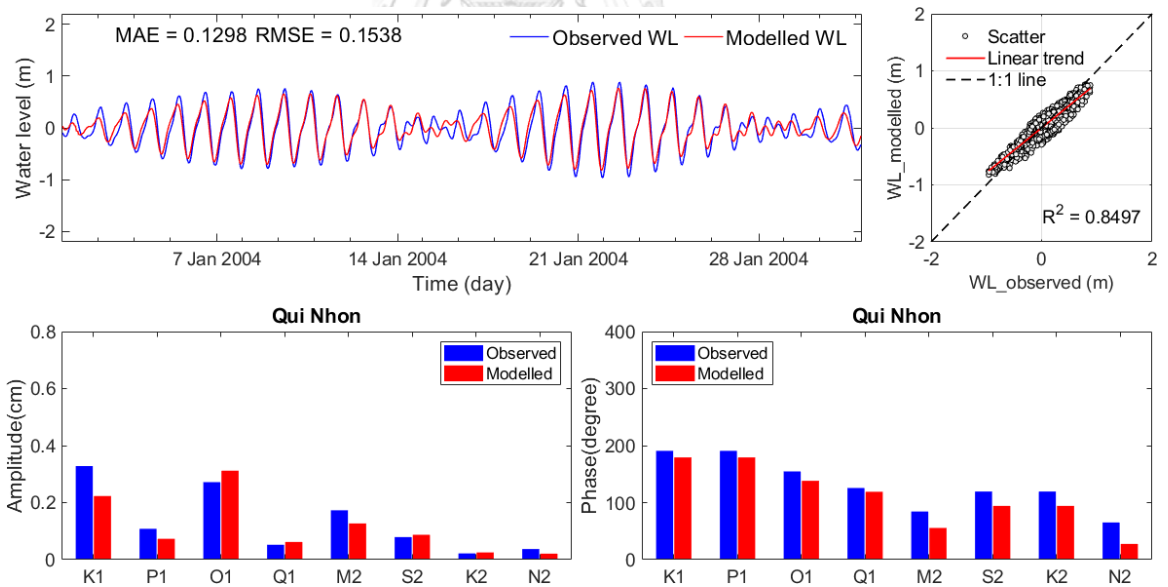


Fig. B18. Water level, phase and amplitude comparison between calibration and observed data during January 1-31, 2004 at Qui Nhon Station.



B3. Validation

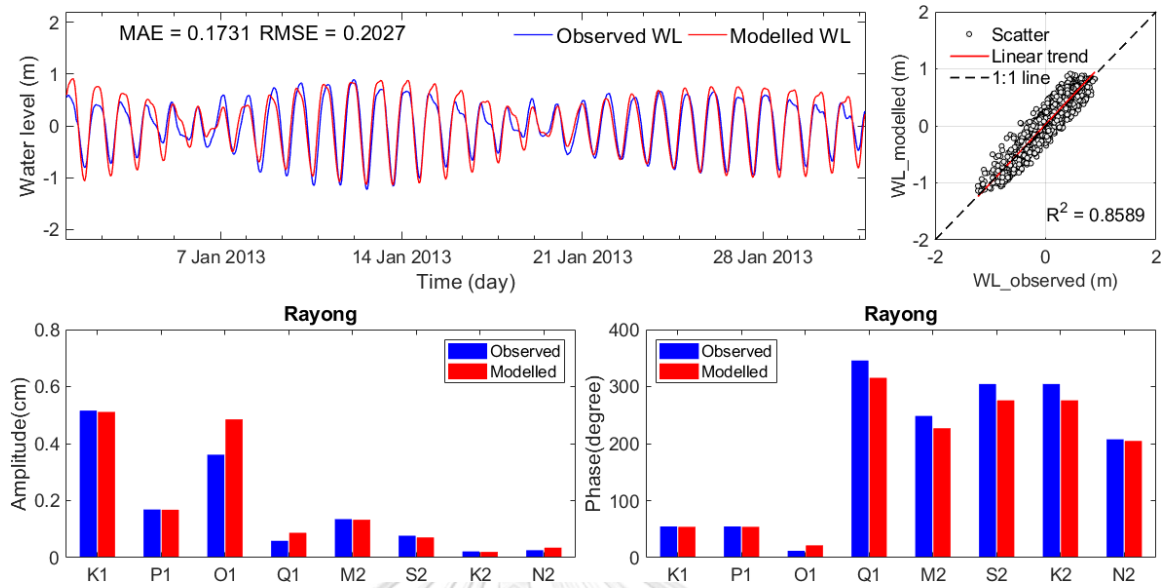


Fig. B19. Water level, phase and amplitude comparison between validation and observed data during January 1-31, 2013 at Rayong Station.

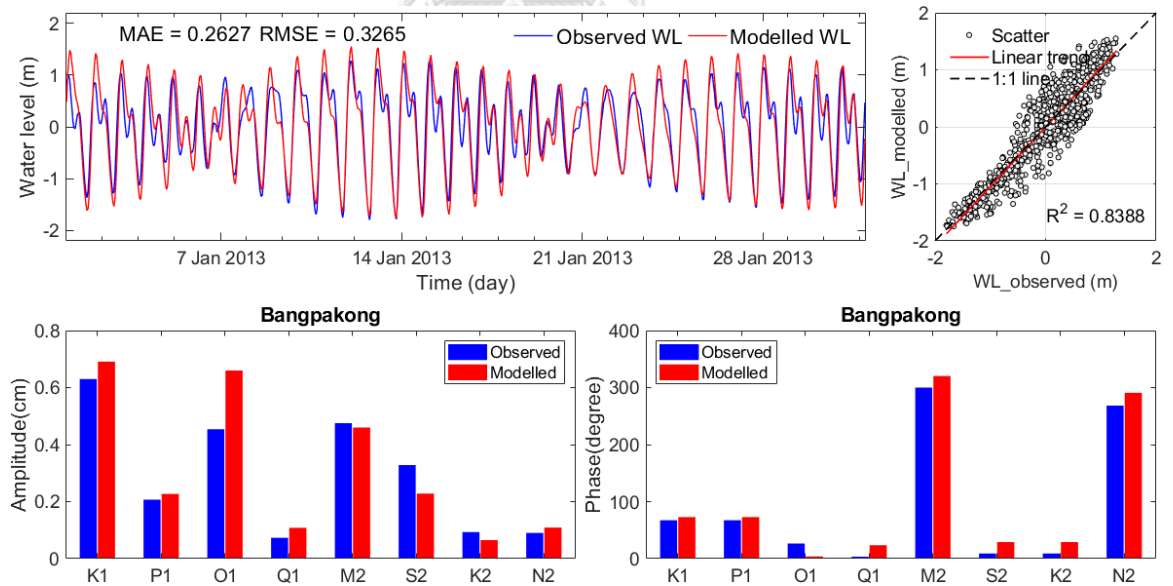


Fig. B20. Water level, phase and amplitude comparison between validation and observed data during January 1-31, 2013 at Bangpakong Station.

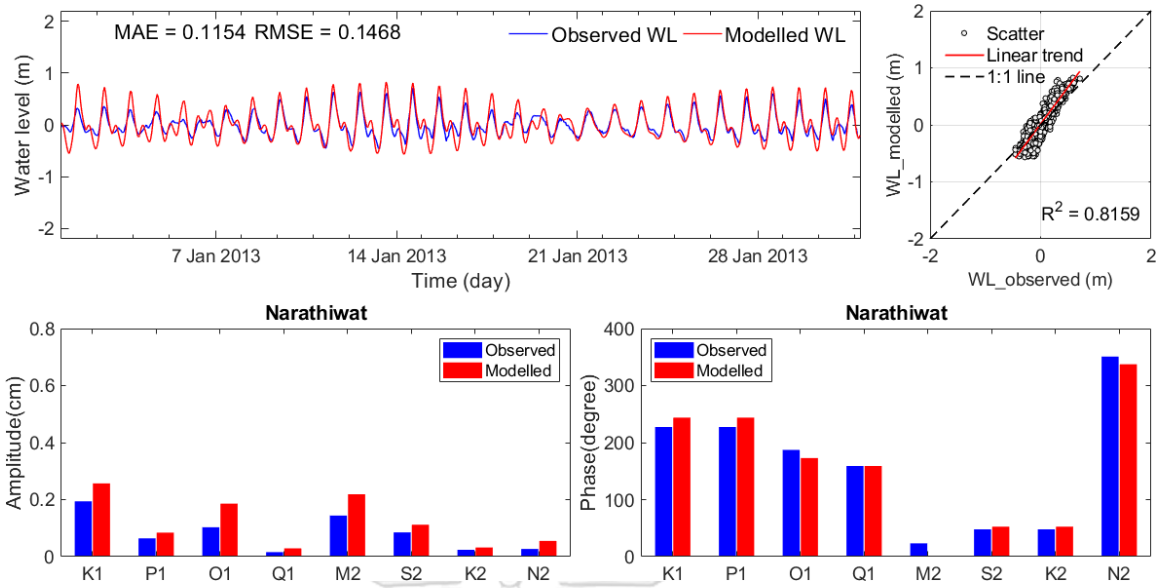


Fig. B21. Water level, phase and amplitude comparison between validation and observed data during January 1-31, 2013 at Narathiwat Station.

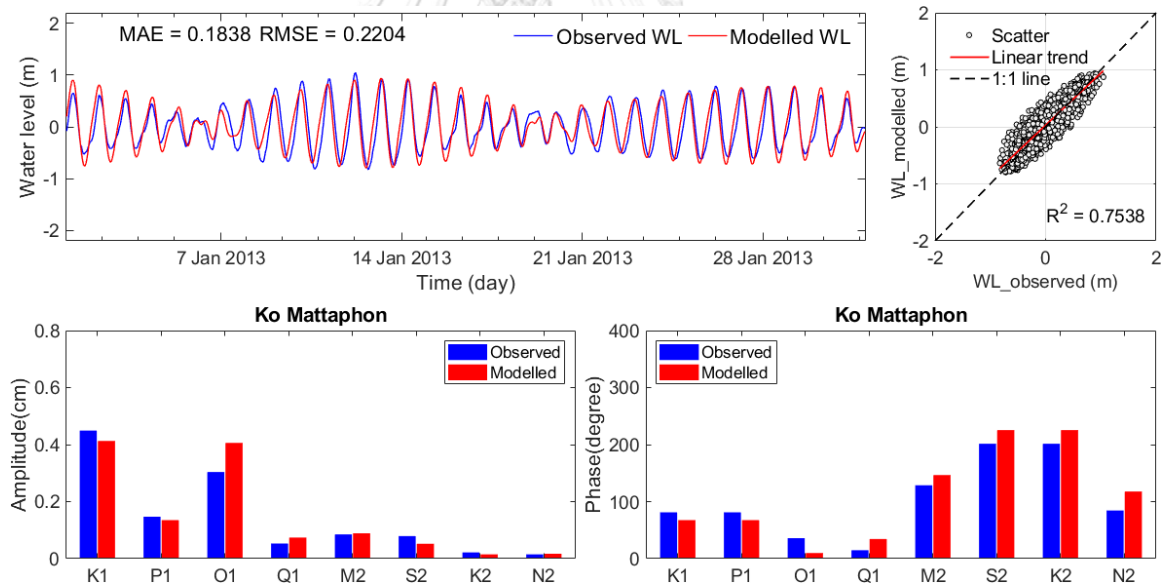
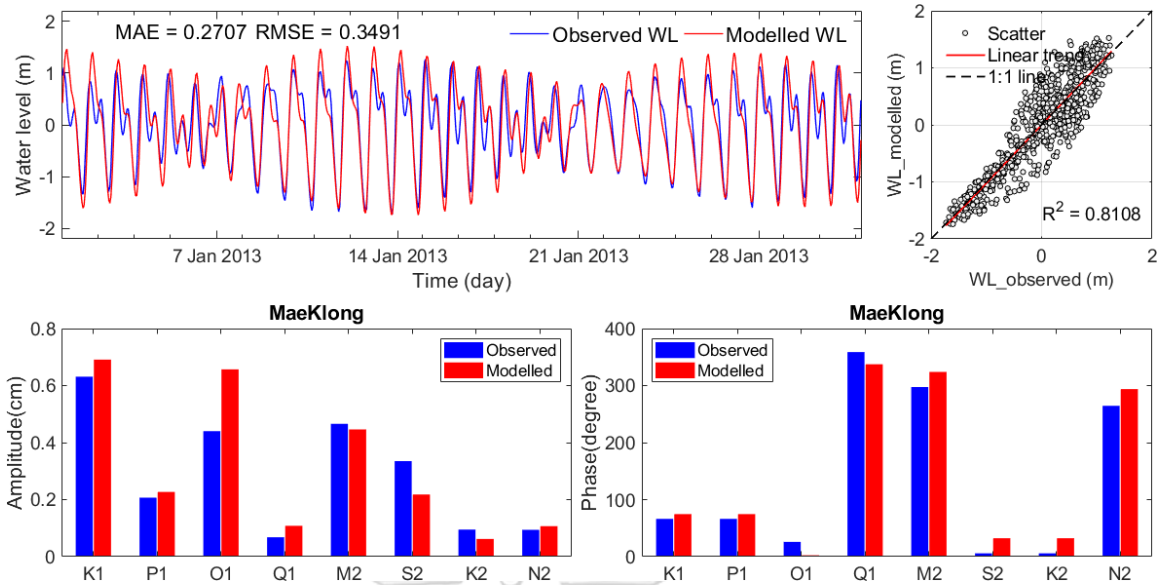
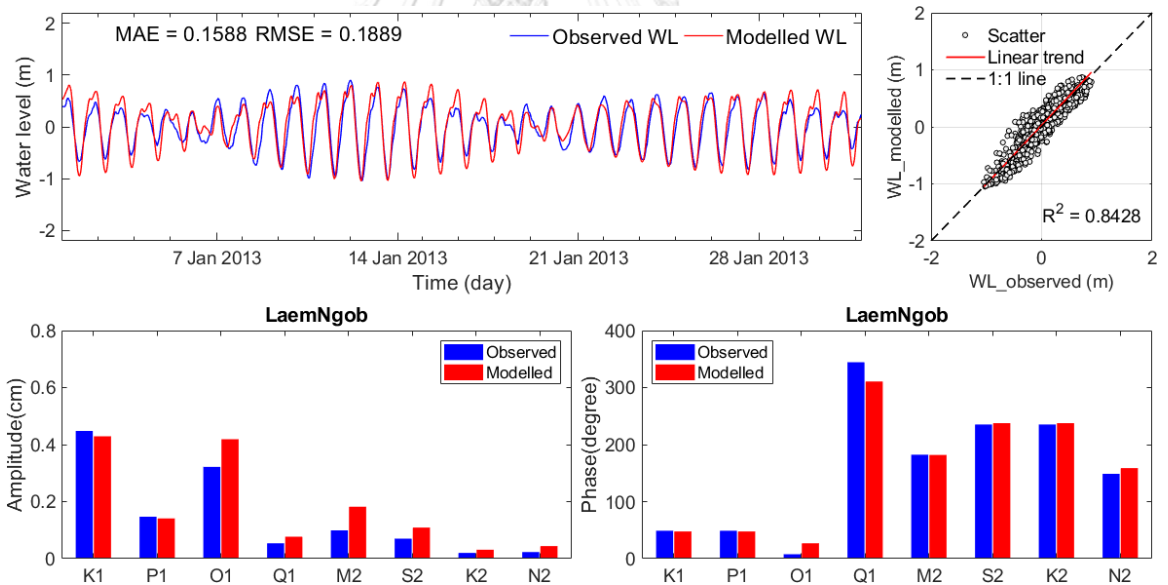


Fig. B22. Water level, phase and amplitude comparison between validation and observed data during January 1-31, 2013 at Ko Mattaphon Station.



*Fig. B23. Water level, phase and amplitude comparison between validation and observed data during January 1-31, 2013 at MaeKlong Station.*



*Fig. B24. Water level, phase and amplitude comparison between validation and observed data during January 1-31, 2013 at LaemNgob Station.*

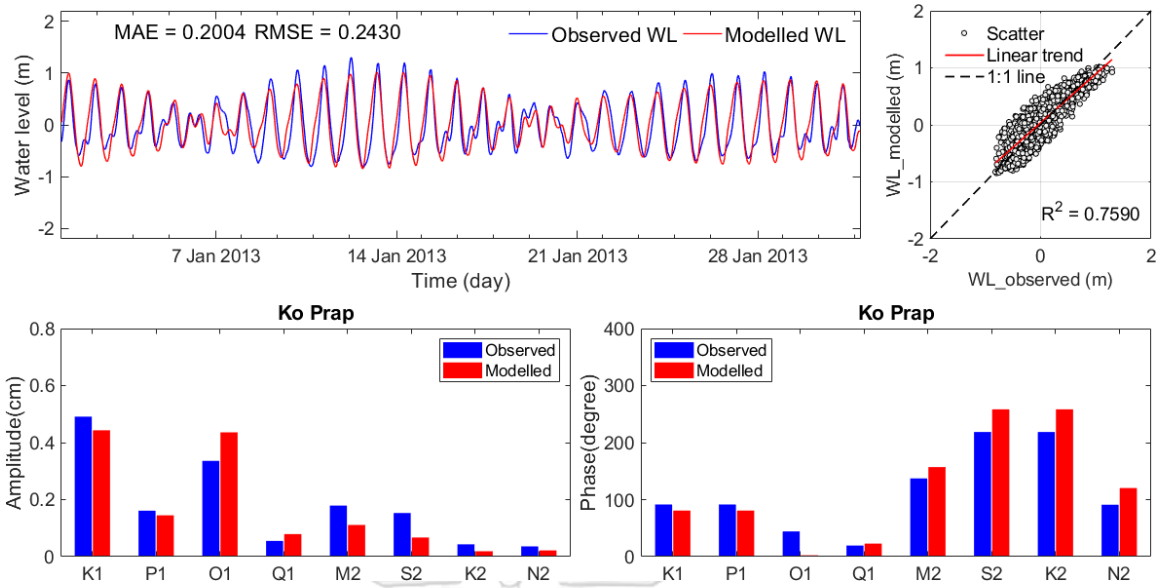


Fig. B25. Water level, phase and amplitude comparison between validation and observed data during January 1-31, 2013 at Ko Prap Station.

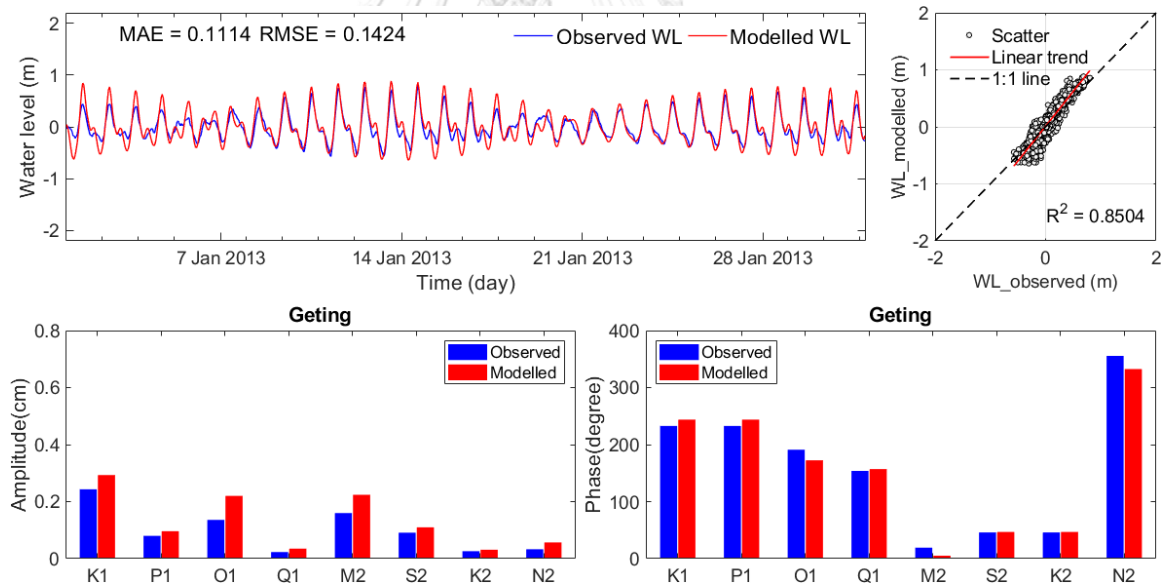


Fig. B26. Water level, phase and amplitude comparison between validation and observed data during January 1-31, 2013 at Geting Station.

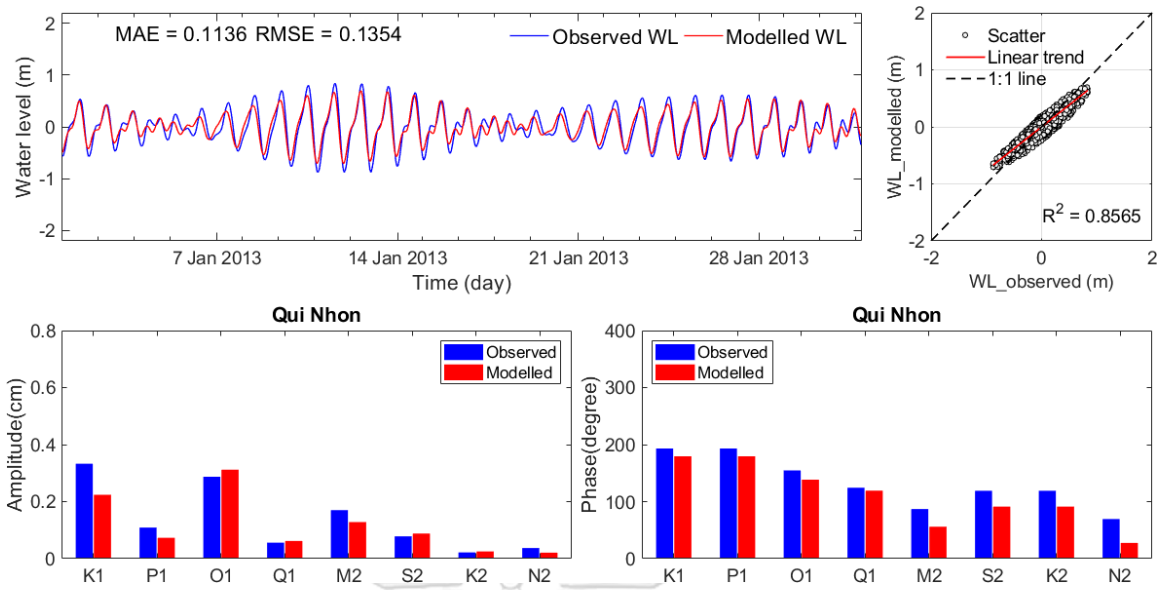


Fig. B27. Water level, phase and amplitude comparison between validation and observed data during January 1-31, 2013 at Qui Nhon Station.

B4. Comparison of spatially averaged surface velocity

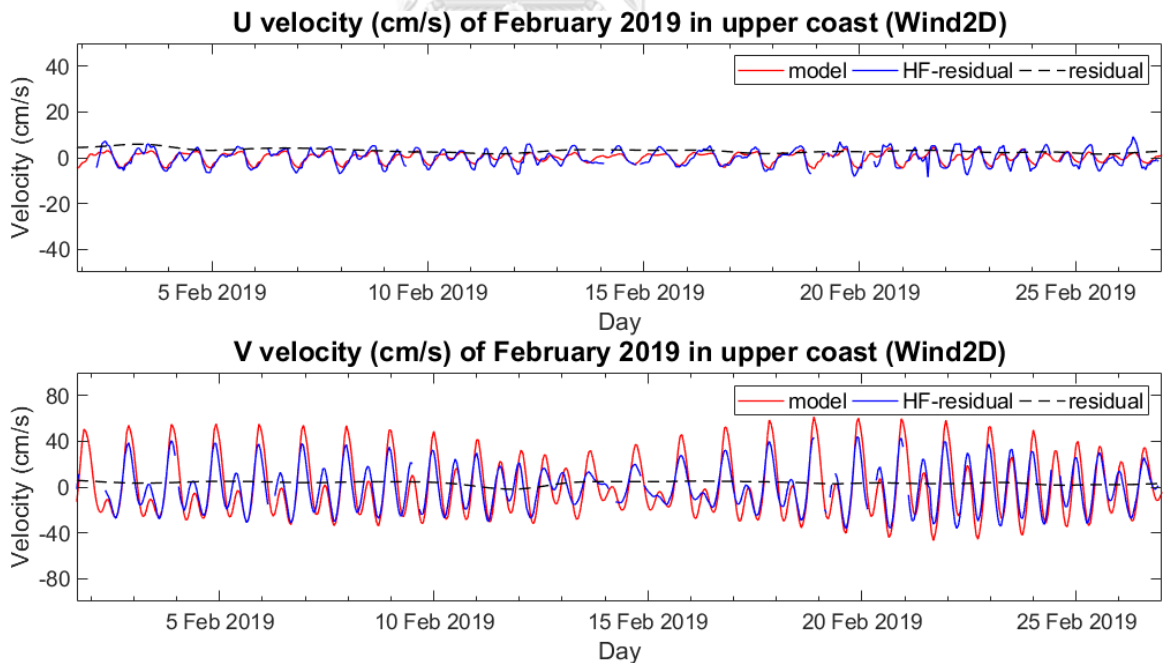
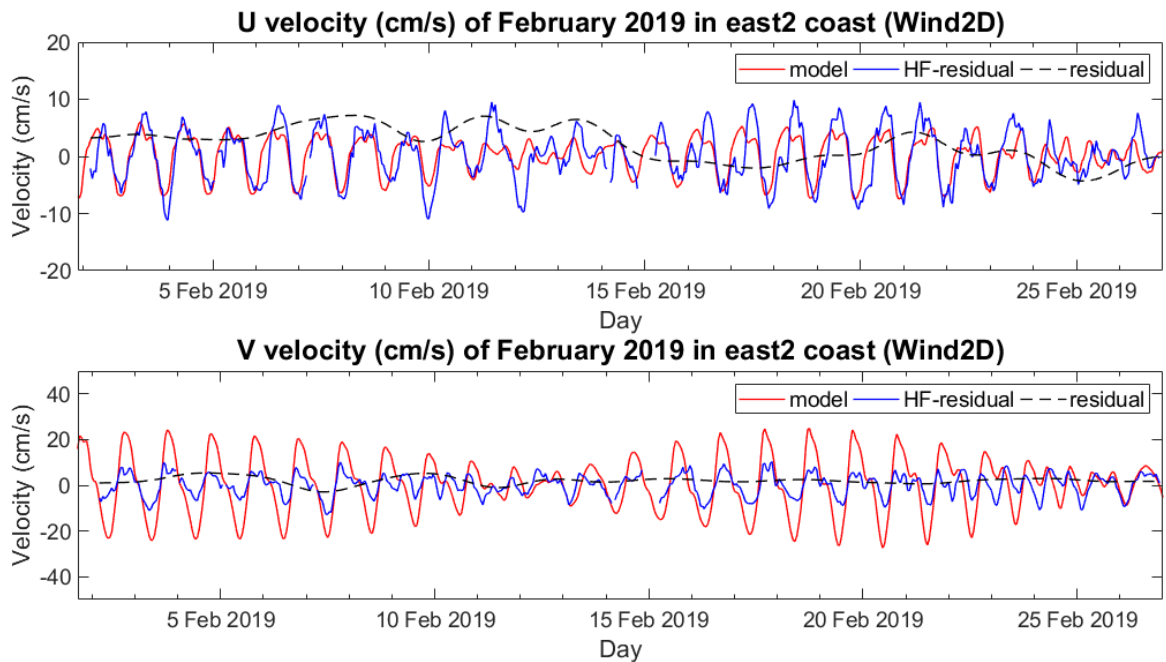
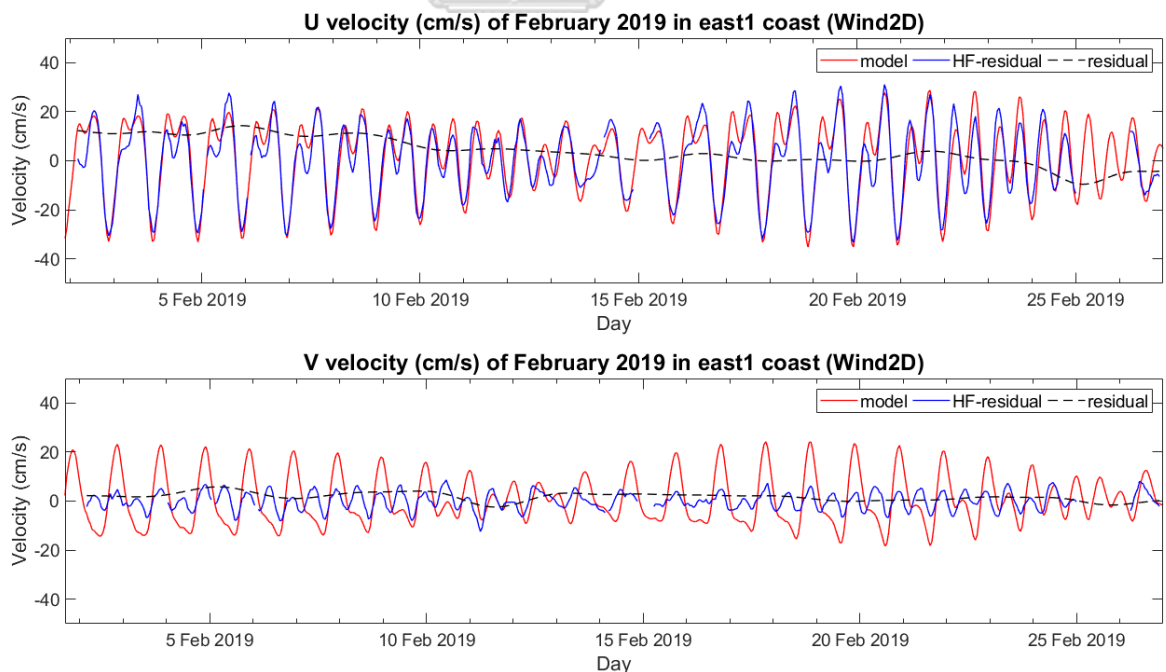


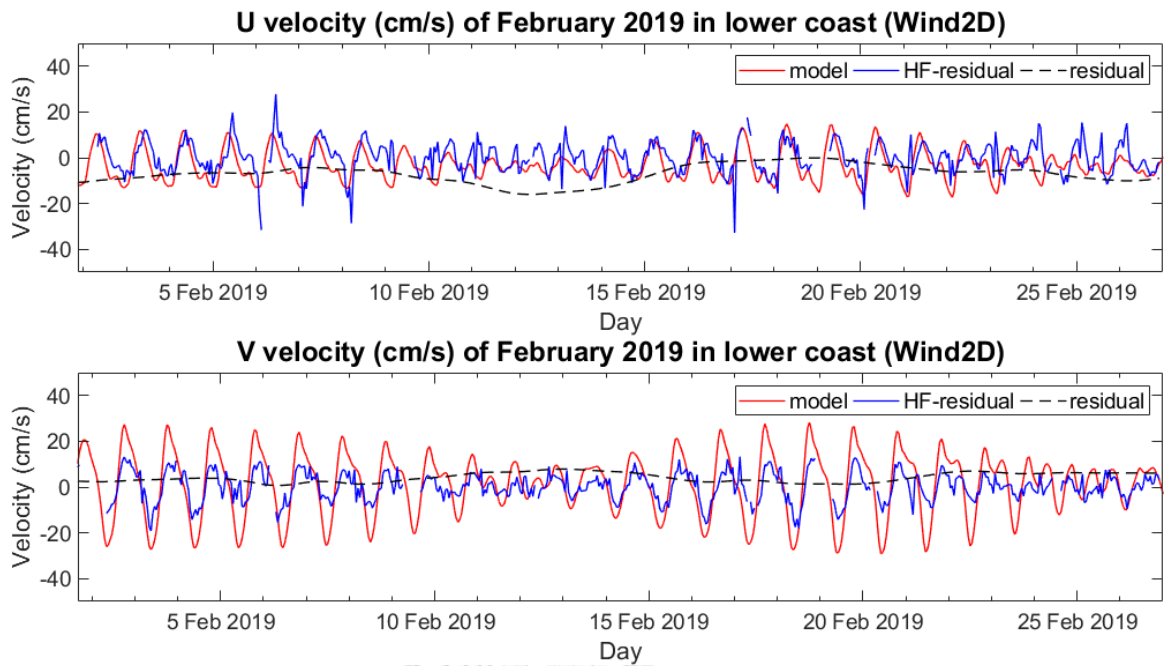
Fig. B28. Comparison of spatially averaged surface current velocity between the simulated (Red) and HF Radar (Blue) off the Upper coast during February 1-28, 2019 in case Wind2D.



*Fig. B29. Comparison of spatially averaged surface current velocity between the simulated (Red) and HF Radar (Blue) off the east2 coast during February 1-28, 2019 in case Wind2D.*



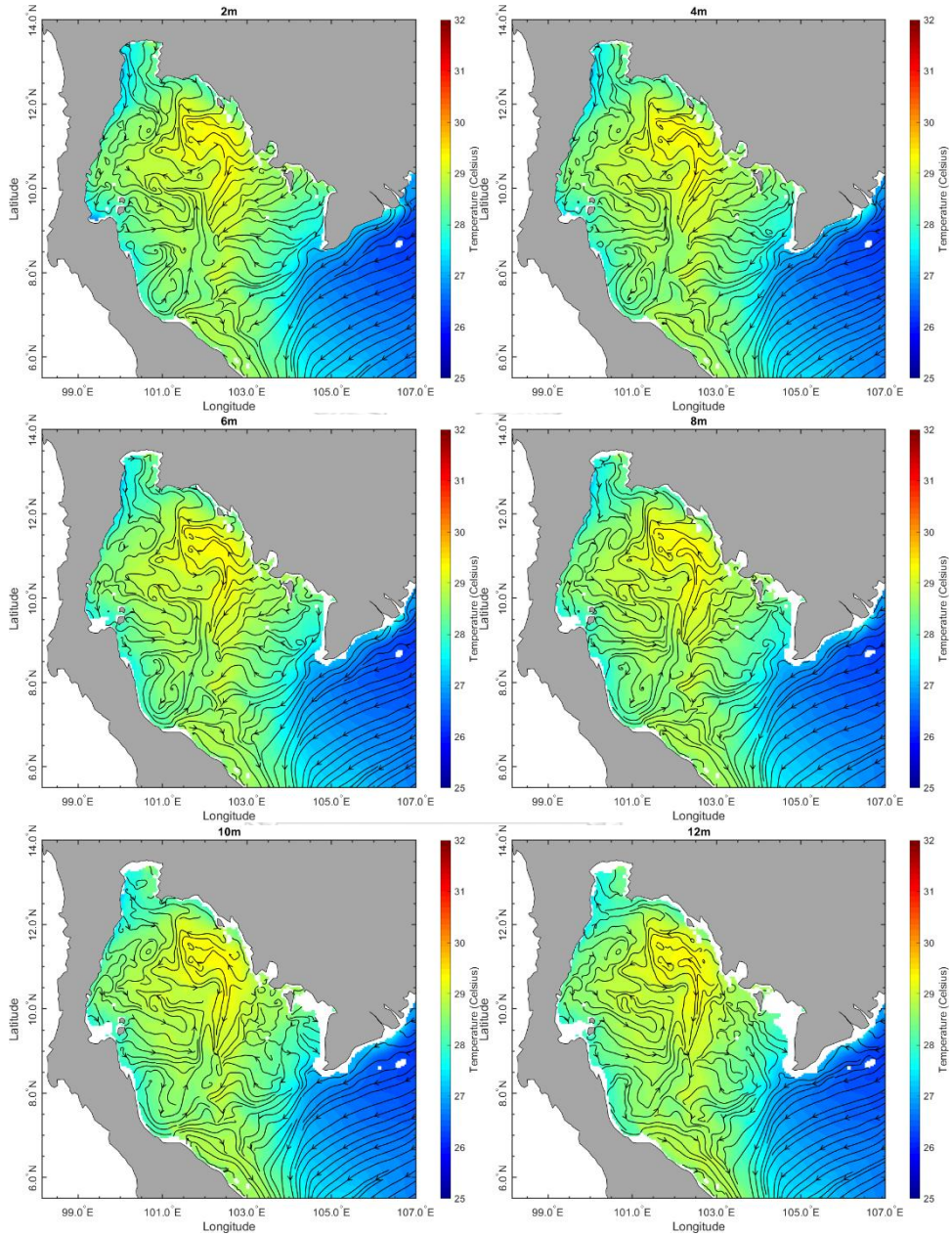
*Fig. B30. Comparison of spatially averaged surface current velocity between the simulated (Red) and HF Radar (Blue) off the East1 coast during February 1-28, 2019 in Case Wind2D.*

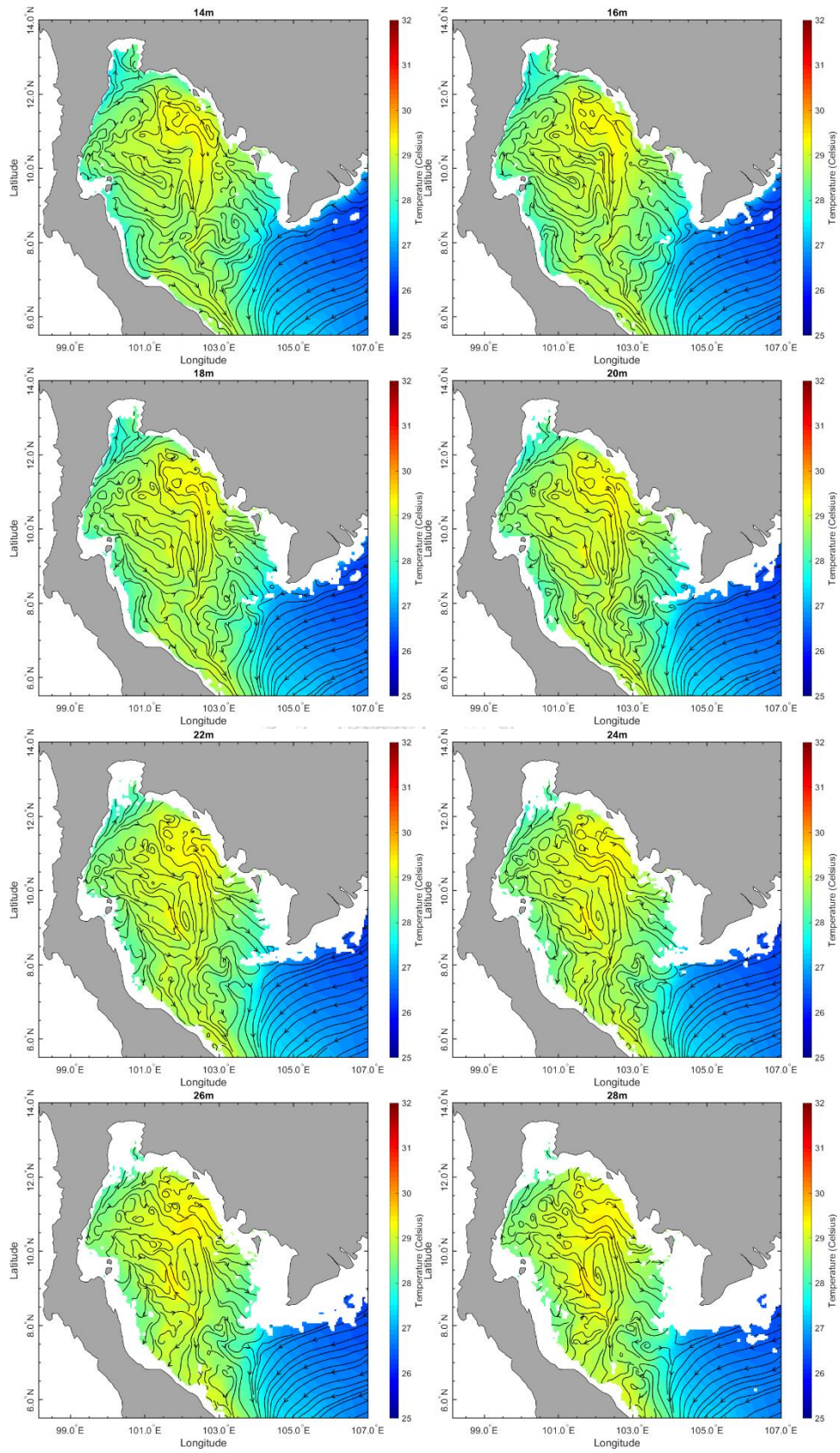


*Fig. B31. Comparison of spatially averaged surface current velocity between the simulated (Red) and HF Radar (Blue) off the lower coast during February 1-28, 2019 in case Wind2D.*

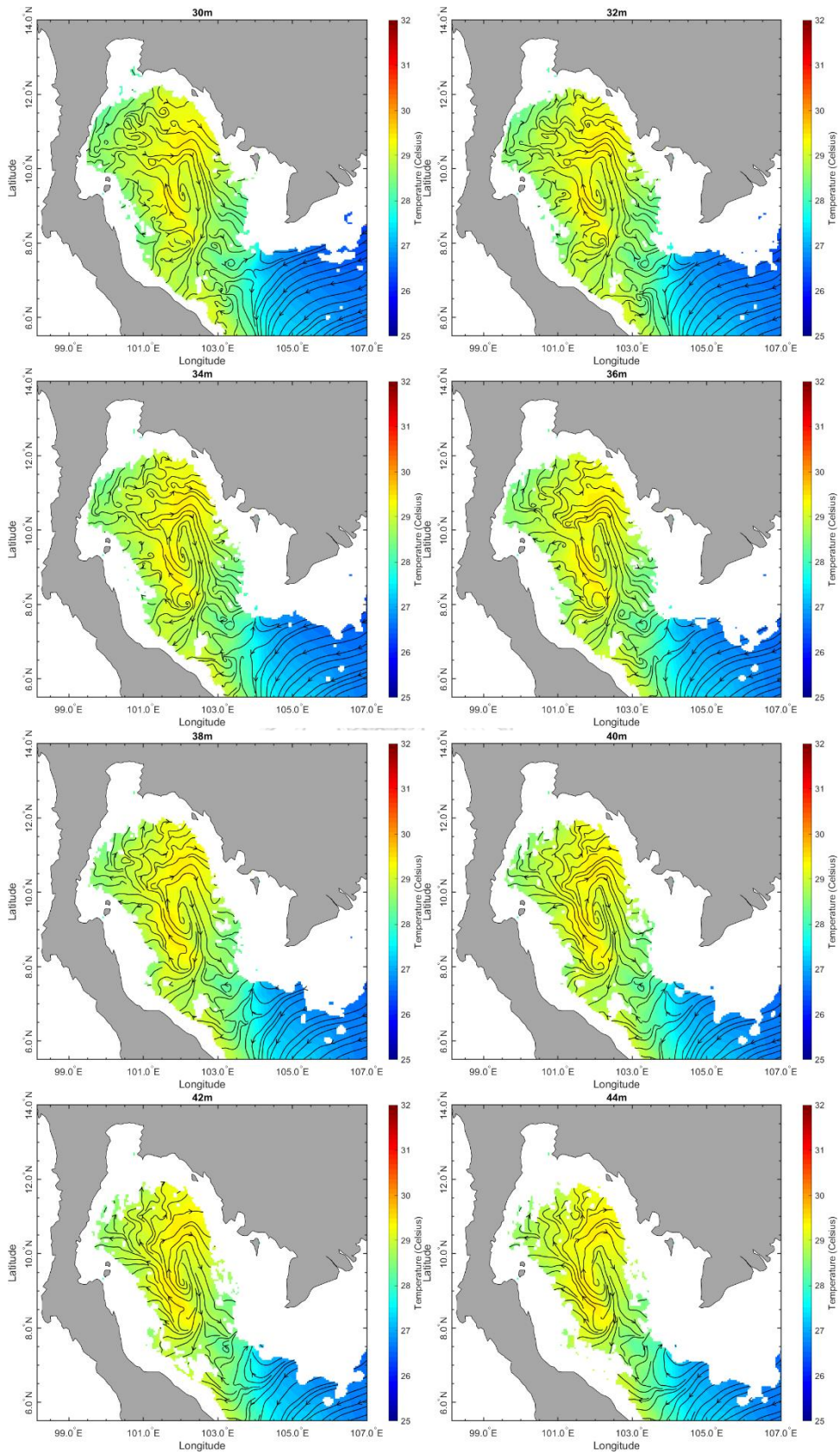


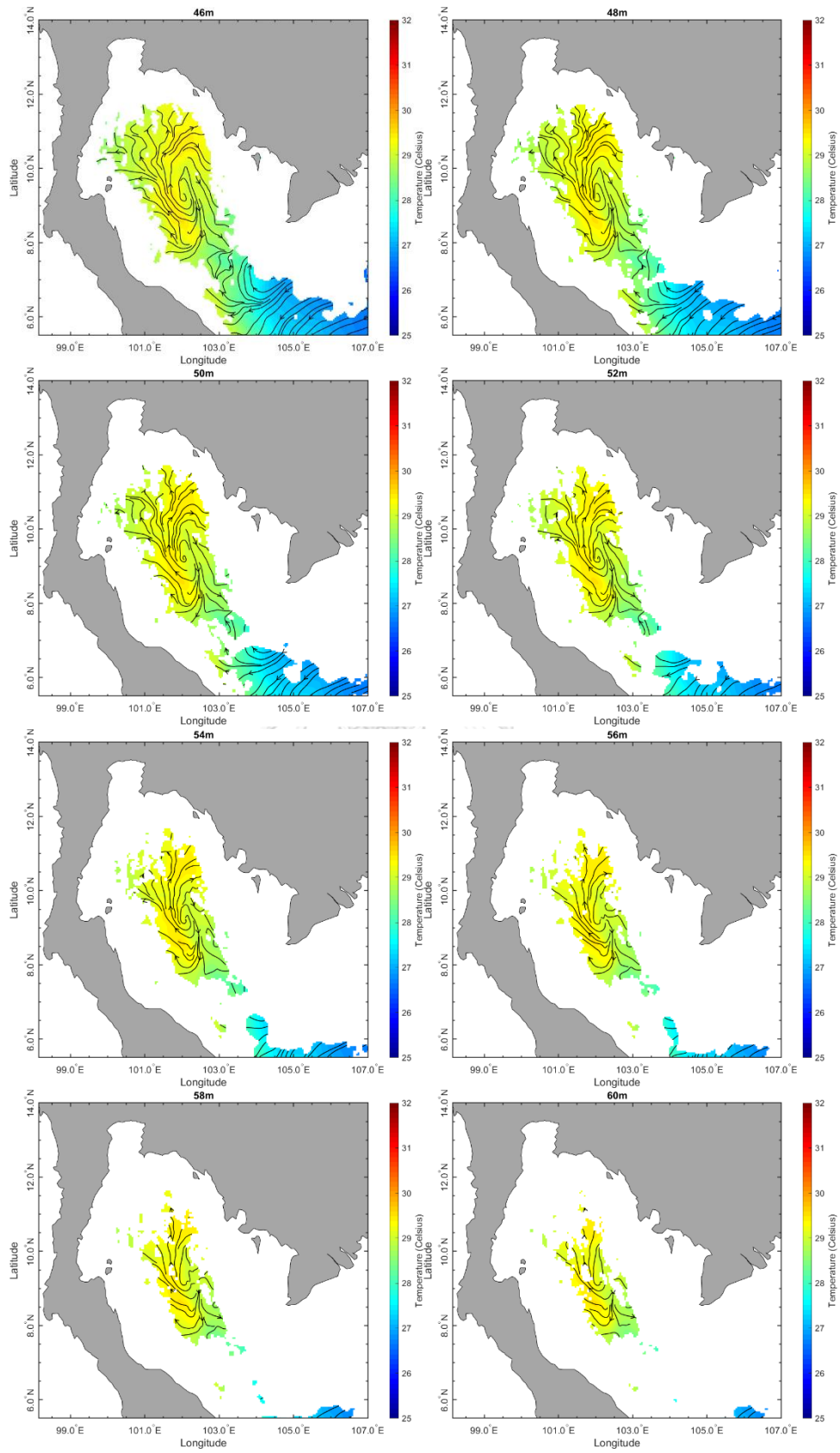
### B5. The distributions of monthly averaged water temperature of northeast monsoon

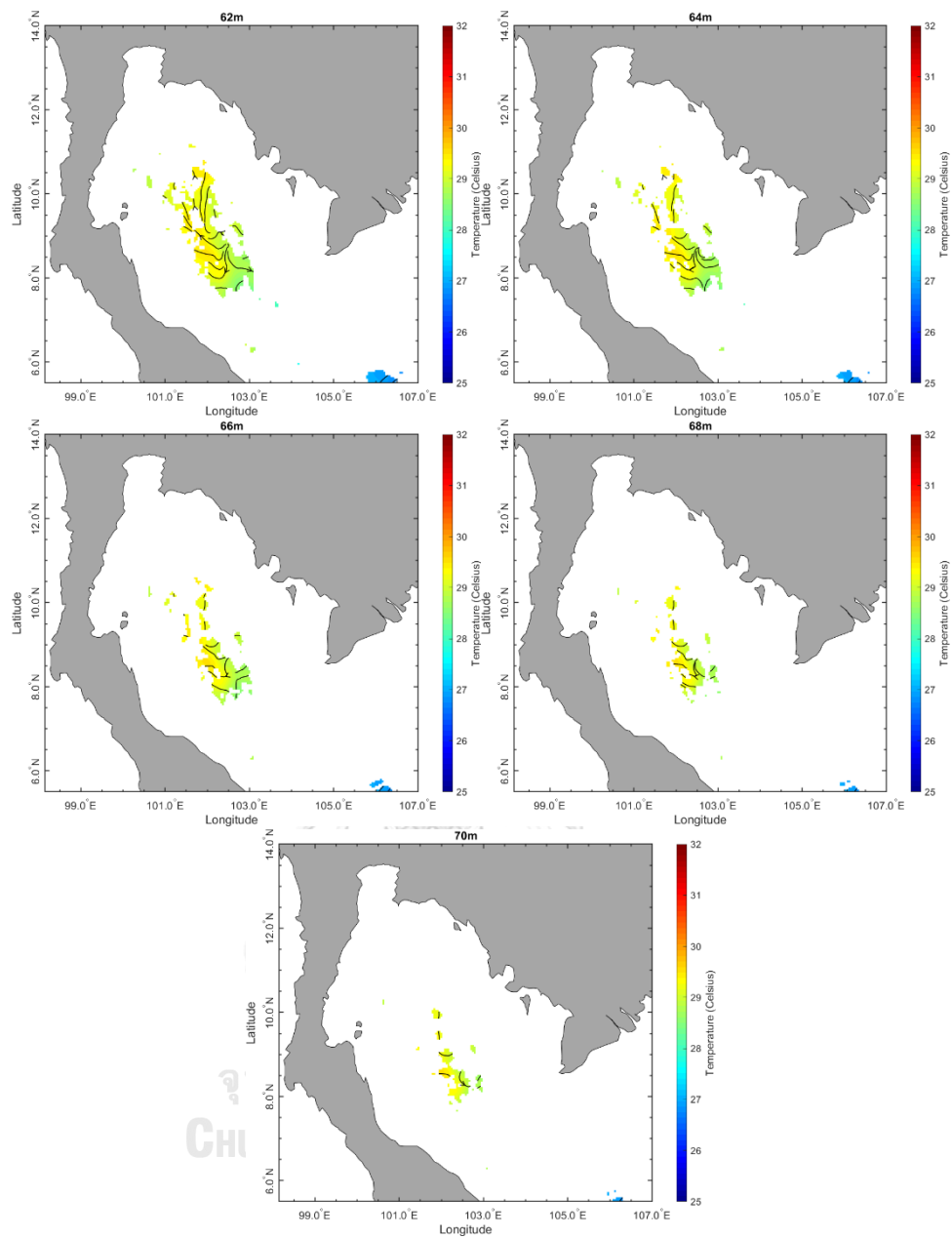






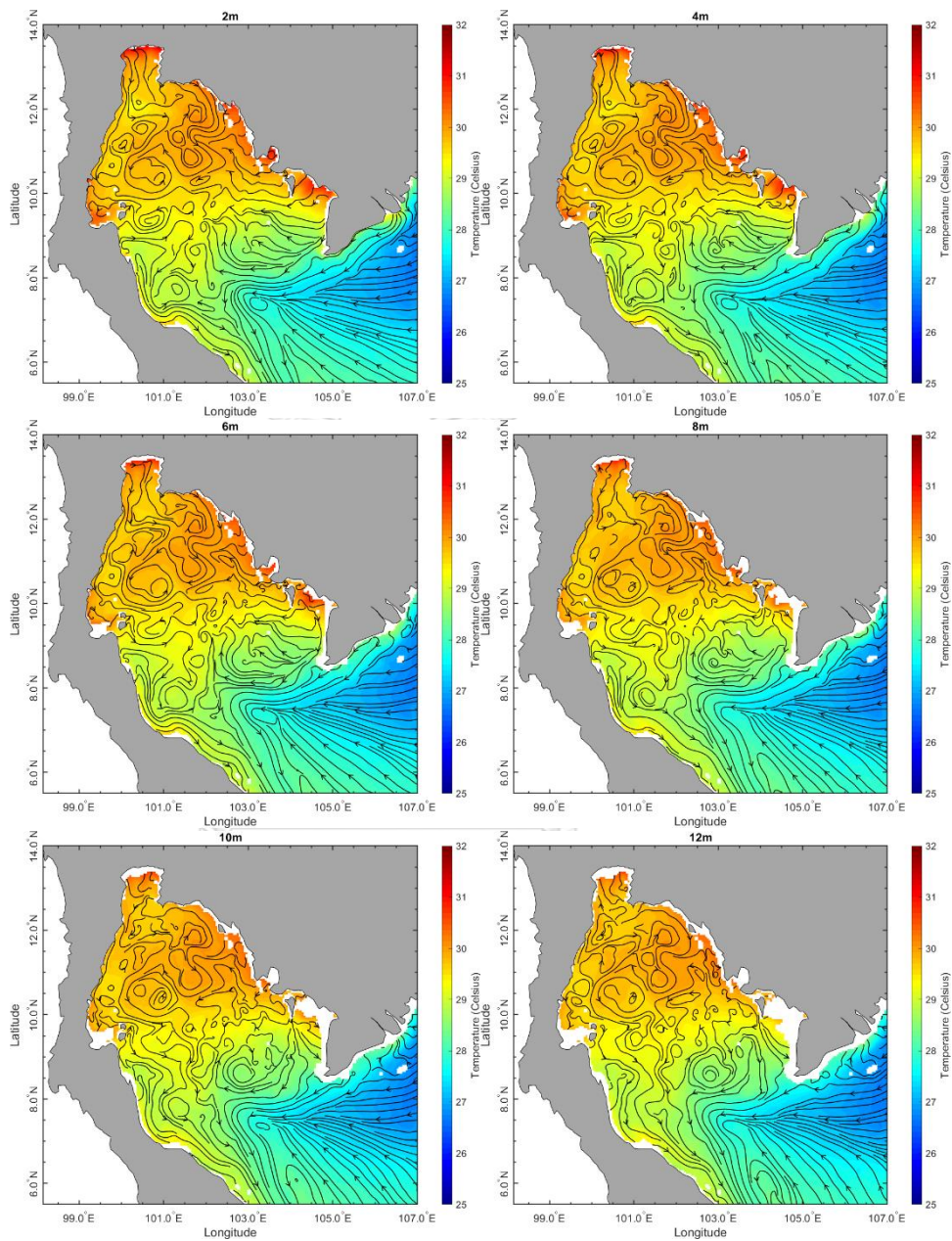




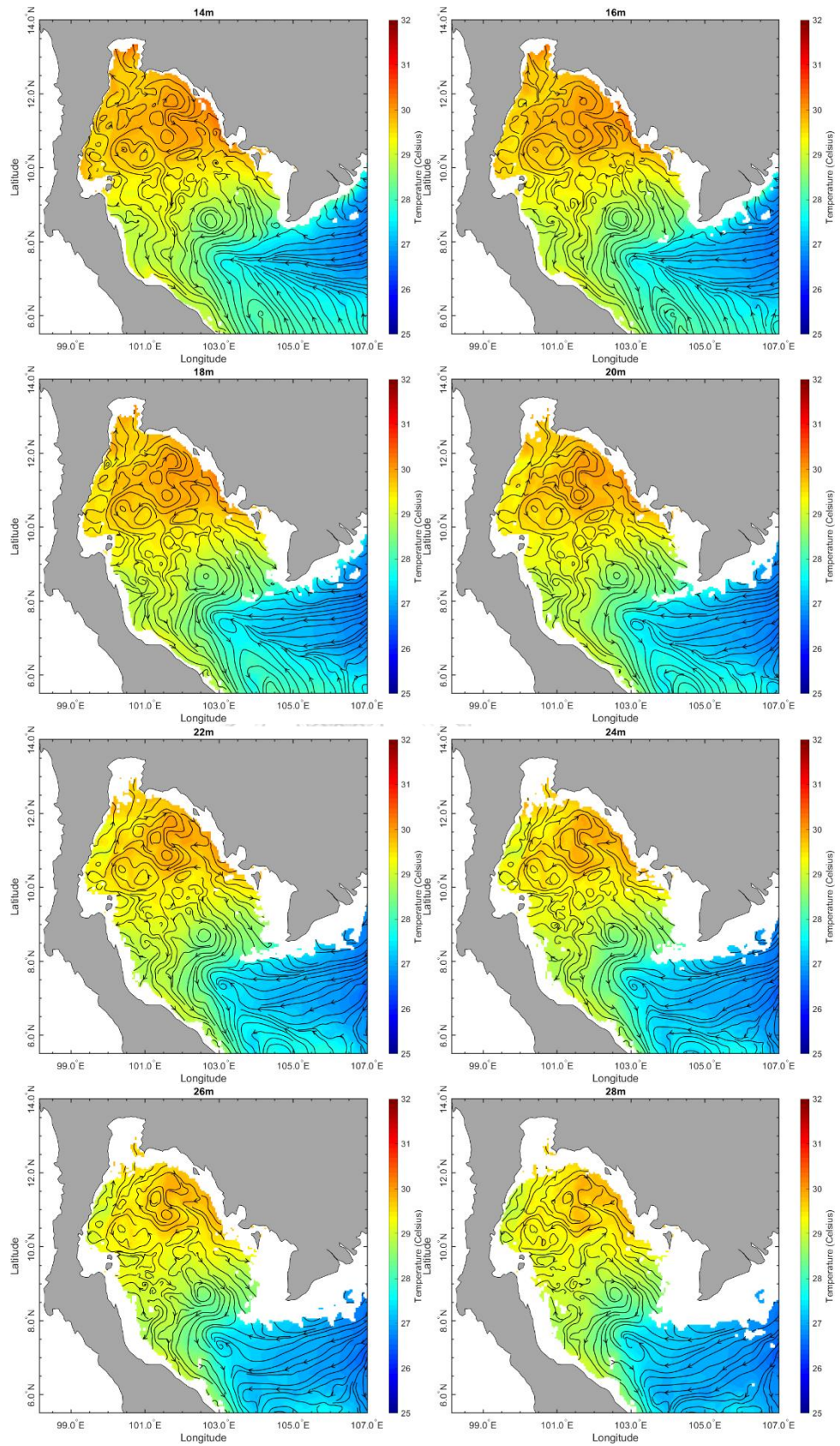


*Fig. B32. The distributions of monthly averaged water temperature of Northeast monsoon in the GoT at depths of 2-70 m.*

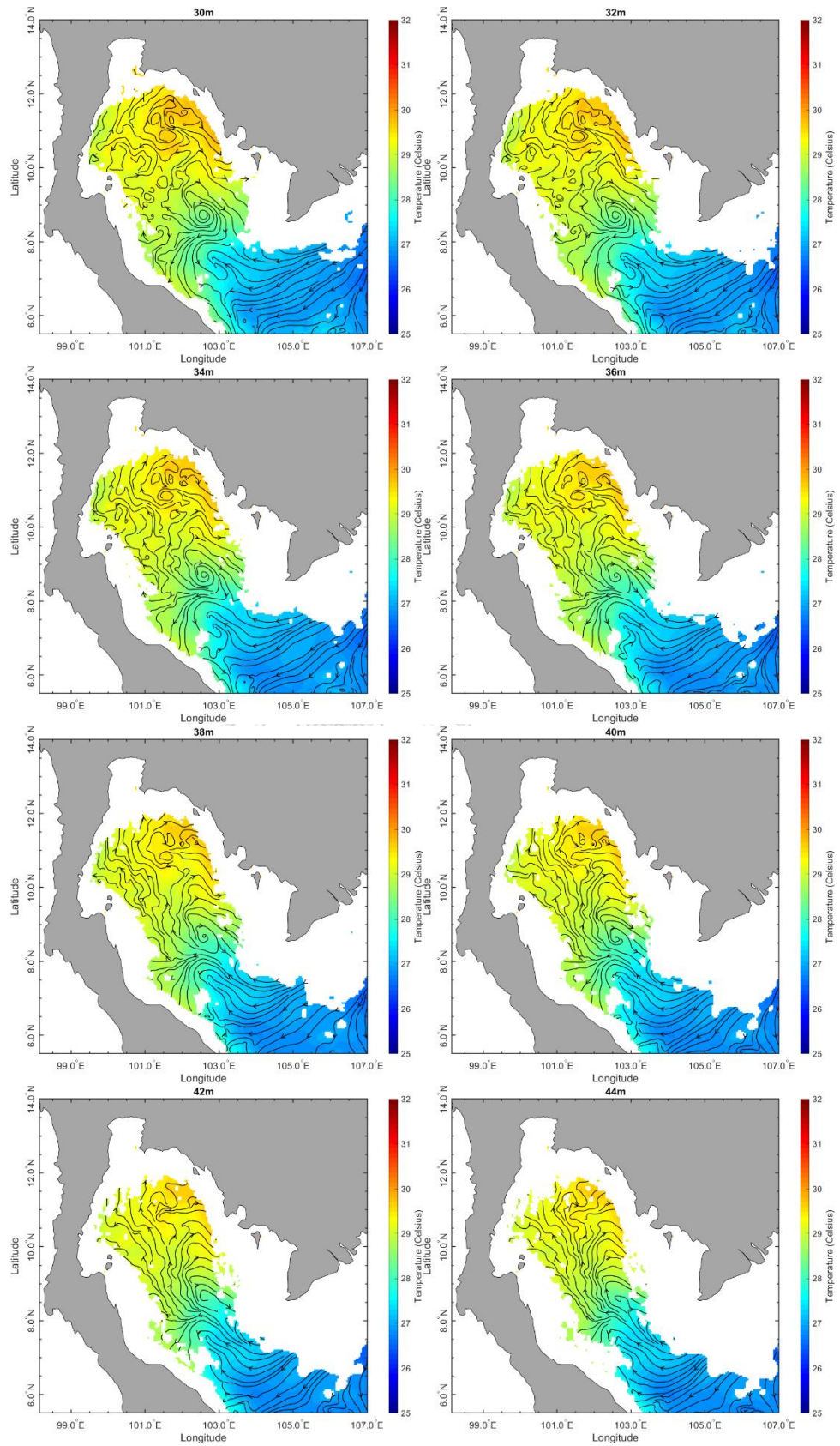
## B6. The distributions of monthly averaged water temperature of 1<sup>st</sup> inter-monsoon

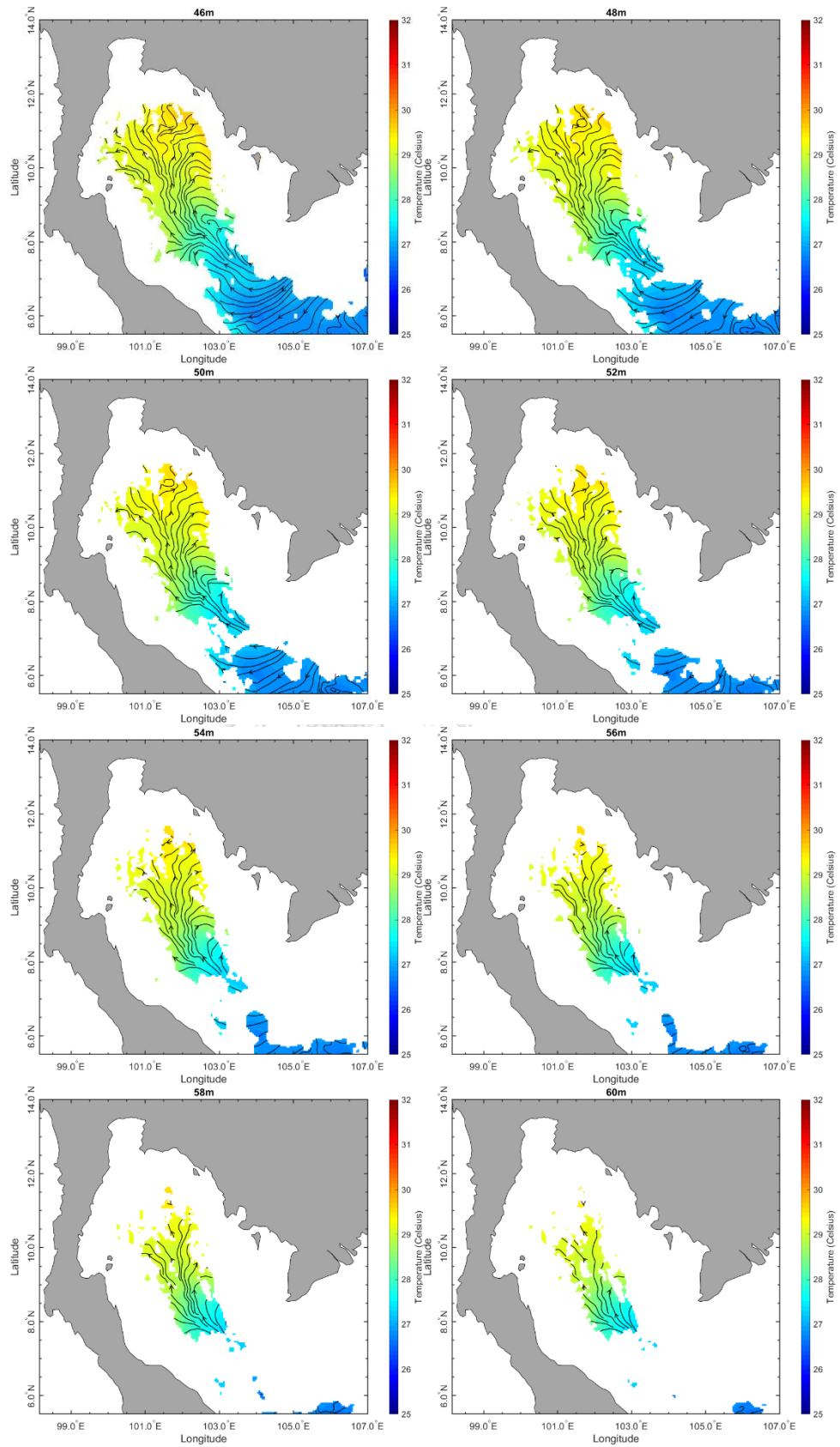


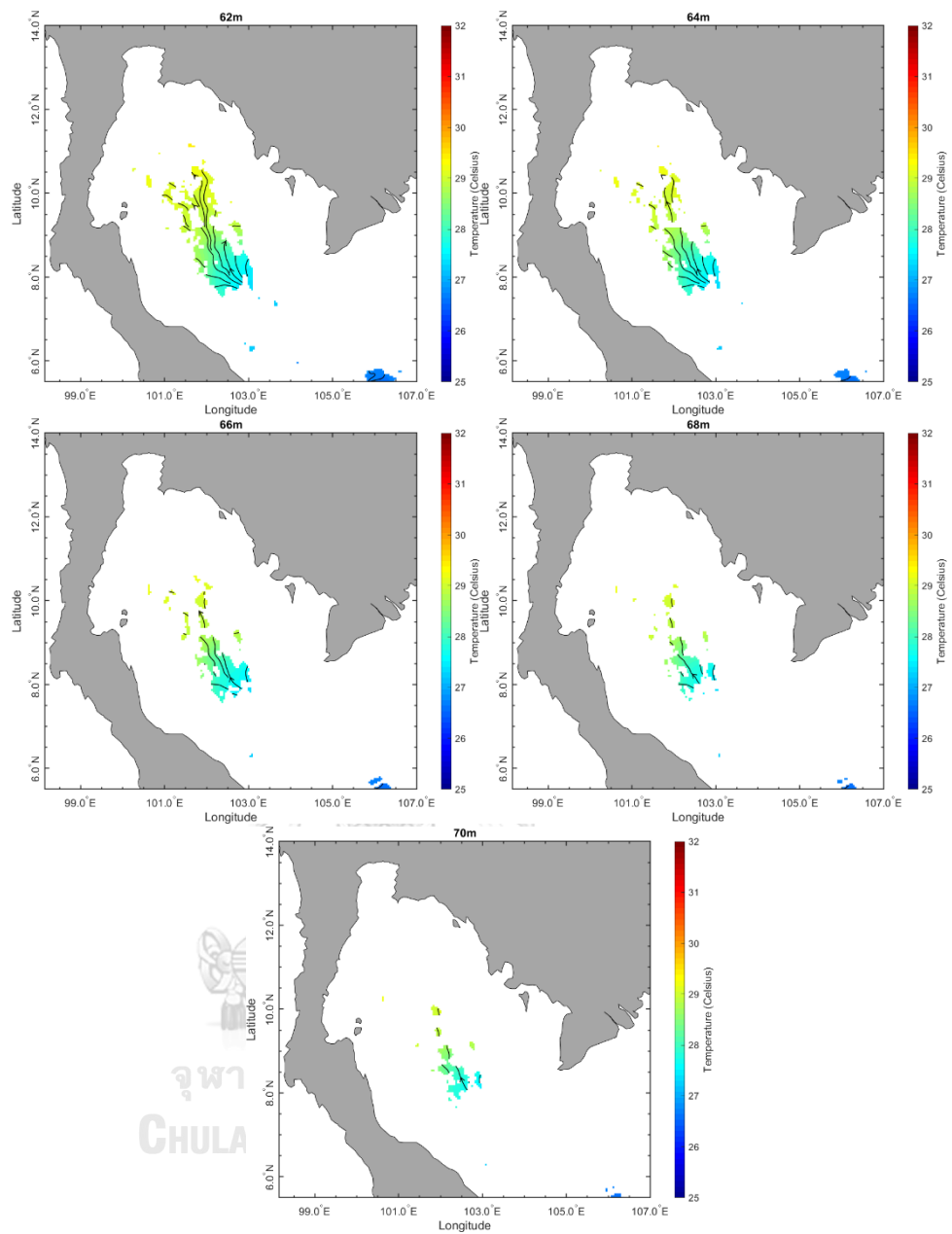






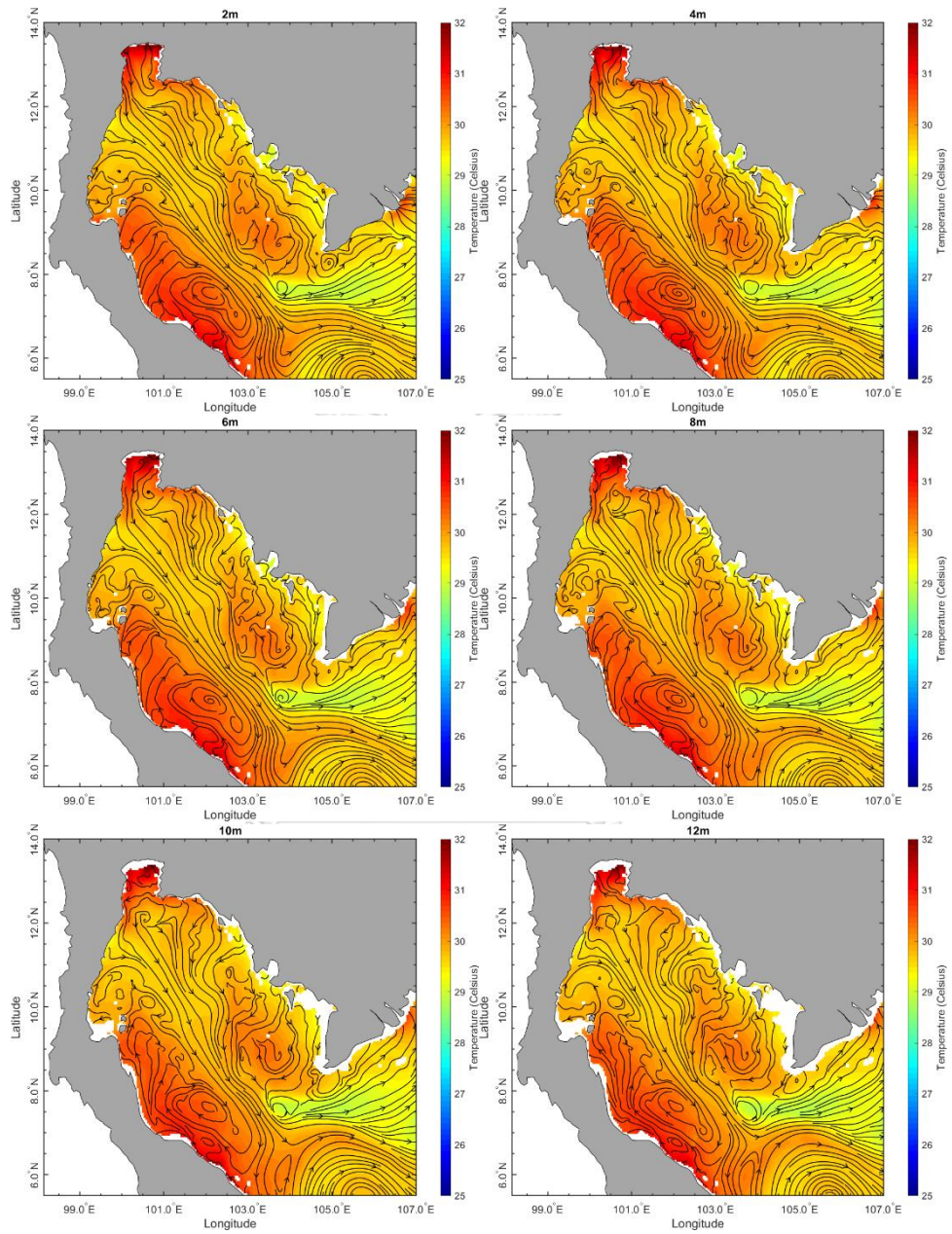




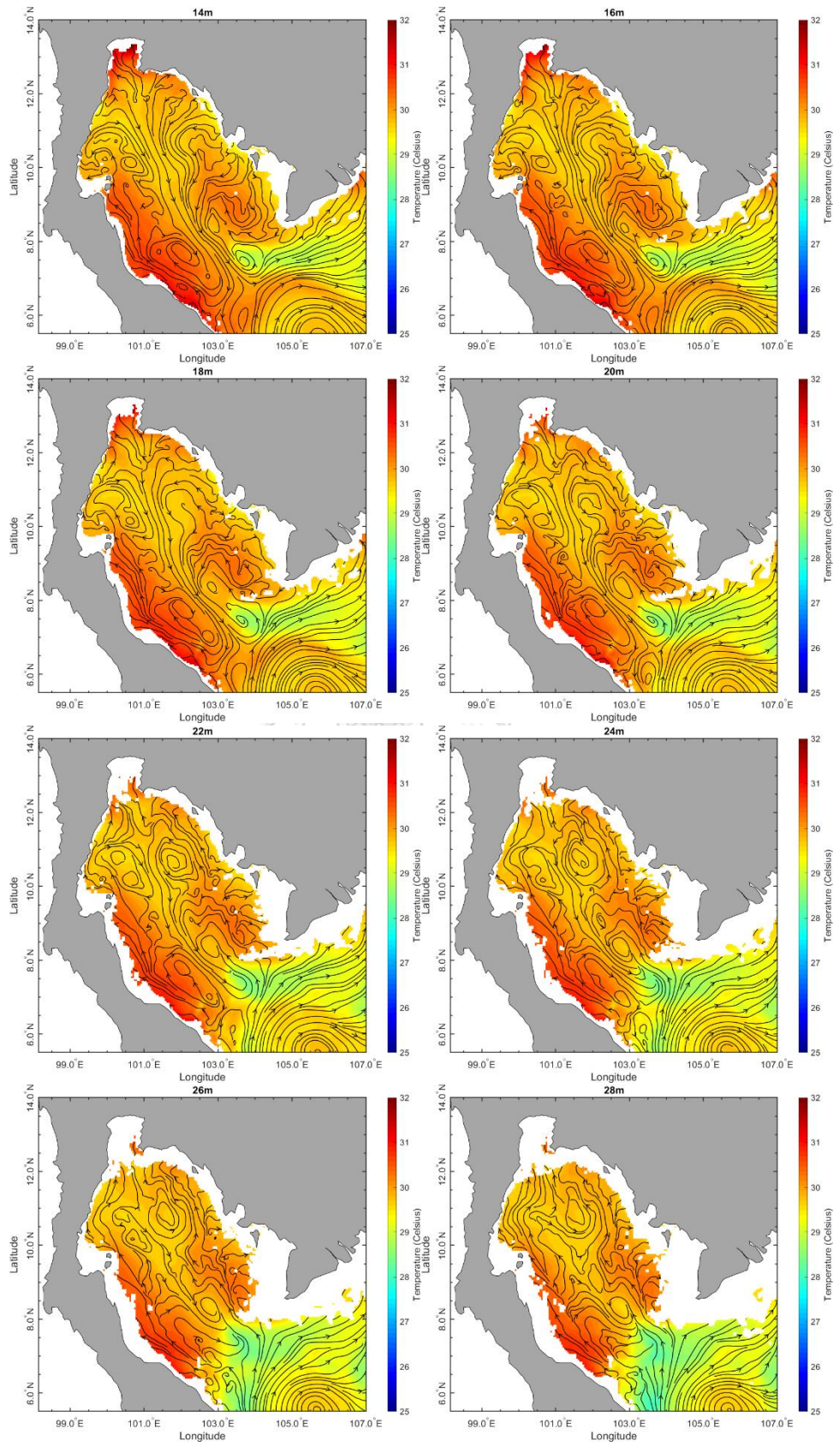


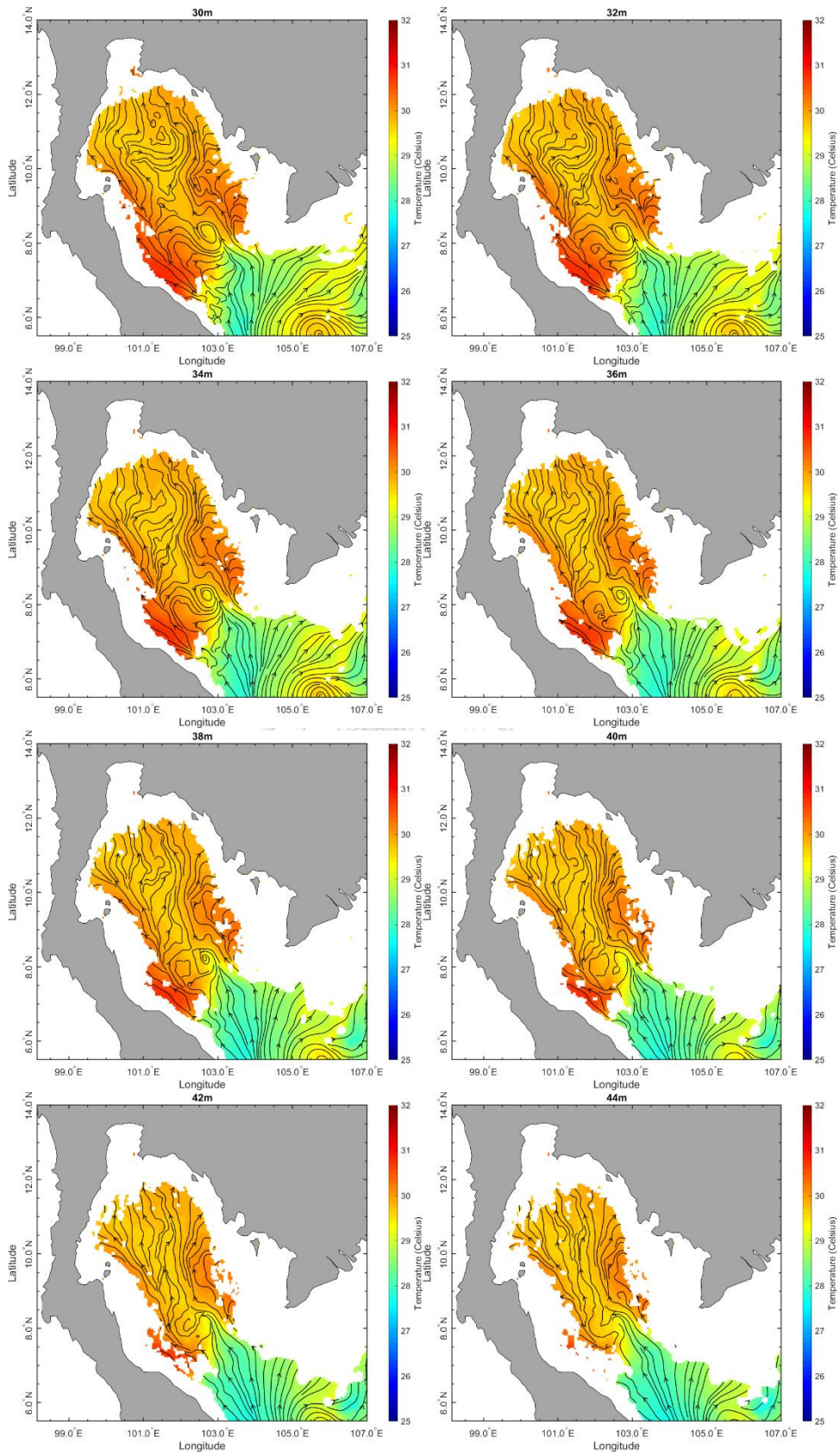
*Fig. B33. The distributions of monthly averaged water temperature of 1<sup>st</sup> Inter-monsoon in GoT at depths of 2-70 m*

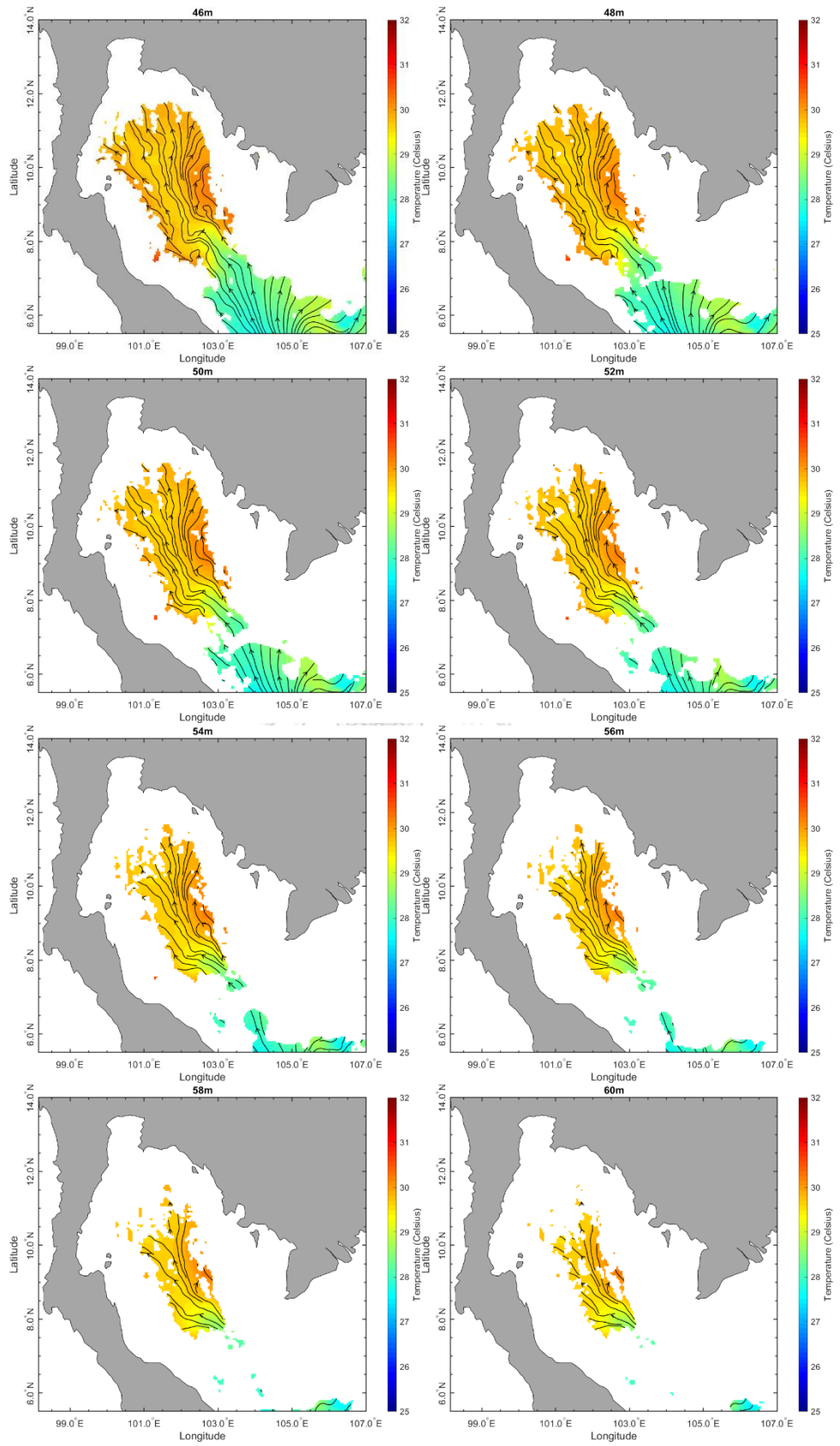
### B7. The distributions of monthly averaged water temperature of southwest monsoon



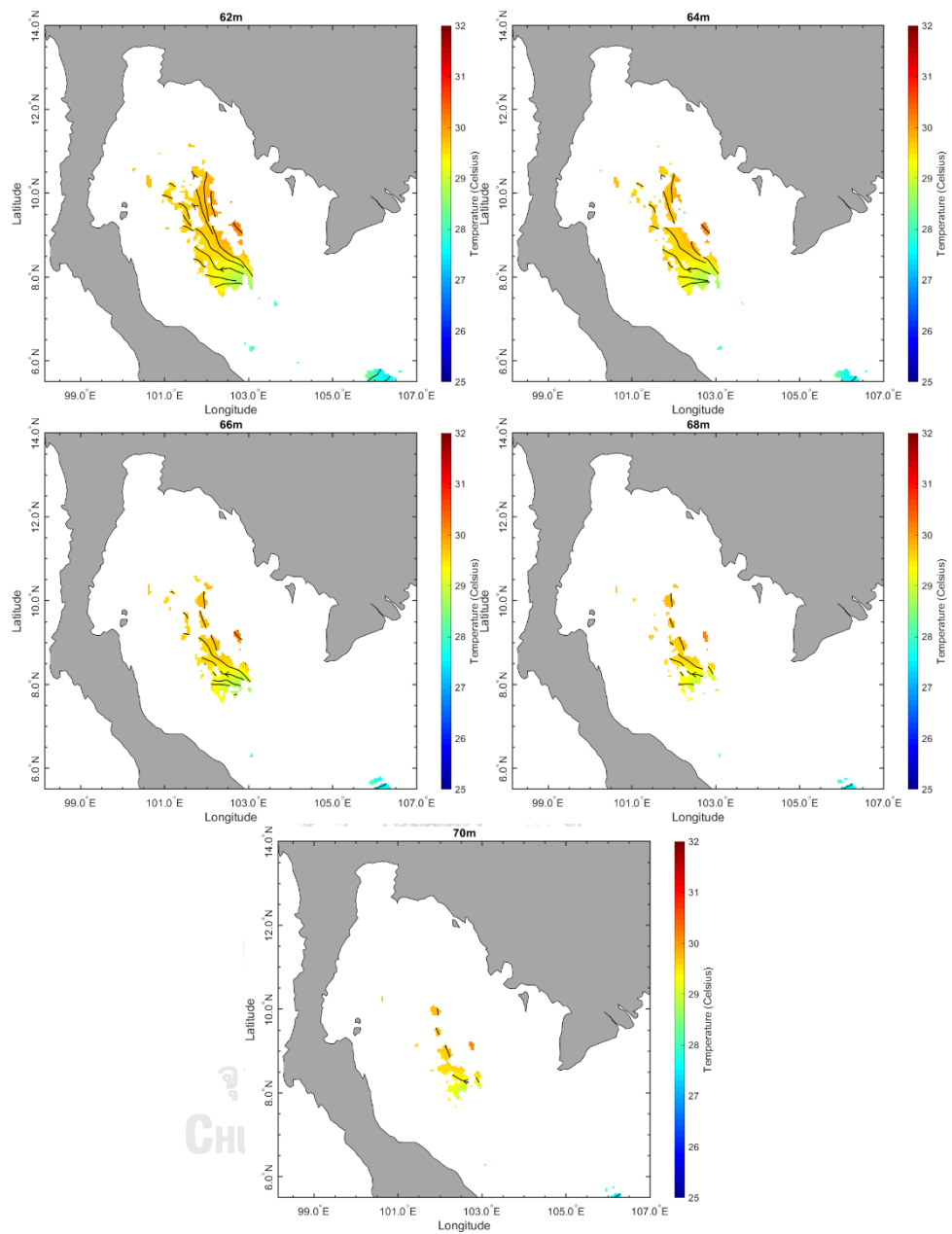






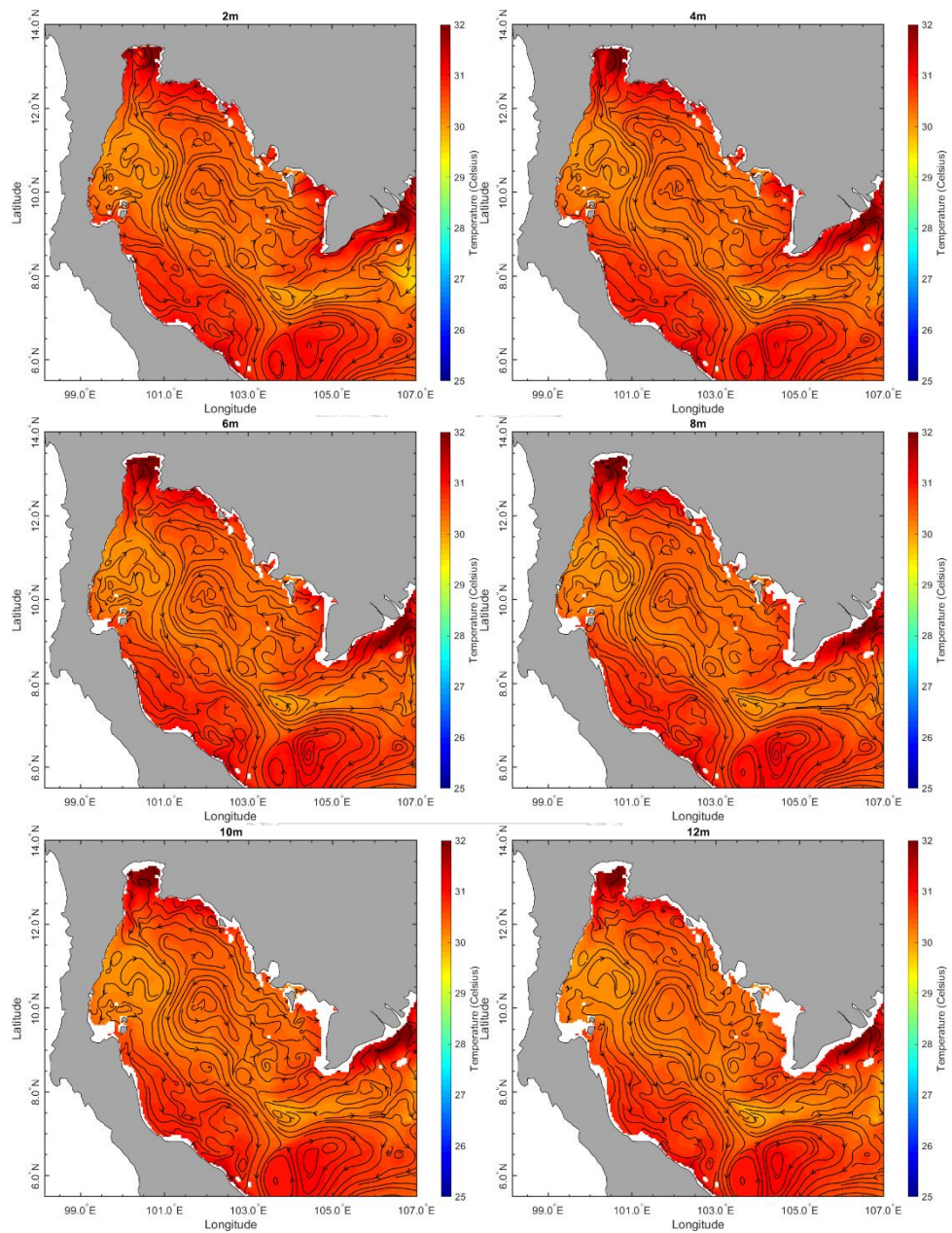


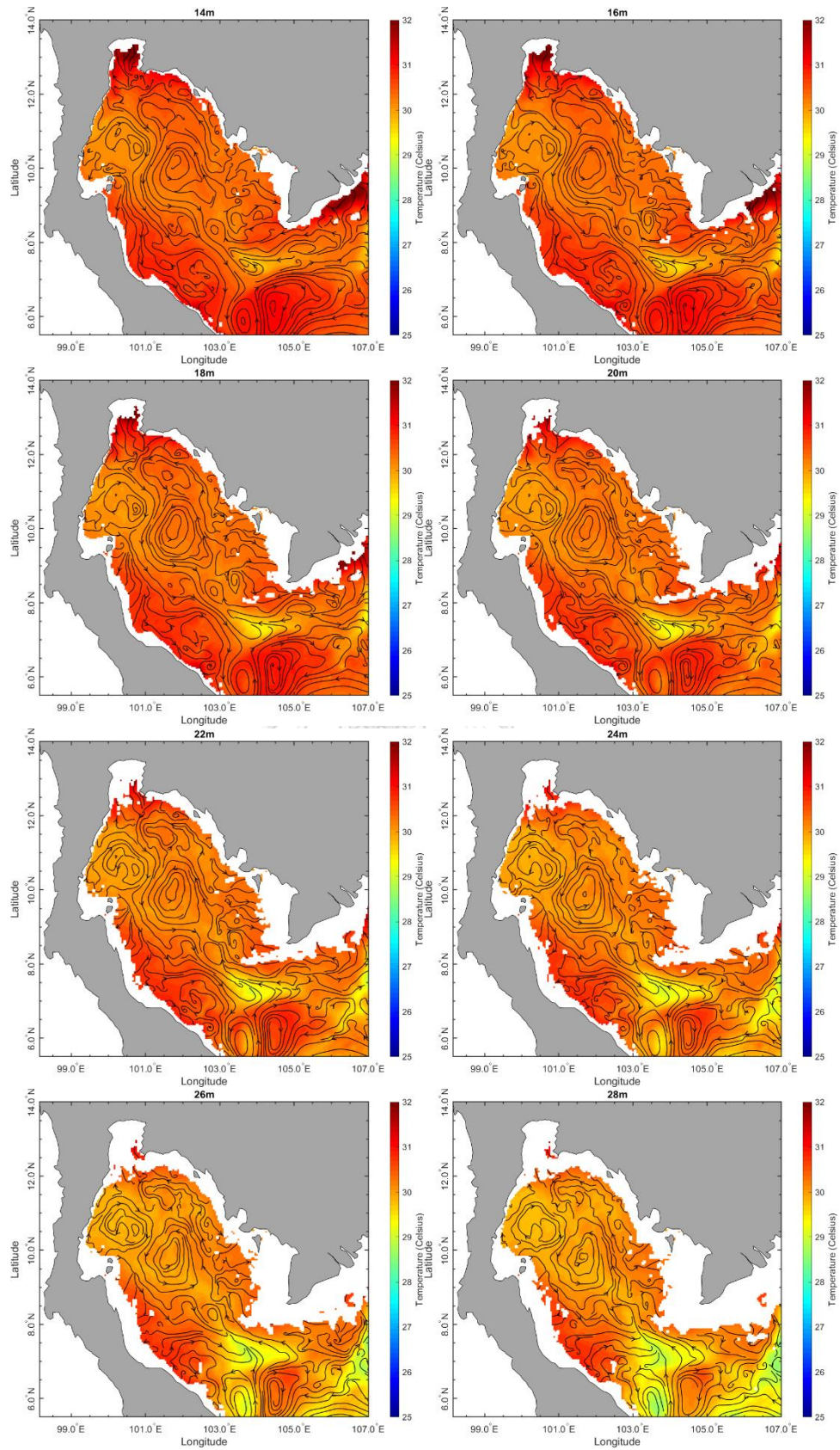




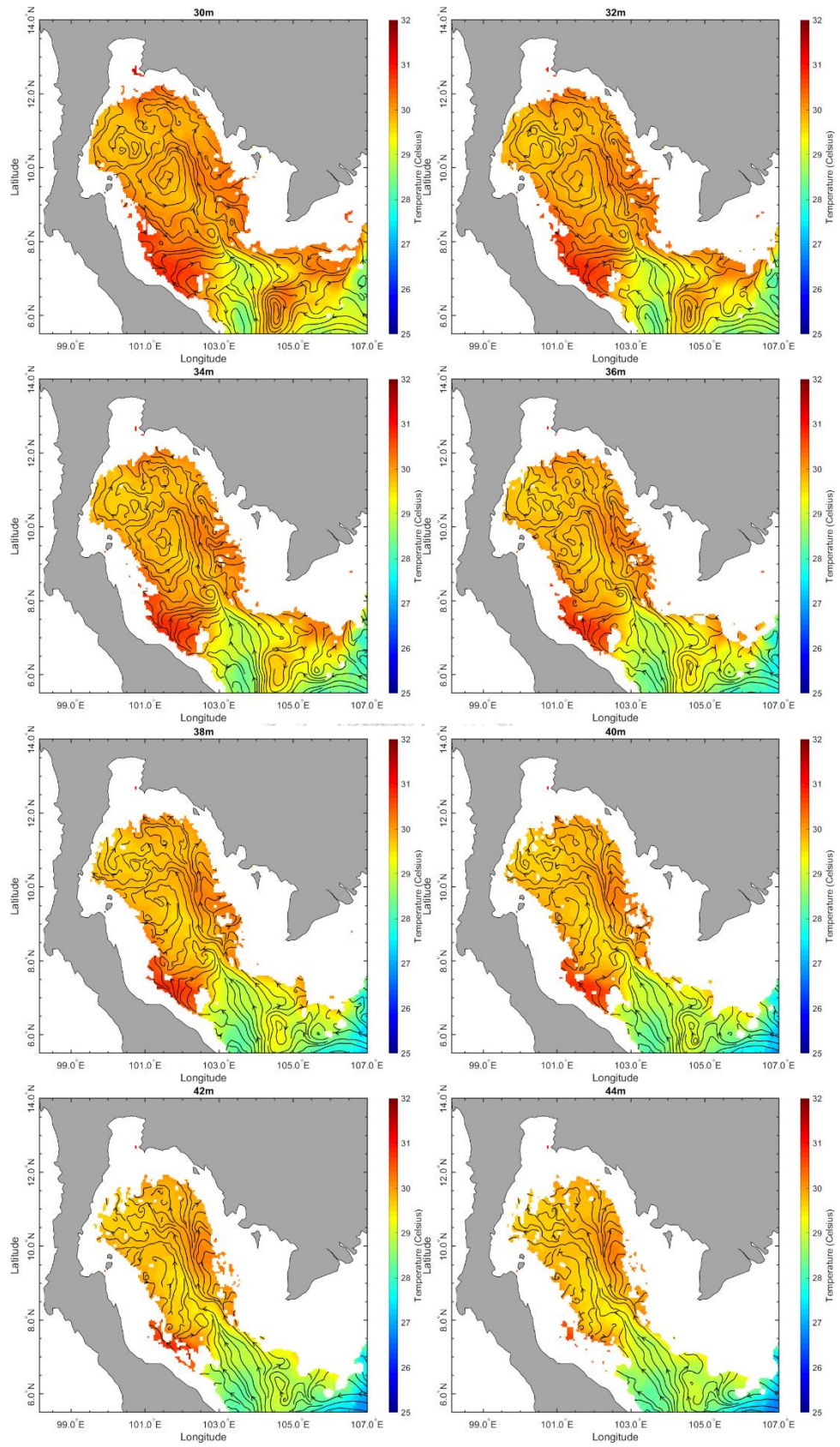
*Fig. B34. The distributions of monthly averaged water temperature of southwest monsoon in GoT at depths of 2-70 m.*

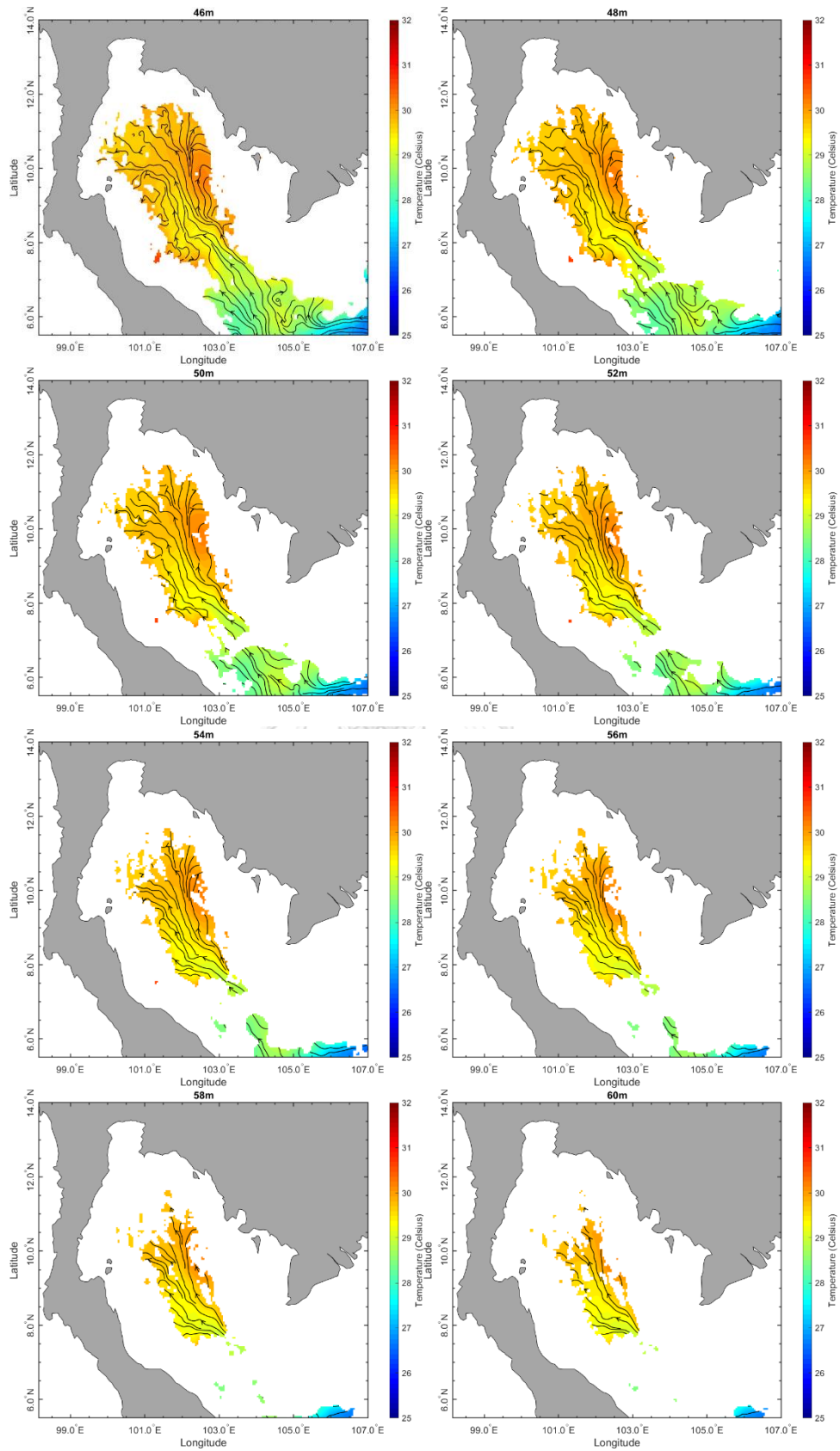
B8. The distributions of monthly averaged water temperature of 2<sup>nd</sup> inter-monsoon

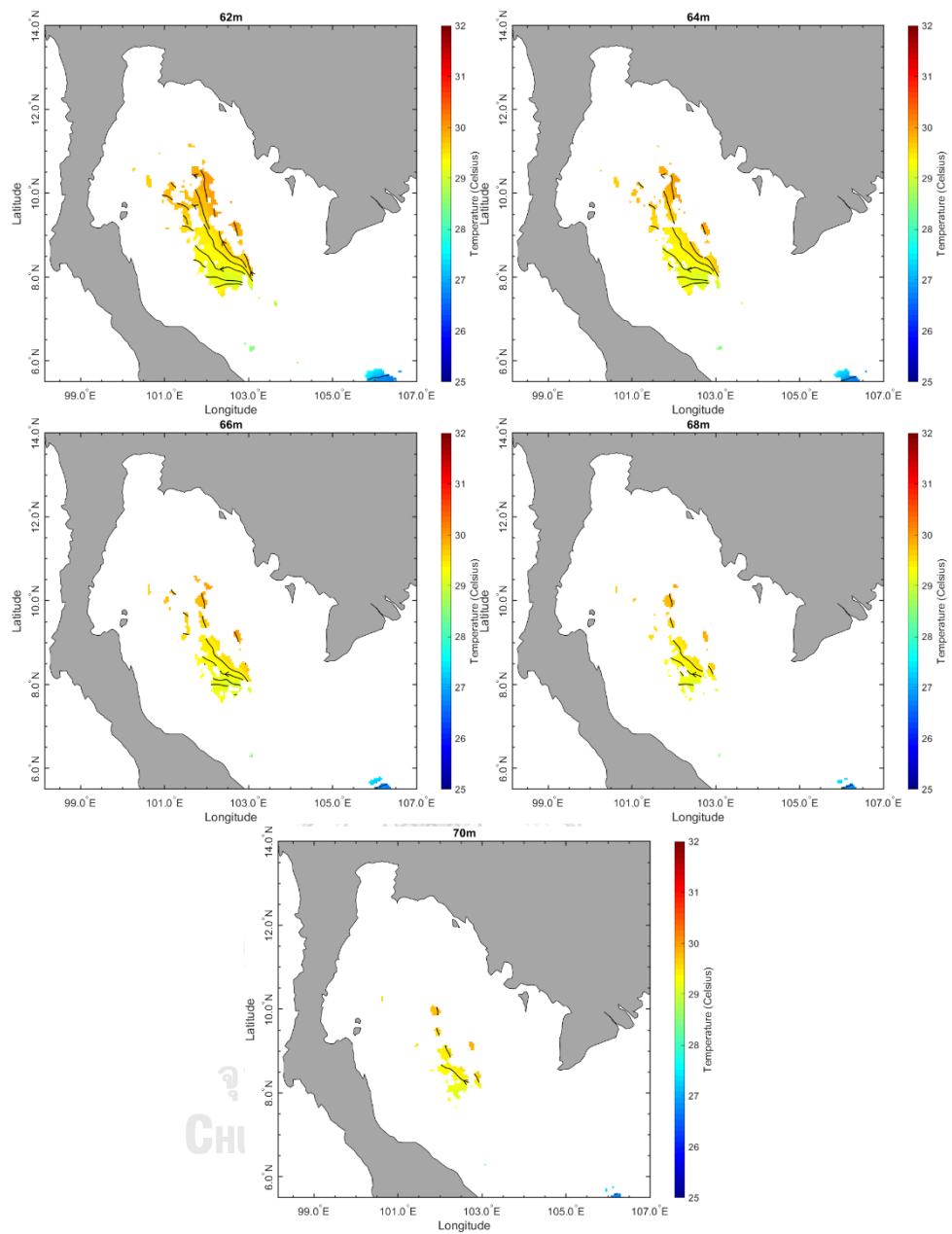








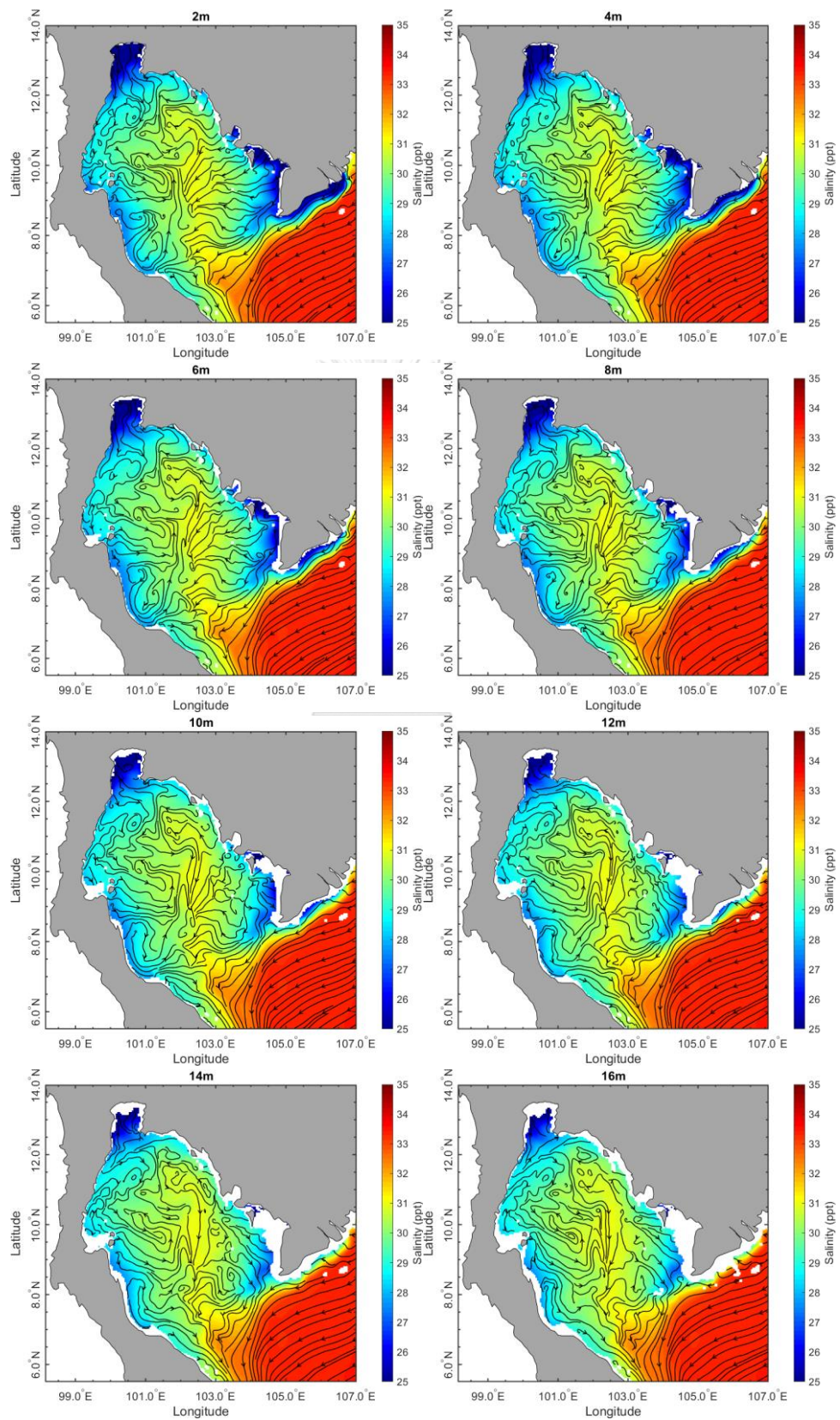


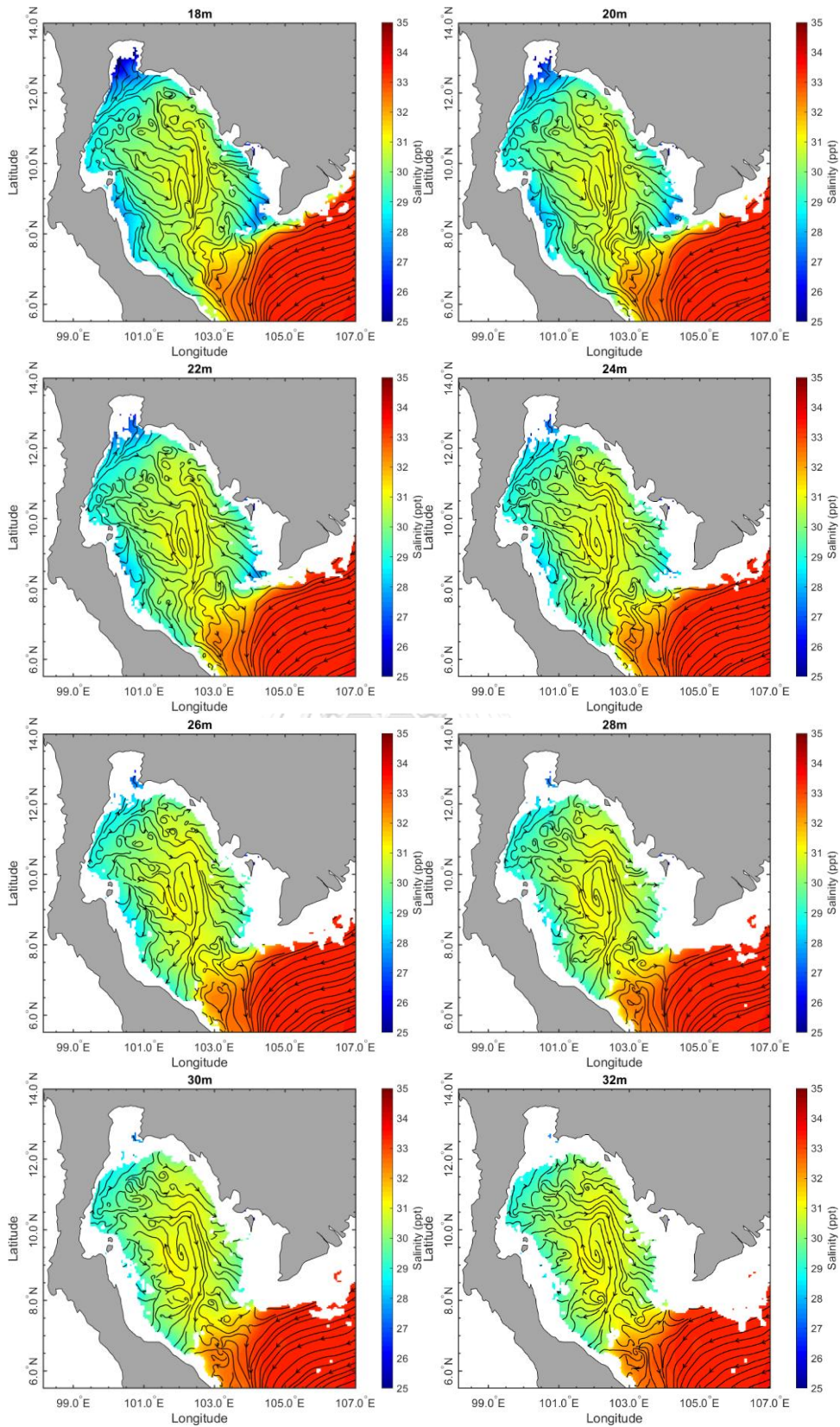


*Fig. B35. The distributions of monthly averaged water temperature of 2<sup>nd</sup> Inter-monsoon in GoT at depths of 2-70 m*

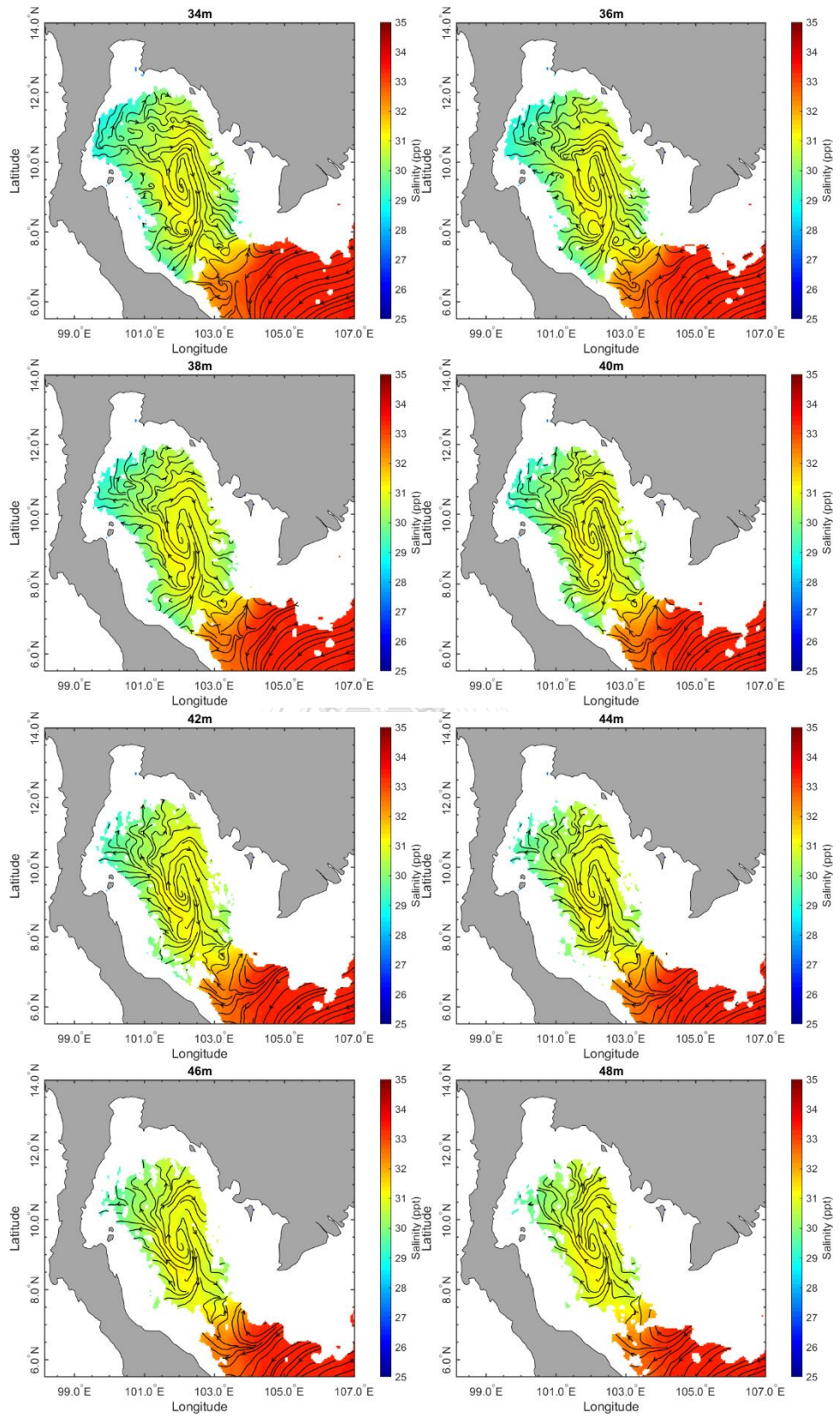


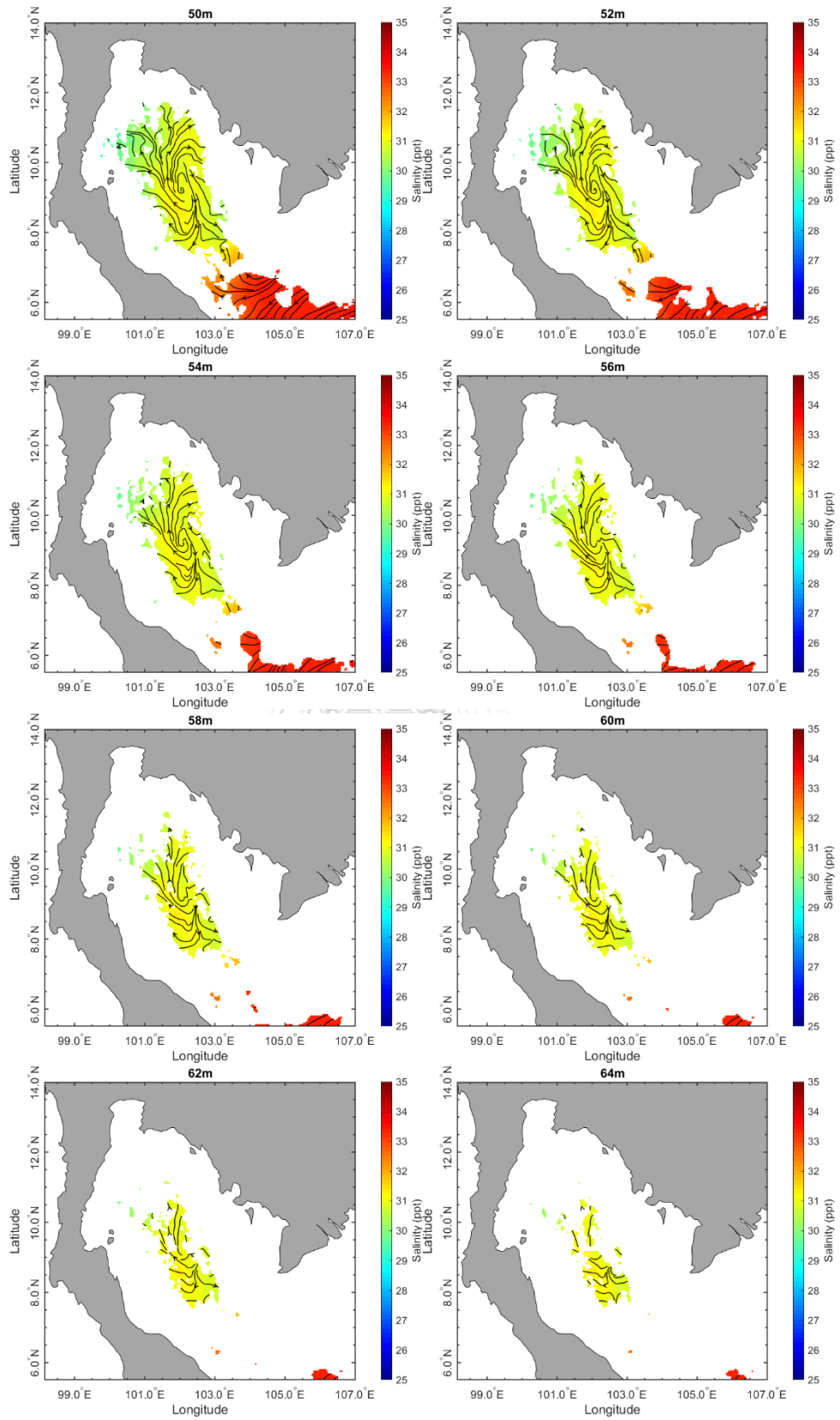
## B9. The distributions of monthly averaged salinity of northeast monsoon

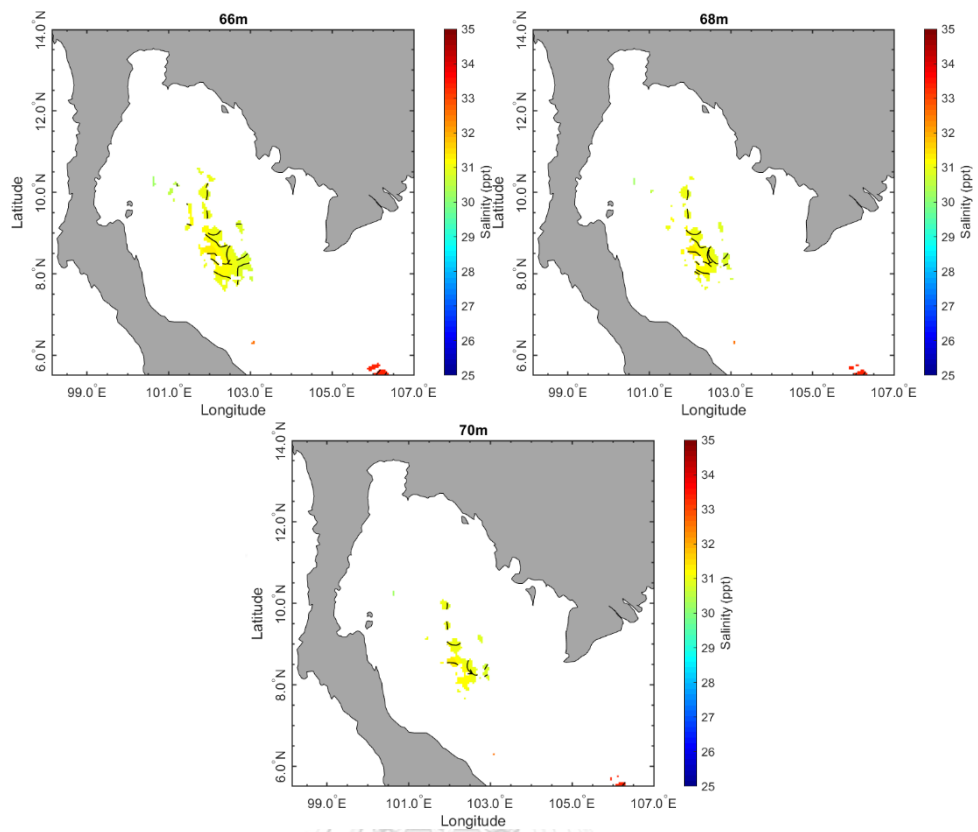




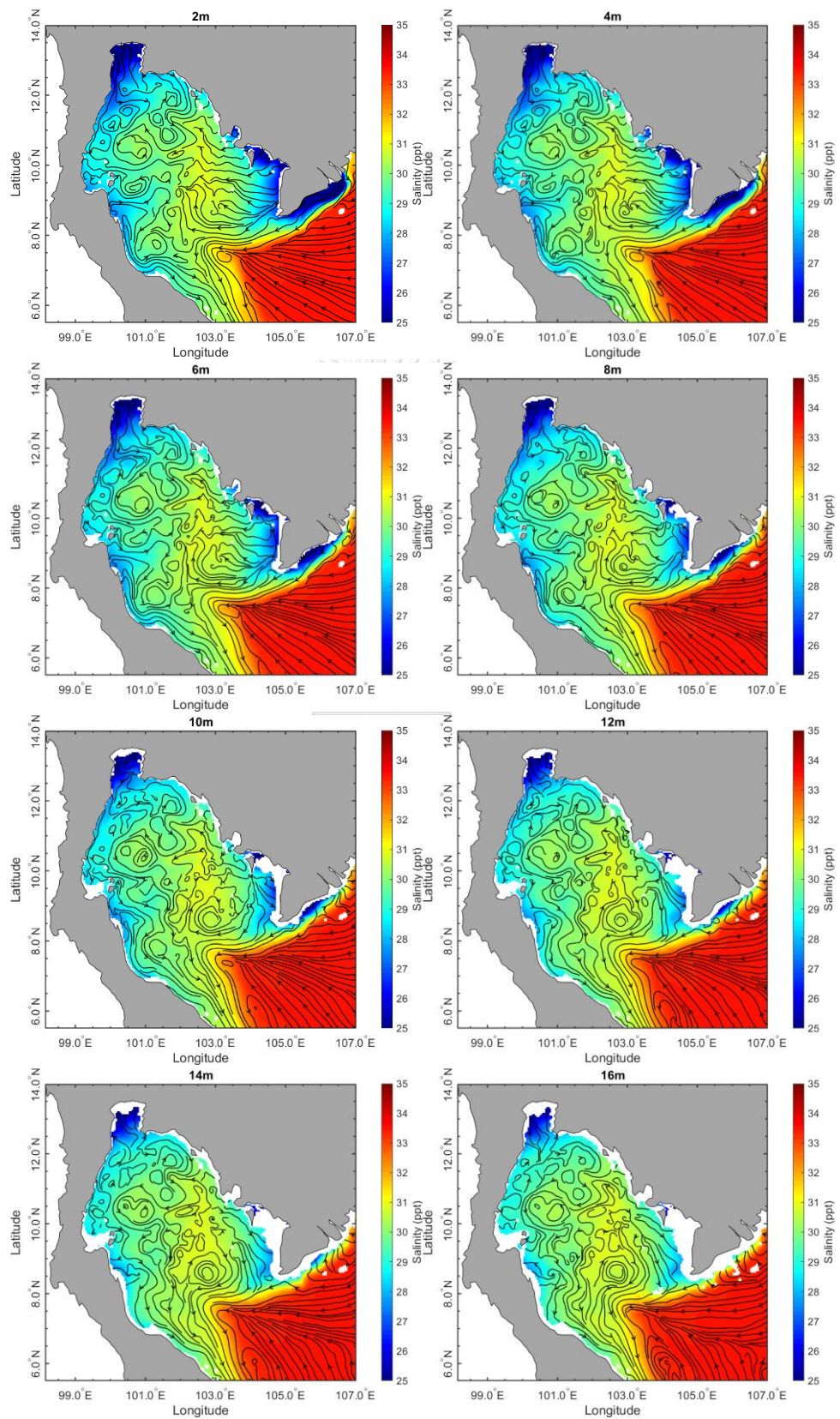




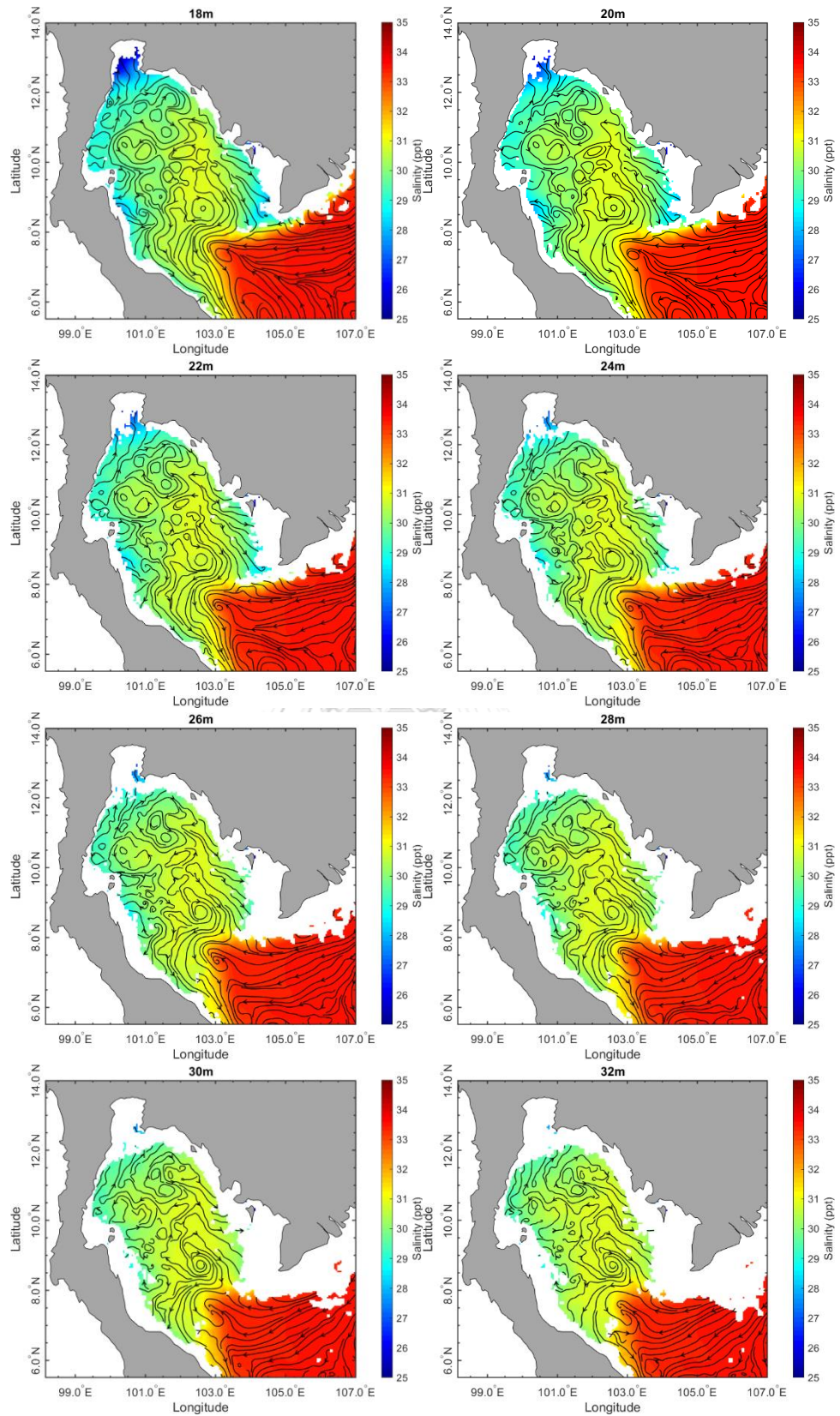


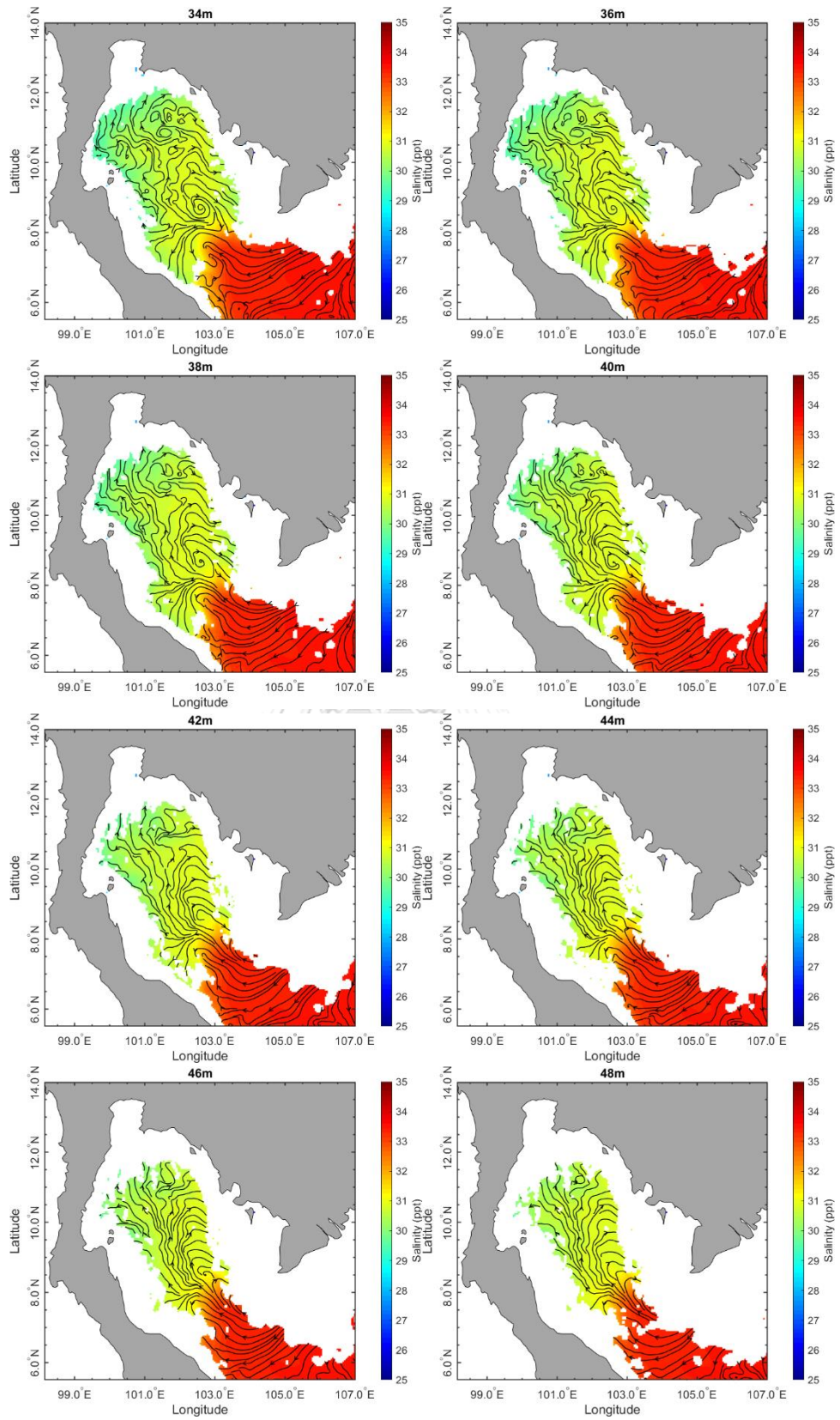


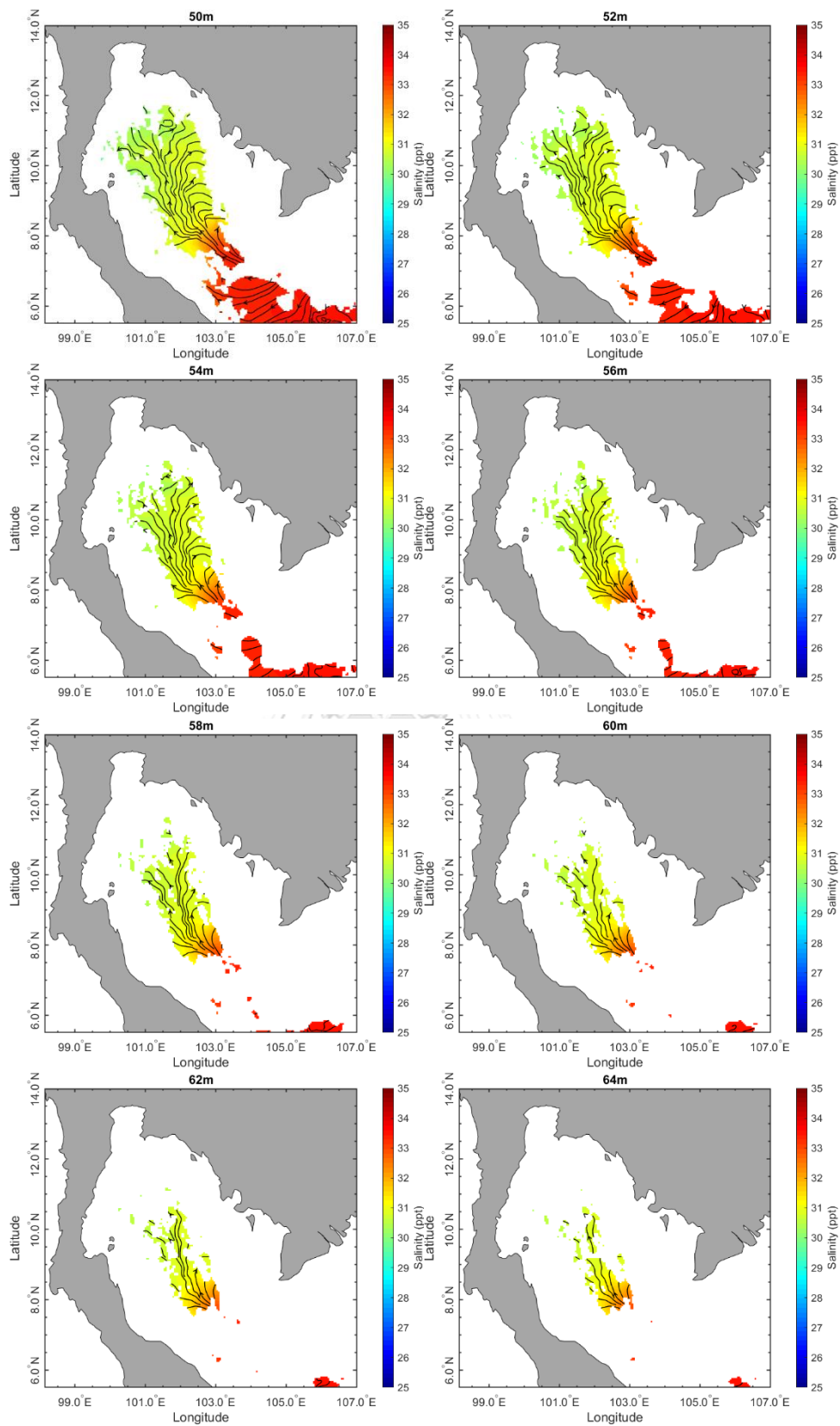
*Fig. B36. The distributions of monthly averaged salinity of Northeast monsoon in GoT at depths of 2-70 m*

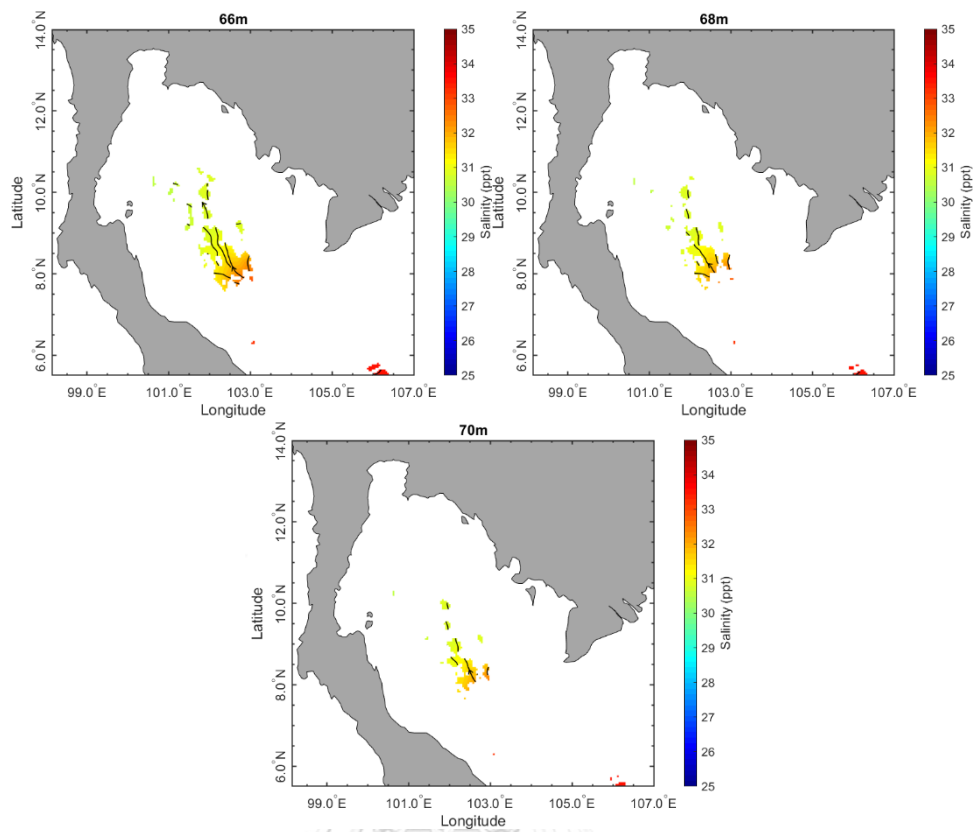
B10. The distributions of monthly averaged salinity of 1<sup>st</sup> inter-monsoon







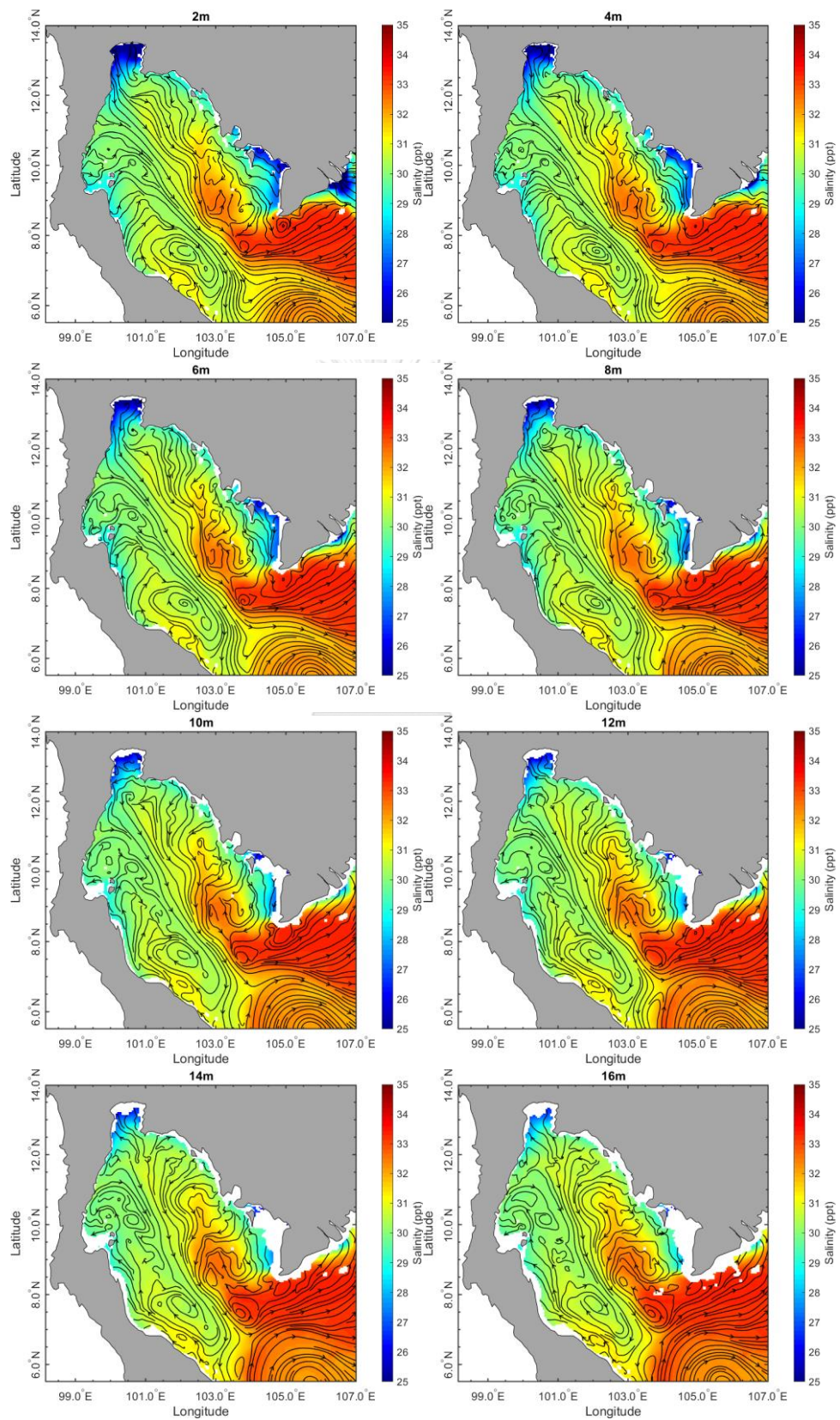


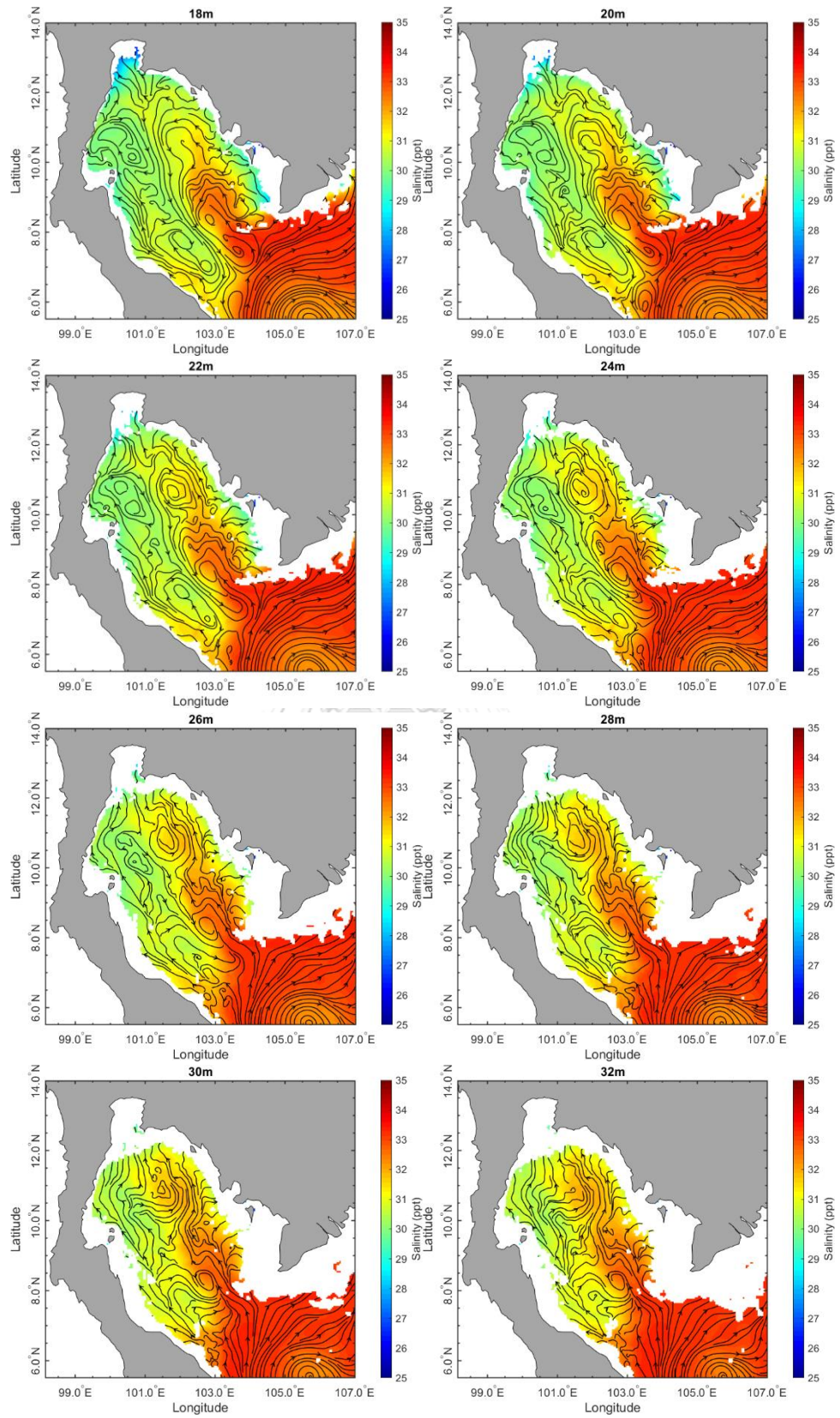


*Fig. B37. The distributions of monthly averaged salinity of 1<sup>st</sup> Intermonsoon in GoT at depths of 2-70 m*

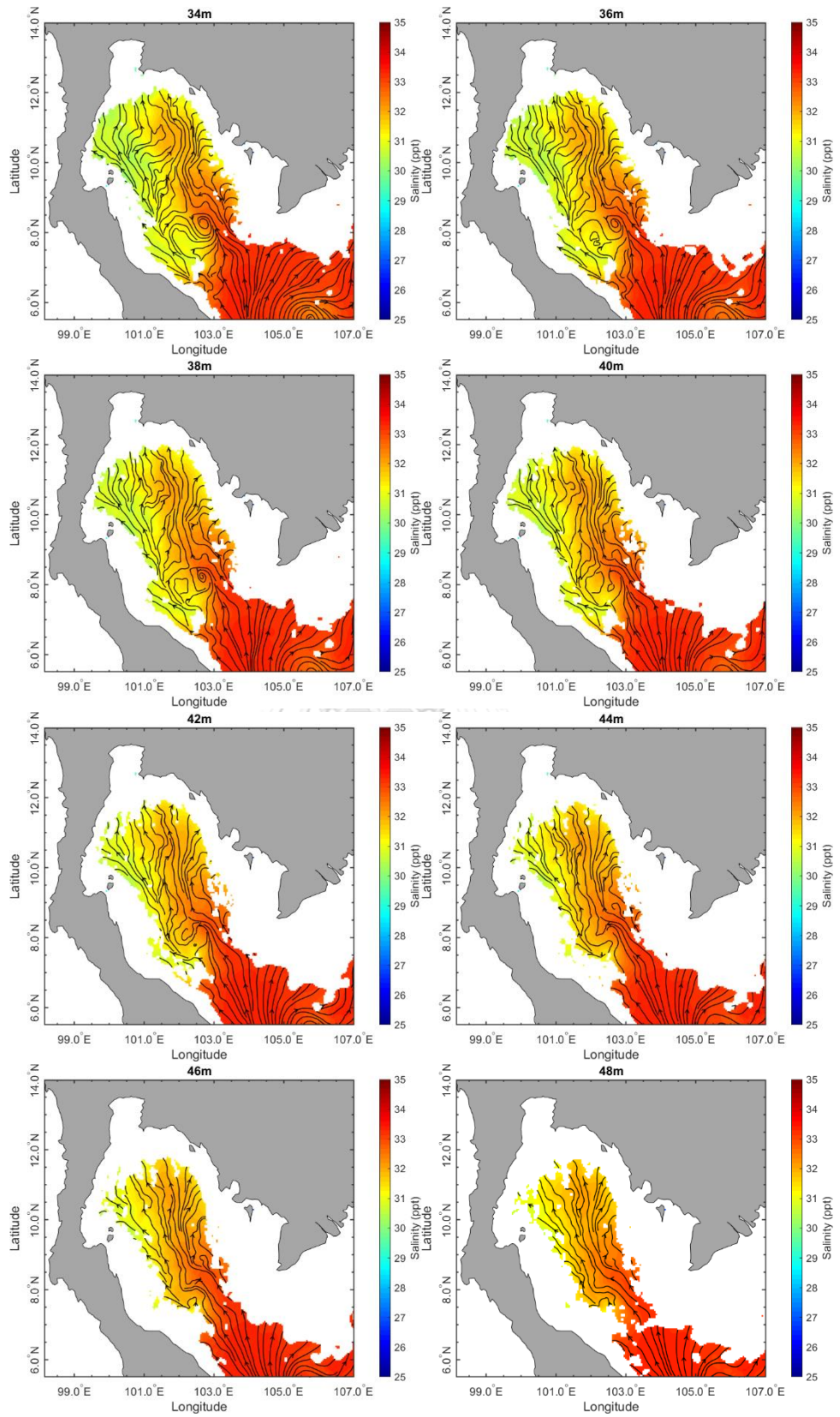


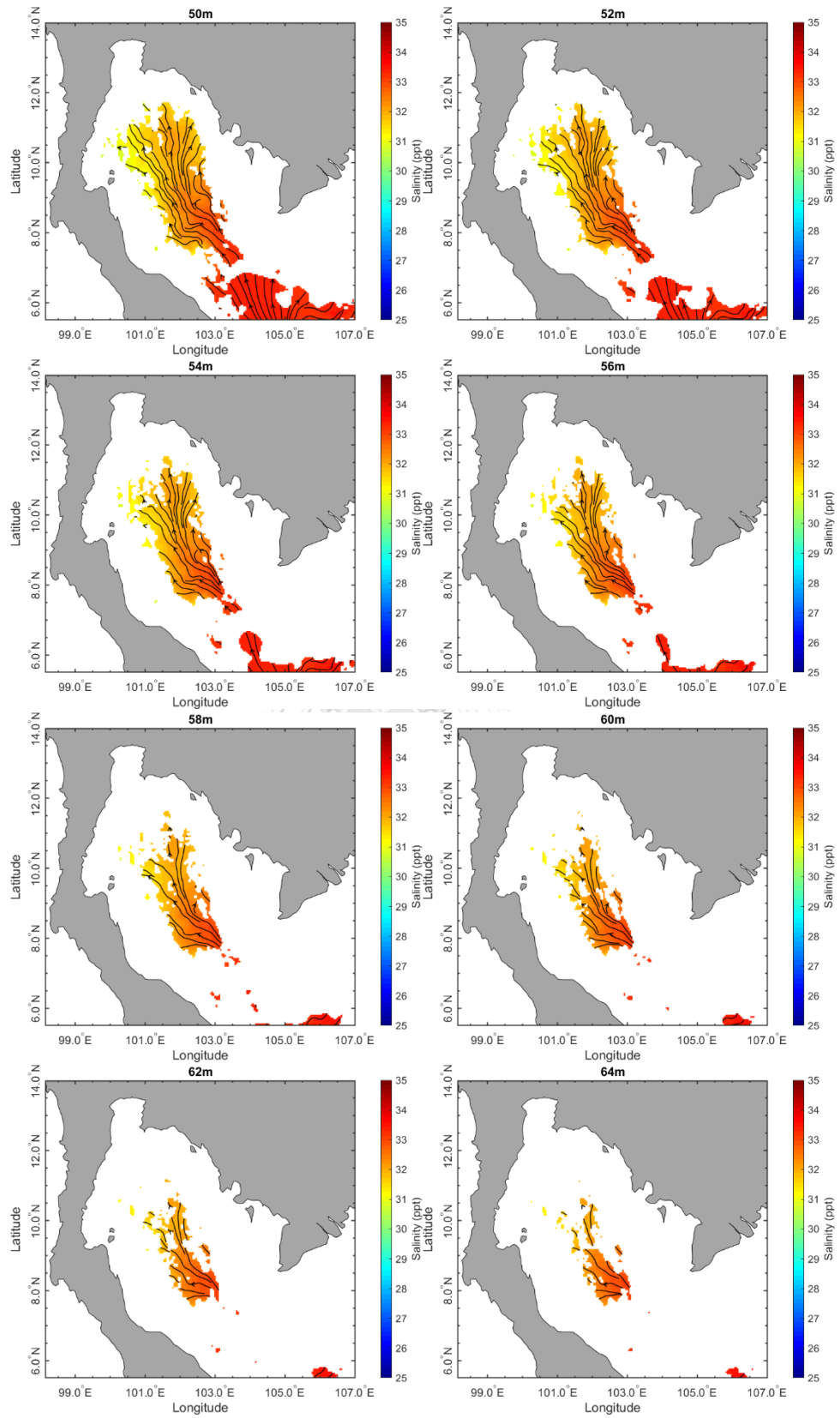
## B11. The distributions of monthly averaged salinity of southwest monsoon

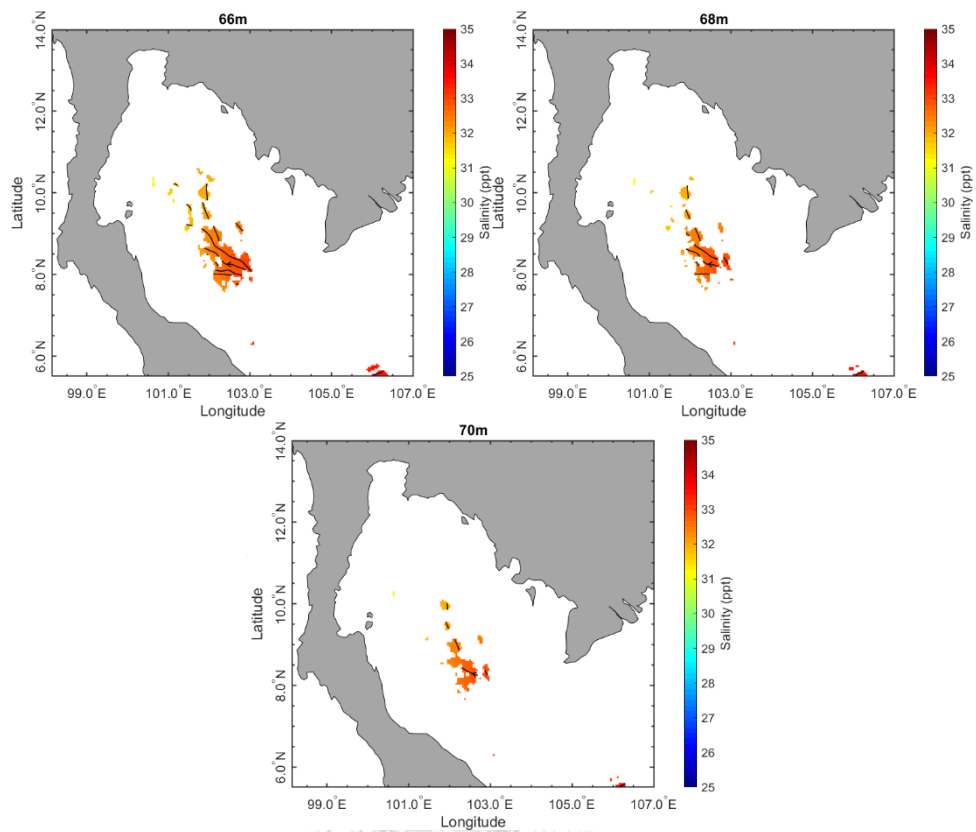




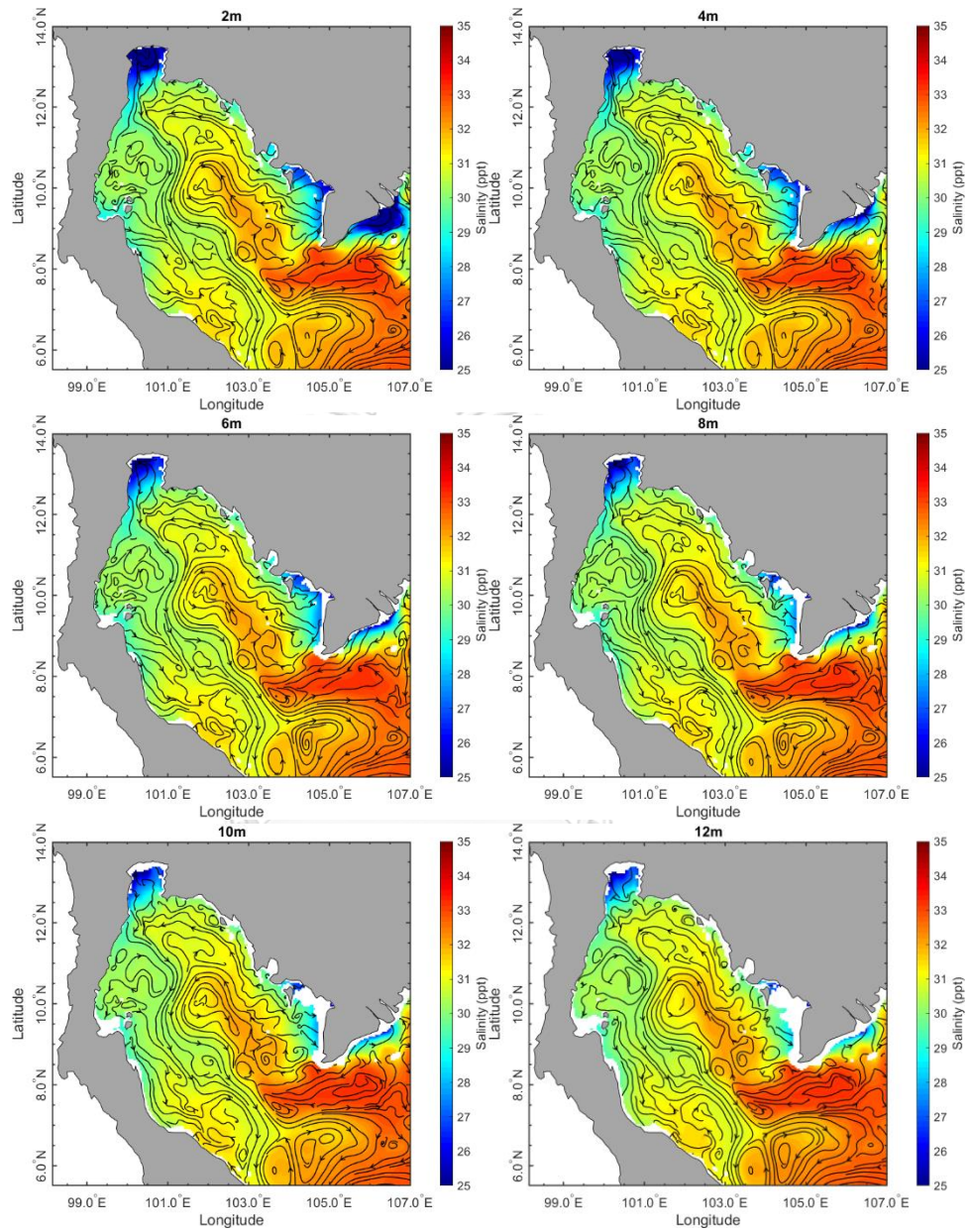




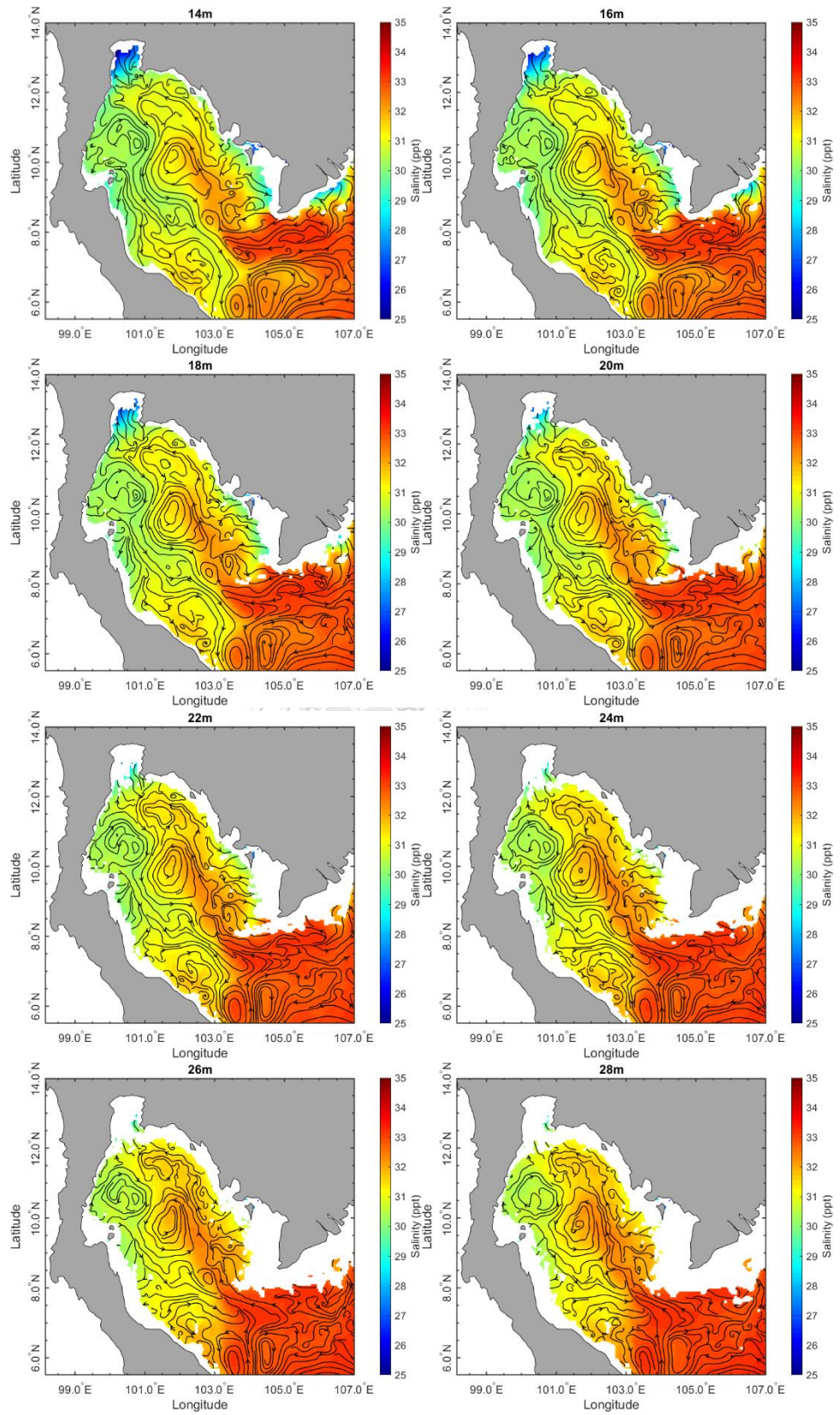




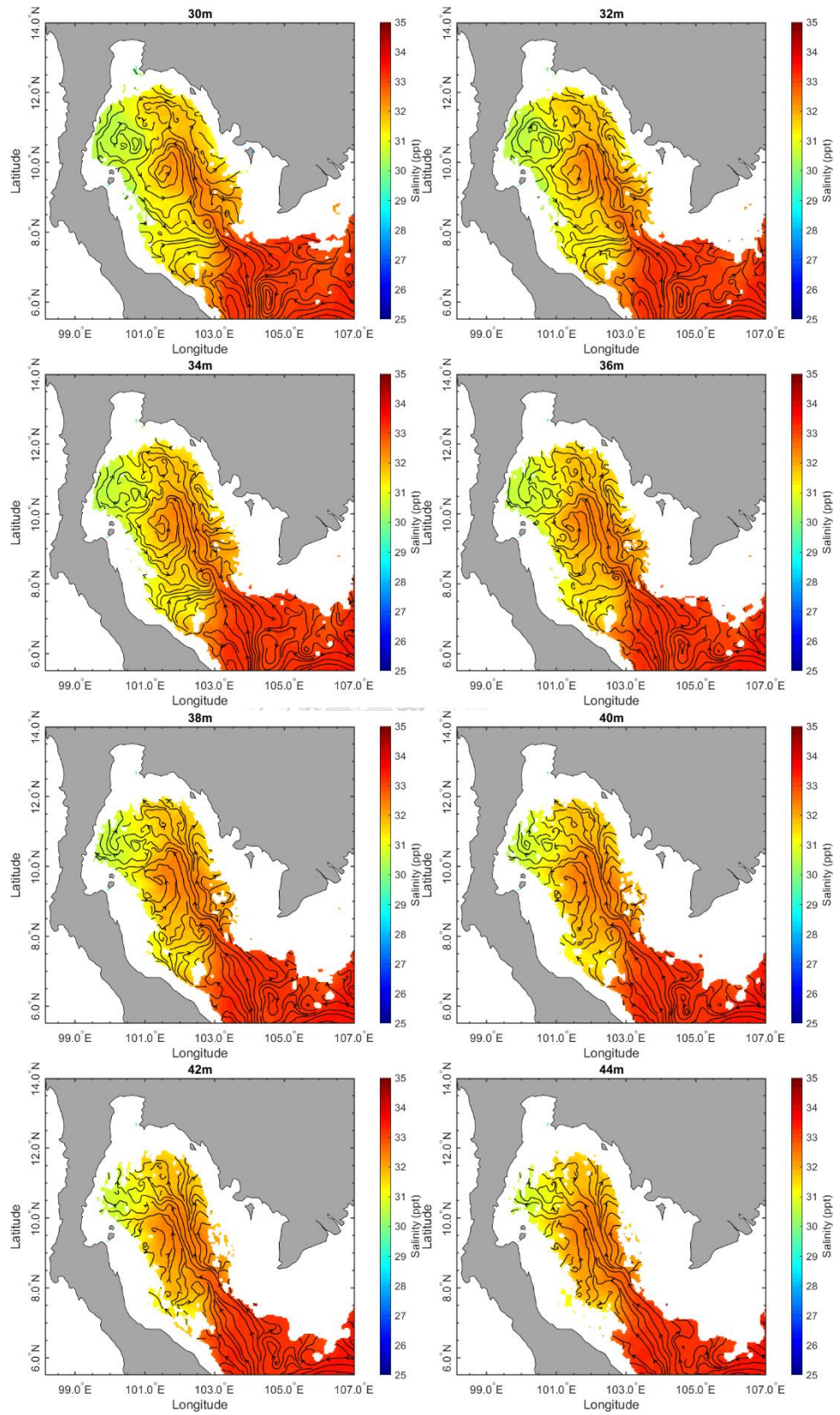
*Fig. B38. The distributions of monthly averaged salinity of southwest monsoon in GoT at depths of 2-70 m*

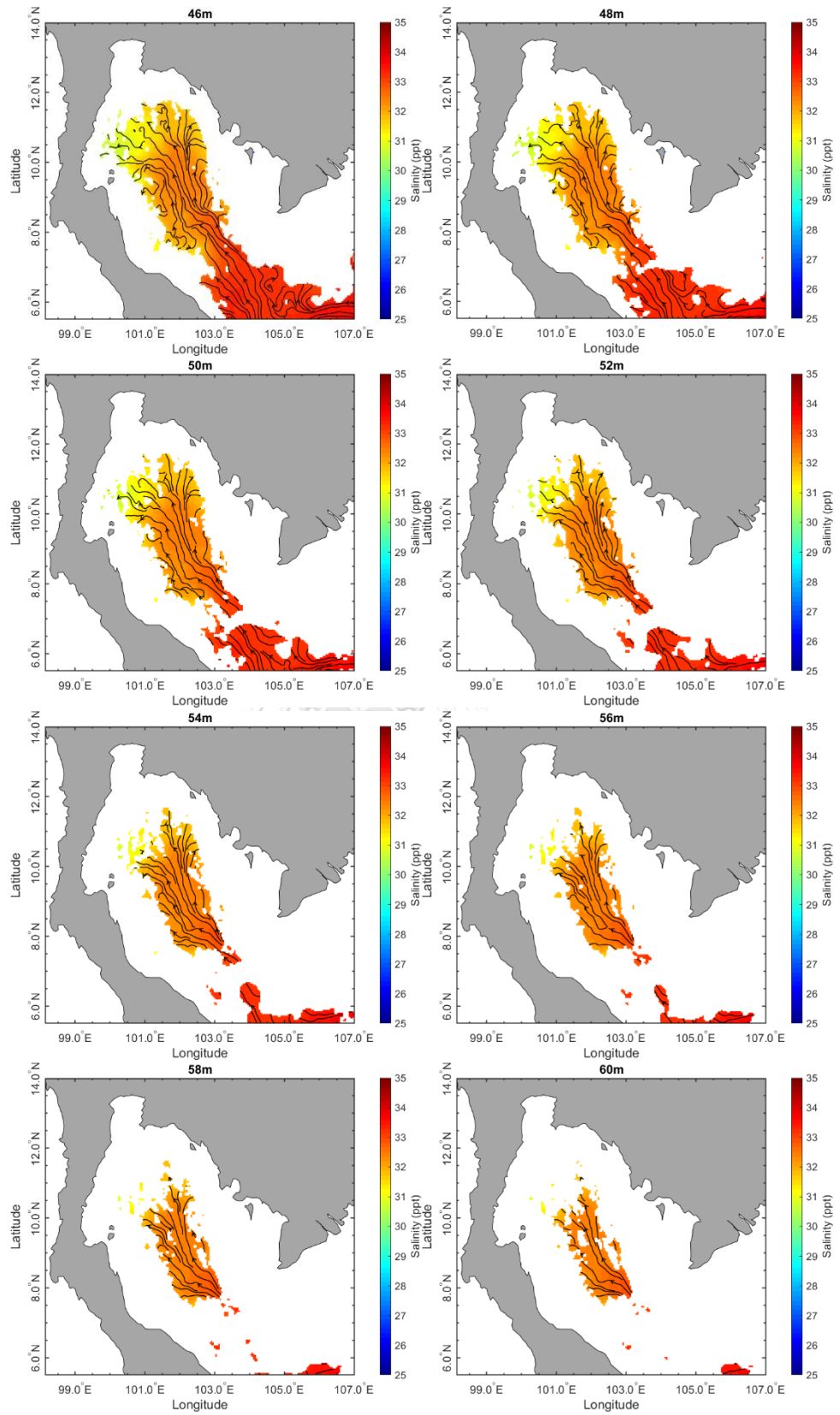
B12. The distributions of monthly averaged salinity of 2<sup>nd</sup> inter-monsoon











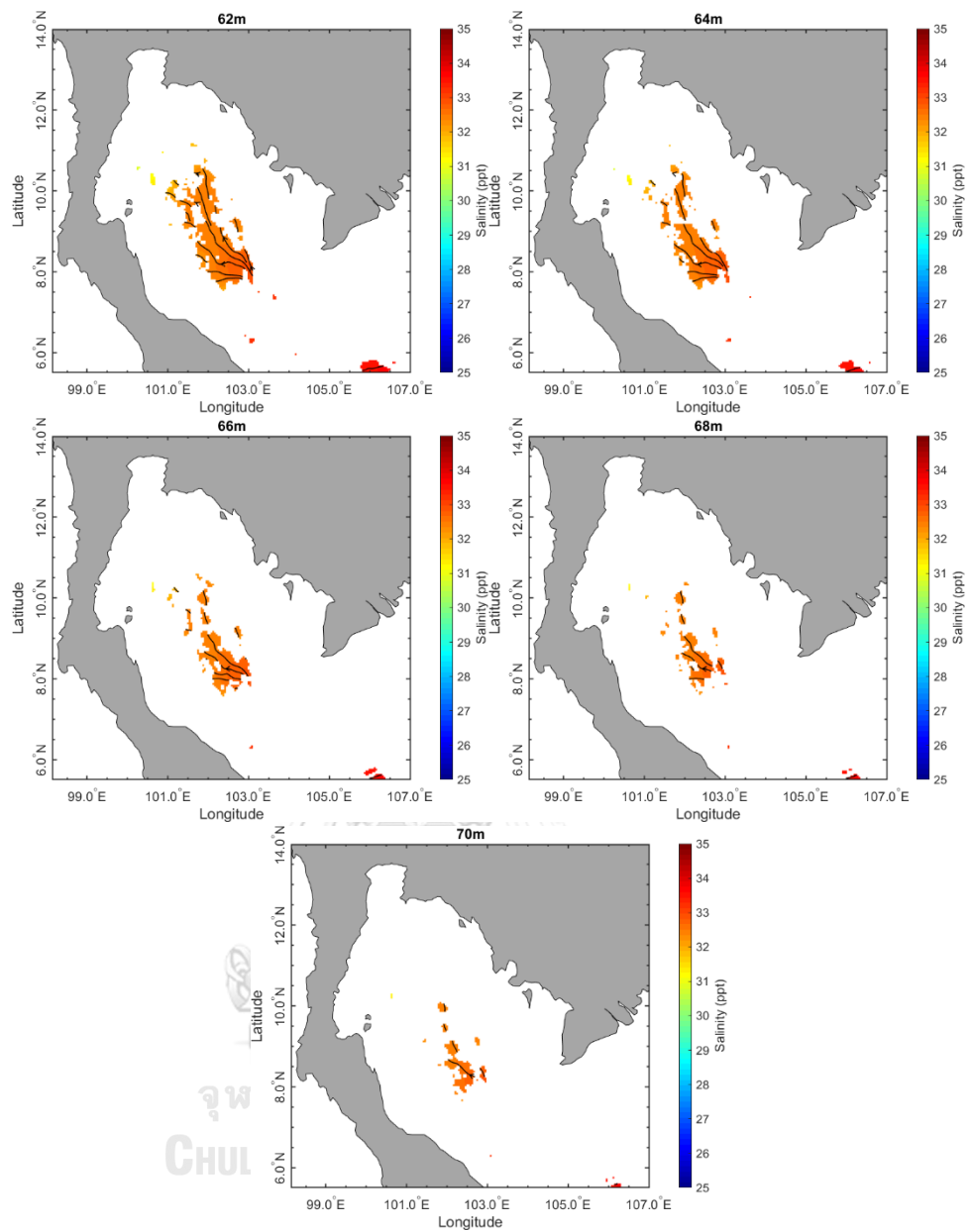
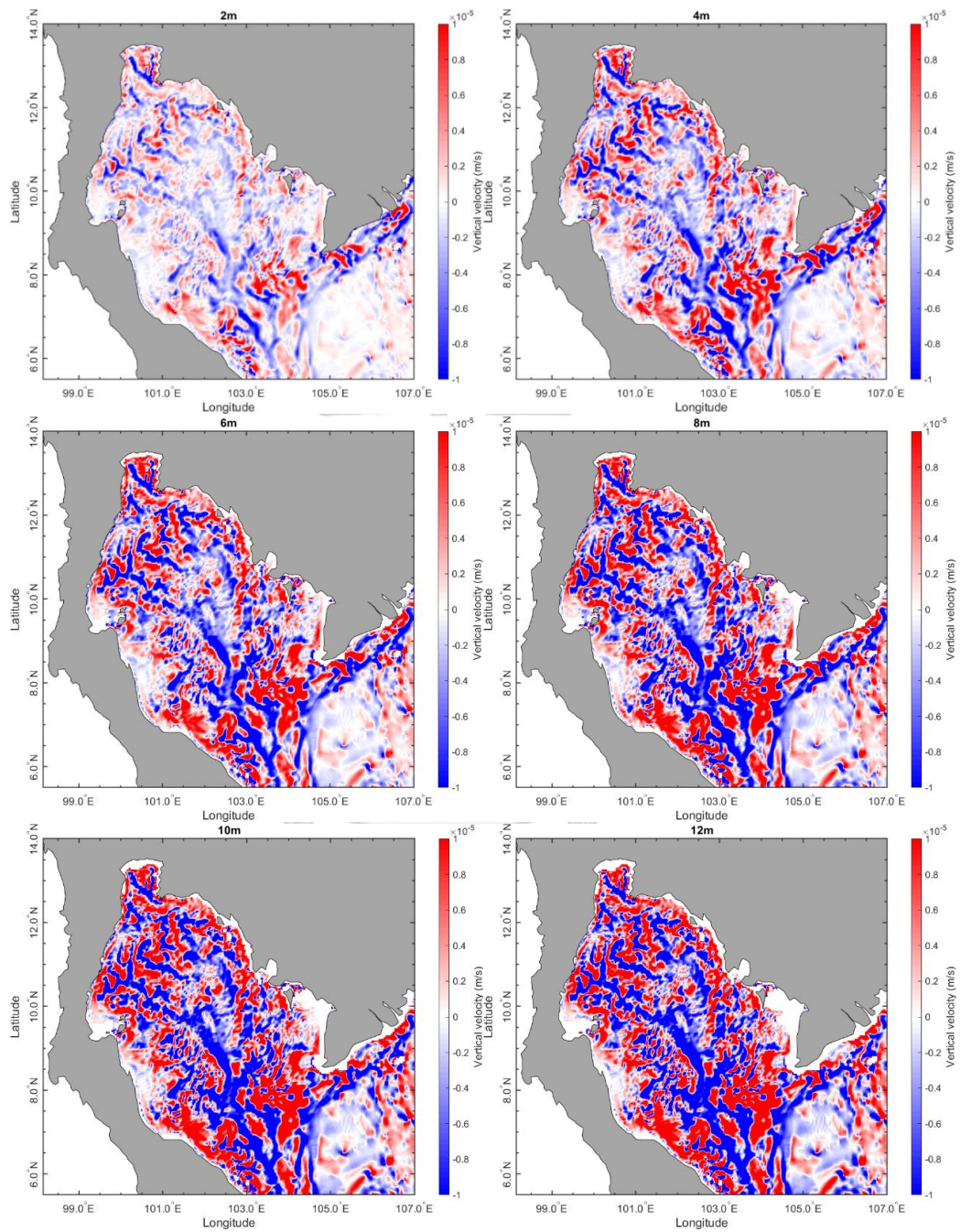
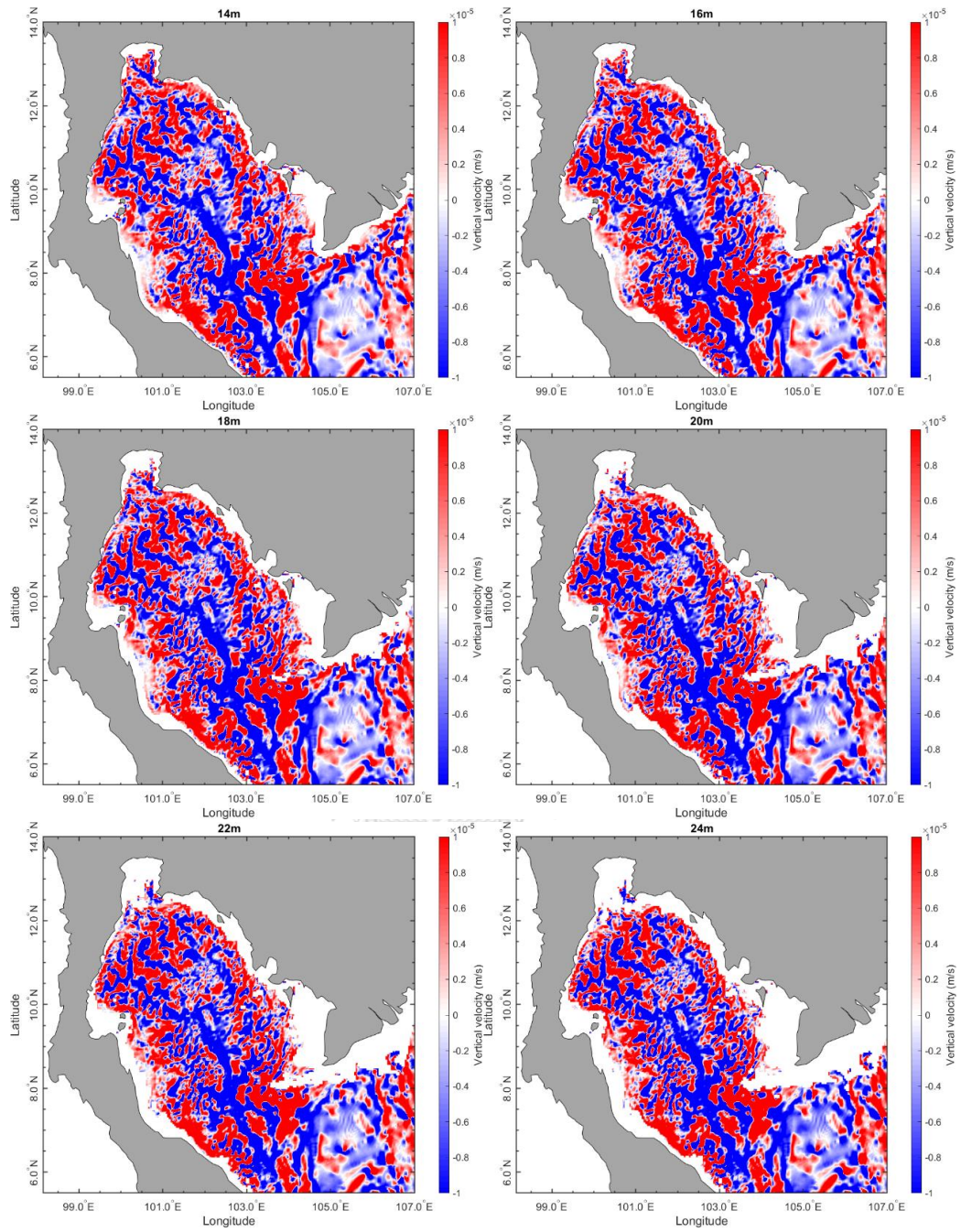


Fig. B39. The distributions of monthly averaged salinity of 1<sup>st</sup> Intermonsoon in GoT at depths of 2-70 m.

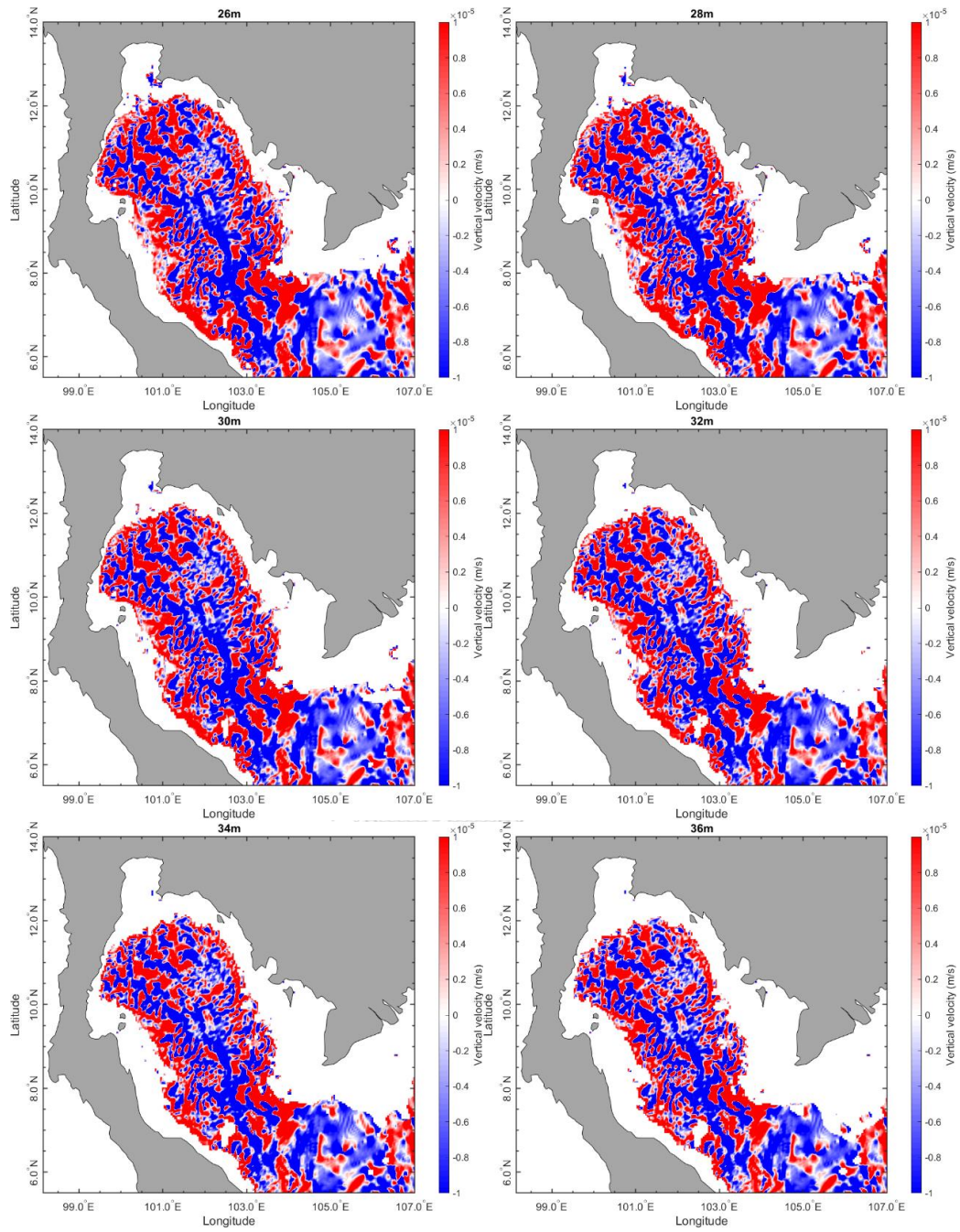
B13. The distributions of monthly averaged vertical velocity of northeast monsoon

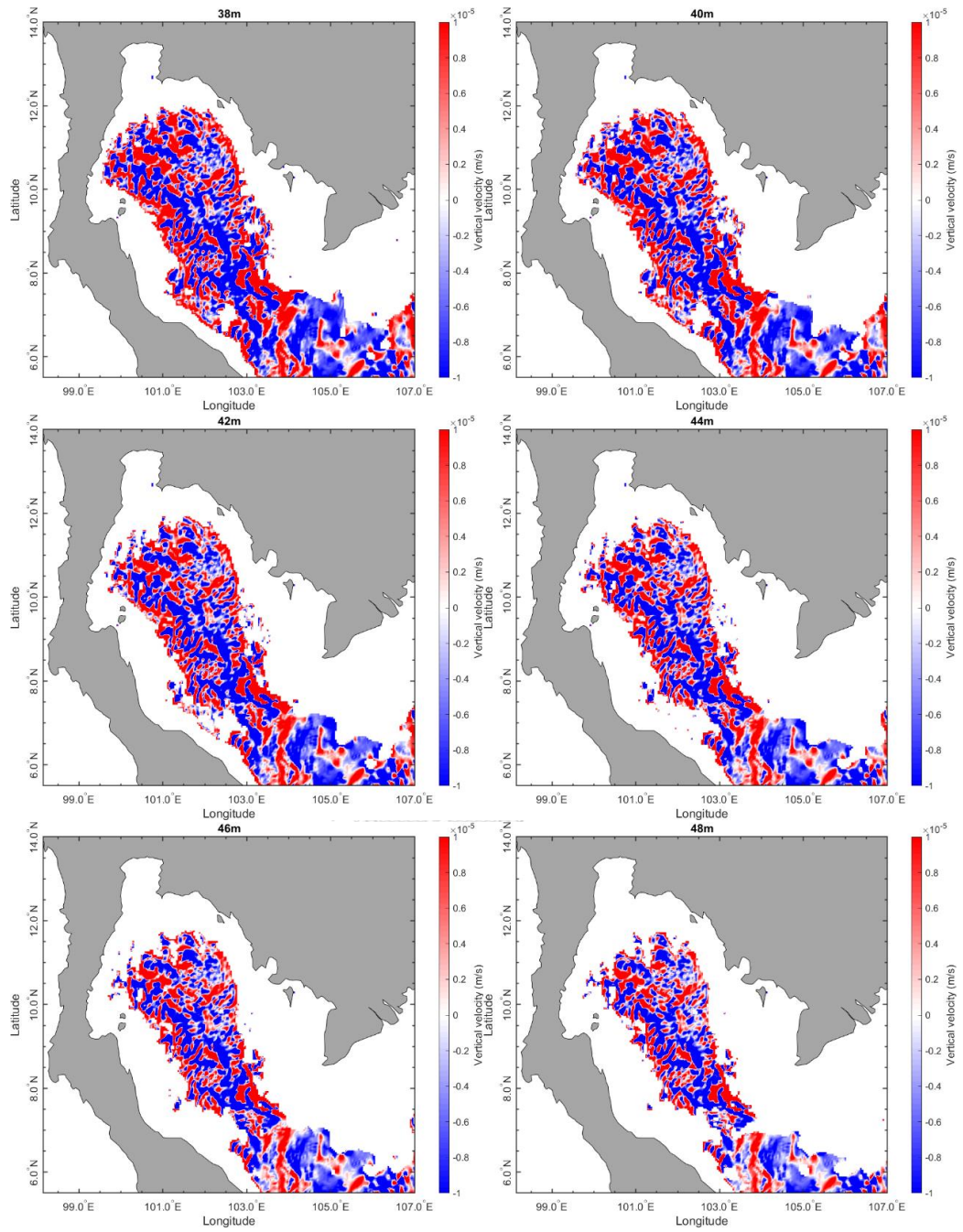


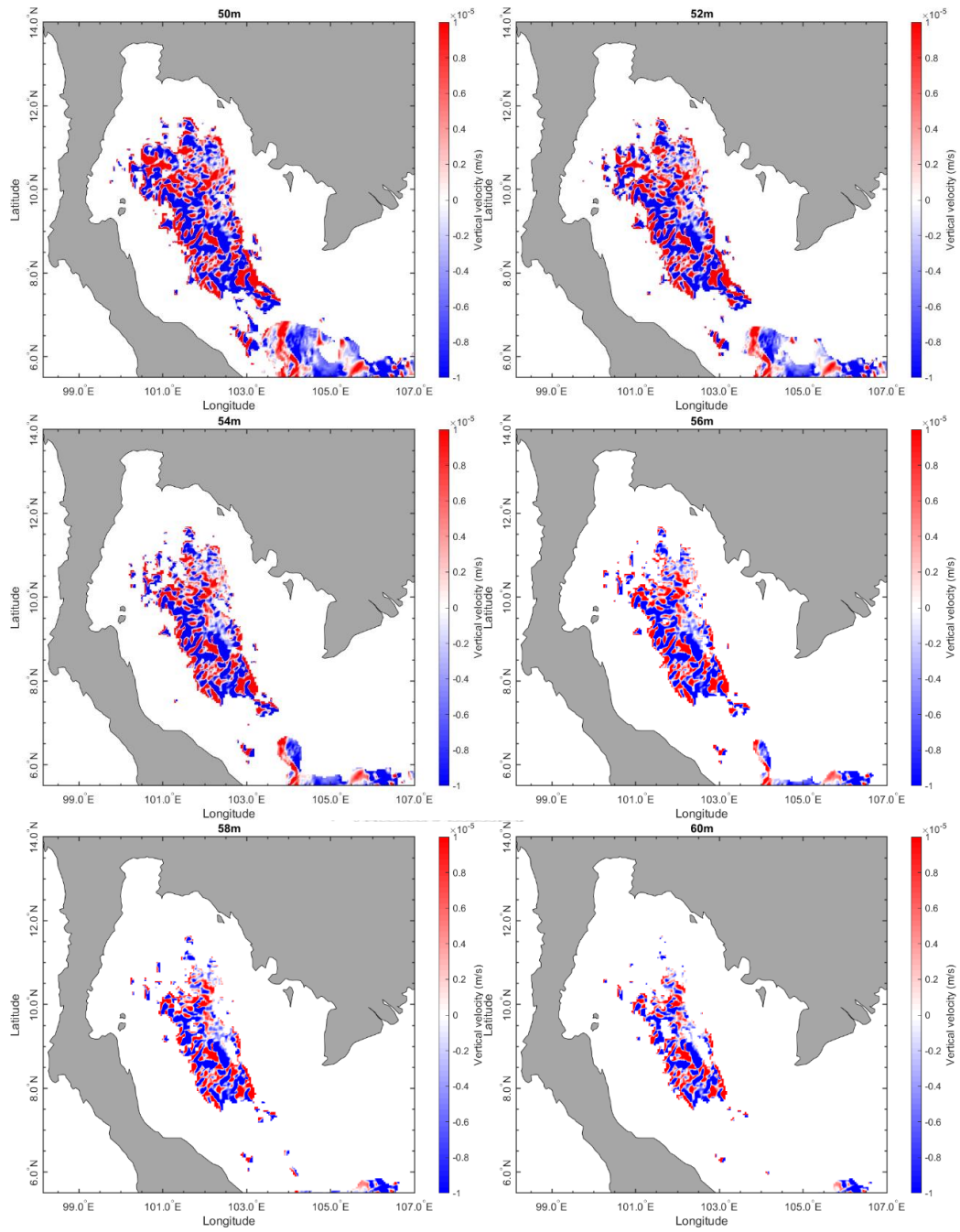


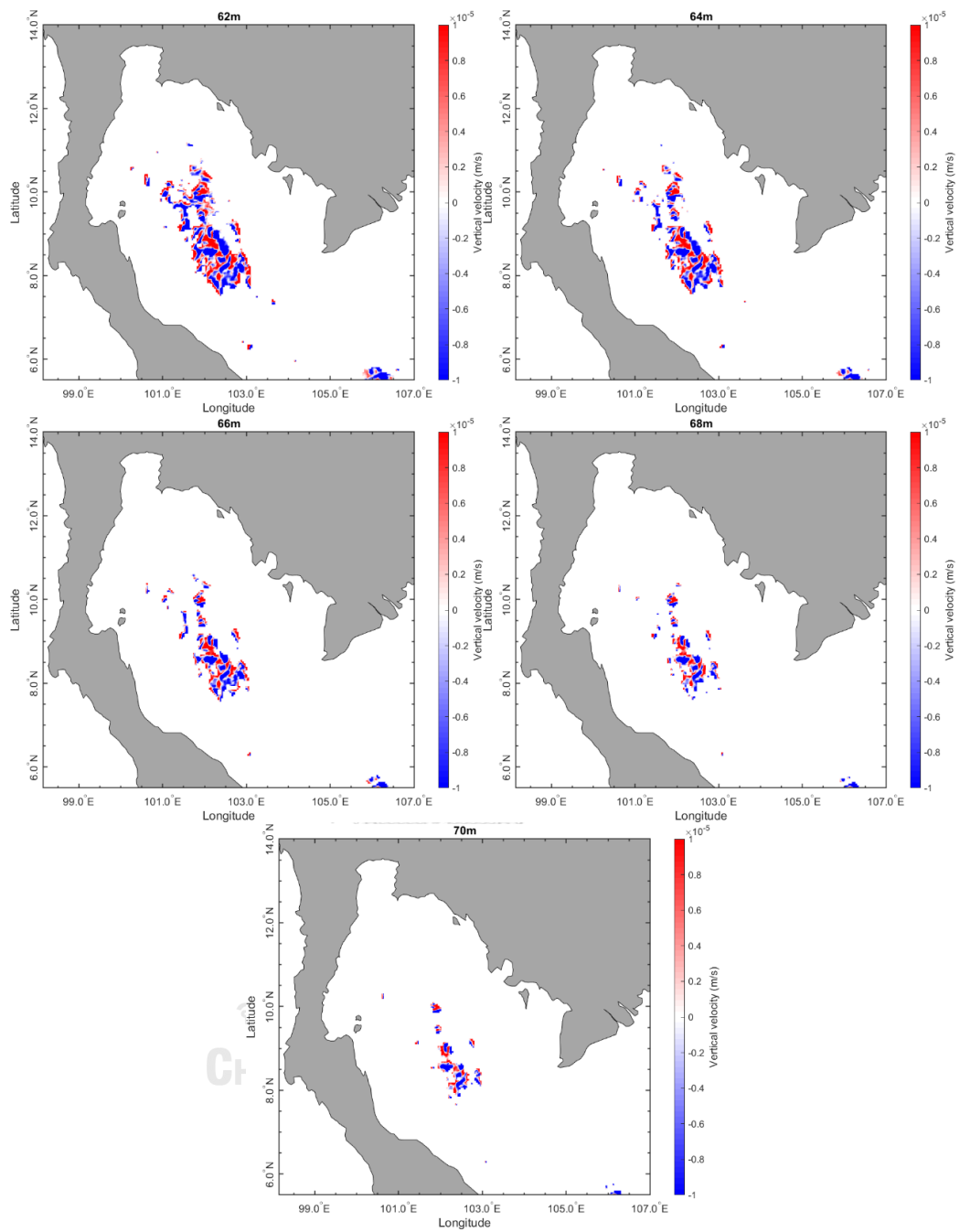








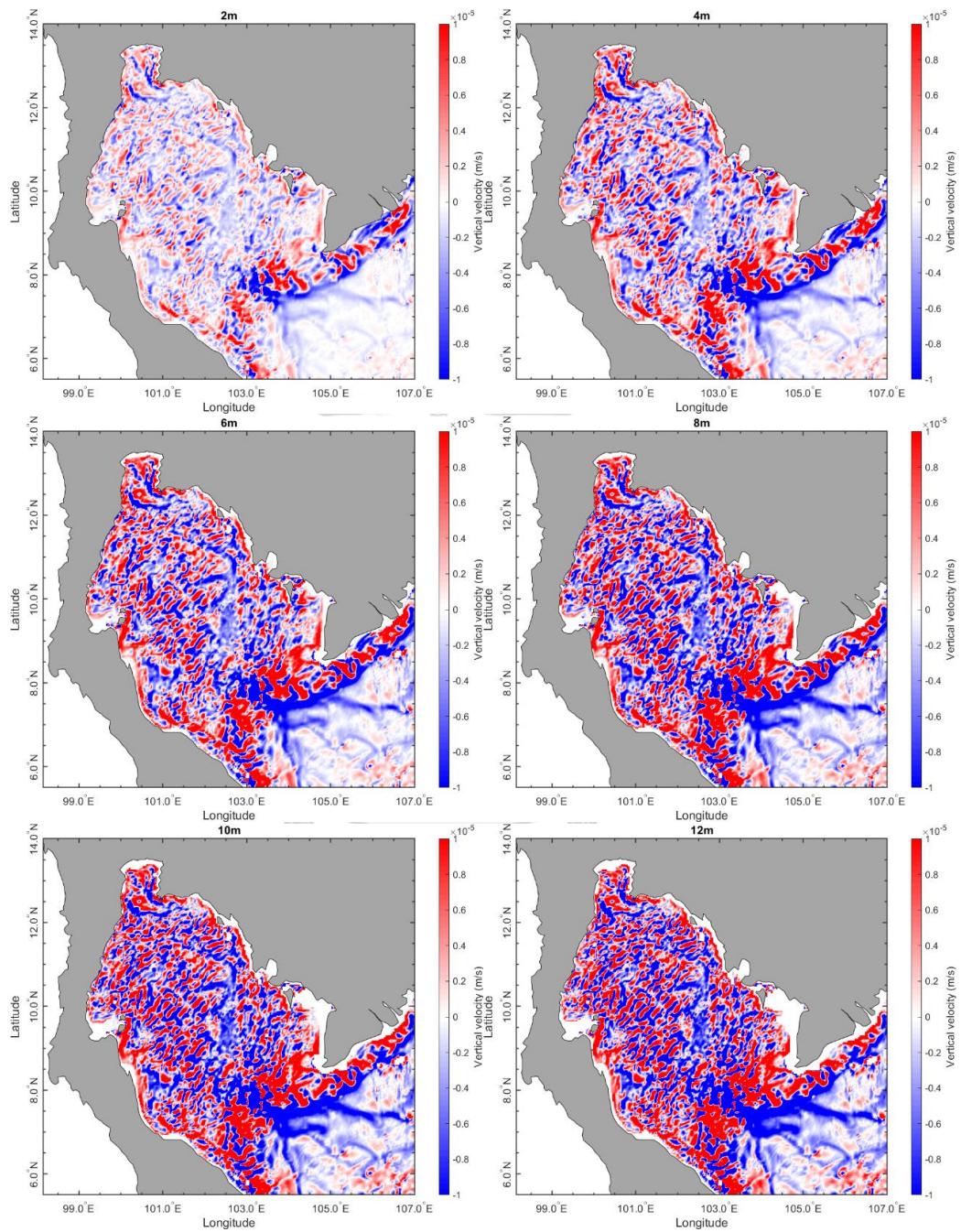




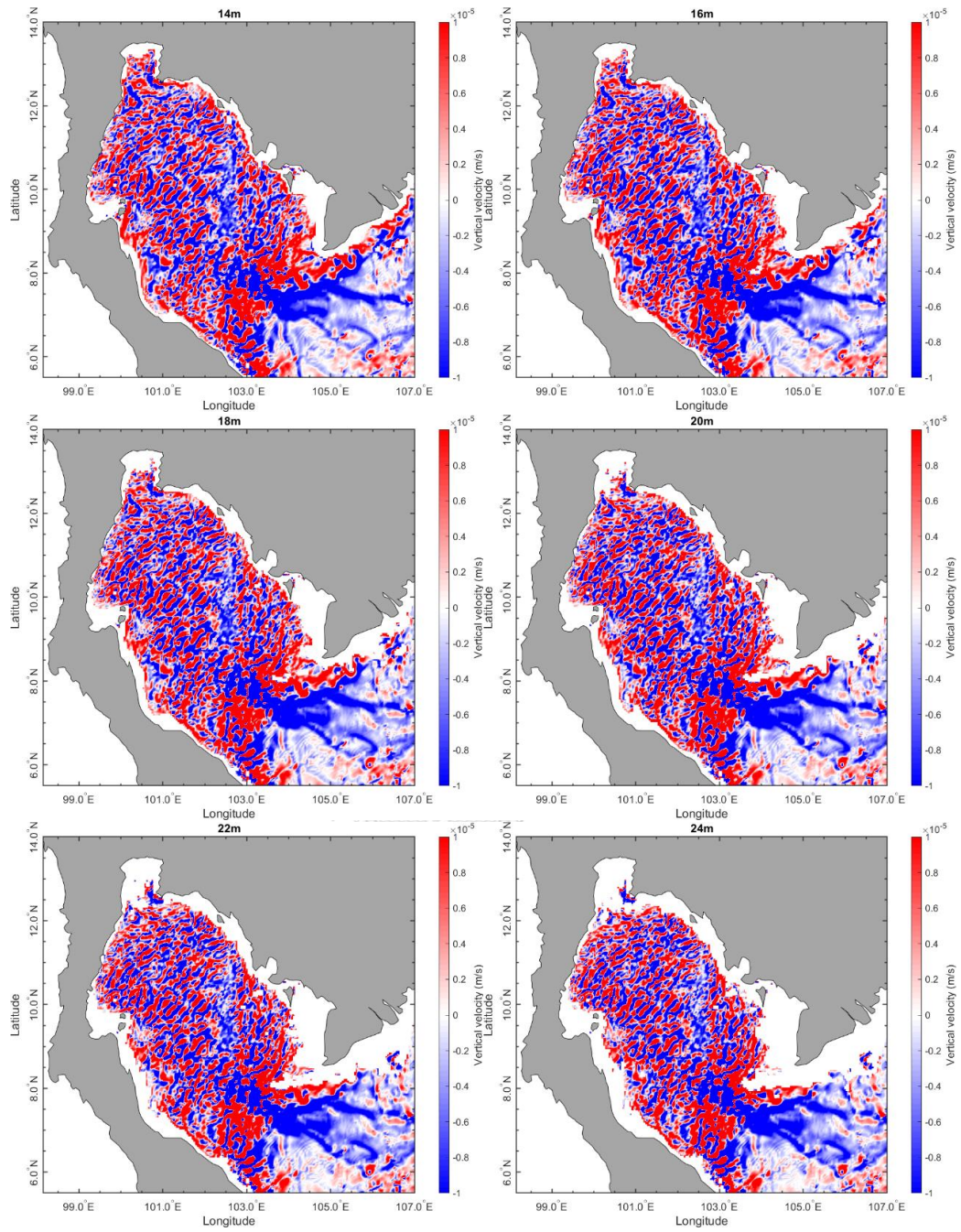
*Fig. B40. The distributions of monthly averaged vertical velocity of Northeast monsoon in GoT at depths of 2-70 m.*

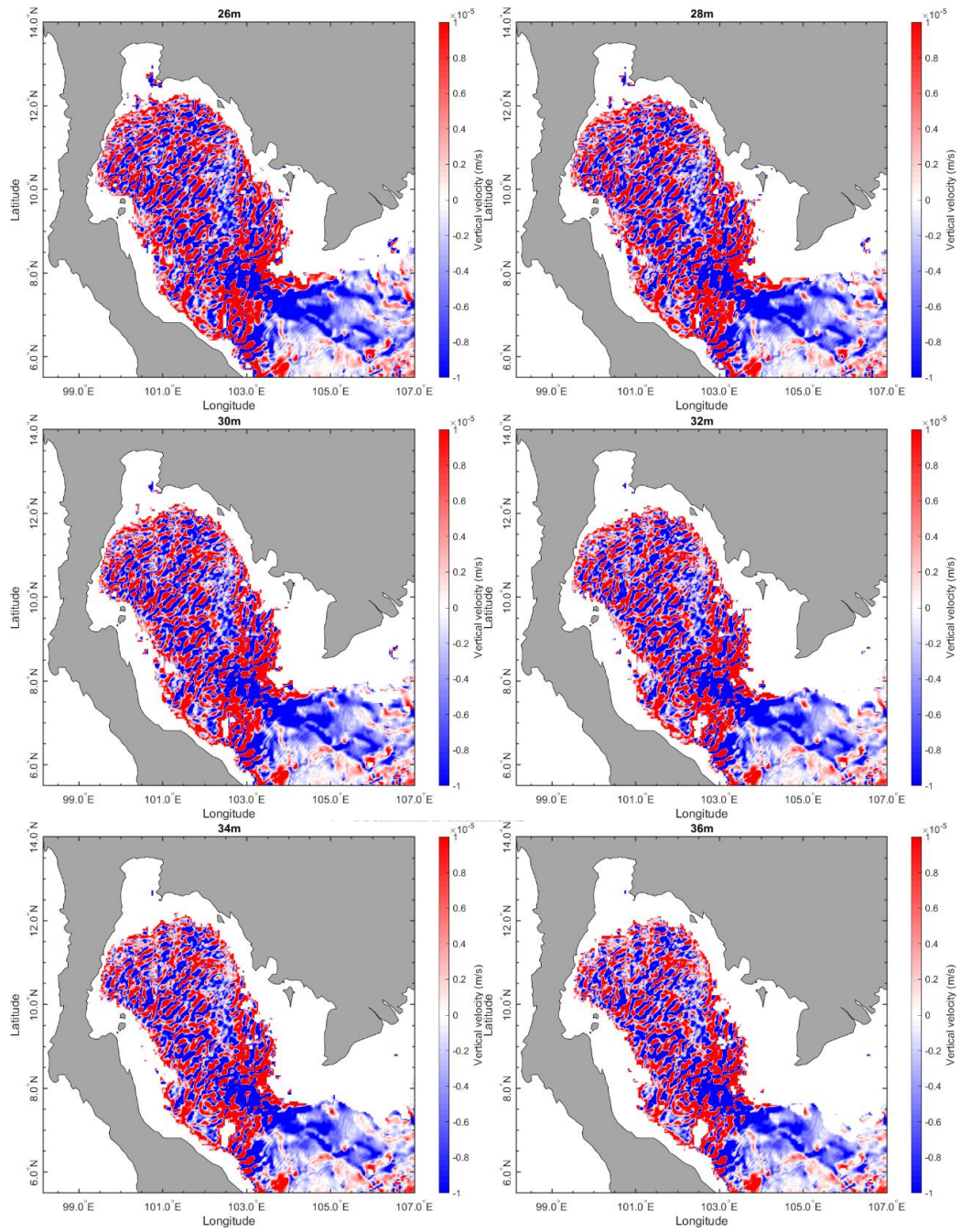


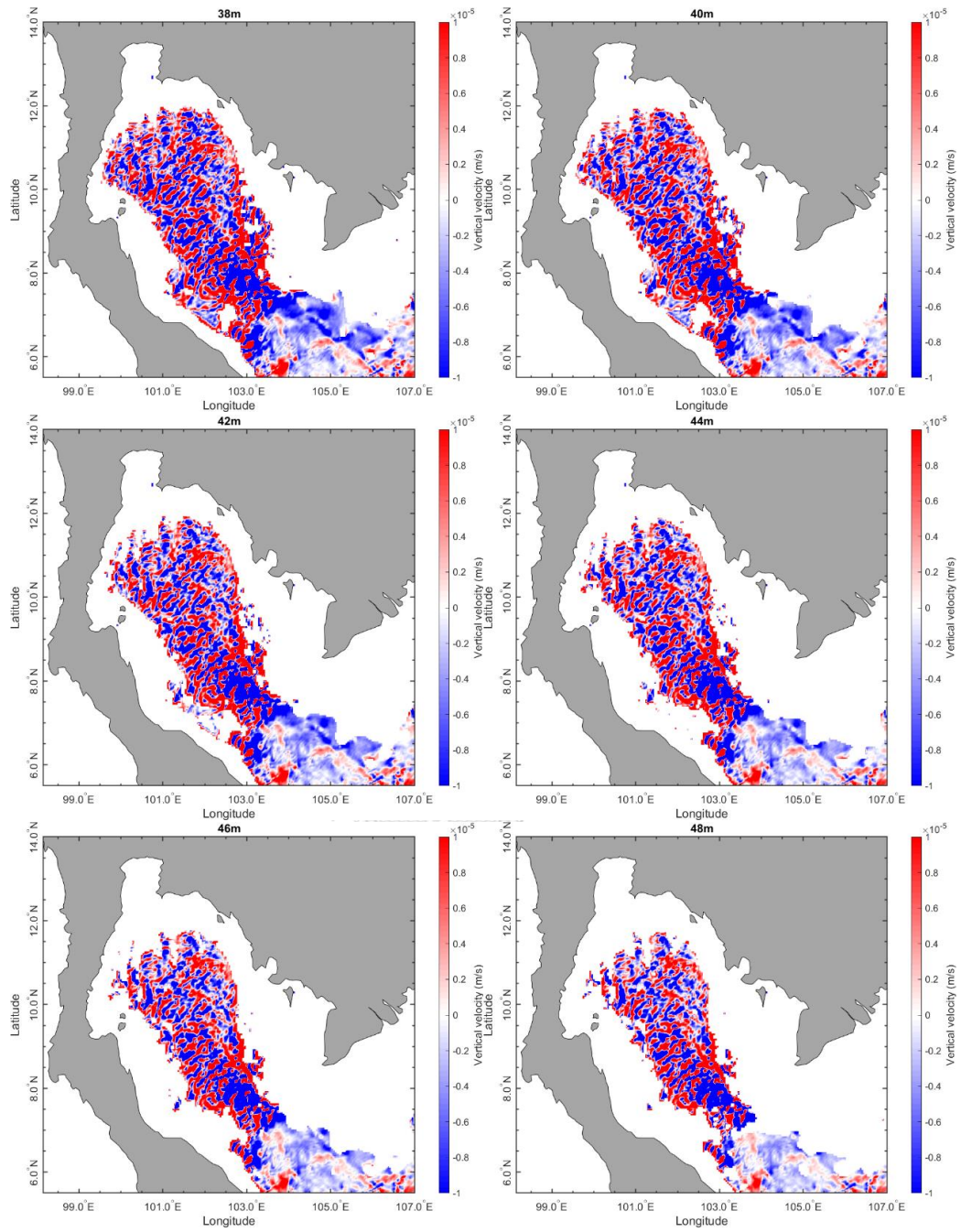
B14. The distributions of monthly averaged vertical velocity of 1<sup>st</sup> inter-monsoon



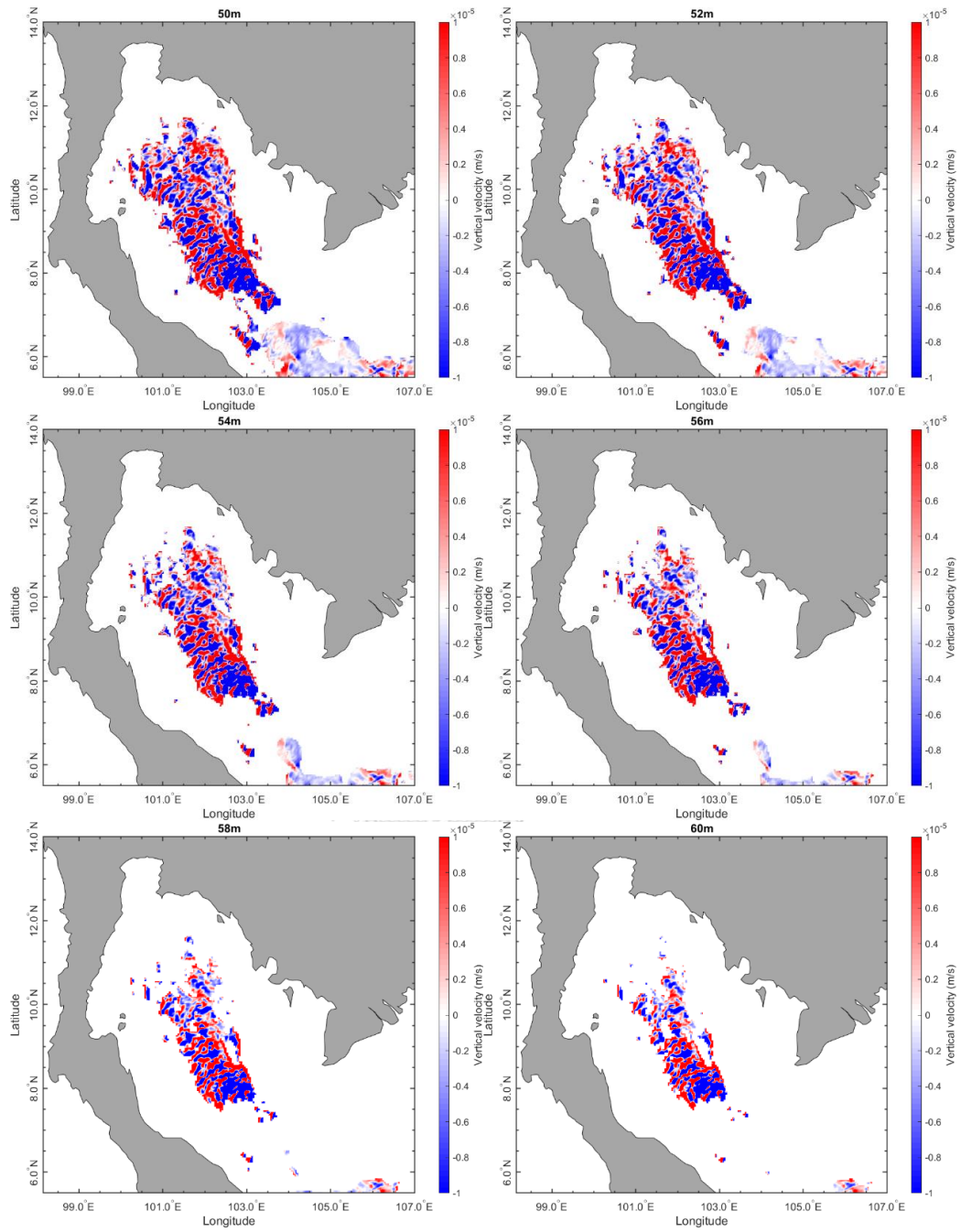












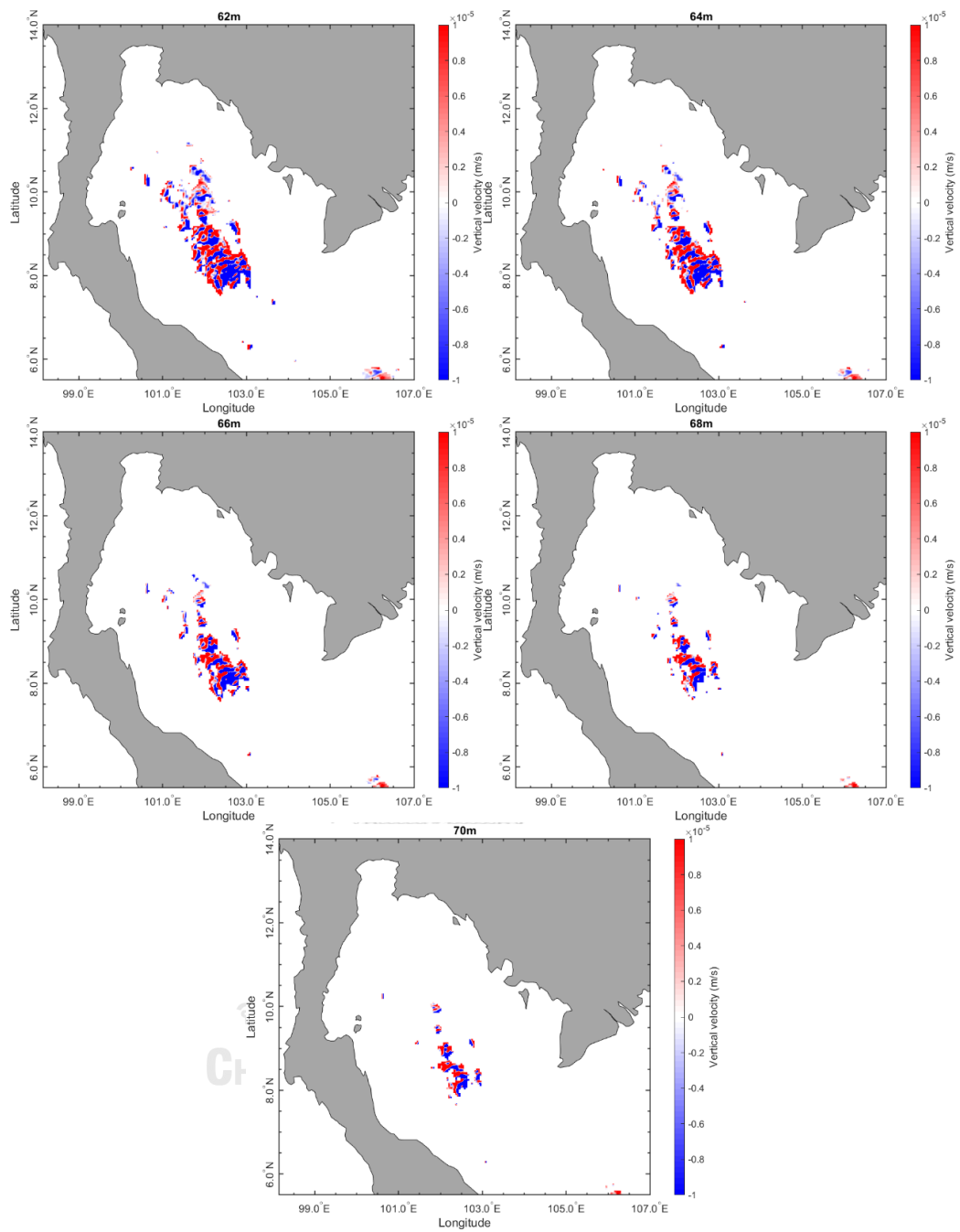
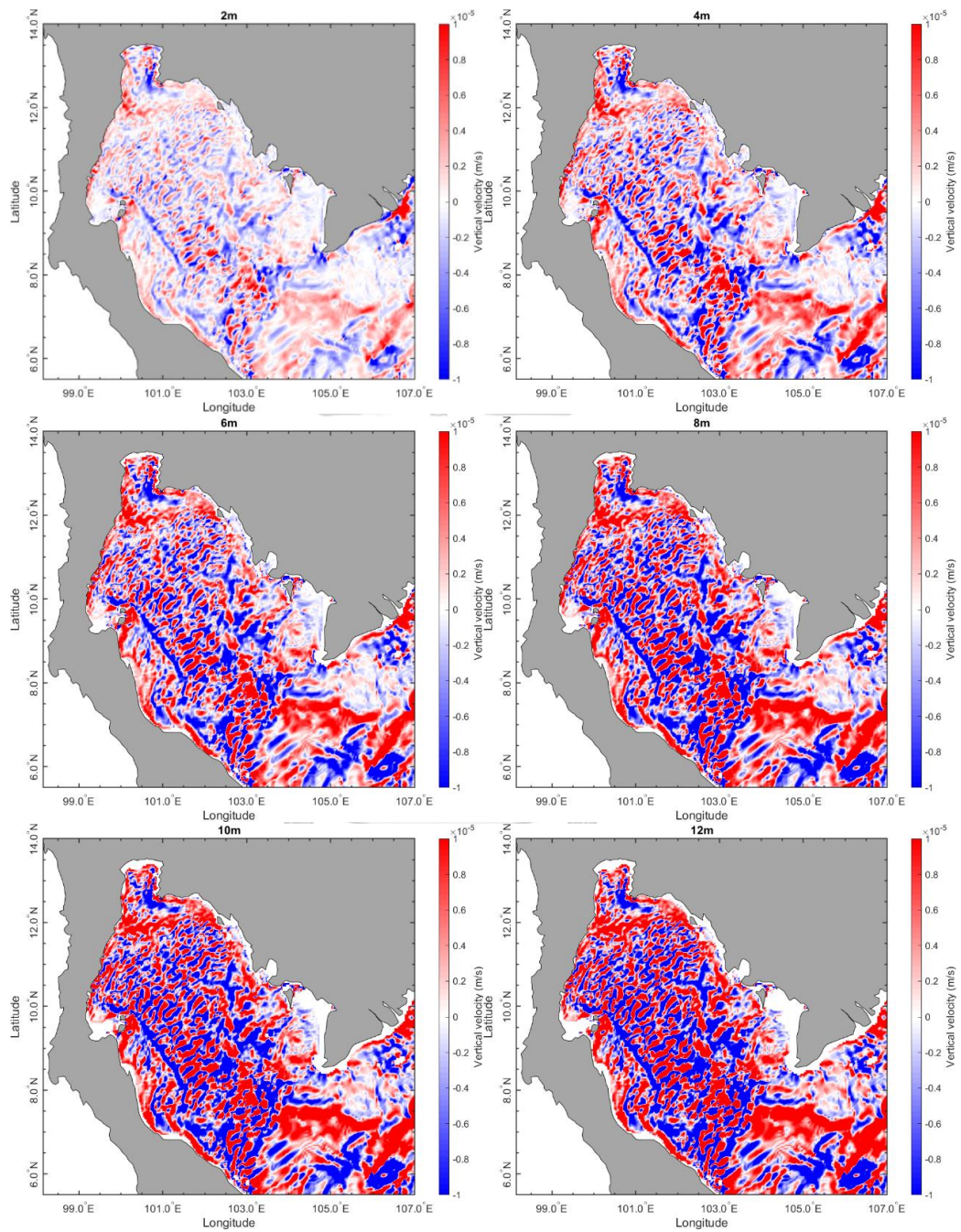
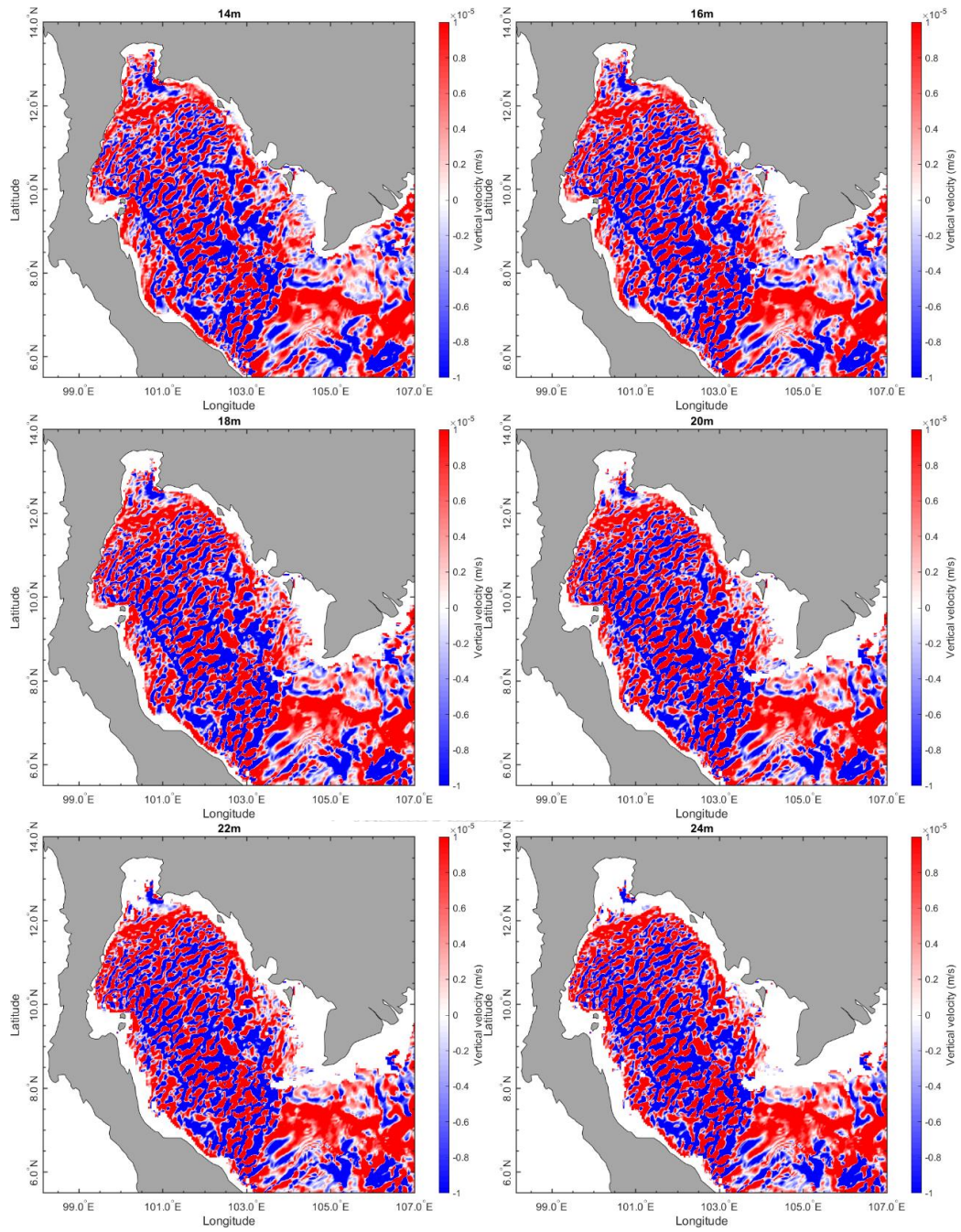


Fig. B41. The distributions of monthly averaged vertical velocity of 1<sup>st</sup> Inter- monsoon in GoT at depths of 2-70 m.

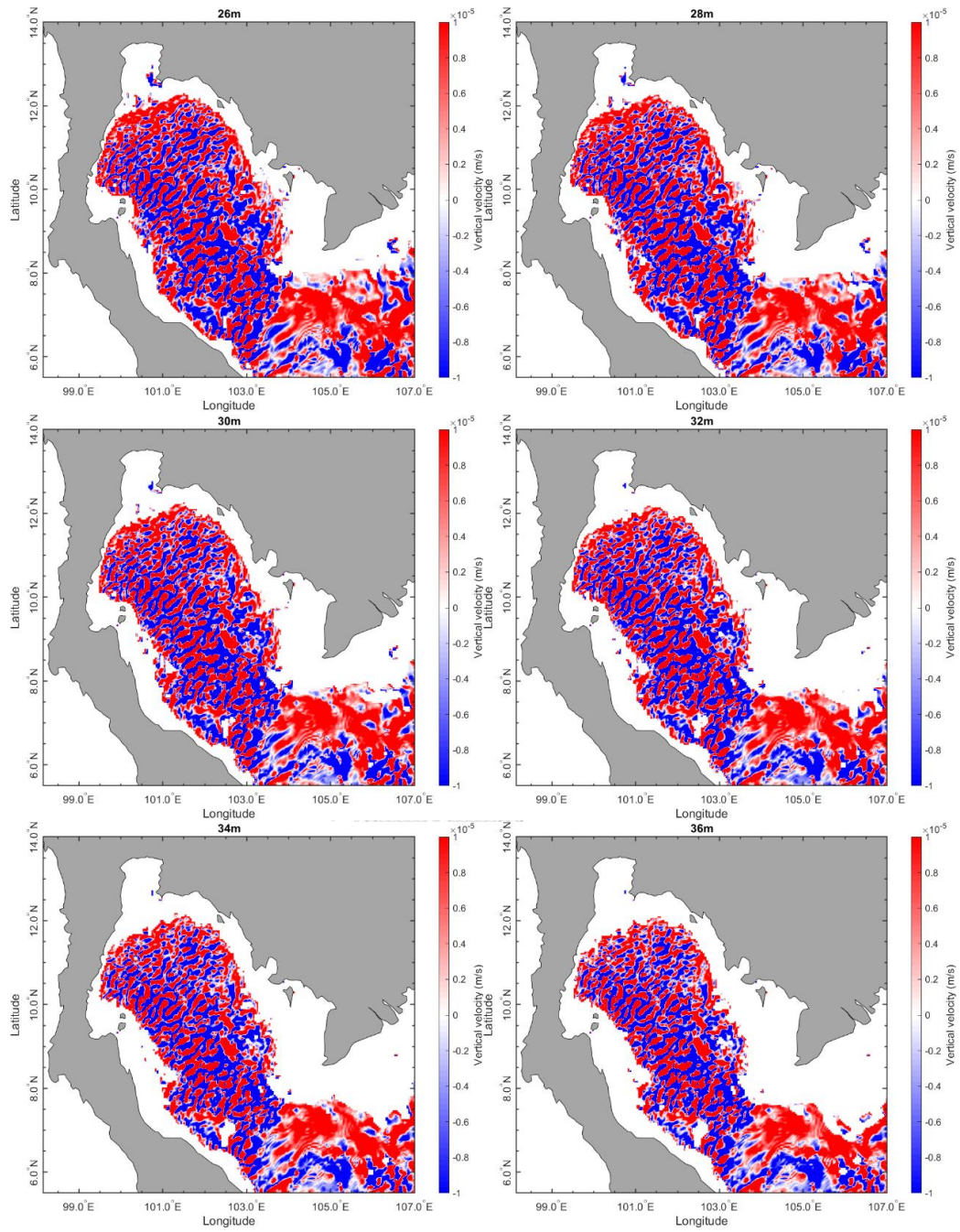


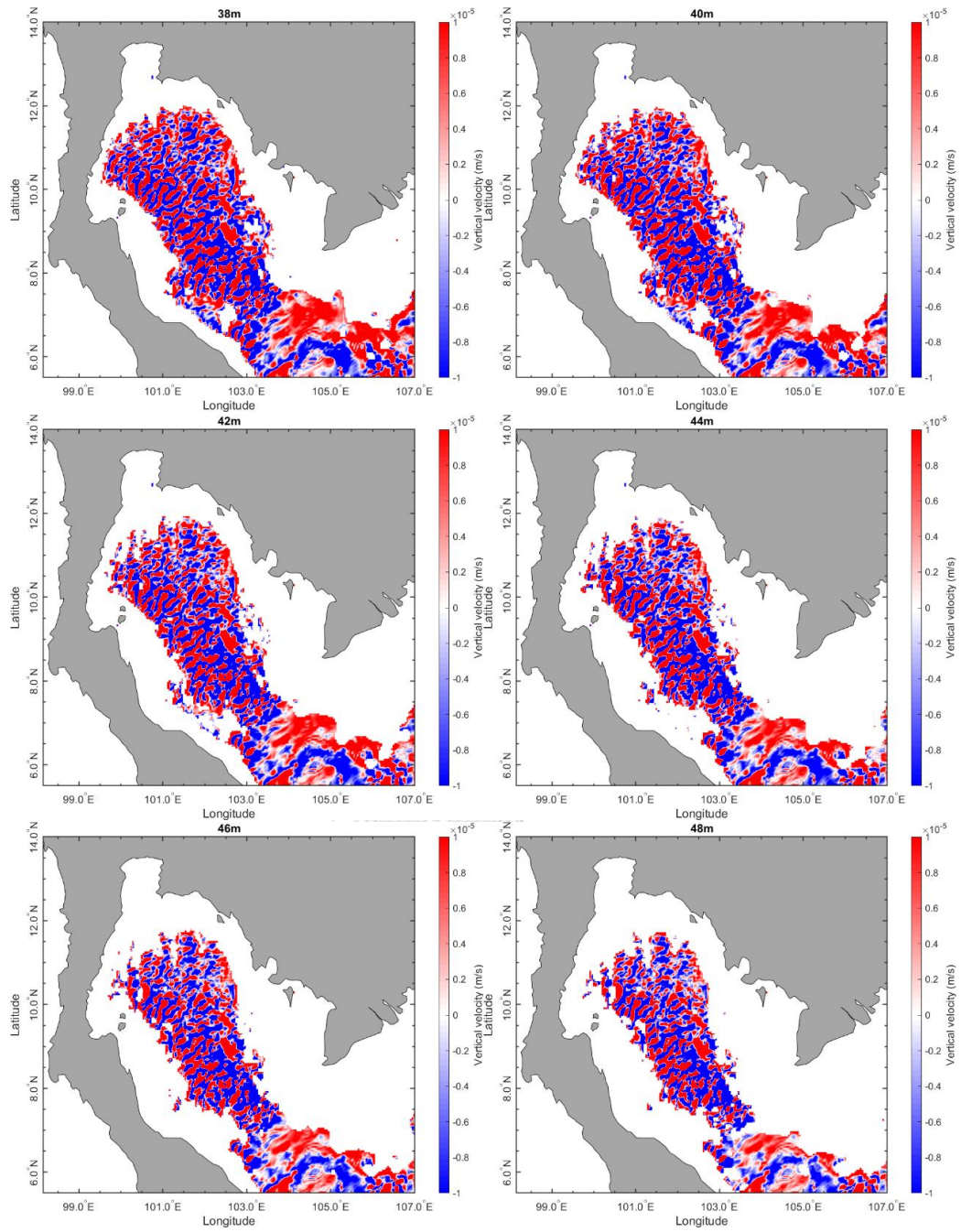
B15. The distributions of monthly averaged vertical velocity of southwest monsoon

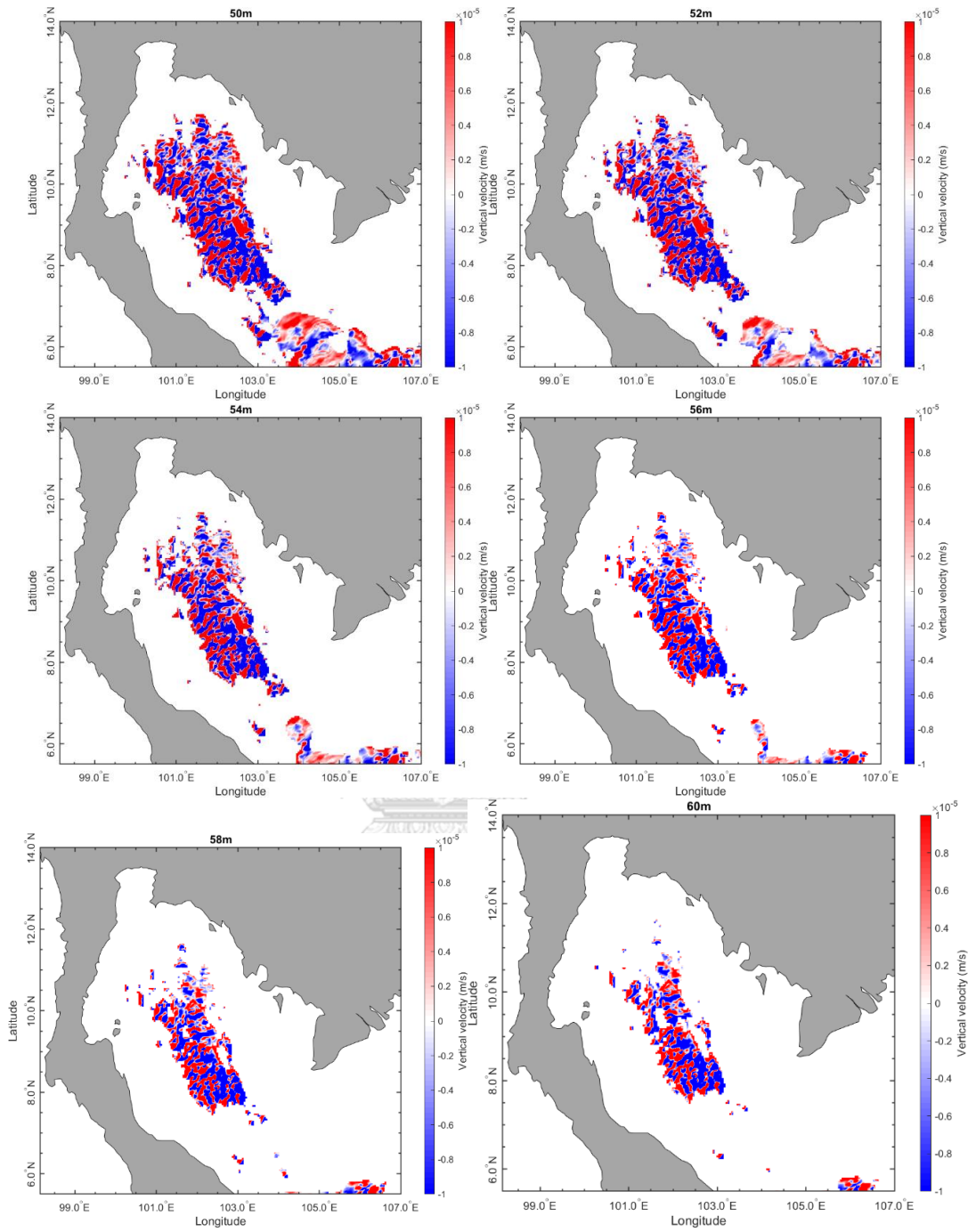




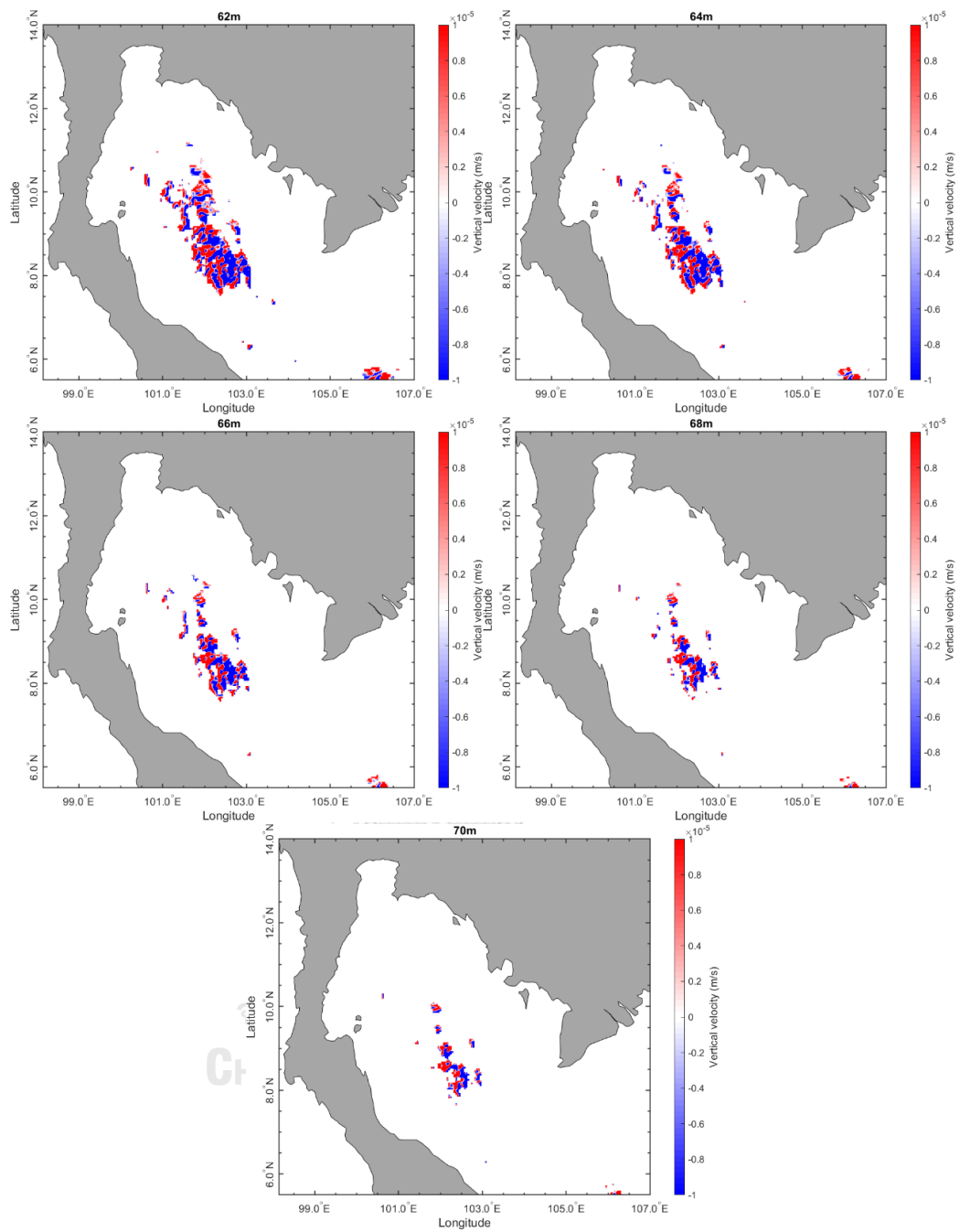






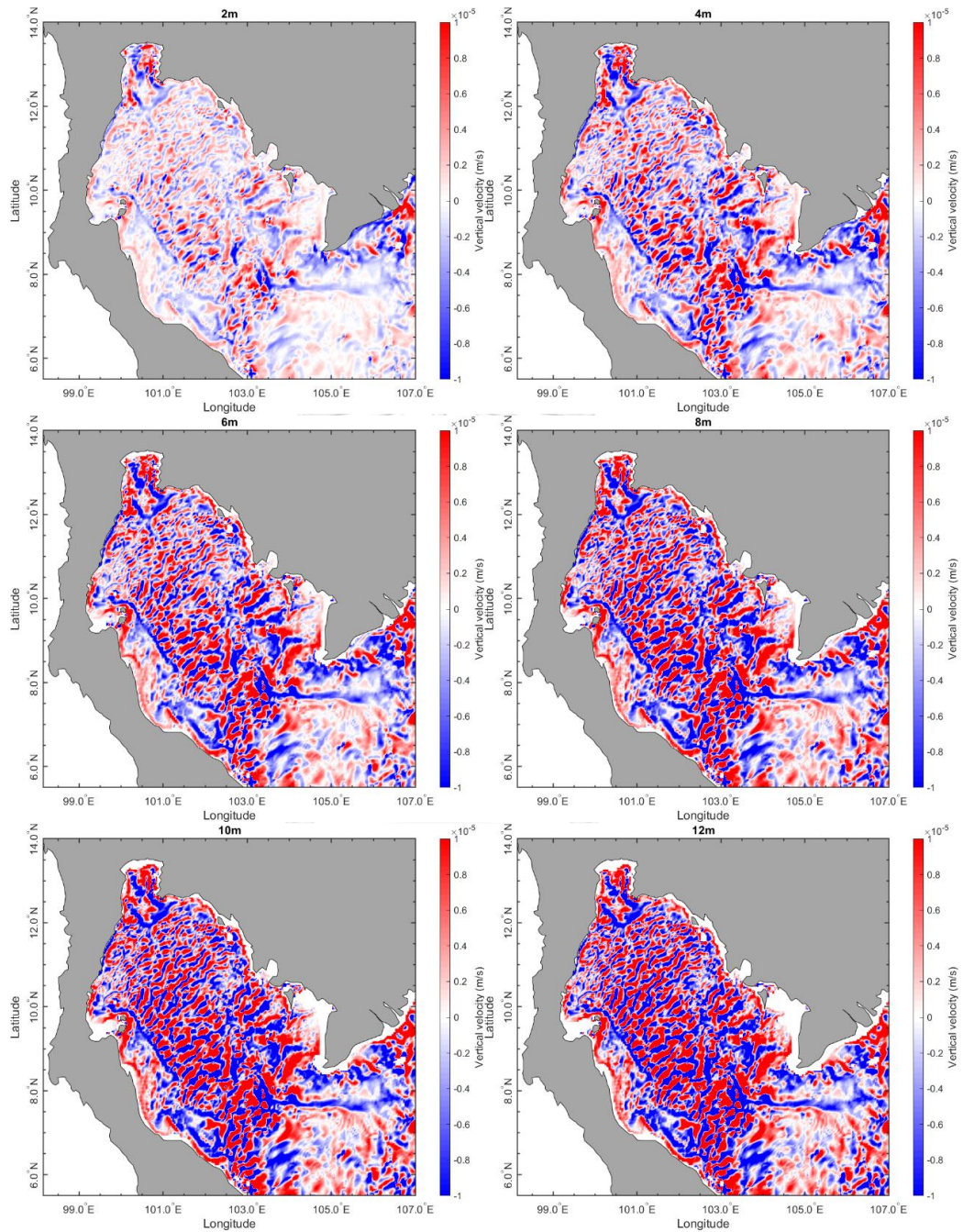


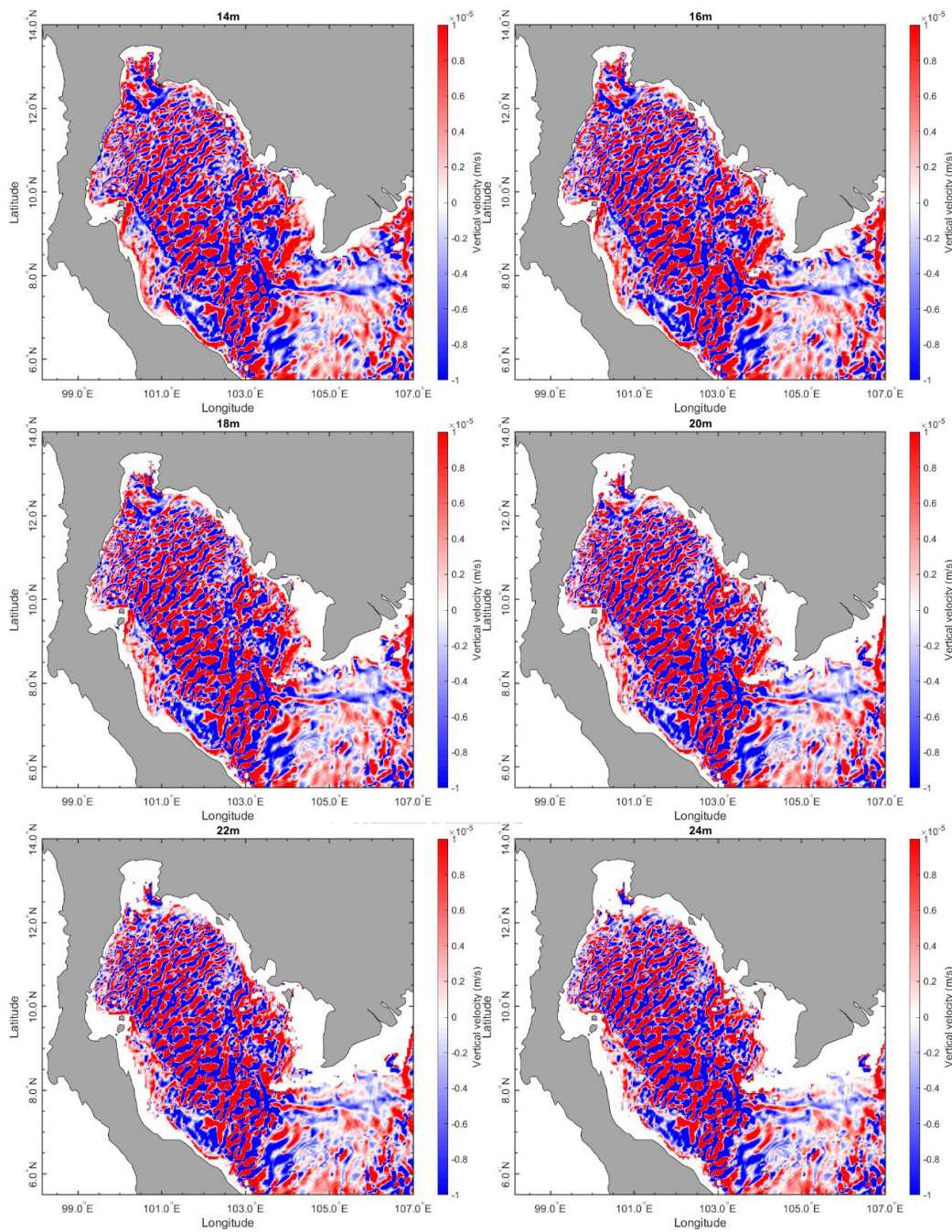




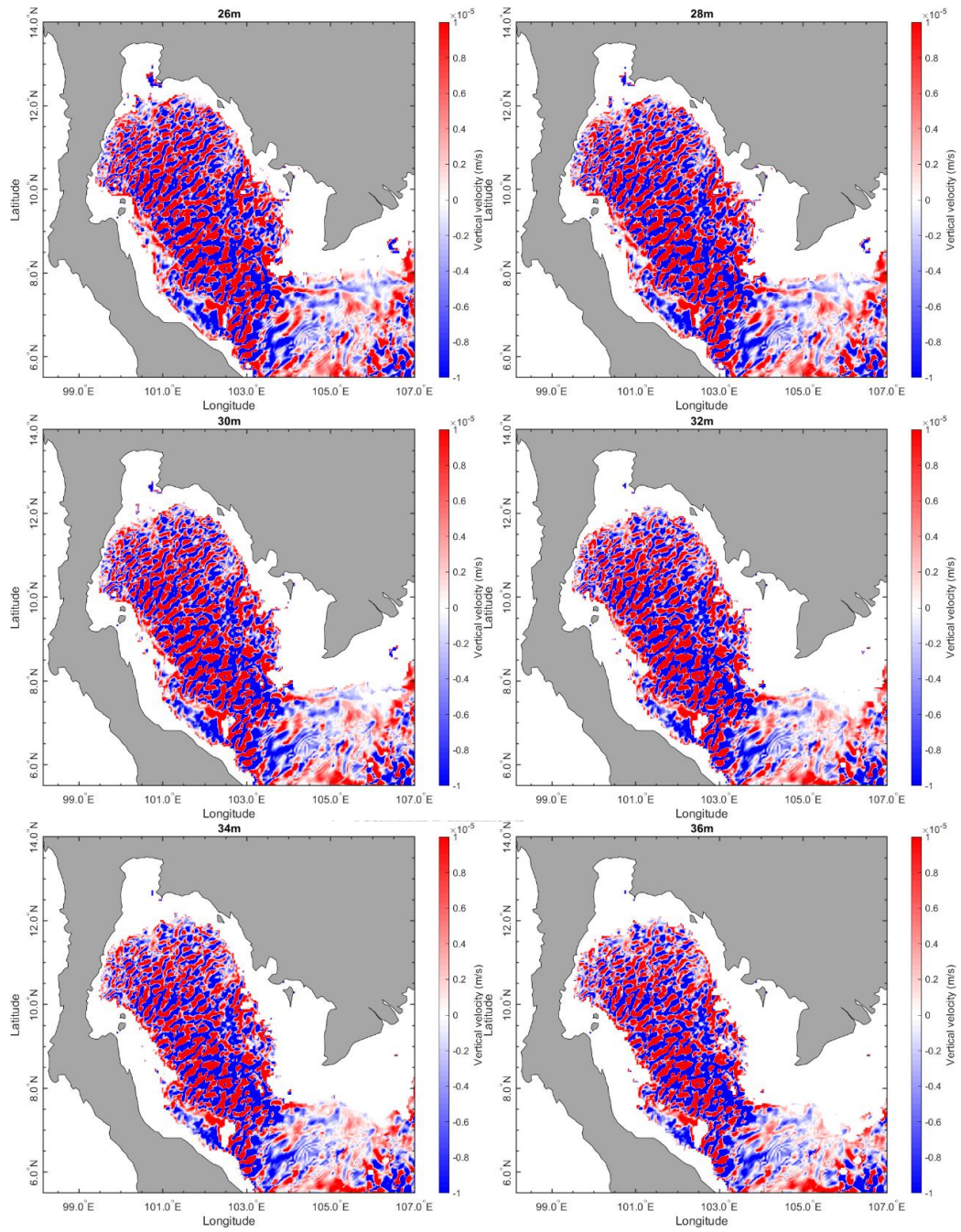
*Fig. B42. The distributions of monthly averaged vertical velocity of Southwest monsoon in GoT at depths of 2-70 m.*

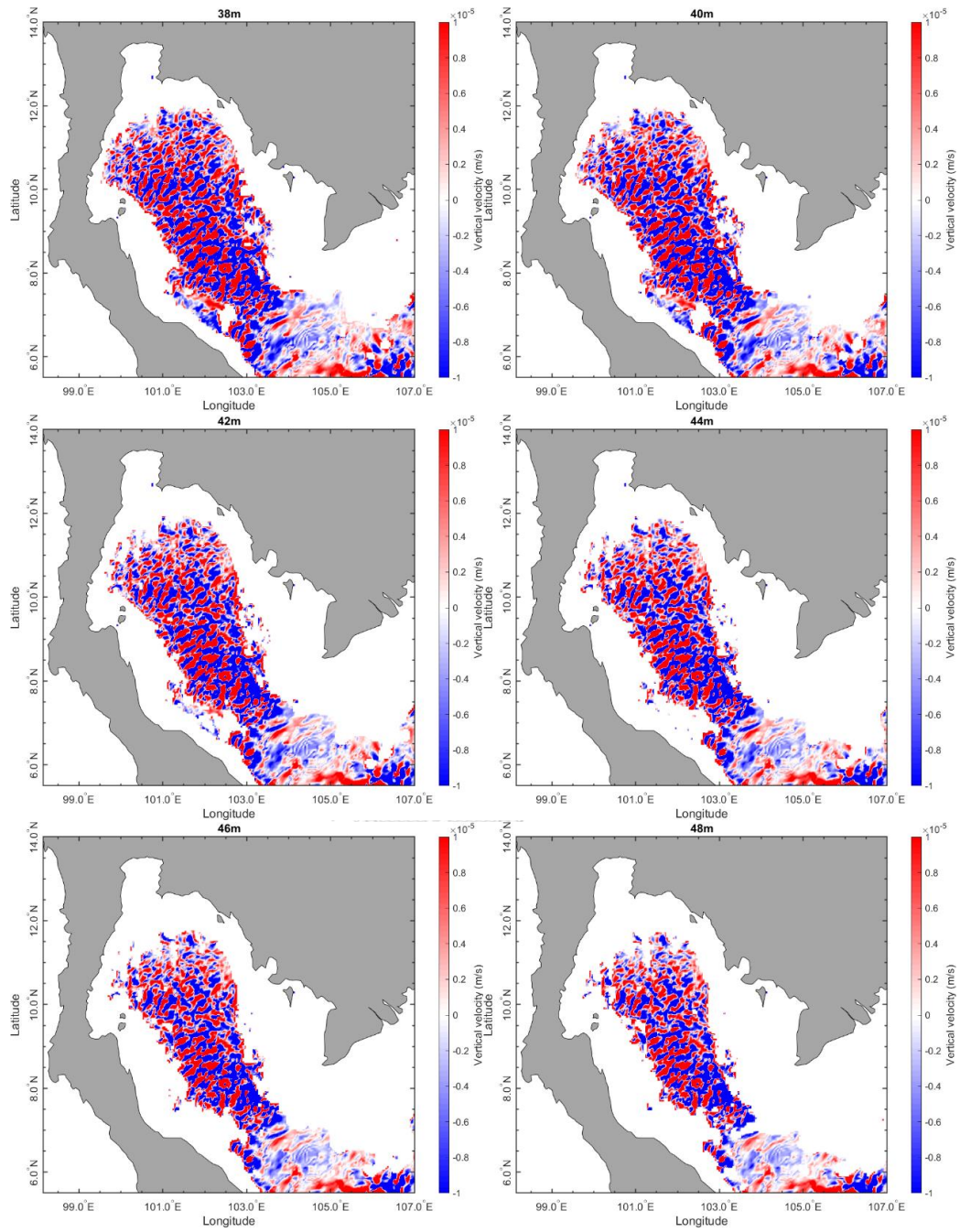
B16. The distributions of monthly averaged vertical velocity of 2<sup>nd</sup> intermonsoon



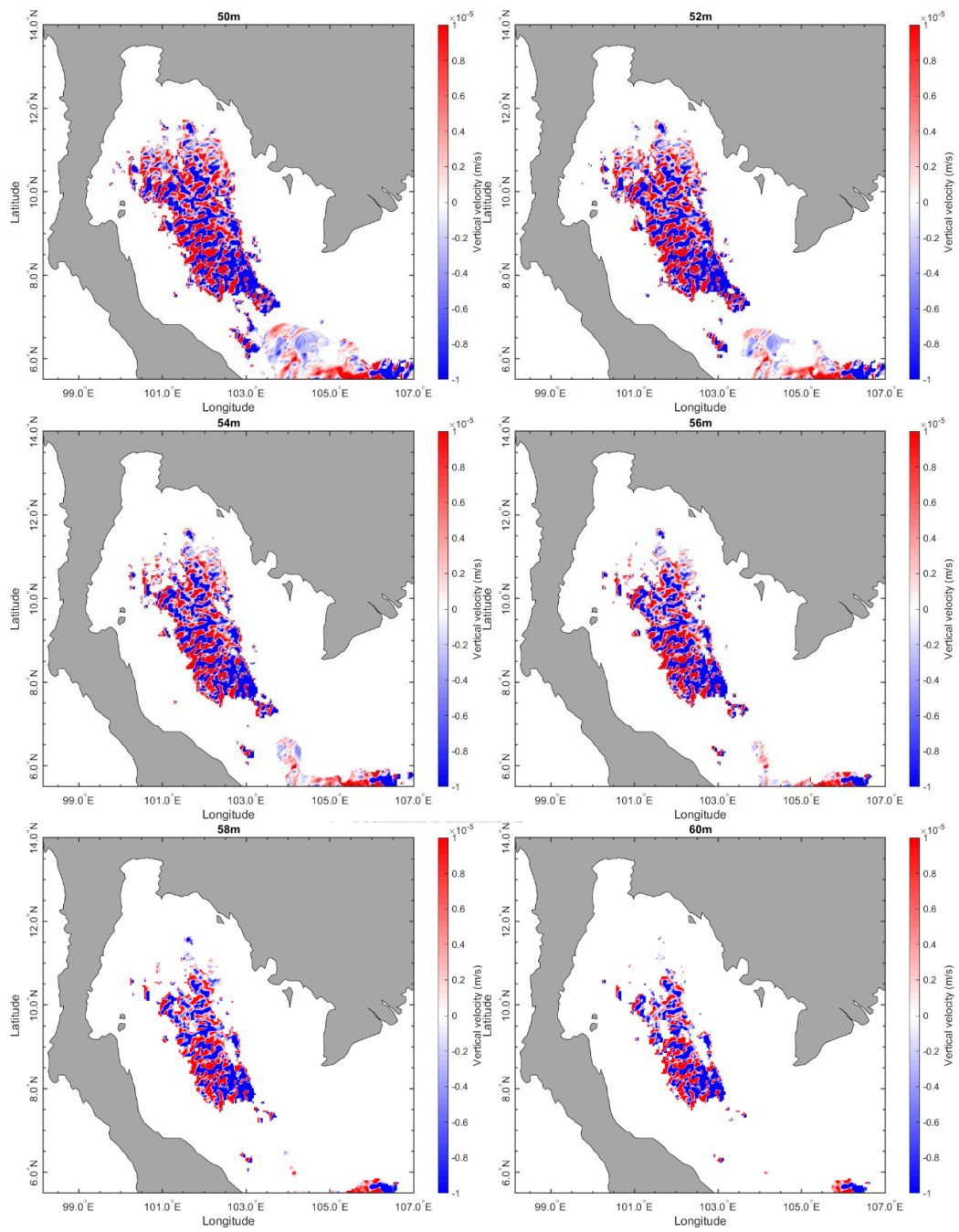












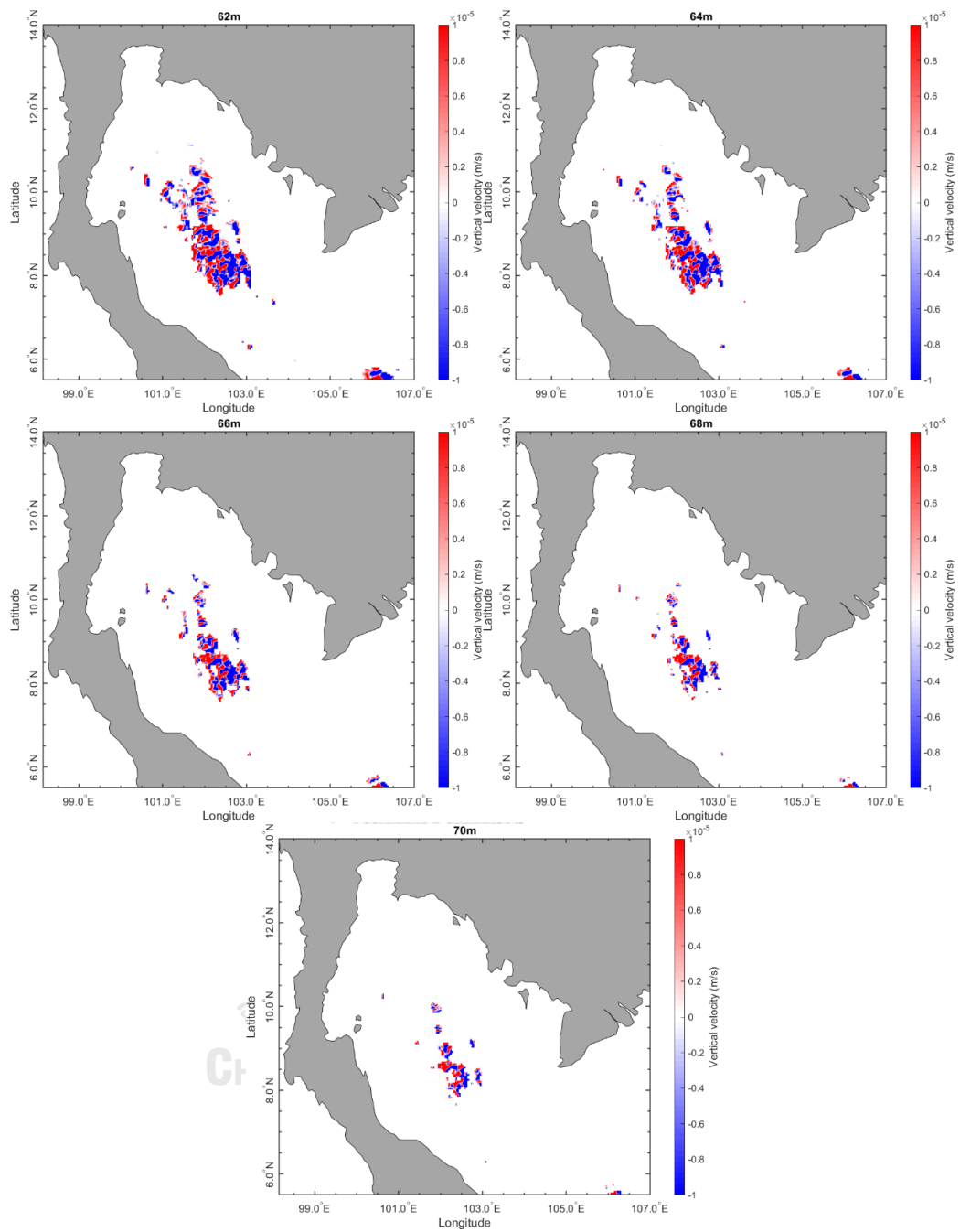


*Fig. B43. The distributions of monthly averaged vertical velocity of 2<sup>nd</sup> Inter- monsoon in GoT at depths of 2-70 m.*

## REFERENCES

- Ahmed, M., Boonchuwongse, P., Dechboon, W., and Squires, D. (2007). Overfishing in the Gulf of Thailand: policy challenges and bioeconomic analysis. *Environment Development Economics*, 12(1), 145-172.
- Alvarez, I., Gomez-Gesteira, M., deCastro, M., Lorenzo, M. N., Crespo, A. J. C., and Dias, J. M. (2011). Comparative analysis of upwelling influence between the western and northern coast of the Iberian Peninsula. *Continental Shelf Research*, 31(5), 388-399. doi:10.1016/j.csr.2010.07.009
- Bakun, A. (1973). *Coastal upwelling indices, west coast of North America, 1946-71*.
- Bakun, A. (1975). *Daily and weekly upwelling indices, west coast of North America, 1967-73*.
- Benazzouz, A., Mordane, S., Orbi, A., Chagdali, M., Hilmi, K., Atillah, A., Pelegrí, J. L., and Hervé, D. (2014). An improved coastal upwelling index from sea surface temperature using satellite-based approach—The case of the Canary Current upwelling system. *Continental Shelf Research*, 34, 38-54.
- Breemen, M. (2008). *Salt intrusion in the Selangor: model study with Delft3D estuary in Malaysia*. University of Twente,
- Chaionkarn, P., and Sojisuporn, P. (2012). Characteristics of Seasonal Wind and Wind-driven Current in the Gulf of Thailand. *Bulletin of Earth Sciences of Thailand*, 5(1), 58-67.
- Chen, C., Lai, Z., Beardsley, R. C., Xu, Q., Lin, H., and Viet, N. T. (2012). Current separation and upwelling over the southeast shelf of Vietnam in the South China Sea. *Journal of Geophysical Research: Oceans*, 117(C3). doi:10.1029/2011jc007150
- Cropper, T. E., Hanna, E., and Bigg, G. R. (2014). Spatial and temporal seasonal trends in coastal upwelling off Northwest Africa, 1981–2012. *Deep Sea Research Part I: Oceanographic Research Papers*, 86, 94-111. doi:10.1016/j.dsr.2014.01.007
- Cushing, D. (1971). Upwelling and the production of fish. In *Advances in marine biology* (Vol. 9, pp. 255-334): Elsevier.
- Davies, A. M., Hall, P., Howarth, M. J., Knight, P. J., and Player, R. J. (2001). Comparison of observed (HF radar and ADCP measurements) and computed tides in the North Channel of the Irish Sea. *Journal of physical oceanography*, 31(7), 1764-1785.
- Dee, D. P., Uppala, S. M., Simmons, A. J., Berrisford, P., Poli, P., Kobayashi, S., Andrae, U., Balmaseda, M. A., Balsamo, G., Bauer, P., Bechtold, P., Beljaars, A. C. M., van de Berg, L., Bidlot, J., Bormann, N., Delsol, C., Dragani, R., Fuentes, M., Geer, A. J., Haimberger, L., Healy, S. B., Hersbach, H., Hólm, E. V., Isaksen, I., Kållberg, P., Köhler, M., Matricardi, M., McNally, A. P., Monge-Sanz, B. M., Morcrette, J. J., Park, B. K., Peubey, C., de Rosnay, P., Tavolato, C., Thépaut, J. N., and Vitart, F. (2011). The ERA-Interim reanalysis: configuration and performance of the data assimilation system. *Quarterly Journal of the Royal Meteorological Society*, 137(656), 553-597. doi:10.1002/qj.828
- Deltares, D. (2013). *Delft3D-FLOW user manual*.
- Dippner, J. W., Nguyen, K. V., Hein, H., Ohde, T., and Loick, N. (2006). Monsoon-induced upwelling off the Vietnamese coast. *Ocean Dynamics*, 57(1), 46-62. doi:10.1007/s10236-006-0091-0

- Egbert, G. D., and Erofeeva, S. Y. (2002). Efficient inverse modeling of barotropic ocean tides. *Journal of Atmospheric Oceanic Technology*, 19(2), 183-204.
- Fang, G., Kwok, Y.-K., Yu, K., and Zhu, Y. (1999). Numerical simulation of principal tidal constituents in the South China Sea, Gulf of Tonkin and Gulf of Thailand. *Continental Shelf Research*, 19(7), 845-869.
- Foreman, M., Henry, R., Walters, R., and Ballantyne, V. (1993). A finite element model for tides and resonance along the north coast of British Columbia. *Journal of Geophysical Research: Oceans*, 98(C2), 2509-2531.
- Gomez-Gesteira, M., de Castro, M., Alvarez, I., Lorenzo, M. N., Gesteira, J. L., and Crespo, A. J. (2008). Spatio-temporal upwelling trends along the Canary Upwelling System (1967-2006). *Ann N Y Acad Sci*, 1146, 320-337. doi:10.1196/annals.1446.004
- Hein, H., Hein, B., Pohlmann, T., and Long, B. H. (2013). Inter-annual variability of upwelling off the South-Vietnamese coast and its relation to nutrient dynamics. *Global and Planetary Change*, 110, 170-182. doi:10.1016/j.gloplacha.2013.09.009
- Inghamjitr, S., and Sricharoendham, B. (2016). *Current status of fish stock enhancement in Thailand*. Paper presented at the Consolidating the Strategies for Fishery Resources Enhancement in Southeast Asia. Proceedings of the Symposium on Strategy for Fisheries Resources Enhancement in the Southeast Asian Region, Pattaya, Thailand, 27-30 July 2015.
- Jiao, J. (2014). *Morphodynamics of a land inlet: medium-term delft3d modelling*. (Master of Science), Delft University of Technology,
- Jing, Z., Qi, Y., and Du, Y. (2011). Upwelling in the continental shelf of northern South China Sea associated with 1997–1998 El Niño. *Journal of Geophysical Research*, 116(C2). doi:10.1029/2010jc006598
- Kämpf, J., and Chapman, P. (2016). The functioning of coastal upwelling systems. In *Upwelling systems of the world* (pp. 31-65): Springer.
- Kok, P. H., Mohd Akhir, M. F., Tangang, F., and Husain, M. L. (2017). Spatiotemporal trends in the southwest monsoon wind-driven upwelling in the southwestern part of the South China Sea. *PLoS One*, 12(2), e0171979. doi:10.1371/journal.pone.0171979
- Kongseng, S., Phoosawat, R., and Swatdipong, A. (2020a). Individual assignment and mixed-stock analysis of short mackerel (*Rastrelliger brachysoma*) in the Inner and Eastern Gulf of Thailand: Contrast migratory behavior among the fishery stocks. *Fisheries Research*, 221, 105372.
- Kongseng, S., Phoosawat, R., and Swatdipong, A. (2020b). Individual assignment and mixed-stock analysis of short mackerel (*Rastrelliger brachysoma*) in the Inner and Eastern Gulf of Thailand: Contrast migratory behavior among the fishery stocks. *Fisheries Research*, 221. doi:10.1016/j.fishres.2019.105372
- Kuo, N.-J., Zheng, Q., and Ho, C.-R. (2000a). Satellite observation of upwelling along the western coast of the South China Sea. *Remote sensing of environment*, 74(3), 463-470.
- Kuo, N.-J., Zheng, Q., and Ho, C.-R. (2000b). Satellite observation of upwelling along the western coast of the South China Sea. *74(3)*, 463-470.
- Lehmann, A., and Myrberg, K. (2008). Upwelling in the Baltic Sea — A review. *Journal of Marine Systems*, 74, S3-S12. doi:10.1016/j.jmarsys.2008.02.010

- Li, Y., Peng, S., Wang, J., Yan, J., and Huang, H. (2018). On the Mechanism of the Generation and Interannual Variations of the Summer Upwellings West and Southwest Off the Hainan Island. *Journal of Geophysical Research: Oceans*, 123(11), 8247-8263. doi:10.1029/2018jc014226
- Liu, W. C., and Huang, W. C. (2019). Influences of sea level rise on tides and storm surges around the Taiwan coast. *Continental Shelf Research*, 173, 56-72.
- Lü, X., Qiao, F., Wang, G., Xia, C., and Yuan, Y. (2008). Upwelling off the west coast of Hainan Island in summer: Its detection and mechanisms. *Geophysical Research Letters*, 35(2). doi:10.1029/2007gl032440
- Malaysia, P. T. S., DARYABOR, F., TANGANG, F., and JUNENG, L. (2014). Simulation of southwest monsoon current circulation and temperature in the east coast of Peninsular Malaysia. *Sains Malaysiana*, 43(3), 389-398.
- Ndah, A. B., Dagar, L., and Becek, K. (2017). Multi-temporal patterns of upwelling–downwelling dynamics in the South China Sea based on a 47-year time-series of the NOAA-ERD upwelling index. *Regional Studies in Marine Science*, 16, 225-239. doi:10.1016/j.rsma.2017.08.017
- Paduan, J. D., and Shulman, I. (2004). HF radar data assimilation in the Monterey Bay area. *Journal of Geophysical Research: Oceans*, 109(C7).
- Patti, B., Guisande, C., Bonanno, A., Basilone, G., Cuttitta, A., and Mazzola, S. (2010). Role of physical forcings and nutrient availability on the control of satellite-based chlorophyll a concentration in the coastal upwelling area of the Sicilian Channel. *Scientia Marina*, 74(3), 577-588.
- Robinson, M. K. (1974). *The physical oceanography of the Gulf of Thailand*, NAGA Expedition (Vol. 3): Scripps Institution of Oceanography.
- Santos, F., Gomez-Gesteira, M., deCastro, M., and Alvarez, I. (2012). Differences in coastal and oceanic SST trends due to the strengthening of coastal upwelling along the Benguela current system. *Continental Shelf Research*, 34, 79-86. doi:10.1016/j.csr.2011.12.004
- Saramul, S. (2017). Seasonal monsoon variations in surface currents in the Gulf of Thailand revealed by high frequency radar. *Engineering Journal*, 21(4), 25-37.
- Saramul, S., and Ezer, T. (2014). Spatial variations of sea level along the coast of Thailand: Impacts of extreme land subsidence, earthquakes and the seasonal monsoon. *Global Planetary Change*, 122, 70-81.
- Singhruck, P. (2001, 5-9 November). *Circulation features in the Gulf of Thailand Inferred from SeaWiFS data*. Paper presented at the 22nd Asian Conference on Remote Sensing, Singapore.
- Sojisuorn, P., Morimoto, A., and Yanagi, T. (2010). Seasonal variation of sea surface current in the Gulf of Thailand. *Coastal Marine Science*, 34(1), 91-102.
- Strass, V. H. (1992). Chlorophyll patchiness caused by mesoscale upwelling at fronts. *Deep Sea Research Part A. Oceanographic Research Papers*, 39(1), 75-96.
- Su, J., and Pohlmann, T. (2009). Wind and topography influence on an upwelling system at the eastern Hainan coast. *Journal of Geophysical Research*, 114(C6). doi:10.1029/2008jc005018
- Teresa K, C., and James F, P. (2001). *Ekman transport and pumping*.
- Teresa, K. C., and James, F. P. (2019). *Upper Ocean Structure: Ekman Transport and Pumping*.



- Tint, K. K., Ngim, K., Sapari, A., Souliphone, K., Suwannapoom, S., Viron, J. G., and Thanh, V. T. P. (2020). Enhancing the Management of the Indo-Pacific Mackerel Resources in the Gulf of Thailand: a synthesis. In *Fish for the People Vol. 18 No. 1* (pp. 14-19): Secretariat, Southeast Asian Fisheries Development Center.
- Tsimplis, M., Proctor, R., and Flather, R. (1995). A two-dimensional tidal model for the Mediterranean Sea. *Journal of Geophysical Research: Oceans*, 100(C8), 16223-16239.
- Wyatt, L. R. (2000). Limits to the inversion of HF radar backscatter for ocean wave measurement. *Journal of Atmospheric Oceanic Technology*, 17(12), 1651-1666.
- Wyatt, L. R., Green, J. J., and Middleditch, A. (2011). HF radar data quality requirements for wave measurement. *Coastal Engineering*, 58(4), 327-336.
- Xie, S.-P. (2003). Summer upwelling in the South China Sea and its role in regional climate variations. *Journal of Geophysical Research*, 108(C8). doi:10.1029/2003jc001867
- Yanagi, T., and Takao, T. (1998a). Clockwise phase propagation of semi-diurnal tides in the Gulf of Thailand. *Journal of Oceanography*, 54(2), 143-150.
- Yanagi, T., and Takao, T. (1998b). Seasonal variation of three-dimensional circulations in the Gulf of Thailand. *La mer*, 36(2), 43-55.
- Zu, T., Gan, J., and Erofeeva, S. Y. (2008). Numerical study of the tide and tidal dynamics in the South China Sea. *Deep Sea Research Part I: Oceanographic Research Papers*, 55(2), 137-154. doi:10.1016/j.dsr.2007.10.007



จุฬาลงกรณ์มหาวิทยาลัย  
**CHULALONGKORN UNIVERSITY**

## VITA

**NAME** PACHARAMON SRIPOONPAN

**PLACE OF BIRTH** Nakhonpathom, Thailand

**INSTITUTIONS ATTENDED** She completed the Bachelor of Science Degree in field of Marine Science at the Department of Marine Science, Faculty of Science, Chulalongkorn University, and graduated on June 11, 2018.



จุฬาลงกรณ์มหาวิทยาลัย  
CHULALONGKORN UNIVERSITY